



UNIVERSITY of the
WESTERN CAPE

A MULTI-WAVELENGTH STUDY OF POWERFUL
HIGH REDSHIFT RADIO GALAXIES

by
Enos Takalani Marubini

Supervisor: Prof. R. Maartens, University of the Western Cape
Co-supervisor: Prof. M. J. Jarvis, Oxford University

*A dissertation submitted in partial fulfillment of the requirements
for the degree of
Doctor of Philosophy
University of the Western Cape
Department of Physics and Astronomy*

03 November 2021



UNIVERSITY *of the*
WESTERN CAPE

Abstract

We present a new sample of distant powerful radio galaxies, in order to study their host-galaxy properties and provide targets for future observations of HI absorption with new radio telescopes. We cross-match the Sydney University Molonglo Sky Survey radio catalogue at 843 MHz with the VISTA Hemisphere Survey near-infrared catalogue using the Likelihood Ratio technique, producing contour plots as a way to inspect by eye a subset of bright sources to validate the automated technique. We then use the Dark Energy Survey optical and near-infrared wavelength data to obtain photometric redshifts of the radio sources. We find a total of 249 radio sources with photometric redshifts over a 148 square degree region. By fitting the optical and near-infrared photometry with spectral synthesis models, we determine the stellar masses and star-formation rates of the radio sources. We find typical stellar masses of $10^{11} - 10^{12} M_{\odot}$ for the powerful high-redshift radio galaxies. We also find a population of low-mass blue galaxies. We then report results from the first search for associated HI 21 cm line absorption with the new MeerKAT radio telescope (shared-risk early science programme). We used a 16-antenna sub-array of MeerKAT to carry out a survey for HI absorption in the host galaxies of nine powerful ($L_{1.4\text{GHz}} > 10^{26} \text{ W Hz}^{-1}$) radio galaxies at cosmological distances ($z = 0.29$ to 0.54). We found no evidence of absorption with 5σ optical depth detection limits. We only obtain a tentative absorption towards a radio source 3C 262 at $z = 0.44$ with significant ongoing star formation at a rate of $10.5 M_{\odot} \text{ yr}^{-1}$. The source consists of two radio lobes separated by 28.5 kpc with no evidence of a compact core. If the absorption arises from neutral gas from an extended disc, the line is redshifted by $79(21) \text{ km s}^{-1}$ with respect to the nucleus and has an average HI column density across the source of $N_{\text{HI}} \sim 7 \times 10^{19-20} \text{ cm}^{-2}$, which is consistent with the rate of star formation. But after further tests, we find that the HI detection towards 3C 262 is likely to be an artefact. We conclude that the new correlator with 32 k channel resolution will be needed before searching for its associated absorption in MIGHTEE data.



UNIVERSITY *of the*
WESTERN CAPE

Declaration

I, Enos Takalani Marubini, declare that this thesis titled, “*A multi-wavelength study of powerful high redshift radio galaxies*” and the work presented in it are my own. I confirm that:

- This work was done wholly or mainly while in candidature for a research degree at this University.
- No part of this thesis has previously been submitted for a degree or any other qualification at this University or any other institution.
- Where I have consulted the published work of others, this is always clearly attributed.
- Where I have quoted from the work of others, the source is always given. With the exception of such quotations, this thesis is entirely my own work.
- I have acknowledged all main sources of help.
- Where the thesis is based on work done by myself jointly with others, I have made clear exactly what was done by others and what I have contributed myself.
- Chapter 3 is based on a paper done in collaboration with my co-supervisor and others: Marubini, T; Jarvis, MJ; Fine, S; Mauch, T; McAlpine, K; and Prescott, M; Published: Monthly Notices of the Royal Astronomical Society (MNRAS) 2019, Volume 489, Issue 3, p.3403-341.
- Chapter 4 is based on an early science project on MeerKAT, MHISHAPS (Principal Investigator Marubini, T), done with my supervisors and others.

Signed: 

Date: 03/11/2021



UNIVERSITY *of the*
WESTERN CAPE

Acknowledgements

Firstly, I would like to express my sincere gratitude to my advisor Prof. Roy Maartens for the continuous positive support contributing to the success of my PhD study, for his patience, and motivation. His guidance helped me in all the time of research and writing of this thesis. I could not have imagined having a better advisor and mentor for my PhD study.

My sincere gratitude also goes to Prof. Matt Jarvis for his commitment, immense knowledge and related research topics, who provided me with an opportunity to join their team in Oxford University, which gave me access to the research facilities. I especially want to thank Dr. James Allison who was helpful for the work with the MHISHAPS collaboration project. Without their precious support, it would not have been possible to conduct this research.

A very big thanks to the University of the Western Cape Astro-group staff and students for their cooperation and of course friendship. I am also grateful to the following: Dr. Tom Mauch, Dr. Kim McAlpine, Dr. Stephen Fine and Dr. Matt Prescott for their unfailing support and assistance.

Dr. Obed Shirinda for always being available for moral support, encouragement and time he spent in proof reading this work.

I would like to thank my friends: Prof. Mboniseni Mulaudzi, Mr. Lufuno Mafhungo, Mr. Zwidofhelangani Khangale, Dr. Hangala Siachiwena for moral support they provided.

Last but not the least, I would like to thank my family: my mother Mrs. Tshinakaho Marubini and to my brothers: Joseph, Freddy, Aaron, and Fhulufhelo for supporting me throughout my studies. My daughter Unarine 'Mufunwa' Marubini every time after getting your smile and laugh I knew you were behind my studies and giving out all your support. I would like to thank my partner Fhulufhedzani Ramalisa who has been there cheering me up during the difficult time of my project.

Thank you all!!!



UNIVERSITY *of the*
WESTERN CAPE

Contents

1	Introduction	1
1.1	History of the Field	1
1.2	High-redshift Radio Galaxies	2
1.3	Properties of HzRGs	5
1.4	Searching for High-redshift Radio Galaxies	10
1.5	Relativistic Plasma	12
1.6	Ionised Gas of HzRGs	15
1.7	Neutral Gas	19
1.8	Star-Formation Rate in HzRGs	22
1.9	Molecular Torus	25
1.10	Dust Characterisation	29
1.11	Massive Stellar Hosts	31
1.12	Active Galactic Nuclei	35
1.13	Motivation and Aims of Thesis	39
2	Surveys Used in this Study: SUMSS, VHS and DES	41
2.1	SUMSS Survey	41
2.2	VISTA Hemisphere Survey	44
2.3	Dark Energy Survey	47
2.4	Conclusions	51
3	A New Sample of Southern Radio Galaxies	53
3.1	Introduction	53
3.2	The Likelihood Ratio	55
3.3	Photometric redshifts	60
3.4	The $K - z$ Relation	61
3.5	Stellar Masses of Radio Galaxies	62
3.6	Star Forming Galaxies	68
3.7	Conclusions	72

4 MeerKAT HI Study of High-powered AGNs	75
4.1 Introduction	75
4.2 MeerKAT Radio Telescope	77
4.3 Sample Selection	81
4.4 Observations and Data	82
4.5 Results and Discussion	83
4.6 Conclusions	88
5 Conclusions and Future Work	89
5.1 Future Work	90
A Tables of Radio Galaxy Properties	93
B Radio Galaxy Contour Plots	107
Bibliography	107



UNIVERSITY *of the*
WESTERN CAPE

List of Figures

1.1	Representation of the radiative-mode and jet-mode core engines of AGN	3
1.2	Example of FR-I galaxy	6
1.3	Example of FR-II galaxy	7
1.4	Radio to X-ray Spectral Energy Distribution (SED) of the radio galaxy 4C+23.56 at $z = 2.483$.	13
1.5	The redshifted HI absorption feature of 0902 + 34 at $z = 2.4$	20
1.6	The x- and y-axes represent the surface density of the molecular gas and surface density of the SFR, respectively.	24
1.7	CO emission toward the powerful radio galaxy 4C 41.17 at $z = 3.8$ with the Plateau de Bure Interferometre (PdBI).	27
1.8	Composite Hubble $K - z$ relation diagram of radio and optically selected galaxies, the red squares representing the radio galaxies.	33
1.9	Schematic view of the dust-torus-based unified model of radio-loud AGN	38
2.1	Sky coverage of VISTA surveys, superimposed on a 2MASS image of the entire sky. From Emerson et al. (2006).	46
2.2	The instrumental transmission as a function of waveband of Blanco/DECam.	49
2.3	The DES SVA1 Gold catalogue footprint in equatorial coordinates using a cartesian projection. From Dark Energy Survey Collaboration et al. (2016).	50
2.4	Sky coverage of the combined Dark Energy Survey and VISTA Hemisphere Survey DR3 (red background).	52
3.1	The magnitude distribution of the background galaxy number density	57
3.2	Method to estimate $1 - Q_0$. The solid yellow line is the best fit to the model $1 - Q_0 F(r)$, with $Q_0 = 0.395$. The points represent the data obtained by dividing the number of sources in the SUMSS catalogue without an NIR match by the number of random positions that did not have a NIR counterpart within radius r , i.e., $U_{\text{obs}}(r)/U_{\text{random}}(r)$.	58

3.3	The variation of the reliability as a function of the LR.	59
3.4	Rest-frame 843 MHz radio luminosity	61
3.5	K band (in Vega magnitude) versus redshift for radio galaxies from our SUMSS+DES+VHS (using the K_s band) catalogue (red circles). We also show the points from 6CE, 6C*, 7C-I, II, III and 3CRR complete samples, with colours denoted in the legend.	63
3.6	Comparison of mass of the two different stellar population synthesis (Bruzual & Charlot 2003, Maraston 2005) with $Z_m = 0.01$, and a total dust extinction in the range $0.0 < A_V < 0.3$	64
3.7	Comparison of mass of the two different stellar population synthesis (Bruzual & Charlot 2003, Maraston 2005) with $Z_m = 0.001$, and a total dust extinction in the range $0.0 < A_V < 0.3$	65
3.8	Comparison of mass of the two different stellar population synthesis (Bruzual & Charlot 2003, Maraston 2005) with $Z_m = 0.02$, and a total dust extinction in the range $0.0 < A_V < 0.3$	66
3.9	Comparison of mass of the two different stellar population synthesis (Bruzual & Charlot 2003, Maraston 2005) with $Z_m = 0.04$, and a total dust extinction in the range $0.0 < A_V < 0.3$	67
3.10	Redshift versus stellar mass for radio galaxies in our sample.	69
3.11	Source counts versus χ^2 -distribution for radio galaxies in our sample.	70
3.12	Stellar mass versus $g - r$ colour for the radio galaxies in our sample.	71
3.13	Radio luminosity against SFR derived using SED fitting in FAST for the host galaxies of the radio sources in our sample.	72
4.1	Overview of the 64 MeerKAT dishes distributed in two components.	78
4.2	HI absorption spectra from MeerKAT observations of our sample. The velocity axis is given in the rest frame defined by the AGN redshift. The grey shaded region denotes three times the rms noise. The red shaded regions indicated the positions of known spectral artefacts due to RFI and correlator issues.	85
4.3	Images of our radio AGN sample: SDSS I band (greyscale), FIRST radio (magenta contours), and MeerKAT radio (blue contours). Contours are given in units of -5, 5, 10, 20, 50, 100, 200, 500, 1 000, 2 000, 5 000, and 10 000 times the image rms noise. Note that MeerKAT contours are not shown for observations where the resolution was less than 1 arcmin.	86
B.1	108

B.2	109
B.3	110
B.4	111
B.5	112
B.6	113
B.7	114
B.8	115
B.9	116
B.10	117
B.11	118
B.12	119
B.13	120
B.14	121
B.15	122
B.16	123
B.17	124
B.18	125
B.19	126
B.20	127
B.21	128
B.22	129
B.23	130
B.24	131
B.25	132
B.26	133
B.27	134
B.28	135
B.29	136
B.30	137
B.31	138
B.32	139
B.33	140
B.34	141
B.35	142
B.36	143
B.37	144
B.38	145



B.39	146
B.40	147
B.41	148
B.42	149



UNIVERSITY *of the*
WESTERN CAPE

List of Tables

2.1	Description of some characteristics of MOST synthesis observations. From Bock et al. (1999).	42
2.2	Summary of the main system parameters of VISTA. From Sutherland et al. (2015).	46
4.1	Summary of our target sample.	84
4.2	Summary of our target sample (continued).	84
A.1	The new sample of 249 radio galaxies overlapping SUMSS+VHS+DES. The photometric redshifts given are from the DES SVA Gold data release. Looking at Sánchez et al. (2014) the typical 1σ photo-z accuracy of BPz is ~ 0.1	93
A.2	Table A.1 extended with further properties.	100





UNIVERSITY *of the*
WESTERN CAPE

Nomenclature

2MASS	Two Micron All-Sky Survey
3CR	Third Cambridge Catalogue of Radio Sources
3CRR	Third Cambridge Revised Version
7CRS	Seventh Cambridge Redshift Survey
AGN	Active Galactic Nuclei
ALMA	Atacama Large Millimetre Array
ADC	Analog to Digital Converter
ASKAP	Australian Square Kilometer Array Pathfinder
ATCA	Australia Telescope Compact Array
BP z	Bayesian Photometric Redshift
BL lac	BL Lacertae
BLR	Broad-Line Radio
CASA	Common Astronomy Software Application
CASU	Cambridge Astronomical Survey Unit
CCD	Charged Coupled Device
CMB	Microwave Background
CBF	Correlator/Beamformer
CTIO	Cerro Tololo Inter-American Observatory
CNM	Cold Neutral Medium
COSMOS	Cosmic Evolution Survey
CSS	Compact-Steep Spectrum
DES	Dark Energy Survey
EVLA	Expanded Very Large Array
FR-0	Fanaroff & Riley Class 0
FR-I	Fanaroff & Riley Class I
FR-II	Fanaroff & Riley Class II
FIR	Far-Infrared
FIRST	Faint Images of Radio Source at Twenty-cm
FITS	Flexible Image Transport System
FPGAs	Field-programmable Gate Arrays
FWHM	Full Width at Half Maximum
GMRT	Giant Metrewave Radio Telescope

GPS	Gigahertz-Peaked Spectrum
H-ATLAS	Herschel Astrophysical Terahertz Large Area Survey
HERG	High Excitation Radio Galaxy
H _z RG	High Redshift Radio Galaxy
HDF-N	Hubble Deep Field North
<i>HST</i>	<i>Hubble Space Telescope</i>
ID	Identity
IMF	Initial Mass Function
IGM	Intergalactic Medium
IR	Infrared
ISM	Interstellar Medium
ISRF	Interstellar Radiation Field
IC	Inverse Compton
VLA	Jansky Very Large Array
KAPB	Karoo Array Processor Building
LARGESS	Large Area Radio Galaxy Evolution Spectroscopic Survey
LERG	Low Excitation Radio Galaxy
LOFAR	Low Frequency Array
LR	Likelihood Ratio
LNM	Lukewarm Neutral Medium
MALS	MeerKAT Absorption Line Survey
MeerKAT	MeerKaroo Array Telescope
MIGHTEE	MeerKAT International GHz Tiered Extragalactic Exploration Survey
MIR	Mid-Infrared
MOST	Molongo Observatory Synthesis Telescope
MWA	Murchison Wide field Array
NLR	Narrow-Line Region
NRAO	National Radio Astronomy Observatory
NIR	Near-Infrared
H _I	Neutral Hydrogen
NVSS	NRAO VLA Sky Survey
OMT	Ortho-mode Transducer

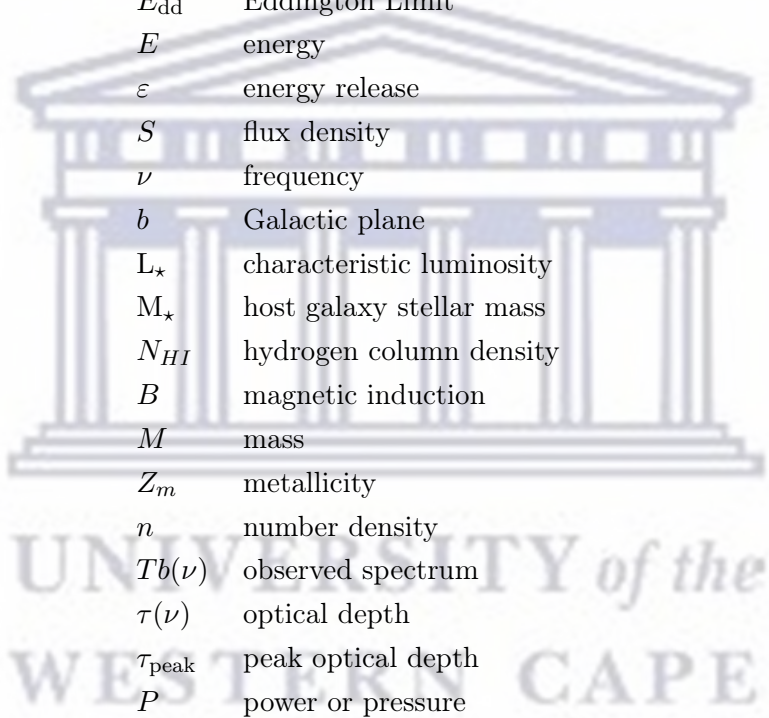
OVV	Optically Violet Variable
PDR	Photon-Dominated Region
PdBI	Plateau de Bure Interferometer
PFB	Polyphase Filter-bank
PSF	Point Spread Function
QSO	Quasi-Stellar Object
RFI	Radio Frequency Interference
RLF	Radio Luminosity Function
rms	Root Mean Square
SED	Spectral Energy Distribution
SLR	Stellar Locus Regression
SVA	Science Verification Archive
SNR	Signal-to-Noise Ratio
SSP	Simple Stellar Population
SDSS	Sloan Digital Sky Survey
SPT	South Pole Telescope
SLED	Spectral-Line Energy Distribution
SKA	Square Kilometer Array
SFH	Star-Formation History
SFR	Star-Formation Rate
SGC	South Galactic Cap
SLR	Stellar Locus Regression
SPS	Stellar Population Synthesis
SQL	Structured Query Language
SMBH	Supermassive Black Hole
SUMSS	Sydney University Molonglo Sky Survey
SR	Synchrotron Radiation
TFR	Time and Frequency Reference
UHF	Ultra High Frequency
ULIRG	Ultra-Luminous Infrared Galaxy
USS	Ultra-Steep Spectra
UV	Ultraviolet
VLA	Very Large Array
VLBI	Very Large Baseline Interferometry

VVDS	VIMOS VLT Deep Survey
VISTA	Visible and Infrared Survey Telescope for Astronomy
VDFS	VISTA Data Flow System
VHS	VISTA Hemisphere Survey
VIRCAM	VISTA Infrared Camera
VIKING	VISTA Kilo-degree Infrared Galaxy
VSA	VISTA Science Archive
VST	VLT Survey Telescope
WNM	Warm Neutral Medium
WSRT	Westerbork Synthesis Radio Telescope
WFAU	Wide-Field Astronomy Unit
WISE	Wide-Field Infrared Survey Explorer



UNIVERSITY *of the*
WESTERN CAPE

List of symbols



T_c	brightness temperature
χ	Chi
c_f	covering factor
δ	Declination
ρ	density
d	distance
A_V	dust extinction
E_{dd}	Eddington Limit
E	energy
ε	energy release
S	flux density
ν	frequency
b	Galactic plane
L_\star	characteristic luminosity
M_\star	host galaxy stellar mass
N_{HI}	hydrogen column density
B	magnetic induction
M	mass
Z_m	metallicity
n	number density
$Tb(\nu)$	observed spectrum
$\tau(\nu)$	optical depth
τ_{peak}	peak optical depth
P	power or pressure
r	radius
z	redshift
α	spectral index
α'	right ascension
σ_T	scattering coefficient
R_{Sch}	Schwarzschild radius
v	speed
T_s	spin temperature
sq deg	square degree
σ	standard deviation

Σ	surface density
T	temperature
M_v	visual magnitude
λ	wavelength

Astronomical Quantities

\AA	angstrom	10^{-10} m
G	gravitational constant	$6.624 \times 10^{-11} \text{ m}^3 \text{ kg}^{-1} \text{ s}^{-2}$
ly	light year	$9.461 \times 10^{12} \text{ km}$
L_{\odot}	luminosity of Sun	$3.86 \times 10^{26} \text{ W}$
M_{\odot}	mass of Sun	$1.99 \times 10^{30} \text{ kg}$
r_{\odot}	radius of Sun	$6.96 \times 10^8 \text{ m}$
\hbar	reduced Planck constant	$1.055 \times 10^{-34} \text{ J s}$
c	speed of light	$2.998 \times 10^8 \text{ m s}^{-1}$
parsec	unit of distance	$3.09 \times 10^{16} \text{ m}$
ergs	unit of energy	$1 \times 10^{-7} \text{ J}$



UNIVERSITY *of the*
WESTERN CAPE

Chapter 1

Introduction

The population of powerful radio galaxies is among the largest, most luminous, most massive galaxies at their redshift and spectacular sources in the Universe. They are the most energetic sources of radiation across the entire electromagnetic spectrum. It is assumed that radio sources are driven by the matter that accretes onto Supermassive Black Holes (SMBHs) in the nuclei of their host galaxies. Not only are powerful radio galaxies in their own right interesting sources, but they also have many features that make them special to explore the early Universe.

1.1 History of the Field

The research of distant powerful radio galaxies has matured in many phases ([Miley & De Breuck 2008](#)):

1. Inception. *Middle of 1940s and middle of 1960s*: Radio astronomy has become one of the most essential tools of observational cosmology following the discovery that Cygnus A is associated with a faint, distant galaxy (e.g., [Baade & Minkowski 1954](#)). In galaxies that are correlated with radio sources, measurements of redshifts of up to $z = 0.45$ have been obtained ([Minkowski 1960](#)).
2. Early developments. *Middle of 1960s and middle of 1980s*: With the 120-inch telescope at Lick, Spinrad spent much of his time determining the redshifts of faint radio galaxies utilising long exposures. Spinrad was able to detect the highest redshift radio galaxy out to $z \sim 1$ ([Spinrad 1976](#), [Spinrad et al. 1977](#), [Smith & Spinrad 1980](#)). During this period, radio sources were not known to interact with their optical hosts, and generally the different wavelength regimes were studied in isolation from each other. They were not assumed to play a vital role in the scheme of galaxy evolution at this time.

3. Youth. *Middle of 1980s and middle of 1990s*: Optical astronomy was revolutionised by the substitution of photographic techniques with Charged Couple Devices (CCDs). With this upgrade, significant numbers of very distant radio galaxies have been discovered with redshifts of up to $z \sim 5$. Surprisingly, the radio sources and the optical host galaxies' alignment revealed that there had to be a strong correlation between the radio source and their host galaxies.
4. Adulthood. *Middle of 1990s to the present*: New effective methods for detecting distant galaxies have been developed. This included photometric searches of “dropout” objects with redshifted Lyman break features as well as narrow-band searches for objects with excess redshifted Lyman fluxes. For example, the two-colour plane and the selection function given by Dickinson (1998) is a very instructive visual representation of the “drop-out” technique for a galaxy at $z = 3$. The advent of these new techniques has offered a fresh insight into the cosmological use of radio galaxies. It became evident that luminous radio galaxies play a significant role in galaxy evolution and large-scale structure formation. The discovery of association between the masses of elliptical galaxies and the inferred masses of nuclear black holes highlighted the possibility that, at some stage in their history, all galaxies may have experienced nuclear activity. The powerful radio galaxy populations will be the focus of this thesis.

In this Chapter, High-Redshift Radio Galaxies (HzRGs) are discussed in Section 1.2, properties of high-redshift radio galaxies are discussed in Section 1.3, a search for high-redshift radio galaxies is discussed in Section 1.4, Section 1.5 presents the relativistic plasma found in these galaxies, ionised gas is discussed in Section 1.6, neutral gas is discussed in Section 1.7, the star-formation rate is discussed in Section 1.8, Section 1.9 presents the molecular torus, dust is discussed in Section 1.10 and massive stellar hosts are discussed in Section 1.11. In Section 1.12 I discuss the AGN. Finally, in Section 1.13 I give a motivation and present the aims of this study.

1.2 High-redshift Radio Galaxies

In this Section, we discuss the existence of HzRGs, and how these structures fit into general galaxy evolution schemes.

There are many arguments in support of the conclusion that HzRGs are massive star-forming galaxies. First of all, their high Near-Infrared (NIR) luminosities suggest that they are among the largest galaxies in the early universe. Second, as predicted from galaxies formed by mergers and in conjunction with hierarchical models of massive galaxy evolution, HzRG hosts have clumpy Ultraviolet (UV) continuum

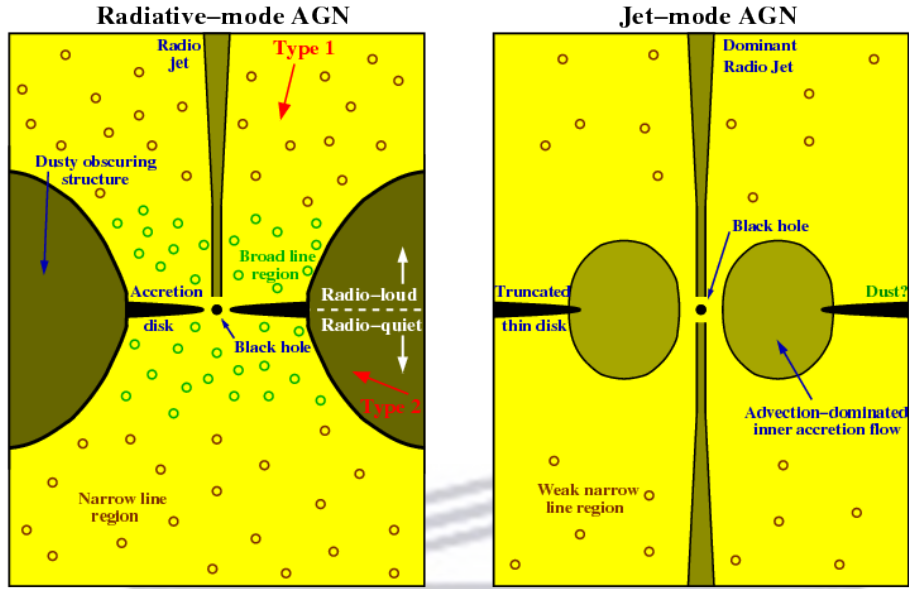


Figure 1.1: Representation of the radiative-mode and jet-mode core engines of AGN. (*Left panel*) a geometrically-thin, optically-thick accretion disc which reaches the radius of the inner core stable orbit around the central SMBH. The broad- and narrow-line emission regions are illuminated by luminous UV radiation from this accretion disc. The obscuring composition of dust molecular gas prevents direct line of sight views of the accretion disc and broad-line regions from some lines of sight e.g., type 2 AGN, while they are evident from others e.g., type 1 AGN. Powerful radio jets are generated by a small (about 10%) proportion of the sources. (*Right panel*) The AGN thin accretion disc in jet mode is substituted by a geometrically-thick advection-dominated accretion flow in the core region. A transition to an outer thin disc with larger radii may occur. Most of the energetic output of these sources is released by radio jets in bulk kinetic form. Radiative emission is much weaker, but can ionise weak low-ionisation narrow-line region, particularly where the truncation radius of the thin disc is relatively low. From Heckman & Best (2014).

morphologies (Larson 1992, Dubinski 1998, Gao et al. 2004a, Springel et al. 2005), see Section 1.11. Third, the rest-frame UV spectra and millimetre Spectral Energy Distribution (SED) suggest HzRGs are undergoing vigorous star formation (Dey et al. 1997), see Section 1.11.

HzRGs are not only responsible for the formation of massive galaxies, but they are also the progenitor of the most massive galaxies in the local universe, i.e., the giant galaxies that are found in the regions surrounded by the rich local galaxy clusters, see Section 1.6.

Generally, what do we learn from studying the structure of HzRGs in the evolution of massive galaxies? Most importantly two mechanisms and model predictions

have been reported in faint galaxies to clarify the discrepancies between the colour and luminosity statistics detected. Contrary to what could be predicted from simple hierarchical merging scenarios, the results were in favour of the possibility that star formation occurs earlier in the history of the most massive galaxies than for the least massive galaxies. This process is known as galaxy ‘downsizing’ (e.g., [Cowie et al. 1996](#), [Heavens et al. 2004](#), [Thomas et al. 2005](#), [Panter et al. 2007](#)). Active Galactic Nuclei (AGN) preferentially reside in much denser regions associated with cluster environments. In order to quench star formation in more massive galaxies, it has been suggested that the AGN feedback mechanism has an effect on star formation in the history of the galaxy. The use of the AGN feedback mechanism ([Di Matteo et al. 2005](#), [Best et al. 2005](#), [Springel et al. 2005](#), [Croton et al. 2006](#), [Hopkins & Hernquist 2006](#)) offers additional parameters for modelers to provide the best fit to the data. The AGN feedback mechanism for the galaxy formation processes has become increasingly relevant after it has been demonstrated that an SMBH may be found at the centre of each galaxy, see [Section 1.12](#), providing a general relation between galaxies and AGN.

H_zRGs are essential laboratories for the study of the downsizing and AGN feedback mechanism. Practically, feedback scenarios are complex, and often multiple simultaneous physical processes are required for the success of these models. As galaxies merge, the satellite galaxies exchange gas with the system’s ambient medium. The fuel for the SMBH is produced as the gas moves inward through cooling and accretion. The relativistic jets and quasars are generated by SMBHs. As a result, the dust is heated up by a hidden and/or dormant quasar. Both radio jets and superwinds from starbursts ([Armus et al. 1990](#), [Zirm et al. 2005](#)) push plasma outwards ([Nesvadba et al. 2006](#)) and may cause a substantial level of star-formation. Furthermore, shocks would be rampant in the chaotic environments where these processes compete with each other.

There are two major types of the AGN feedback mechanism as described in theoretical models for the coupling of the AGN energy production to the surrounding gas. First, ‘Quasar-mode’ also known as the ‘radiative mode’, see [Figure 1.1](#). This feedback mechanism occurs only in the wake of large gas-rich galaxy mergers ([Hopkins & Hernquist 2006](#)). Second, ‘radio-mode’ coupling or ‘kinetic mode’ ([Best 2007](#)), is attributed to radio jets, see [Figure 1.1](#). The star formation is slowed down by the mechanical energy of the synchrotron radio jets that inhibit cooling flows of the ambient gas. An excellent recent review of the AGN feedback mechanism has been provided by [Heckman & Best \(2014\)](#).

1.3 Properties of HzRGs

HzRGs are characterised by various spectral regimes that have several properties that distinguish them from their low-redshift counterparts

Redshift Distribution of HzRGs

The redshift distribution of HzRGS indicates that typical luminosities are characterised by $L_{2.7\text{GHz}} > 10^{33} \text{ erg s}^{-1} \text{ Hz}^{-1} \text{ sr}^{-1}$ in the redshift range $2 < z < 5$ (Willott et al. 2001, Venemans et al. 2007) with number densities of about 10^{-8} Mpc^{-3} . This possibly indicates that they are extremely rare. The analysis of co-moving space density of the most luminous steep-spectrum radio sources shows evidence of significant increase in the redshift range $0 < z < 2.5$ by a factor of 100 – 1000 and then it begins to flatten out at $z > 2.5$ (Willott et al. 2001, Jarvis et al. 2001c). While the evolution of the luminosity function at highest redshifts includes huge uncertainties, no substantial cut-off in space density has yet been reported. Interestingly, when the radio sources' space density is maximum, a critical period is reached in the evolution of the Universe: not only is it the time in which the Star Formation Rate Density (SFRD) increases by more than an order of magnitude, but also the time in which the most luminous quasars tend to reach their highest space density (Pei 1995, Fan et al. 2001, Madau et al. 1998) and the epoch in which galaxy clusters began to evolve. The question of what happened when the most luminous radio sources including the most luminous quasars became extinct in the local Universe is still poorly understood.

Radio Galaxy Redshifts and Morphologies

Using the Fanaroff-Riley (FR) system, the powerful extended radio sources can be roughly divided into two groups, the FR-I (see Figure 1.2) sources are brightest near the centre, while the FR-II (see Figure 1.3) sources with double structures are brightest near the edges of the lobe (Fanaroff & Riley 1974). Radio galaxies with one or more hot spots positioned at the extremities of their lobes are additionally associated with more collimated jets (Miley 1980, Carilli et al. 1994; 1997, Pentericci et al. 2000). Another significant difference in radio source morphology is the luminosity between the two groups, with the more powerful FR-II sources having $L_{1.4\text{GHz}} \gtrsim 10^{25} \text{ W Hz}^{-1}$, whereas the FR-I sources are predominantly luminous below this value. Recently, a further classification category known as the FR-0 radio galaxies (e.g., Sadler et al. 2014, Baldi et al. 2015) has been added, the members most of which lack the usual extended emission typical of FR-I and FR-II sources.

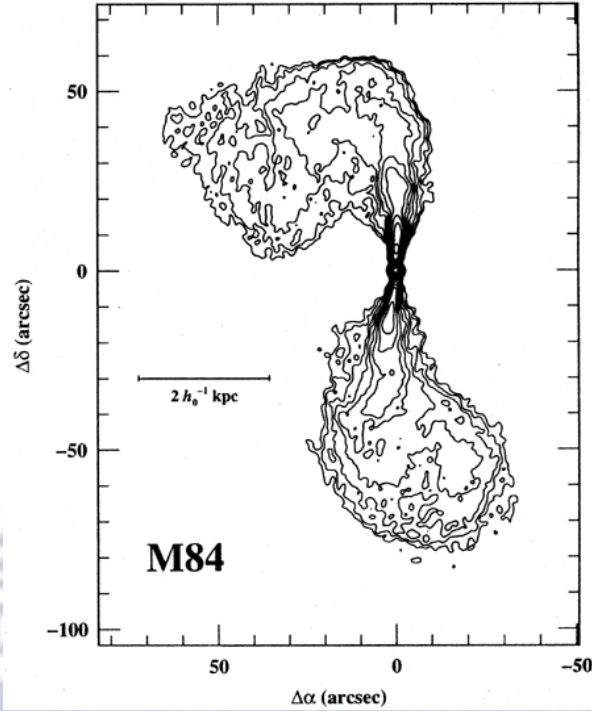


Figure 1.2: Example of FR-I galaxy. This is a radio map of the Virgo cluster elliptical galaxy M84 (3C 272.1 = NGC 4373), based on VLA 4.9 GHz results. From [Peterson \(1997\)](#).

Generally, powerful radio sources are usually not associated with a flat-spectrum at their nuclei and the use of the ultra-steep spectrum criterion in searching for powerful radio sources discriminates against finding HzRGs with flat-spectrum cores. It is now well known that the host galaxies of powerful FR-II sources are most frequently associated with ellipticals which offer some traces of recent interactions between galaxies ([Heckman et al. 1986](#), [Zirbel 1996](#)).

For radio astronomy one of the most useful techniques is the Very Long Baseline Interferometry (VLBI). Several powerful radio sources associated with HzRGs have been observed using the VLBI technique ([Gurvits et al. 1997](#), [Cai et al. 2002](#), [Pérez-Torres & De Breuck 2005](#), [Pérez-Torres et al. 2006](#)). [Pérez-Torres et al. \(2006\)](#) reported a 65 pc component several kpc away from the radio galaxy nucleus 4C 41.17 at $z = 3.8$. Energy considerations suggest that the radio component is correlated with a $M \geq 1.5 \times 10^8 M_{\odot}$ mass of clumpy gas ([Miley & De Breuck 2008](#)). This is remarkably representative of the masses of ‘pre-disrupted clumps’ known as the progenitor globular clusters ([Fall & Rees 1977](#)). The use of the VLBI technique is important for the analysis of fine scales in radio galaxies and exploration of radio

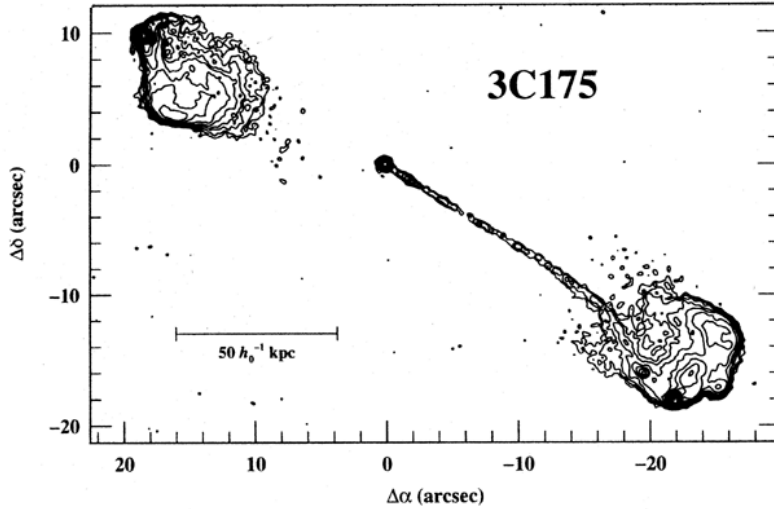


Figure 1.3: Example of FR-II galaxy. This is a map of the $z = 0.768$ quasar 3C 175, as observed with the VLA at 4.9 GHz (Peterson 1997). The quasar itself coincides with the compact bright source at $(\Delta\alpha, \Delta\delta) = (0, 0)$.

jet interactions in the Interstellar Medium (ISM) of the early Universe. The Square Kilometre Array (SKA) pathfinder telescopes and upgrades are especially exciting with the potential of enhanced Multi-Element Remote-Linked Interferometer Network (e-MERLIN), Very Large Array (VLA), European VLBI Network (e-EVN), and MeerKaroo Array Telescope (MeerKAT) to study selected areas and sources with extremely high sensitivity and resolution.

Three observational aspects that are related to radio sources size (Röttgering et al. 2000) are:

1. A connection with optical morphology for 3CR radio sources at $z \sim 1$. Smaller linear size (< 150 kpc) radio sources have multiple bright optical knots positioned around the radio axis, whereas larger sources are less lumpy and aligned (Best et al. 1998a).
2. A connection with the UV-emission line properties of 3CR radio galaxies at $z \sim 1$. In general, smaller linear size radio sources consist of lower ionisation, higher emission line fluxes and broader line widths than larger sources (Best et al. 1999).
3. A link with $Ly\alpha$ absorption. Powerful radio sources with smaller radio scales are more likely to have $Ly\alpha$ absorption than larger sources (van Ojik et al. 1997), see Section 1.7.

All of these observations are in broad consistency with an evolutionary scenario where

radio scale may be used as a “clock” that tracks the time elapsed in its environment while moving away from the host radio activity. It should be recalled that the large sizes of radio sources (generally many tens of kpc) suggest that the host galaxy nucleus has been undergoing activity for at least $> 10^5$ yr up to $> 10^8$ yr. Hence, it is now well understood that AGN correlated with extended radio sources must be long-lived. This is not valid for quasars or radio-quiet galaxies, which could have been active quasars for a few hundred years (Miley & De Breuck 2008).

High- and Low-redshift Radio Galaxies

1. The significant feature of extended extragalactic radio sources is the non-thermal spectra properties, with spectral indices of $\alpha \sim 0.7$ (Condon et al. 1998a). In general, the radio spectrum has an approximate power-law form, $S_\nu \propto \nu^{-\alpha}$, where S_ν is the flux density and ν is the frequency.
2. The majority of radio sources detected in high-frequency radio surveys are compact and are embedded in lobes with smaller scales typically < 1 pc and have relatively flat spectral indices, $\alpha < 0.4$.
3. There are just a limited fraction of extragalactic sources with linear scales varying from 100 pc to a few kpc. Such sources have peaked spectra that are self-absorbed synchrotron emission that peaks at ~ 100 MHz up to a few GHz and are referred to as Gigahertz-Peaked Spectrum (GPS) sources (O’Dea et al. 1991) or Compact-Steep Spectrum (CSS) sources (Dallacasa et al. 1993, Fanti & Fanti 1994).

Radio galaxies and quasars comprise all three types of extragalactic sources, with extended radio sources primarily related to galaxies and compact sources primarily related to quasars.

Radio Size and Redshift Correlation

Since the 1960s, it has been recognised that there is a pronounced decrease of the angular scale of radio sources (Miley 1968) with redshift. Several authors measured the angular size-redshift ($\theta - z$) relation for luminous extended radio sources (e.g., Nilsson et al. 1993, Neeser et al. 1995, Daly & Guerra 2002), compact radio sources (Gurvits et al. 1999) and quasars (Buchalter et al. 1998).

Over a decade, a variety of attempts have been made to utilise the $\theta - z$ relation to extract information on the structure of the Universe such as the determination of deceleration (q_0) and mass density (Ω_0) parameters, and also to impose limits on

dark energy (e.g., Podariu et al. 2003). In addition, as there are several observational selection effects, differentiating between the various structures of the Universe and the physical evolution of the radio sources is difficult, as well to differentiate between the host galaxy and the surrounding medium. Consider the sizes of radio sources which decrease as redshift increases due to a gradual change in the density of the ambient medium. The energy density of the Cosmic Microwave Background (CMB) rises as $(1+z)^4$, and this significantly enhances Inverse Compton (IC) losses (Krolik & Chen 1991). Therefore, it would continue to extinguish radio sources early in their lives, making them smaller on average.

Because of several non-cosmological effects, the $\theta - z$ relation has rendered it difficult to draw conclusions regarding cosmology from these analyses.

Radio Spectral Index vs Redshift Correlation

One of the most successful relations regarding the relativistic plasma in HzRGs is based on the relation between the radio source spectral index and the association of the redshift of radio galaxies (e.g., Tielens et al. 1979, Blumenthal & Miley 1979, Chambers et al. 1996). While the Ultra-Steep Spectrum (USS; $\alpha \leq 1$) of radio galaxies is not a fundamental requirement for the detection of high redshifts and, in addition, the USS selection misses a potentially significant fraction of the HzRGs (e.g., Waddington et al. 1999, Jarvis et al. 2001b; 2009, Schmidt et al. 2006), a higher fraction of high-redshift sources may be classified from those with the steepest radio spectra. Nevertheless, this observational connection between radio spectral steepness and redshift has proven to be an effective tool for identifying the most massive radio galaxies (De Breuck et al. 2000, Jarvis et al. 2004, Cruz et al. 2006).

For the $z \sim \alpha$ correlation explanations, the first one is the K -correction. In this case, the observed SED of the radio spectrum is generally concave as a result of the spectral index increasing with frequency (Bornancini et al. 2010). As a result, the observed spectral index measured at a defined observed frequency would be sampled at higher rest-frame frequencies where the concave spectrum is steeper.

In observing the relation of $z \sim \alpha$, one of the possibilities is that the $z \sim \alpha$ relation is an inverse manifestation of luminosity, the effect of $L \sim \alpha$ (Chambers et al. 1990, Blundell & Rawlings 1999). The observed $z \sim \alpha$ relation can be explained as predicted in classical Synchrotron Radiation (SR). This theory predicts that the continuous particle injection will give rise to a low-frequency cut-off (ν_l), the frequency of which depends on the source luminosity (L). Taking into account the selection of a flux-limited sample of radio sources, Malmquist bias (Malmquist 1924) would make higher redshift sources preferably the most luminous sources. The Malmquist bias

is an observational phenomenon that leads to the selective detection of intrinsically bright sources. The effect of $L^{-6/7}$ versus L will result in the observation of an $z \sim \alpha$ within the respective frequency range. However, this spectrum luminosity relation is unlikely to be the right explanation. Athreya & Kapahi (1998) reported that a $z \sim \alpha$ relation still exists, despite that samples being limited to a small range of L .

Another theory is based on some physical effect that induces steepening of the spectral index with higher ambient density and that raises the ambient density with redshift (Athreya & Kapahi 1998, Klamer et al. 2006). When a radio source is in a denser environment this allows the velocity of the relativistic particles upstream to decrease, as result, a steeper synchrotron spectrum will be produced by the first-order Fermi acceleration mechanism. Klamer et al. (2006) demonstrated that a mechanism for first-order Fermi acceleration would give rise to a similarity between $z \sim \alpha$ and $L \sim \alpha$, as well as a natural physical connection between HzRGs and nearby cluster halos.

All theories have problems in completely reproducing the $z - \alpha$ correlation observed, which means that the cause of this phenomenon is still uncertain and that more detailed information is required on the redshift dependence of the radio spectra.

1.4 Searching for High-redshift Radio Galaxies

The population of the most massive radio galaxies is relatively small, which indicates that they are both rare and challenging to find. There are several steps involved in obtaining the catalog of distant radio galaxies, and these steps are described in four primary aspects:

1. Filtering of HzRGs from a large volume of radio sources (e.g., Röttgering et al. 1994, Blundell et al. 1998, De Breuck et al. 2000; 2004) by a process that accounts for the (i) radio colour (i.e., spectral steepening) parameter and (ii) minimal angular scale.
2. Most luminous nearby radio sources are filtered out through matching radio positions with wide-field shallow surveys in both optical and Infrared (IR) wavelengths.
3. The radio source positions are optimised to arc-sec precision to identify their counterparts in optical and NIR wavelengths. Radio identifications were performed using optical Charged Coupled Device (CCD) data (e.g., Röttgering et al. 1995, McCarthy et al. 1996) until the 1990s. With the advent of sensitive NIR detectors in the early 1990s, fortunately, it was noted that the NIR K

band was more effective for the detection of HzRGs (e.g., [Jarvis et al. 2001a](#), [De Breuck et al. 2002](#), [Willott et al. 2003](#), [De Breuck et al. 2004](#), [Jarvis et al. 2004](#), [Cruz et al. 2006](#)). The NIR K band magnitude can detect above 94% of luminous radio sources that are observed down to $K = 22$ ([McAlpine et al. 2012](#)). In addition, the K -band magnitude of massive radio sources provided an initial identification of its redshift, using the Hubble $K - z$ relation, see [Section 1.11](#).

4. Conducting spectroscopic follow-up measurements of the remaining HzRG candidates using large optical and IR telescopes, which are important for redshift estimation utilizing emission lines (e.g., [Röttgering et al. 1997](#), [De Breuck et al. 2001](#), [Jarvis et al. 2001b](#), [De Breuck et al. 2006](#), [Bornancini et al. 2007](#)).

The difficulty in discovering HzRGs was the lack of sufficient observation time for the final step in the process on large optical/IR telescopes. Moreover, these galaxies are located far apart enough in the sky that multi-object spectroscopy is not possible. However, many independent fields have to be considered when determining the redshifts of HzRG candidates.

Departing from the fact that radio selection ensures that dust properties are not selected *a priori*, the first apparent cause of bias is that the spectroscopic redshift determination relies on the ability to detect bright emission lines with optical and NIR surveys. The principal line luminosity for these redshift estimations (e.g., [McCarthy 1993](#)) is $Ly\alpha$ $\lambda 1216 \text{ \AA}$ (typically with equivalent widths of several hundred). Other important emission lines that are strongly useful are C IV $\lambda 1549 \text{ \AA}$, HeII $\lambda 1640 \text{ \AA}$ and CIII] $\lambda 1909 \text{ \AA}$ (equivalent widths in excess of ~ 60). The redshift range $1.2 < z < 1.8$ is known as the “redshift desert” due to historical difficulties in obtaining spectroscopic redshifts in this range (e.g., [Cruz et al. 2006](#)). This suggests that the HzRG samples in the “redshift desert” are always under-represented in any form.

The second source of bias is due to both unreliability and incompleteness in the redshift distribution. There is no identification down to $K \sim 22$ for a tiny fraction ($\sim 4\%$) of radio sources and around one-third of those with K -band detection display neither emission nor absorption lines. This is true even after long exposure times used by the largest optical/IR telescopes with apertures of about 10 m. Such artifacts include ([De Breuck et al. 2001](#), [Reuland et al. 2003](#)):

1. Emission lines arising from obscuration of significant dust obscuration, or
2. at greater redshifts, $Ly\alpha$ and other bright emission lines fall outside the observable spectral window, or

3. based on their characteristics, these radio sources do not radiate powerful emission lines.

Constituents of the High-redshift Radio Galaxies

There are numerous emitting components of radio galaxies that provide a variety of diagnoses for early Universe physical constituents. As they are extremely luminous and spatially resolved (unlike quasars) from Earth, most of the HzRG components offer valuable descriptive details regarding the spatial distribution of processes inside and around HzRGs. The idea that various components are found in the same objects, and that it is possible to study the interconnections and correlations between them, allows HzRGs to provide special laboratories for exploring the early Universe.

Figure 1.4 displays a typical HzRG Spectral Energy Distribution (SED) from radio to X-ray wavelengths, alongside a disintegration into different observable radio galaxy components such as relativistic plasma, gas and dust emission, massive stellar host and AGN.

The host galaxies of HzRGs have large stellar mass (up to $10^{12} M_{\odot}$) and molecular gas with mass up to $10^{11} M_{\odot}$ (Miley & De Breuck 2008). In Section 1.5 to 1.11 each of the building blocks of radio galaxies will be discussed individually. These building blocks play a vital role in the diagnosis of early Universe physical conditions.

Note that it is challenging to distinguish between the various optical and IR components, see Figure 1.4 and the results are always highly model-dependent, so some alternative approach may be equally consistent with the available multi-wavelength data.

1.5 Relativistic Plasma

Following the discovery of extragalactic radio sources (i.e., galaxies beyond of our own Milky Way), their spectral properties and polarisation led to the hypothesis that their emission was triggered by SR from relativistic electrons spiraling through the magnetic field. The high luminosity of these radio sources, along with the lifetime of the synchrotron-emitting electrons imply a total energy of $\geq 10^{60}$ erg (Miley 1980). Such an enormous amount of energy confined to small scales, and the resemblance in orientation between the compact and general radio structures contributed to the hypothesis that collimated relativistic beams are produced by spinning SMBHs situated at the core of the host galaxies.

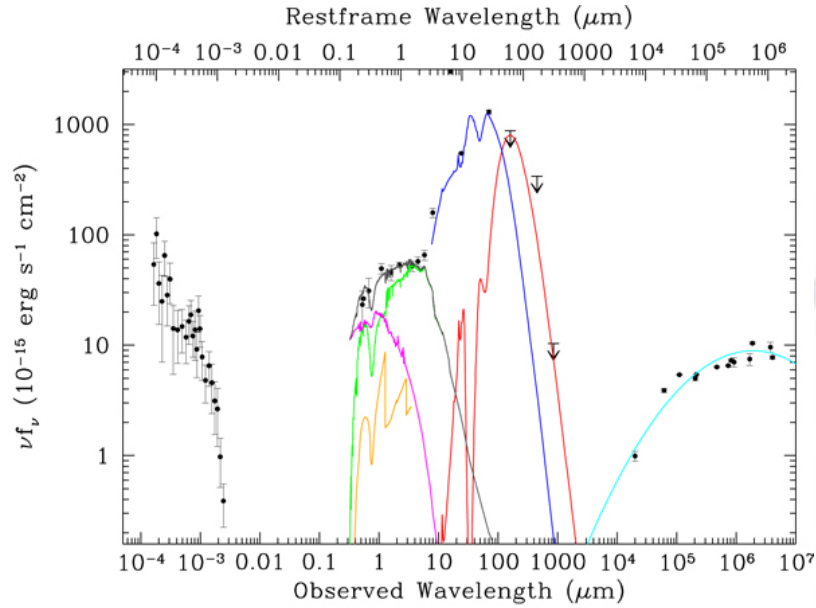


Figure 1.4: Radio to X-ray Spectral Energy Distribution (SED) of the radio galaxy 4C+23.56 at $z = 2.483$. Coloured lines show the decomposition of the SED into various related components, under several assumptions. The direct line of sight to the nucleus is blocked by an obscuring torus that absorbs soft X-ray radiation that is re-emitted as hot thermal dust emission (blue). Radiation escaping through the opening of the torus is scattered towards the observer providing a unique view of the nucleus (magenta). Radiation produced by the interstellar medium from the nebular continuum emission is indicated by orange. The massive stellar host galaxy is directly observed in the NIR (green) rest-frame, whereas obscured starburst is confirmed by sub-millimetre cool dust re-emission (red). The bolometric effects from the accretion to the SMBH are strikingly identical to the stellar nucleosynthesis. From [Fosbury et al. \(2007\)](#).

Non-thermal X-ray Emission of HzRGs

While powerful radio galaxies have sensitive limitations in the X-ray measurements, progress has significantly improved over the past two decades with the advent of *Chandra* and *Multi-Mirror Mission-Newton (XMM Newton)* X-ray telescopes. About twelve HzRGs and radio-loud quasars have detection of extended X-ray emission (Scharf et al. 2003, Belsole et al. 2004, Overzier et al. 2005, Blundell et al. 2006, Erlund et al. 2006, Johnson et al. 2007). The physical connection between the X-ray emission and the relativistic plasma is supported by the detection of an elongated X-ray emission in the direction of the radio source.

There are many processes that are responsible for producing the extended X-ray emission over large scales and the most widely recommended is the Inverse Compton (IC) scattering of the CMB (Fabian et al. 2003, Scharf et al. 2003, Belsole et al. 2004, Erlund et al. 2006, Johnson et al. 2007). In addition to radiation field energy density of CMB photons that increases as $(1+z)^4$, IC scattering of the CMB becomes increasingly important when the jets are relativistic. The analysis of radio and X-ray luminosities (Felten & Rees 1969) producing magnetic field strength associated with equipartition (Belsole et al. 2004, Overzier et al. 2005, Johnson et al. 2007) depends on the assumptions that the X-ray emission is associated with IC scattering. Furthermore, since the radiative lifetimes of (highly energetic) radio SR-emitting electrons are typically shorter than those of (less energetic) lifetimes of the X-ray emitting IC electrons, the IC emission traces older particle populations. However, at redshift $z < 1$, the energy density of the CMB is low and the IC of the CMB (IC) emission is predicted to be the most important in sources where the jets are relativistic (Tavecchio et al. 2000, Erlund et al. 2006). Johnson et al. (2007) presented an *XMM Newton* observation of the radio galaxy 4C 23.56 at $z = 2.48$. They found that the X-ray emission coincides with the ~ 0.5 Mpc radio lobes, suggesting that the energy in both relativistic and IC emitting electrons is $\geq 10^{59}$ erg, an energy reservoir equivalent to $\sim 10^8$ supernovae.

Some processes involving the production of extended X-ray emission over broad spatial scales from these sources include:

1. thermal emission produced by shocks (Belsole et al. 2004),
2. inverse up-scattering of SR scattered in the jet (Synchrotron Self-Compton emission - SSC) (Scharf et al. 2003), and
3. photons provided by both SR and IC scattering (Harris & Krawczynski 2002).

1.6 Ionised Gas of HzRGs

Gas emission is an essential component of HzRGs in different states, and therefore play a fundamental role in their evolution. Gas in HzRGs has been observed over a wide range of temperatures and takes a variety of forms.

Warm ionised Gas

The bright emission lines produced by luminous radio galaxies enable the determination of their redshifts, which explains why they are such useful targets for probing conditions in the distant Universe. The emission lines are produced by warm gas of temperature of $\sim 10^{4.5}$ K and provide an important method for understanding physical conditions within the HzRGs.

AGN produce both ‘permitted’ recombination lines and ‘forbidden’ collisionally-excited emission lines. Once an atomic nucleus absorbs a free electron, it cascades into the ground state releasing a series of recombination lines. The two most abundant elements in the Universe, Hydrogen and Helium yield the most prominent recombination lines identified in the spectra of HzRG.

The brightest lines contained in the spectra of nebulae are referred to as ‘forbidden’ lines with a small probability of occurrence compared to the permitted lines. Their energy level lies within a few kT of the ground level, and can be effectively populated by collisions. Individual element has a critical density below which most of the de-excitation would be through radiation and, as a result, a spectral line is observed. Forbidden lines are formed only by gas with densities ranging from 10 to 10^5 cm^{-3} and the line ratios provide significant information on the physical condition of the density, temperature, ionisation and abundance of the emitting gas (e.g., [Osterbrock & Ferland 2006](#), [Peterson 1997](#)).

In the 1990s, the analysis of HzRGs using composite emission-line spectra found that, for HzRGs, nuclear emission lines were generally surrounded by emission lines from an additional component that is extremely spatially extended ([McCarthy 1993](#)). A remarkable feature of HzRGs is that they can be surrounded by giant haloes of luminous ionised gas ([Reuland et al. 2003](#)). The size of the gas nebula may reach regions of ~ 200 kpc and the analysis of this offers a wealth of information about kinematics, physical conditions inside and around the HzRGs and the origin of the gas surrounding the HzRGs.

Usually, the gas nebulae have $Ly\alpha$ luminosities of $10^{43.5} \text{ erg s}^{-1}$. The physical properties of the gas nebula as seen from the emission-line diagnostic tool ([Osterbrock & Ferland 2006](#)) have indicated a temperature of $T_e \sim 10^4 - 10^5$ K, density of $n_e \sim$

$10^{0.5} - 10^{1.5} \text{ cm}^{-3}$ and masses of $\sim 10^9 - 10^{10} M_{\odot}$. For HzRG, the estimation of filling factors for warm gas nebulae is $\sim 10^{-5}$, which is small compared to about unity filling factors for the hot gas nebula. The filling factor is the fraction of the background continuum filled by the absorbing gas. Using properties of the emission line and the covering factor diagnostic tools to model the nebula, [van Ojik et al. \(1997\)](#) demonstrated that the nebula is composed of $\sim 10^{12}$ clouds with sizes of ~ 40 light years, i.e., equivalent to our solar system. In addition, they hypothesised that these clouds may be correlated with early formation stages of individual stars.

The $Ly\alpha$ halo morphology is clumpy, irregular and its overall structure is often aligned with the radio axes, and sometimes extending beyond the size of the radio source. The nebula is defined by two distinct regimes, the inner and outer regions: the inner regions close to the radio jets and the outer regions. The analysis of the inner region using the emission line width revealed that the radio jet is clumpy with a velocity width of $\sim 1000 \text{ km s}^{-1}$ which is perturbed by the jets. However, the emission line width revealed that the outer regions contain more quiescent medium, with velocity ranges of a few 100 km s^{-1} (e.g., [Villar-Martín et al. 2003](#)). The outer regions are more relaxed than the inner regions.

Hence, it is possible to disentangle the effects of ionisation, abundances, densities and temperatures by the relative intensities of the emission line. Below is a detailed discussion of the physical conditions in the warm nebula gas.

Ionisation Mechanism

There may be various mechanisms for exciting the gas:

1. photo-ionisation attributed to an AGN,
2. photo-ionisation attributed to stars,
3. photo-ionisation from ionising X-ray photons emitted by shocked hot gas, and
4. collisional ionisation by shocks.

For nearby active galaxies, optical-line ratios were extensively utilised to study the ionisation of the gas, that provided evidence of jet- and accretion-powered shocks and central AGN photo-ionisation (e.g., [Villar-Martin et al. 1997](#), [Villar-Martin & Binette 1997](#), [Bicknell et al. 2000](#), [Groves et al. 2004](#)). These optical-line diagnostic diagrams were further developed for use in UV (e.g., [Allen et al. 1998](#), [Groves et al. 2004](#), [Feltre et al. 2016](#), [Hirschmann et al. 2019](#)), the spectral region of HzRGs sampled by optical observations. As a result of the dust emission and viewing angles, interpretation of emission line ratios are complicated. Moreover, most HzRG

spectra are spatially distributed across regions of 10 kpc or more, where conditions and excitation of sources may change. [Humphrey et al. \(2006\)](#) used 35 emission lines over the rest-frame UV and optical spectra. They concluded that the photo-ionisation in the quiescent gas is the dominant source of excitation. A harder source of photo-ionisation than stars is needed, consistent with photons from an AGN.

Here I describe the process of a quasar that excites the warm gas in the halo. The standard theory is that the quasar emits anisotropic radiation. It is strongly absorbed along the line of sight, see Section 1.10. This idea is supported by large optical polarisation estimated for some HzRGs. However, if the main cause of excitation is the highly anisotropic flux from a hidden quasar, it is hard to explain that all of the $Ly\alpha$ halo structures are roughly symmetric. Another theory is that quasar activity is both isotropic and highly variable. Despite the fact that quasar photo-ionisation is currently the best choice for the dominant source of excitation, it is unlikely to be the only primary cause. General characteristics of emission lines vary from object to object and then within each HzRGs are seen with high differences. There is strong evidence that there is additional collisional excitation due to shocks, especially near the radio jets (e.g., [Bicknell et al. 2000](#), [Best et al. 2000](#)), see Section 1.11

Kinematics

Kinematics of the ionised gas halos may indicate a nuclear turbulent regions, where there is evidence of outflows and outer passive regions, with the most likely dominant systematic motions are inwards. The slow shocked gas in the inner component is correlated with the radio lobes. Furthermore, the kinematics of the disrupted inner components have a velocity dispersion $> 1000 \text{ km s}^{-1}$ as well as evidence of the existence of starburst superwind in the $Ly\alpha$ halos ([Armus et al. 1990](#), [Zirm et al. 2005](#)). For certain sources, there are significant correlations between radio jets and their ambient gas, mostly in radio galaxies at low-redshifts ([Heckman et al. 1982; 1984](#), [van Breugel et al. 1984; 1985b;a](#)). The dynamics of the radio sources can be observed to excite the emission, disturb the gravity and penetrate the surrounding gas. Similarly, the gas can also have an impact on the jet due to the shock-driven particle acceleration by bending and decollimating the radio jets and increasing the intensity of their radio emission. [Best et al. \(2000\)](#) demonstrated that small-scale radio sources exhibit more jet-gas interactions than the large-scale radio sources, while for $z > 2$ shows far more extreme signatures of intense jet-gas interactions (e.g., [Villar-Martin et al. 1998](#), [Villar-Martín et al. 1999; 2003](#), [Humphrey et al. 2006](#)). The kinematics of gas perturbations and the ionisation states are greater in the region of the jet than in the more quiescent outer halo ([Humphrey et al. 2006](#)).

The kinematics in the outer components of the giant halos provide important clues as to the origin of the warm gas. The jet apparently keeps these outer components undisturbed. Such regions exhibit evidence of a structural change in velocity variations of a few hundred km s^{-1} , which could be the consequence of either rotation (e.g., van Ojik et al. 1996, Villar-Martín et al. 2003; 2006), outflows (Zirm et al. 2005, Nesvadba et al. 2006) or inflows of gas material. Differentiating between a variety of kinematic scenarios solely from velocity data is difficult, and thus integrating them with spectroscopic and radio data offers additional relevant detail. Interaction asymmetries between the kinematics of the halo and asymmetries in the radio structures were found in the analysis of 11 HzRGs at $2.3 < z < 3$ by Humphrey et al. (2007) and also by Villar-Martín et al. (2007). The quiescent nebula appears systematically redshifted on the brighter side of the radio jet as opposed to the fainter side of the radio jet.

The quiescent gas must travel inward, which implies that the bright radio jet is moving towards Earth, and because of Doppler boosting (Kellermann 2003), this is brightened, so that it is redshifted. The investigation of whether this infalling gas is a cooling flow can be carried out using the measurement of roto-vibrational lines from H_2 molecules at ~ 2000 K (Jaffe & Bremer 1997, Jaffe et al. 2005) as the diagnostic tool, since these lines for high-redshift sources shifts from the NIR to mid-IR bands that can be observed using *Spitzer* Space Telescope (Papovich 2008). Both the cooling flows in HzRGs and the excitation mechanisms can be investigated using the H_2 line as a diagnostic tool.

Kinematic studies of HzRGs have often used the $L\gamma\alpha$ feature, due to its relatively large equivalent width, which can be observed by optical telescopes. However, the $L\gamma\alpha$ feature is a resonant line and is subject to greater effects of scattering and optical depth. In addition, the resultant kinematics of the halo represented by $L\gamma\alpha$ feature might not be totally representative of the gas as a whole, with a particular emphasis on the inner components. Although these are considered to be useful diagnostic tools for understanding of the gas properties, they are complex and need substantial modelling.

Hot Ionised Gas

The study of HzRG X-ray observations show widespread hot ionised gas at the centre of clusters and around radio galaxies at low redshifts. The derived parameters of this gas are a temperature of $\sim 10^{7.5}$ K and density of $\sim 0.05 \text{ cm}^{-2}$ (Miley 1980). The gas with these physical properties is sufficient to confine the presence of the radio-emitting plasma and $L\gamma\alpha$ halo of HzRG, see Section 1.6. Bubble-like structures

observed in X-ray are produced by the injection of extra energy into a hot intracluster medium through jets for low and intermediate-redshift clusters (McNamara et al. 2000). In the present X-ray telescope generation, there is only marginally sufficient sensitivity to detect related nebula gas of up to $z \sim 2$, with $z = 2.2$ for the Spiderweb galaxy (Carilli et al. 2002). The nebular gas observed in X-ray emission along the axis of this radio source is linked with thermal emission generated by shocks as the relativistic synchrotron-emitting jet that propagates out of the galactic centre.

The effect on background polarisation might be used as a tool for detecting and analysing hot nebula gas (e.g., Miley 1980). As the linearly polarised radio emission propagates, the polarisation plane is rotated through an angle which scales as the square of the wavelength via a magnetoionic medium. This rotation is referred to as the Rotation Measure (RM), and a clear interpretation of high rotation measures is that HzRGs are located in dense gas. Ge & Owen (1994) found that high rotation measures for radio sources are detected at low redshifts in X-ray emitting clusters which are believed to be cooling flows. However, the large rotation measure observed in HzRGs implies that such objects are mostly located in cluster environments.

1.7 Neutral Gas

Cold HI gas in HzRGs can be studied using emission or absorption, although studying HzRG HI in emission is observationally challenging. For absorption, we calculate redshifted absorption of the 21 cm Hydrogen line against the bright radio continuum, and another approach is to analyse the deep narrow absorption troughs that are often present in the $Ly\alpha$ profiles. These approaches are useful in constraining physical properties of the HI of HzRGs like spatial sizes, masses, filling factor, spin temperatures and kinematics (Röttgering et al. 1999).

HI Absorption

Neutral Hydrogen (HI) atoms are much more abundant in low-density regions of the Interstellar Medium (ISM). They are observed via emission by a hyperfine spin-flip transition of the electron in the ground state of the Hydrogen atom at 1420.405751 MHz (~ 21 cm). Atomic HI observations through this line have been one of the most important diagnostic tools in radio astronomy ever since its inception. The study of the 21 cm HI line in absorption is essential to explore the presence and kinematics of the gas. While HI absorption is an essential diagnostic tool, such detection does not occur very commonly. Limitations of these HI searches in HzRGs include the availability of low-noise detectors covering the target redshift frequency detection band

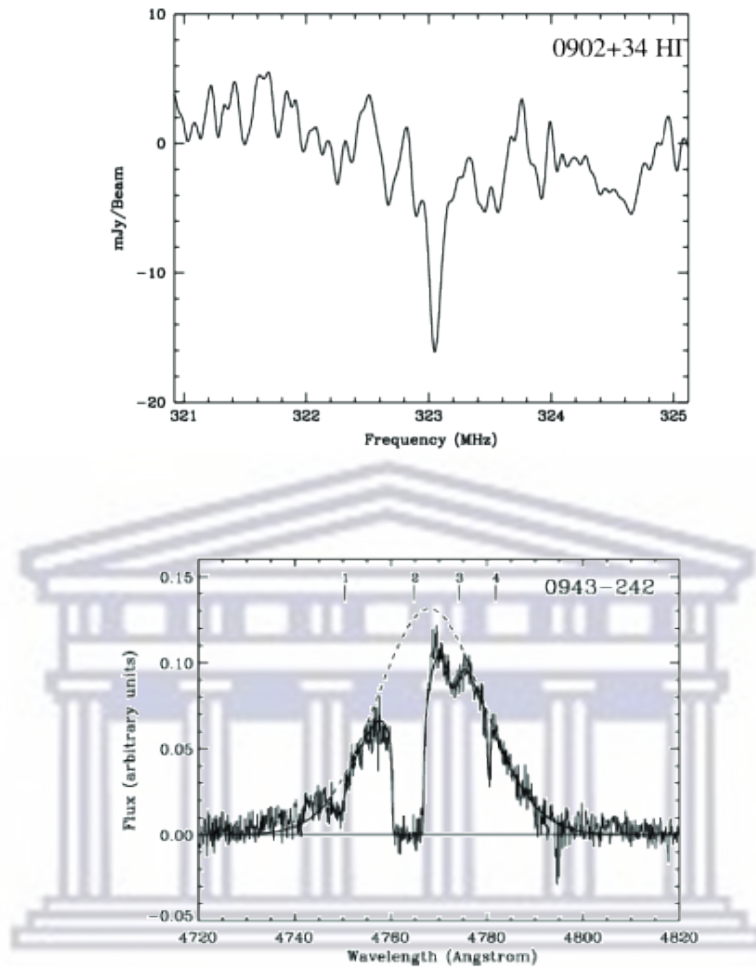


Figure 1.5: *top*: The redshifted HI absorption feature of 0902 + 34 at $z = 2.4$. From [Cody & Braun \(2003\)](#). *bottom*: The redshifted $Ly\alpha$ absorption feature of 0943 – 242 at $z = 2.9$ with the absorption model overlaid. From [Jarvis et al. \(2003\)](#).

and Radio Frequency Interference (RFI) difficulties. [Uson et al. \(1991\)](#) observed HI absorption in the HzRG, 0902 + 34 at $z = 3.4$, See [Figure 1.5](#). Development in this area has become frustrating, see review by [Röttgering et al. \(1999\)](#). In addition to some subsequent studies on 0902 + 34 (e.g., [Briggs et al. 1993](#), [De Bruyn 1996](#), [Cody & Braun 2003](#), [Chandra et al. 2004](#)), there were only two additional preliminary but unconfirmed HI absorption detections in 0731 + 438 at $z = 2.4$ and 1019 + 053 at $z = 2.8$.

The HI absorption line is essential for the measurements of the mean column density. With the assumption of a spin temperature of $T_s \sim 10^3$, [De Bruyn \(1996\)](#) derived an HI column density of $\sim 2 \times 10^{21} \text{ cm}^{-2}$ for 0902 + 34 and a corresponding

HI mass of $\sim 3 \times 10^7 M_{\odot}$.

The explanation for not detecting HI absorption in a greater number of HzRGs could be due to small (~ 100 pc) scales of circumstellar discs or torus-like structures that are aligned perpendicular to the jet of the radio source (Röttgering et al. 1999). Unlike most HzRGs, the radio emission of 0902 + 34 is more centrally concentrated, this is consistent with the assumption that such a small disc induces the absorption. The disc-covering fraction would be very small for the more extended radio sources associated with many HzRGs, so that the disc would not produce sufficient absorption in these cases.

Ly α Absorption

In 1997, van Ojik et al. (1997) found that strong absorption features are commonly found in the *Ly* α profiles of HzRGs. These features were found in most of the 18 HzRGs that were investigated using adequate spectral resolution. They found column densities ranging from $10^{18} - 10^{19.5} \text{ cm}^{-2}$.

Absorption is generally considered to be a feature of HI that surrounds the most massive galaxies. It is a useful diagnostic tool to measure the spatially neutral gas surrounding HzRGs. Due to the possibility of constraining the spatial extension of the absorbing region, the *Ly* α absorption lines provide details about the absorbing gas properties such as dynamics and morphologies that cannot be investigated using quasar absorption lines. Since *Ly* α emission is absorbed in most situations over the entire spatial range up to 50 kpc, the absorbers must then have a covering fraction close to unity. The derived masses of HI are typically $\sim 10^8 M_{\odot}$ from the column densities and the spatial scales of the absorbing clouds.

Wilman et al. (2004) studied a sample of 7 HzRGs in the redshift range $2.5 < z < 4.1$. They found two populations of HI absorbers: strong column density absorbers in the range $\sim 10^{18} - 10^{20} \text{ cm}^{-2}$ and weaker systems with $N_{HI} \sim 10^{13}$ to 10^{15} cm^{-2} . They found no intermediate column density. They suggested that the strong absorption could be caused by material cooling behind the expanding bow shock of the radio jet and that the weaker absorbers would form part of the multi-phase proto-intracluster medium responsible for the *Ly* α forest.

Jarvis et al. (2003) used a high spectral resolution to study the profiles of HI and C IV absorption in HzRGs 0943 – 242 at $z = 2.9$ and 0200 + 015 at $z = 2.2$. They demonstrated that absorbing gas has a low density and low metallicity and is distributed in a smooth absorbing shell located beyond the emission-line gas. However, the metallicity, inferred from C IV absorption, is significantly lower in 0943–242 than the larger source 0200+015. The difference in metallicity is explained

as due to chemical enrichment through a starburst-driven superwinds, see Section 1.7. Furthermore, observations and modeling of the 0943 – 242 spectrum by Binette et al. (2000) indicated that the absorbing gas could actually be ionised in this object, see also Binette et al. (2006). However, 0943–242 could be a special case with a relatively small radio size and one of the deepest $Ly\alpha$ absorption of all known absorbers.

Chemical Abundance in HzRGs

The main emission line from the warm gas halos is $Ly\alpha$, and other lines are also observed. In case of radio galaxy 4C 41.17 at $z = 3.8$, the kinematic structures in the $Ly\alpha$ line are closely followed using carbon C IV, oxygen [OII] and [OIII] emission lines, with the [OIII] $\lambda 5007$ emission reaching out to as far as 60 kpc from the nucleus (Reuland et al. 2007).

The chemical abundance of halo gas is comparable to that of the abundance of solar chemicals (Humphrey et al. 2006), in line with the fact that in earlier epochs HzRG had experienced tremendous star-formation. More hints that the star-formation rate was higher in the past come from the estimation of $Ly\alpha$ luminosities and $Ly\alpha / \text{HeII}$ ratios, both of which are significantly higher for HzRGs with $z > 3$, than for those within $2 < z < 3$.

1.8 Star-Formation Rate in HzRGs

One of the most frequently considered topics in the extragalactic surveys and even more theoretical studies of star formation is the concept of a power-law relation between Star-Formation Rate (SFR) density, in $M_{\odot} \text{yr}^{-1}$ and gas density. This was introduced by Schmidt (1959) and Schmidt (1963), and such relations are generally called the Star-Formation Law, the Kennicutt-Schmidt or the KS-relation. This law is generally given in terms of the detectable density of gas as:

$$\Sigma_{\text{SFR}} = \epsilon' \Sigma_{\text{gas}}^{\beta}, \quad (1.1)$$

where Σ_{SFR} (in $M_{\odot} \text{yr}^{-1} \text{kpc}^{-2}$) is the SFR surface density in a galaxy, Σ_{gas} (in $M_{\odot} \text{pc}^{-2}$) is the gas surface density, ϵ' is the SFR efficiency and β is the density-dependent slope.

For today's star formation, the SFR efficiency of the law, ϵ' , gives the inverse of the time taken to absorb the gas reservoir. This describes a mixture of the timescale for the formation of stars by gas and the amount of gas that ultimately ended up in stars. The star-forming gas depletion timescale depends on both stellar feedback

processes which drive the turbulence density distribution function and dynamical processes within the ISM. Moreover, this factor was shown to be ~ 10 times greater for Ultra-Luminous Infrared Galaxies (ULIRGs) and sub-millimetre galaxies than for disc galaxies which means that a ULIRG can form stars 10 times faster than a disc galaxy with the same gas surface density (e.g., Sanders et al. 1991, Sanders & Mirabel 1996, Gao et al. 2004b). KS-law density dependent slope is not used only to distinguish different theoretical models, but also to provide information about the underlying physics on a small scale.

Kennicutt (1998) studied a sample of 36 nearby IR selected galaxies. He applied a constant conversion factor from CO-to-H₂, and found a slope of the integrated Schimdt law of $\beta = 1.4$. Other studies have also shown that SFR and the H₂ gas are strongly correlated instead of HI gas and, more generally, β ranges from 1 to 2 at high surface densities (e.g., Wong & Blitz 2002, Heyer et al. 2004, Boissier et al. 2007, Bigiel et al. 2008, Roychowdhury et al. 2009). Therefore, much of the KS-law is used in literature to refer the density of molecular gas, which discards any contribution from the atomic gas. This has also been confirmed by several authors (e.g., Walter et al. 2005, Leroy et al. 2009, Helfer et al. 2003, Bigiel et al. 2008).

Figure 1.6 shows the slope of the KS-law between normal galaxies and starburst galaxies, which may reflect a difference in physical conditions of the ISM in these galaxies, resulting in a decrease in the time scale of star formation. This difference may be attributed to the conversion factor from CO-to-H₂, see Section 1.9.

While significant advances have been made in understanding of the KS-law as it applies to high-redshift dusty galaxies, there are still unanswered questions in the field. The precise determination of the observed slope and the dispersion around the curve is very difficult to work out, but it is important for constraining the star-formation theory.

Dense Molecular Gas

The KS-law is not only restricted to the relation between the SFR surface density and gas surface density, but also to the relation between the gas content and physical conditions of the gas and the efficiency of the star formation from the gas. Stars are thought to be formed in giant molecular clouds with average densities of 100 particles cm⁻³ where the main component of Hydrogen is abundant in the form of H₂ instead of HI. On the surface of the dust grains, H₂ molecules are primarily formed by the transformation of H into H₂ in an environment with typical densities of 50 particles cm⁻³. The region where this transition occurs is known as the photo-dissociation or Photon-Dominated Region (PDR). In addition, the H₂ molecules are

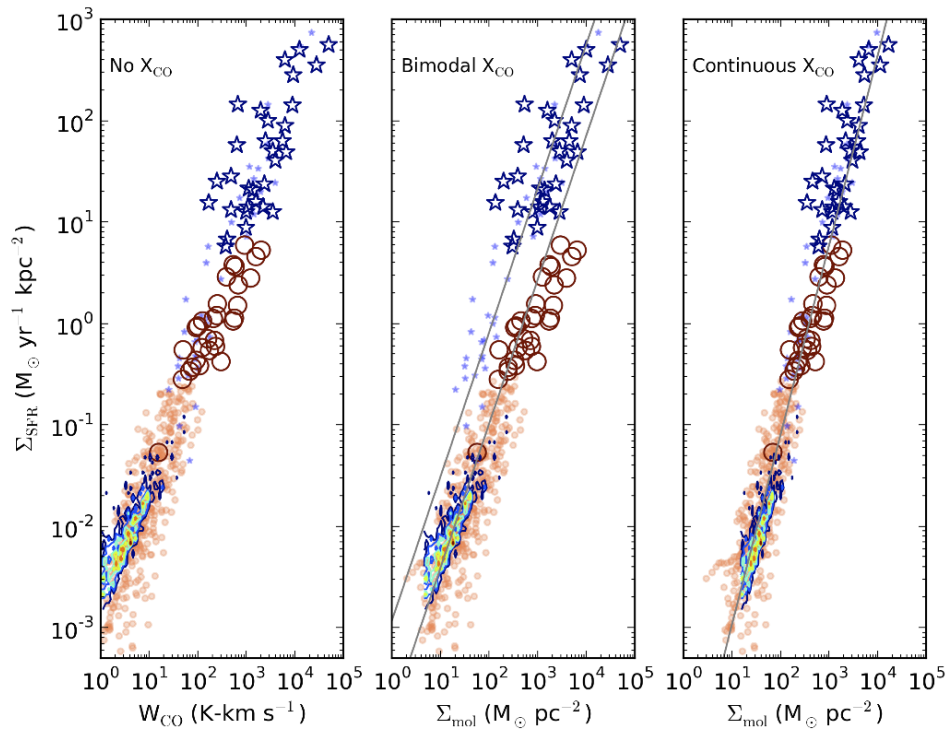


Figure 1.6: The x- and y-axes represent the surface density of the molecular gas and surface density of the SFR, respectively. For all three panels, the circles represent quiescently star-forming galaxies and stars represent starbursts galaxies. Both of these populations are further classified into local galaxies denoted by small orange circles and high-redshift galaxies denoted by blue stars. *Left:* KS-relation prior to the CO-to-H₂ conversion. *Middle:* The KS-law where the traditional bimodal CO-to-H₂ conversion factor is assumed. The grey lines represent the best-fit sequences for the quiescent galaxies and ULIRGs which are critical in distinguishing between a quiescent mode and a starburst mode. *Right:* The KS-law in which a variation of CO-to-H₂ is assumed give rise to unimodal star formation. From Casey et al. (2014).

dissociated by UV photon energy of 11.2 eV or higher, which is why H₂ has to be shielded against the Interstellar Radiation Field (ISRF) by dust grains or self-shielding. [Krumholz et al. \(2011\)](#) and [Glover & Clark \(2012\)](#) suggested that the shielding effects would trigger H₂ formation. H₂ molecules are destroyed by photo-dissociation (resonant absorption of Lyman- and Werner-band photons) over the large spatial scale of the molecular clouds, but remains shielded at a column density of $\sim 10^{20} \text{ cm}^{-2}$. One of the essential aspects about self-shielding and dust extinction is that it prevents the dissociation deep into the cloud.

It is worth noting that H₂ is a mono-atomic molecule. This means that H₂ has no permanent electric dipole moment and the rotational transitions from H₂ are unlikely to be detected ([Stahler & Palla 2004](#)). However, H₂ is the most stable and abundant molecule that is followed by CO. Because of undetected properties of H₂, CO is then used as a molecular gas tracer. CO has a permanent electric dipole moment and therefore the detection of molecular gas is fundamentally dependent on CO, which emits strongly at radio frequencies. In addition, CO has a strong binding energy of 11.1 eV, which preserves the molecules from being destroyed by further reactions. Nonetheless, CO is also subjected to photo-dissociation against the surrounding ISRF, which results in a comparable build-up to H₂ in the outer components of molecular clouds, while CO remains dissociated to greater depth. It should be noted that the main isotope of CO is ¹²C ¹⁶O which can be easily detected at a high optical depth and are also used to trace kinematics. Although other CO isotopes such as ¹³C ¹⁶O, ¹²C ¹⁸O, ¹²C ¹⁷O and ¹³C ¹⁸O are mostly optically thin, they can be used to probe different environments at the centres of molecular clouds. The only distinction is that they are not easily detected as ¹²C ¹⁶O due to lower abundances.

In the case of HzRGs, the analysis of the CO transition depends on the following redshifted lines: J=CO(1 – 0), CO(2 – 1), CO(3 – 2), CO(4 – 3) and CO(5 – 4) at 115.271, 230.538, 345.796, 461.041 and 576.268 GHz, respectively. In addition, evidence of those lines indicates the cold gas reservoir required for star-formation.

1.9 Molecular Torus

Molecular clouds are believed to be the raw material for star formation and an important factor in determining both the morphology and evolution of galaxies. The HI observations may occur in various components of the Cold Neutral Medium (CNM) with $T \sim 100 \text{ K}$, Warm Neutral Medium (WNM) with $T \sim 10^4 \text{ K}$, and Lukewarm Neutral Medium (LNM) ([Kulkarni & Heiles 1987](#), [Dickey & Lockman](#)

1990) usually with these various components in our direct line of sight. H_2 is known only to be correlated with HI to provide essential cooling (McKee & Ostriker 1977, Wolfire et al. 2003; 2010), but unfortunately this population does not emit spectral lines that are easily detected.

CO-to- H_2 conversion factor

It is of particular importance to assume a standard conversion factor to convert the CO atoms into H_2 . This factor is determined from ULIRG observations for high- z CO studies (Downes et al. 1993, Bolatto et al. 2013). Assuming this value extends to objects with high- z , the strength of the (1 – 0) CO transition is essential for the derivation of molecular gas masses. The inferred masses of H_2 observed in the CO transition are between 10^{10} and $10^{11} M_\odot$, suggesting that there is a large mass of molecular gas in these objects and a substantial reservoir of material available for future star formation. In addition, the calculated masses should be treated cautiously due to many assumptions in the derivation (e.g., Downes et al. 1993). Observations of higher CO transitions are biased towards detecting gas denser than ground-state observations and may lead to overestimation of the total mass of molecular gas.

Several studies have demonstrated that CO emission is spatially resolved (Papadopoulos et al. 2000, Greve et al. 2004, De Breuck et al. 2005) and ranges from 10 to 20 kpc, see Figure 1.7, providing kinetic details on the molecular gas. There is evidence of interaction between molecular gas and radio morphology in several of the observed CO emissions of powerful radio galaxies (Klamer et al. 2004), as is required for the jet-induced star-formation, see Section 1.11, but recent studies have shown that this is not always the case (e.g., Emonts et al. 2014; 2015, Gullberg et al. 2015). Nonetheless, high resolution, large signal to noise and more data are required before any conclusions can be made about potential alignments.

De Breuck et al. (2003b;a), De Breuck & Reuland (2005) estimated velocity offsets of up to 500 km s^{-1} which are between molecular gas (CO) and warm gas (e.g., $\text{HeII}\lambda 1640$). Furthermore, as the density of H_2 exceeds the density of the warm ionised gas $\text{Ly}\alpha$ halos by the order of magnitude, the CO emission lines provide a better estimate of the structural redshift of powerful radio galaxies at high redshifts than the UV and optical emission lines.

Dense Molecular Gas Tracers

The fraction of the gas observed at high redshifts is greater than in low-redshift galaxies. This claim is supported by the peak CO Spectral-Line Energy Distributions (SLEDs) at higher- J CO transitions than for low- z systems. While dense molecular

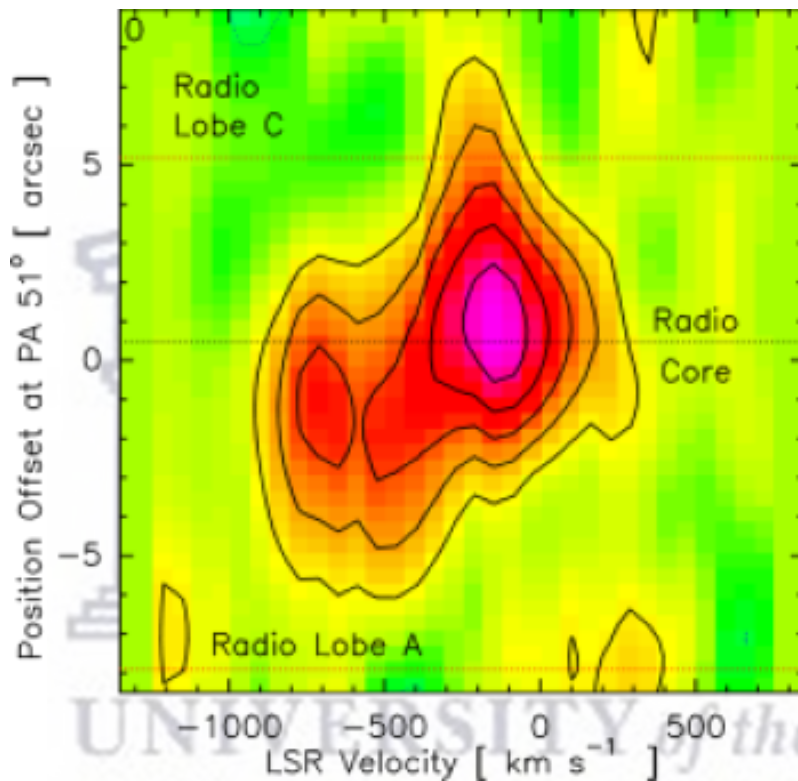


Figure 1.7: CO emission toward the powerful radio galaxy 4C 41.17 at $z = 3.8$ with the Plateau de Bure Interferometre (PdBI). The Figure indicates position offset of the CO(4 – 3) transition versus velocity, extracted along a Position Angle (PA) of 51° . At 96.093 GHz ($z = 3.798$), the central frequency is centered on the wavelength of the optical HeII $\lambda 1640 \text{ \AA}$ emission line. From [De Breuck & Reuland \(2005\)](#).

gas can be traced by the high- J CO lines, it can also be traced by molecules with a higher critical density such as CS, HCO⁺, HCN or H₂O.

Using HCN as the dense gas diagnostic tool, among others, it may trace the places where star formation occurs. HCN studies in very dense regions have shown a correlation between HCN and total Far-IR (FIR) luminosity (e.g., Solomon et al. 1992, Gao & Solomon 2004, Gao et al. 2004b; 2007, Privon et al. 2015). This luminosity correlation shows an offset between high redshifts compared to the low-redshift correlation. However, the cause of this offset is not clear-whether it is caused by a higher gas density probability distribution function (Krumholz & Thompson 2007, Narayanan et al. 2008) or by an AGN contribution to IR luminosity. There is also a non-linear FIR-HCN trend observed for high redshifts systems by Greve et al. (2006) and Riechers et al. (2007).

The H₂O rotational transition is also used as a diagnostic tool to trace the dense gas of the star-forming clouds. It has a critical density of $\sim 10^8 \text{ cm}^{-3}$, which makes it possible to trace even the extremely dense parts. Omont et al. (2013) used a sample of high- z starburst galaxies and they found a relation between the Far-Infrared (FIR) and H₂O luminosities. More interestingly, for the reddest galaxy HFLS3, seven rotational H₂O line intensities have been detected at $z = 6.34$ by Riechers et al. (2013). The general case of the H₂O line intensities studies confirm a clear correlation between the IR and the H₂O luminosities in the IR luminosity range $L_{\text{IR}} \sim 10^{12} - 10^{14} L_{\odot}$. The importance of the H₂O line intensity detection is to probe the conditions associated with a starburst during the end of the re-ionisation epoch in addition to collisional excitations. Overall, the HCN and H₂O line diagnostic tools are important for future studies in high- z systems as compared with low- z systems. They will be demonstrating understanding of the physical conditions that affect star formation (e.g., Krumholz & McKee 2005, Andrews & Thompson 2011, Hopkins et al. 2013).

Molecular Gas in High- z Radio Galaxies

In order to analyse CO emission measurements in HzRGs and the evolution of molecular gas, it is important to perform deep CO emission observations on well-defined samples of HzRGs in multiple CO transitions, without pre-selection of their cold dust emission properties. Moreover, the faintness of the CO emission lines, along with the uncertainties in their redshifts, ensure that detailed searches for CO involves a large amount of observation time. However, the limiting factors are the sensitivities of the telescopes and the relatively limited instantaneous bandwidth covered by the receiver back-ends.

The biases which are caused by the current CO observations are:

1. Selection based on a dust emission of $850\ \mu\text{m}$: Sources detected in CO are not detected for two galaxies in $850\ \mu\text{m}$ continuum emission: for 53W002 at $z = 2.39$ (Scoville et al. 1997, Alloin et al. 2000) and TNJ0924–2201 at $z = 5.2$ (Klamer et al. 2004), suggesting a systematic underestimation of the gas/dust ratio in powerful high- z CO samples as a result of bias in favour of the dusty galaxies.
2. A positive detection is more likely to be published than a non-detection.
3. It is only possible to observe at particular wavelengths where the atmosphere is transparent. This fact limits the observability for some CO transitions at certain redshifts. The high- z sources must be detected in high-transition CO emission lines: this implies that CO emission primarily probes the denser molecular gas of powerful radio galaxies at high redshifts. Nevertheless, this could also lead to an inconsistent CO spectral line energy distribution, which can complicate density and temperature constraints (Miley et al. 2006).

Observations with ATCA, Expanded Very Large Array (EVLA) and Atacama Large Millimetre Array (ALMA) are important to confirm the general presence of large reservoirs of cold molecular halo gas in powerful radio galaxies and study them in more detail. Such facilities also include an immense improvement in sensitivity and exploration of space across the sub-millimetre, millimetre and centimetre wavebands.

1.10 Dust Characterisation

Dust is a significant constituent of HzRGs as well as an additional diagnostic tool of star formation. It is both a major constituent of the molecular clouds from which stars are generally formed, and an indication that there has already been significant star formation, since the presence of dust indicates the presence of chemically enriched material. The SED of HzRGs at millimetre and sub-millimetre wavelengths is also dominated by thermal dust re-radiation, see Figure 1.4, and dust is observable as a polarising and absorbing medium in optical and UV wavelengths.

Dust in HzRGs

Following detection of the radio galaxy 4C 41.17 at $z = 3.8$ (Dunlop et al. 1994, Chini & Kruegel 1994, Ivison 1995), a significant number of HzRGs were observed at millimetre wavelengths (Archibald et al. 2001, Reuland et al. 2004). A sample of 69 radio galaxies with $1 < z < 5$ detected at 850 and/or $450\ \mu\text{m}$ was analysed by Reuland et al. (2004). Isothermal fits to the sub-millimetre spectrum at temperatures

of about 50 K (Archibald et al. 2001) give a dust mass of $2 \times 10^8 M_{\odot}$. The evidence of higher SFR and brighter quasars in HzRGs with $z > 3$ is supported by the typical sub-millimetre luminosity (and hence dust mass) of HzRGs which strongly increases with redshift, with a $(1+z)^3$ dependence out to $z \sim 4$ (Miley & De Breuck 2008).

From the analysis of dust in HzRGs, the AGN must play a significant role in the dust heating in the majority of HzRGs (Drouart et al. 2014). In HzRGs, the dust temperature can reach as high as 300 K (Rocca-Volmerange & Remazeilles 2005). This difference is caused by the dust-absorbing emission contributed by an AGN. The stars in HzRGs, however, often heat the dust, and it is difficult to disentangle the two heating sources, due to the processes that generate dust with varying temperatures. Evidence for young stellar population heating comes from the Rayleigh-Jeans part of the thermal dust emission detected at millimetre and sub-millimetre wavelengths. This possibly suggests that the temperatures of dust emission are fairly cold, ~ 50 K, consistent with the temperature observed for starburst-heated dust emission (Archibald et al. 2001, Stevens et al. 2003, Reuland et al. 2004). However, there is also evidence of a warmer temperature (~ 300 K dust emission) in radio galaxies, consistent with AGN heating (Rocca-Volmerange & Remazeilles 2005). In addition, observations by *Spitzer* at $5 < \lambda_{\text{obs}} < 70 \mu\text{m}$ have also shown that the Wien tail part of the dust SED is inconsistent with low dust temperatures. The sub-millimetre luminosity of the HzRGs is not directly associated with radio luminosity, suggesting no strong dependence on the strength of the quasar/AGN emission (Reuland et al. 2004).

Using high spatial resolution observations that are possible with facilities such as ALMA, AGN- and starburst-heated dust can now be properly disentangled (Gullberg et al. 2015).

UV Continuum Polarisation

Another essential tool to investigate the inner structure of the HzRGs is the use of UV polarisation in the rest frame (Di Serego Alighieri et al. 1989, Di Serego Alighieri 1997, Cimatti et al. 1993; 1998, Vernet et al. 2001a). Polarisation offers a unique tool for determining both the contribution of the different possible components and the dominant source of the UV continuum, while the angle of polarisation allows determination of the location of the scattering medium. Polarisation measurements of HzRGs need high sensitivity as well as high precision. The shape of the polarised flux in the continuum slope and the presence of broad emission lines are identical to that of a non-obscured quasar (Vernet et al. 2001b). This provides strong evidence of there being an obscured quasar present in the nuclei of the HzRGs. The SED of

a typical quasar is bluer than most of the other components that contribute to the SED of HzRGs between UV and NIR.

In most cases, the polarisation is nearly perpendicular to the radio structure, suggesting that the scattering occurs inside the cones traced by the radio jets (Vernet et al. 2001b). Generally, spatially-resolved narrow emission lines are not polarised, see Section 1.6, and the scattering medium must be located between broad and narrow line regions.

Cimatti et al. (1993) used a dust-scattering model which explains the polarisation properties, structure and the SED of the UV aligned light via optically thin Mie scattering of radiation emitted by a quasar in a cone of 47° half-opening angle (Mie 1908). They found that the amount of spherically distributed dust was $(1 - 3) \times 10^8 M_\odot$, which is consistent with the measurements for the dust mass by the *Infrared Astronomy satellite (IRAS; Neugebauer et al. 1984)*, which produces only a small dust extinction ($A_v = 0.1$) along a line of sight to a quasar. Vernet et al. (2001b) suggested that the dust responsible for scattering the AGN emission would have a sub-millimetre emission that is fainter by an order magnitude than what is observed.

Not all of the HzRGs have significant polarisation. These evidences were supported by Vernet et al. (2001b) who found that two of the eight objects that they had observed had a fractional polarisation $f_p < 2.4\%$. There is no convincing evidence for the obscured quasars in the nuclei of these HzRGs.

1.11 Massive Stellar Hosts

In the last two decades, attention has been paid to the importance of stellar populations and their being a significant component of HzRGs. The SEDs of high- z radio galaxies are defined by:

1. A plateau between 1 and $2 \mu\text{m}$ characteristic of stellar populations, and is known as the $1.6 \mu\text{m}$ bump (Simpson & Eisenhardt 1999, Seymour et al. 2007) as shown in Figure 1.4,
2. UV-rest frame discovery of several stellar absorption lines from HzRGs (Dey et al. 1997), and
3. *Hubble Space Telescope (HST)* morphological estimations of many HzRGs supported de Vaucouleurs profiles (e.g van Breugel et al. 1998, Pentericci et al. 2001, Zirm et al. 2005).

Theoretically, SEDs are a good diagnostic tool for stellar populations and galaxy evolution. Young stars (< 0.5 Gyr) dominate the UV part of the SED while the

optical rest frame ($\lambda_{\text{rest}} > 4000 \text{ \AA}$) offers details of populations older than ~ 1 Gyr. The separation of non-stellar components from stellar contribution to the SEDs is complicated, see Figure 1.4. Contributions from scattered quasar light and nebular continuum must be taken into account at rest-frame UV wavelengths, while on the other hand re-radiation by dust contributes to the SED at FIR and millimetre wavebands, see Figure 1.4.

Old Stellar Populations

Old ($> 1 \text{ Gyr}$) stellar populations peak in the NIR portion of the SEDs. HzRGs are found in the early Universe with the highest luminosities in the K band. Since the stellar mass of a galaxy is dominated by old stars, the brightness of the detected K band emission has been found to suggest that distant radio galaxies are very massive, with masses of up to $10^{12} M_{\odot}$ (Rocca-Volmerange et al. 2004), see Figure 1.8. This puts them at the top of the stellar mass function over the whole redshift range $0 < z < 4$ (e.g., Rocca-Volmerange et al. 2004).

The Hubble $K - z$ relation diagram, developed by Lilly & Longair (1984), is an important tool in HzRG research. Given major spectral correction effects, radio galaxies form a relatively narrow series up to $z \sim 3$, particularly when compared to field galaxies chosen at NIR wavelengths (e.g., De Breuck et al. 2002). It was found that the small dispersion in the Hubble $K - z$ relation for HzRGs was weakly correlated with radio luminosity (e.g., Best et al. 1998a). Such a connection can be understood when radio power is dominated by the Eddington limiting luminosity of the nuclear SMBH (Rawlings & Saunders 1991), and thus is a measure of Black Hole (BH) mass. The association between BH and bulge mass as found by e.g., Magorrian et al. (1998) suggests that the radio power is associated with host galaxy mass, as is obviously the case with low- z , less-luminous radio galaxies (Best et al. 2005).

Young Stellar Populations - UV Absorption Line

The HzRGs experience intense star formation. The detection of UV rest-frame photospheric stellar absorption lines and P-Cygni-like features driven by stellar winds provide the most concrete evidence for this effect. Since observation of these lines involves long exposure time on 10m-class telescopes, their detection is restricted to the S V $\lambda 1502$ stellar photospheric absorption line in radio galaxy 4C 41.17 (Dey et al. 1997), tentative measurements of C III $\lambda 1428$ in TN J2007–1316 (De Breuck & Reuland 2005) and Very Large Telescope (VLT) spectroscopy of the Spiderweb Galaxy (Miley et al. 2006, Nesvadba et al. 2006, Hatch et al. 2008). Direct proof of

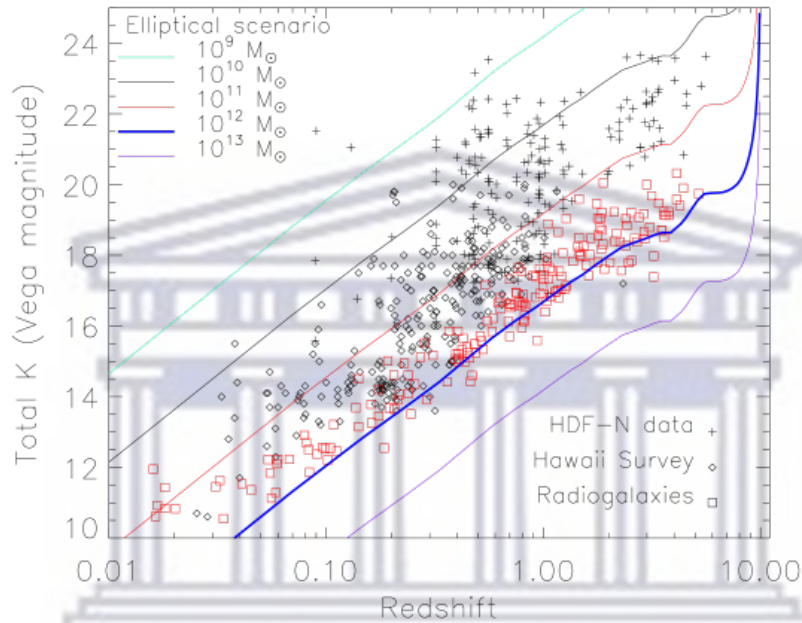


Figure 1.8: Composite Hubble $K - z$ relation diagram of radio and optically-selected galaxies, the red squares representing the radio galaxies. The optically-selected galaxies are indicated in black; Hubble Deep Field–North (HDF-N; Williams et al. 1996) are indicated by crosses and the Hawaii survey are in dots. The radio galaxies trace the upper envelope of the Hubble $K - z$ diagram, with HzRGs among the most luminous galaxies in the early Universe. Note that the continuum fluxes are derived from the K band or H band magnitudes and may be contaminated by bright emission lines in the band. K band magnitude tracks for elliptical galaxies formed from various initial reservoir gas masses (baryonic) are also plotted. From Rocca-Volmerange et al. (2004).

tremendous star formation in 4C 41.17 of up to $1500 M_{\odot} \text{ yr}^{-1}$, following the extinction correction is provided by the appearance of absorption lines (Dey et al. 1997, Reuland et al. 2004). The scattered AGN continuum emission (Vernet et al. 2001a) makes it difficult for radio galaxies whose rest-frame UV continuum is polarised to directly measure the SFR. Furthermore, more proof of the fact that significant star formation occurs in HzRGs is provided by sub-millimetre dust observations, for which heating star-formation rates of thousands of $M_{\odot} \text{ yr}^{-1}$ are required.

Alignment Effect

One of HzRGs' most notable properties is the approximate alignment of their radio and optical continuum emissions. Upon the discovery of this phenomenon more than three decades ago it was absolutely surprising (Chambers et al. 1987, McCarthy et al. 1987). The 'alignment effect' is defined for redshifts $z \geq 0.7$. Many more models were proposed to account for this alignment (e.g., McCarthy 1993). Among these models, the promising ones were (i) dust scattering emission from the hidden quasar at the nucleus of the HzRG (Tadhunter et al. 1998) and (ii) the synchrotron jet induced star formation as it propagates outward from the nucleus.

The correlation between the radio and UV rest-frame and optical morphologies were first reported by Pentericci et al. (1999) and also Pentericci et al. (2001). They used the *HST* observations combined with similar resolution VLA radio maps. They found that the alignment effects extend into the optical rest frame, in the redshift range > 2.5 , with radio galaxies displaying a much more clumpy structure than their low- z counterparts, which are well represented by the de Vaucouleur profiles. van Breugel et al. (1998) proposed that HzRGs tendency to become clumpier at $z > 3$ was because of the increased importance of jet-induced star formation in the earlier epochs. The most extensive investigation of jet-induced star-formation was conducted by Bicknell et al. (2000) for radio galaxy 4C 41.17 at $z = 3.8$. They indicated that the interaction between a high-powered ($\sim 10^{46} \text{ ergs}^{-1}$) jet and a dense cloud in the 4C 41.17 halo produces shock-excited emission lines and causes star formation. Such shock-initiated star formation could proceed on a time scale of at least few $\times 10^6$ yr, which is within the expected life span of the radio source of least few $\times 10^7$ yr.

So far little has been learned about how the first population of stars in galaxies were created. Albeit unconventional, it is possible to believe that the jet-induced star formation played a significant role in the production of stars within the 3 Gyr after the Big Bang. Krishna et al. (2004) proposed that a significant fraction of all proto-galactic material within the cosmic web of filaments were influenced by

the expanding lobes of radio galaxies during the quasar period, which triggered the star-formation mechanism.

1.12 Active Galactic Nuclei

Generally, the luminous collimated radio emission had to be formed in their centres of HzRGs, and the nucleus of all HzRGs had to be active at some stage in their lives.

Unification Model

The idea that the presence of an SMBH of mass $10^6 - 10^9 M_{\odot}$ in the centre of the accreting matter of the galaxy is the cause of the radio source, has been suggested in the 1980s and was the cornerstone of the so-called Orientation unification model. In this model, the active nucleus is an axial structure where the central BH accumulates material from the surrounding gas and dust disc extending over 100 AU from the centre. The result is that the AGN emits an enormous amount of energy due to the release of gravitational potential energy of material which is transferred to radiation through viscous dissipation, yielding a source which radiates across the entire electromagnetic spectrum (Lynden-Bell 1969, Ho & Kormendy 2000).

The X-ray emitting region is surrounded by a Broad-Line Region (BLR). The broad emission lines play an important role in understanding the kinematics and structure of the AGN central part. Furthermore, the line emitted by the BLR is Doppler-broadened and can be taken from a single spectrum containing a broad emission line to measure both the BLR velocity dispersion and optical luminosity of the AGN which can be used to infer the BLR radius. However, the disadvantage is that this line broadening can be caused by blending together, making it impossible to de-blend completely.

The Narrow-Line Region (NLR) region is a low-density gas nebula which is dense enough to produce emission lines that may result from the magnetic dipole transition. The NLR is a larger region on a spatial scale than the BLR, where gas is being ionised and heated by the AGN. These give information about how the AGN central engine illuminates the NLR in a non-isotropic way, and may also provide an indication of how the AGN central engine is fuelled. In nearby AGNs, the large spatial scale of the NLR outflows ensures that the physical conditions and kinematics of the emission line gas can be mapped directly. The observations of some optical forbidden line intensity ratios can be utilised in measuring the electron densities and temperatures of the NLR gas nebula (Peterson 1997). The optical forbidden line intensities would be isotropic, unlike the broad lines observed in BLR, since self-absorption is not

significant in the narrow line component, and thus does not indicate variation in the underlying spectrum.

In the case of unresolved AGN, the optically thick torus surrounds the AGN environment, thus limiting the radiation from the AGN to escape only along the torus axis. Furthermore, the radio-loud sources of the radio axis are aligned with the torus axis, but they do not indicate the preferred orientation of the rotation axis of the host galaxies (e.g., [Drouart et al. 2012](#)).

The AGN unification model assumes that the intrinsic diversity is due to differences in the orientation with respect to the observational line of sight and/or environments of the central object. The observed AGN varieties are influenced by the physical parameters and apparent variations, depending on the viewing angle. The AGN classification is therefore a function of the viewing angle. In face-on observed AGNs, both the central accretion disc and the BLR are un-obscured and the broad lines are detectable. These are classified as Seyfert I galaxies or Quasi-Stellar Objects (QSOs) for the radio-quiet galaxies, and BL Lacertae (BL Lac) or Optically Violet Variables (OVVs) for the radio-loud galaxies. On the other hand, the central part is not visible in edge-on observed AGNs and the broad lines are not detected. These are classified as Seyfert II galaxies, for the radio-quiet, and FR-I or FR-II for the radio-loud galaxies, see [Figure 1.9](#).

Seyfert galaxies are divided into Seyfert I and Seyfert II:

1. At the Seyfert II stellar continuum ratio, the continuum AGN is about a magnitude weaker than Seyfert I and
2. broad emission lines are observed for Seyfert I which is not the case for Seyfert II.

These differences are due to dust obscuring. However, there are problems to this hypothesis:

1. The featureless optical continuum observed for Seyfert IIs appears to follow power laws, although the reddened power law should no longer appear as a power law ([Peterson 1997](#)).
2. The optical continuum of Seyfert IIs is only about one magnitude weaker than that of Seyfert Is, which is surprising given that the broad lines are completely extinguished.

In 1978, Osterbrock introduced an additional component commonly known as the scattering medium in order to clarify the visible continuum of the Seyfert IIs

(Osterbrock 1978). The scattering medium is believed to lie above the plane of the torus and scatters the continuum emission so that it is visible to the observer viewing the system edge-on. The theory of scattering medium is supported by the weak scattered broad emission lines in their polarised spectrum observed for the nearby Seyfert II NGC 1068 galaxy (e.g., Antonucci & Miller 1985). In principle, the polarised spectrum may occur through scattering of starlight on SMBH by free electrons or by reflection on dust grains.

The challenge presented by the unification model is the clarity of the fundamental parameters of the model. However, the most commonly used are the intrinsic luminosity and orientation angle, but other important factors, such as the morphology and gas content, are likely to affect the appearance of the system. Despite this, the unification model has become a popular interpretation scheme for the different types of AGN.

Supermassive Black Hole

It is believed that a rotating SMBH generates gravitational energy that is necessary for powering extragalactic radio sources and AGN. The galaxies accrete material such as gas and dust onto the rapidly rotating SMBHs. This material is converted into kinetic energy and ejected along the rotation axes of SMBHs as collimated relativistic jets and is eventually emitted as radiation, resulting in a thermal spectrum detectable by outside observers, see review by Blandford (2001). Strong proof for the presence of SMBHs in the centres of galaxies, however, has been lacking until very recently.

Observationally, the evidence for the widespread presence of SMBHs in galactic nuclei include:

1. Spectroscopic study of the gigamaser in the centre of galaxy NGC 4258 (Miyoshi et al. 1995),
2. in early type galaxies, both spectroscopy and photometry of galactic nuclei with the *HST* contribute to the association between bulge properties and the mass of the SMBH (e.g., Magorrian et al. 1998, Kormendy & Gebhardt 2001, Häring & Rix 2004, Novak et al. 2006),
3. measurement of the small-scale collimation of radio sources using VLBI (Junor et al. 1999),
4. the comparison of the large-scale and small-scale orientation of some giant radio sources suggests that the collimation axis could last for as long as about 10^8 yr (Schilizzi et al. 1979).

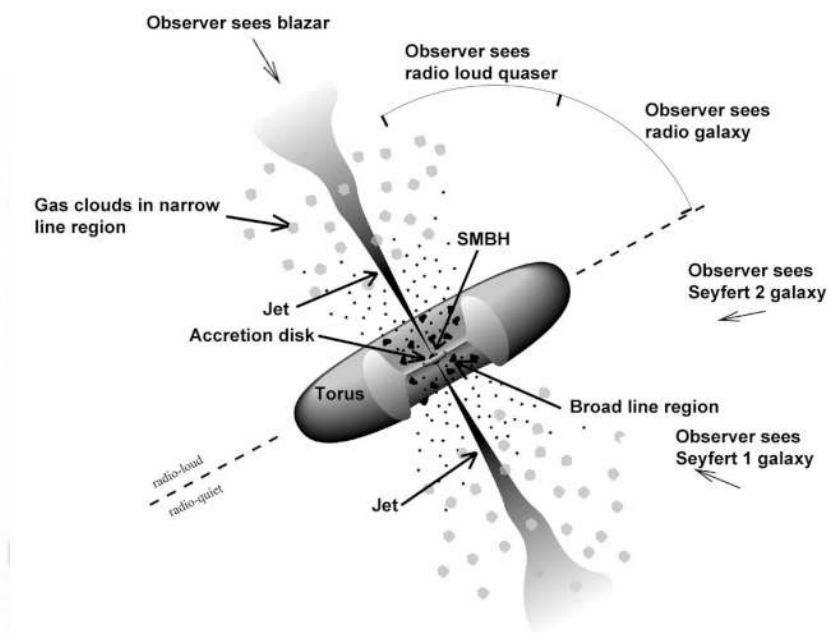


Figure 1.9: Schematic view of the dust-torus-based unified model of radio-loud AGN. If the broad-line region is visible, the AGN is seen with broad and narrow lines. When the torus obscures the line-of-sight to the broad-line region, the AGN is seen with narrow lines only. When the jet is pointed directly along the line-of-sight, the jet luminosity can sometimes swamp the rest of the active nucleus. From [Torres \(2003\)](#).

Due to the interaction of the radio jet with the gas, as with radio-quiet galaxies, line widths in the nuclear core of HzRGs cannot be used to determine the central masses. Häring & Rix (2004) studied the correlation between the SMBH mass with their host galaxies such as bulge mass. They found that BH masses of $10^9 M_{\odot}$ would be predicted at the centre of a $10^{12} M_{\odot}$ HzRG. Their studies supported the SMBH masses obtained by McLure & Jarvis (2002), which from the width of their emission lines found comparable masses for SMBH in radio-loud quasars, but McLure & Jarvis (2002) estimates should be treated with caution. Unfortunately, little is understood as to how the SMBHs were assembled in the process of formation and evolution at high redshifts, so it might not be correct to extrapolate outcomes from lower redshifts. The widths of the emission lines are expanded as a consequence of pressure from the radio jets. Silk & Rees (1998) postulated that SMBHs form within the first sub-galactic structures that virialise at high redshifts, which were located before the formation of galactic stars.

1.13 Motivation and Aims of Thesis

This thesis explores the properties of radio galaxies, with the aim to construct a new sample of powerful radio galaxies. This is done by cross-matching the overlapping regions of the large-area Sydney University Molonglo Sky Survey (SUMSS) radio sources with the Vista Hemisphere Survey (VHS) NIR counterpart. The photometric redshifts of the sample were determined from Dark Energy Survey (DES). Historically, most of the follow up (with optical/NIR imaging and spectroscopy) has been conducted on Northern Hemisphere samples. This is all fine astrophysically as there is no expectation that there is any differences between Northern and Southern Hemispheres for extragalactic objects, but it is problematic as some of the best observing facilities are now in the Southern Hemisphere (e.g., MeerKAT/SKA, ALMA, VLT). Science goals include identifying powerful high-redshift radio sources for absorption line studies with MeerKAT, to understand the population of bright AGN at high-redshift, and the NIR properties of radio sources. The Southern Hemisphere sample is really needed for studies of bright AGN at high-redshift, which would be useful for studying the fuelling and feedback from those sources using a new generation of telescopes, particularly MeerKAT radio telescope.

The second part of this thesis focuses on the MeerKAT shared-risk early science programme. Observationally, in recent years there have been significant efforts to study the kinematic and physical conditions of cold atomic (HI) and molecular (H_2) gas in nearby AGN (e.g., Maccagni et al. 2018, and most references therein). In some

cases these have yielded direct evidence for infalling clouds of cold gas towards the SMBH (e.g., Tremblay et al. 2016). However, due to insufficient telescope bandwidth and the RFI-environment, and lack of large samples of spectroscopically identified radio galaxies at cosmological distances, this work is typically carried out in nearby radio AGN. The MeerKAT Array was used to determine the cold gas content of a well-defined sample of nine powerful ($L_{1.4} > 10^{26} \text{ WHz}^{-1}$) radio galaxies at cosmological distances with a range of accretion states. HI 21-cm absorption was used as an effective means of surveying the cold gas in radio-loud AGN to large distances ($z \gg 0.1$). At these epochs, the volume density of radiatively efficient AGN is an order of magnitude greater than in the local Universe, and it is expected to see a similar strong evolution on the cold gas at these galaxies. This study will pave the way for future deeper surveys with MeerKAT that will probe low-power radio AGN.

The instruments and the sample selection of multi-wavelength data used to define our new sample selection of powerful radio sources are discussed in Chapter 2.

The new Southern sky catalogue is introduced in Chapter 3 and can be used to investigate the impact of powerful AGN on the evolution of host galaxies for follow-up with MeerKAT radio telescopes, along with other observatories in the Southern Hemisphere.

Chapter 4 describes a search for HI in absorption in a study of nine radio AGNs using a 16-element version of the South African MeerKAT array. It is worth noting that the sample used for this analysis is not drawn from the catalogue in the thesis.

Finally Chapter 5 gives general conclusions and future prospects.

UNIVERSITY *of the*
WESTERN CAPE

Chapter 2

Surveys Used in this Study: SUMSS, VHS and DES

One of the main aims of this thesis is the construction of a new catalogue of powerful radio galaxies in the Southern Hemisphere for absorption line studies with MeerKAT. The sample was obtained by cross-matching the overlap region of the Sydney University Molonglo Sky Survey (SUMSS; [Mauch et al. 2003](#)) with the VISTA Hemisphere survey (VHS; [McMahon et al. 2013](#)). Photometric redshifts for the sample were obtained in the overlapping region of Dark Energy Survey (DES; [Flaugher et al. 2015](#)). The constructed catalogue[†] is presented in Chapter 3. In Section 2.1, I discuss the SUMSS radio survey and how we have selected our radio sources. In Section 2.2, I discuss the VHS NIR survey as well as how we have selected the NIR sources. In Section 2.3 I discuss the DES optical telescope, and finally, I give conclusions in Section 2.4.

2.1 SUMSS Survey

Radio surveys play an important role in developing our understanding of the high-redshift galaxy population in the Universe. Many of the radio survey projects, including the SUMSS survey, have several science goals, but they have a general purpose in common, and that is to survey the radio continuum emission from galaxies, to understand the formation and evolution of galaxies over cosmic time as well as the cosmological parameters and large-scale structure that influence them. The study of radio sources in the mJy regime includes studies of a cosmologically significant radio source population of Star-Forming Galaxies (SFGs) which are incredibly uncommon

[†]It is worth mentioning that the sample of nine radio AGN presented in Chapter 4 was not drawn from the catalogue presented in Chapter 3

Table 2.1: Description of some characteristics of MOST synthesis observations. From [Bock et al. \(1999\)](#).

Parameter	Values/Description
Frequency	843 MHz
Bandwidth	3 MHz
Polarisation	Right-hand circular (IEEE)
δ range (12 hr synthesis)	$-90^\circ \leq \delta < -30^\circ$
Synthesised beam (FWHM)	$43'' \times 43'' \operatorname{cosec} \delta $
Image area	elliptical, $163' \times 163' \operatorname{cosec} \delta $
rms noise level (1σ)	$1 - 2 \text{ mJy beam}^{-1}$
Dynamical range (typical)	250:1

at brighter flux densities. For cosmological investigations, large-area radio source surveys at mJy-levels have some significant benefits. They not only generate huge quantities of large structures that can be observed, but they also sample objects that are at comparable redshifts to the Jy-level sources, but are 100 to 1 000 times less radio luminous ([Sadler & Hunstead 2002](#)).

In order to create a new sample of powerful radio galaxies in the Southern Hemisphere, we first require a parent radio survey which covers enough sky area that it provides a statistically significant number of bright radio sources. The parent radio survey that we use in this study is the SUMSS. The SUMSS catalogue is constructed from data obtained with the Molonglo Observatory Synthesis Telescope (MOST; [Mills 1981](#)). The MOST is a radio telescope operating at 843 MHz. The telescope is located in Hoskinstown, Australia. It consists two cylindrical paraboloids, $778 \text{ m} \times 12 \text{ m}$, separated by 15 m.

The MOST samples have a good coverage of short spacing in the (u, v) plane due to the dense layout of the receptors and the cylindrical design. Hence, the MOST is more sensitive to large-scale diffuse radio emission than many other synthesis telescopes in the Southern Hemisphere.

The MOST images are affected by a number of artefacts whose characteristic appearance can usually be distinguished from genuine astronomical sources. The artefacts of the survey are the following ([Bock & Wagner 1994](#)):

1. sidelobe response of the MOST due to the periodic structure array,
2. atmospheric and ionospheric effects due to the position of the fan comb beam that shifts irregularly,
3. terrestrial interference as a result of the unprotected radio astronomy band of

the MOST, 843 MHz, and

4. solar interference due to the Sun, which can cause significant interference with MOST observations generated during the day.

SUMSS is a sensitive radio imaging survey of the Southern Hemisphere at 843 MHz with a similar resolution and sensitivity to the Northern National Radio Astronomy Observatory (NRAO) VLA Sky Survey (NVSS; [Condon et al. 1998b](#)) at 1.4 GHz and these overlap in the declination (δ) zone -30° to -40° . The survey has rms noise of about 1 mJy/beam, it has a completeness limit of about 10 mJy. SUMSS surveyed the sky at $\delta < -30^\circ$ with latitude above the Galactic Plane, $|b| > 10^\circ$. It has a resolution of $\text{cosec}|\delta| \times 45''$ and a 5σ sensitivity of 6 mJy/beam at $\delta < -50^\circ$ and 10 mJy/beam at $\delta > -50^\circ$. The SUMSS catalogue covers roughly 3500 sq deg of the Southern Hemisphere sky with $\delta \leq -30^\circ$ which is $\sim 43\%$ of the total area of the survey. Radio positions in the catalogue are usually precise to within $1 - 2''$ for sources with peak brightness $A_{843} \geq 20 \text{ mJy beam}^{-1}$ and are always better than $10''$ ([Mauch et al. 2003](#)).

SUMSS data products include $4.3^\circ \times 4.3^\circ$ mosaic images and a source catalogue made by fitting elliptical Gaussians to 5σ peaks in the images. MOST has a collecting area of 18000 m^2 making it the largest of any radio telescope in the Southern Hemisphere. Individual observations are made of a grid of overlapping pointing centres which approximate hexagonal close packing, and the images were then mosaiced to recover sensitivity in the overlap regions ([Condon et al. 1998b](#)). MOST has a 2.7° diameter field of view ([Bock et al. 1999](#)), and this enables it to provide a sensitive radio imaging survey of the entire Southern sky, see [Table 2.1](#) for a summary of the survey parameters. The survey observations were made at night to reduce the effect of solar interference.

SUMSS's main goals were the following:

1. detecting and statistical studies on diffuse and giant radio sources,
2. to study the clustering at large scales of faint radio sources at a few hundred Mpc,
3. to study the space distribution and the evolution of star-forming galaxies,
4. measurements of the radio spectral index for 30 000 NVSS radio sources within the overlap region at $-40^\circ < \delta < -30^\circ$, and selection of objects with flat or Ultra-Steep-Spectrum (USS),
5. studies of Southern optical/FIR-selected radio source samples,

6. detection of radio-loud and X-ray sources by cross-matching SUMSS with the *Röntgen Satellite* (ROSAT; Voges 1993) all-sky survey, and
7. measurement of the local Radio Luminosity Function (RLF) of AGN and starburst galaxies as well as their redshift evolution.

The Observations of SUMSS are now complete, and both digital images and a source catalogue are available online.

Sample Selection

We selected sources from the SUMSS catalogue detected at $\geq 10\sigma$, i.e., a limiting peak brightness of 12 mJy/beam at $\delta \leq -50^\circ$ and 20 mJy/beam at $\delta > -50^\circ$. The 10σ limit ensures a robust sample of radio sources with good positional accuracy and below this limit the sample becomes incomplete. Using this selection criterion, we retrieved 5380 radio sources at declinations $-60^\circ < \delta < -45^\circ$ and right ascensions $60^\circ < \alpha' < 90^\circ$. SUMSS image cutouts of size $1.20' \times 1.20'$ around each of these sources were then downloaded from the skyview server*. The SUMSS images from the selected part of the sky were extracted in Flexible Image Transport System (FITS) format.

We then used the MERGEDCLASS source classifier in the VHS catalogue, see Section 2.2, to separate objects as ‘galaxy’, ‘star’, ‘probable star’, ‘probable galaxy’, ‘noise’ or ‘saturated source’. The rejection of spurious sources is necessary to provide a clean sample of galaxies. The total number of NIR sources in the sky region bounded by $-60^\circ < \delta < -45^\circ$ and $60^\circ < \alpha' < 90^\circ$ is 3991998. We applied MERGEDCLASS= 1 to the NIR source catalogue so that we only retain probable galaxies. This may remove some radio galaxies from our sample, which may be at lower signal-to-noise ratio and therefore classed as ‘probable galaxies’ but this is not an issue for our core aims of defining a sample for follow-up studies. Sources that were ‘saturated’, ‘probable star’, ‘stars’ and ‘noise’ were therefore removed. Following these selections, we remain with 2287733 sources classified as galaxies in the VHS catalogue.

2.2 VISTA Hemisphere Survey

The VHS is an NIR photometric redshift survey carried out using the VISTA telescope at Paranal Observatory in Chile. It covers 18000sq deg of the Southern celestial Hemisphere to a depth 30 times fainter than the previous generation NIR Two

*<http://www.skyview.gsfc.nasa.gov>

Micron all-Sky Survey (2MASS; [Skrutskie et al. 2006](#)) in at least two wavebands (J and K_s). The South Galactic Cap (SGC) covers an area of $\sim 4\,500$ sq deg of the sky, and the overlap with DES is being imaged deeper in order to better supplement the optical data available from DES. This area has a median depth of $J_{AB} = 21.4$ and $K_{AB} = 20.4$ for 5σ detection of point sources. The surveying of the remaining high galactic latitude sky is carried out in the Y, J, K bands and coupled with optical photometry from the VLT Survey Telescope (VST)-ATLAS survey. The VST-ATLAS region contains 5σ nominal magnitude limits of $J = 20.9$ and $K_s = 19.8$ and includes the data in the H band. The low galactic latitude sky termed VHS-Galactic Plane Survey also goes down to $K_s = 19.8$.

VISTA is the fastest NIR survey telescope and has a 4 m $f/1.0$ primary mirror and a 1.2 m secondary mirror. The telescope is equipped with a large array of 16 individual infrared detectors with a total coverage of 1.5 sq deg of field. The VHS imaging data have been processed using the VISTA Data Flow System (VDFS; [Emerson et al. 2004](#), [Lewis et al. 2006](#)) connected to the Cambridge Astronomical Survey Unit (CASU) software and the VISTA Science Archive (VSA) is designed and run by the Wide Field Astronomy Unit (WFAU) in Edingburgh.

VHS covers 18 000 sq deg with magnitude limits of $H = 19.8$, $J = 20.6$, $K_s = 18.5$, where the values of H, J and K_s are in Vega magnitude, see Figure 2.1. The VHS sky coverage is divided into 3 sub-regions:

1. VHS-North Galactic Cap: $b > 30^\circ, \delta < 0^\circ$, covering 2 500 sq deg with baseline exposures of 60 s per band in J, H and K_s bands.
2. VHS-South Galactic Cap: $b < -30^\circ, \delta < 0^\circ$, covering 8 000 sq deg with baseline exposure of 60 s per band in J, H and K_s bands.
3. VHS-Galactic Plane Survey: $5^\circ < |b| < 30^\circ$, covering 8 500 sq deg with baseline exposures of 60 s per band in J and K_s bands.

The VST-ATLAS area is covered with 60 s exposures in the Y, J, H, K_s bands. The remaining area is covered with 60 s exposures at J and K_s bands.

VHS scientific goals include the following ([McMahon et al. 2013](#)):

1. the discovery of the nearby and lowest-mass stars,
2. interpreting the history of the galaxy's merger through the stellar galactic structure,
3. to measure the properties of dark energy through the examination of large-scale structure of the Universe out to $z \sim 1$,

Table 2.2: Summary of the main system parameters of VISTA. From [Sutherland et al. \(2015\)](#).

Parameter	Values/Description
Site	Paranal Observatory, Chile
Primary mirror diameter	4.10 m
Secondary mirror diameter	1.241 m
Focus	Cassegrain
System focal length	12.072 m
M1-M2 spacing	2715.7 m
Mount type	Alt-azimuth
Moving mass	90 tonnes
VISTA Infrared Camera wavelength range	0.8 – 2.3 μm
VIRCAM Field of view	1.65° (diameter)
Field on infrared pixels	0.6 sq deg
Mean pixel scale	0.339 arcsec
VIRCAM science detectors	Sixteen Raytheon-VIRGO HgCdTe, 2048 ² format
VIRCAM guide/wavefronts detectors	Six E2V CCD 42 – 40, 2 048 sq deg format
Filter set (current)	Z, Y, J, H, K, two narrowbands, one dark

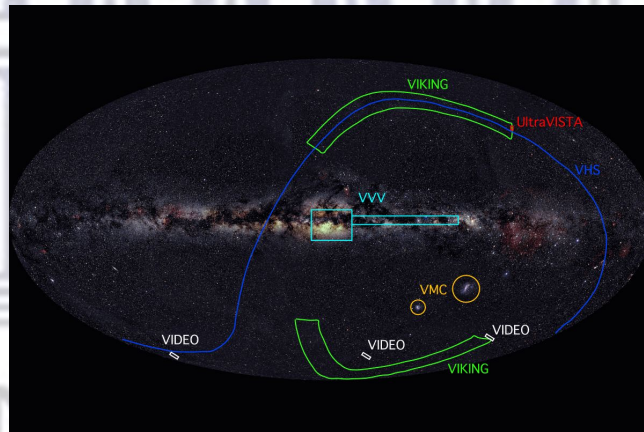


Figure 2.1: Sky coverage of VISTA surveys, superimposed on a 2MASS image of the entire sky. From [Emerson et al. \(2006\)](#).

4. search for high-redshift quasars with $z > 7$ for the studies of baryons in the Intergalactic Medium (IGM) during the epoch of re-ionisation, and
5. in the Southern Hemisphere, the observations of very bright quasars at all redshifts which explores the IGM and the formation of the most massive SMBH in the Universe.

VHS Sampling Using the SQL

The NIR photometric data was accessed via the VISTA Science Archive (VSA)*. The VHS database release used for this work was VHS DR3. The data in the VHS region were accessed using Structured Query Language (SQL) in the VSA web-browser-based interface using the following code:

```
Select 1.*vhs.ra, 1.*vhs.dec, vhs.sourceID, vhs.mergedClass, vhs.pStar,
vhs.pGalaxy, vhs.pNoise, vhs.pSaturated, vhs.yPetroMag, vhs.yAperMag3,
vhs.yAperMagNoAperCorr3, vhs.yPetroMagErr, vhs.yAperMag3Err, vhs.yErrBits,
vhs.jPetroMag, vhs.jAperMag3, vhs.jAperMagNoAperCorr3, vhs.jPetroMagErr,
vhs.jAperMag3Err, vhs.jErrBits, vhs.hPetroMag, vhs.hAperMag3,
vhs.hAperMagNoAperCorr3, vhs.hPetroMagErr, vhs.hAperMag3Err, vhs.hErrBits,
vhs.ksPetroMag, vhs.ksAperMag3, vhs.ksAperMagNoAperCorr3,
vhs.KsPetroMagErr, vhs.ksAperMag3Err, vhs.ksErrBits
FROM vhsSource AS vhs WHERE vhs.ksAperMag3 > 0.AND vhs.ksAperMag3
< 16. AND vhs.dec < -45. AND vhs.dec > -60. AND vhs.ra > 330.
AND vhs.ra < 345. AND (vhs.priOrSec=0 or vhs.priOrSec=vhs.framesetID)
```

The data were then loaded to TOPCAT for selection of galaxies and other scientific uses. TOPCAT is a collaborative graphical display and tabular data editor. It is utilised for investigation and manipulation of source catalogues and other tables. The viewer can import different astronomically important formats (such as FITS, VOTable and CDF) and more formats can be added (Taylor 2005).

The NIR photometric data, which have a resolution of ~ 1.2 arcsec was accessed via the VISTA Science Archive and we used the VHS DR3.

2.3 Dark Energy Survey

The Dark Energy Survey (DES) is a visible and NIR survey that is designed to investigate the dynamics of the expansion history of the Universe and the growth of large-scale structure. The survey uses a dedicated camera on the 4m Victor M. Blanco Telescope located at the Cerro Tololo Inter-American Observatory (CTIO; Flaugher et al. 2015) in Chile, outfitted with the Dark Energy Camera (DECam). DECam consists of the widest field of view 2.2° diameter available for ground-based optical and infrared imaging. The survey covers 5 000 sq deg in the Southern Galactic Plane region in the g, r, i and z bands, which overlaps with SPT and Stripe 82. The

*horus.roe.ac.uk

aim of the DES is to understand the nature and evolution of dark energy by measuring the large-scale structure of the Universe using four probes: Type Ia supernovae, Baryon Acoustic Oscillations (BAO), weak gravitational lensing, and galaxy cluster counts, in particular from the millimetre wavelength SPT Sunyaev-Zeldovich cluster survey. Additionally, DES also includes a deeper multi-epoch supernova survey over 30 sq deg. However, the depth and areal coverage of the DES mean that it is ideal for the identification of rare sources such as radio galaxies.

DES's primary goal is to determine the dark energy equation of state given by

$$w = \frac{p}{\rho} \quad (2.1)$$

where p is the pressure and ρ is the energy density using complementary techniques in a single survey, namely: counts of galaxy clusters, weak gravitational lensing, and galaxy power spectra. In addition, it aims to measure other cosmological parameters to high precision over a much wider redshift range. The DES catalogue contains 300 million galaxies with accurate photometric redshifts, up to $z \sim 1.4$, and approximately 200 million of these galaxies have shape measurements for weak lensing. DES measured thousands of Type Ia supernovae over a region of 27 sq deg in its time-domain fields.

The DES first light was in 2012 September and then followed by a period of commissioning and Science Verification Archive (SVA) observations between 2012 October and 2013 February. The first year's and second year's observations were taken between 2013 August and 2014 February and between 2014 August and 2015 February, respectively, and its last observation session was concluded on 09 January 2019. The first year and second year catalogues together yielded 100 million galaxies with photometric redshifts of which 80 million galaxies have shape measurements for weak lensing studies.

Several fields were targeted as part of the SVA phase and these regions are: SN-X3 at a right ascension of 36:27:00.00 and declination of $-04 : 36 : 00.00$, SN-C3 at a right ascension 52:38:54.24 and declination of $-28 : 06 : 00.00$, VIMOS VLT Deep Survey (VVDS) F14, and Cosmic Evolution Survey (COSMOS), see Figure 2.3. The SN-X3 region was chosen from among the four spectroscopy training set fields as it has complete overlap with VHS NIR imaging. The SN-C3 field is partially covered by the VISTA Kilo-degree Infrared Galaxy (VIKING) survey which complement VHS and VVDS F14 and the COSMOS field lie outside the VHS survey region. These fields include spectroscopic training set fields of overlapping spectroscopy surveys like VVDS, Arizona CDF-S Environment Survey (ACES; Cooper et al. 2012), and z COSMOS as well as ~ 250 sq deg of area covered by the SPT survey.

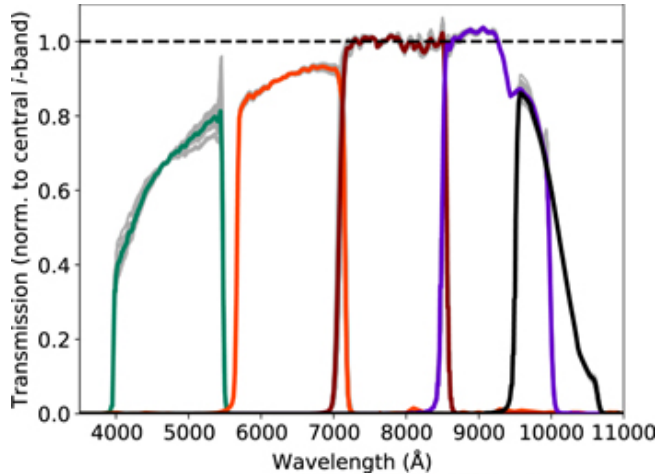


Figure 2.2: The Instrumental transmission as a function of waveband of Blanco/DECam, as measured by the DECam system. The solid colour lines represent the focal-plane average for g band (blue-green), r band (light red), i band (dark red), z band (purple), and Y band (black). Furthermore, one light grey line plotted for each individual CCD indicates the g band response variation. From [Burke et al. \(2018\)](#).

The DES imaging data products were observed in the six filters u, g, r, i, z, y , see Figure 2.2. This data was processed to two imaging depths: main and deep. ‘Main’ corresponds to DES main exposure time, and ‘deep’ corresponds to approximately three times the exposure time of a single observation in the DES supernova deep field (for SN-X3 and SN-C3) or deeper (for COSMOS). Data reduction and exposure time details are provided in [Sánchez et al. \(2014\)](#). The u band part of the DECam was not used for DES SV survey. DES differs from the previous generation of optical surveys like Sloan Digital Sky Survey (SDSS; [York et al. 2000](#), [Adelman-McCarthy et al. 2008](#)) owing to its red-sensitive CCDs used by the DECam and its high throughput out to wavelengths of almost $1 \mu\text{m}$ in the z and y filters.

In this work we used the DES data products from the first annual reduction of the Science Verification Archive (SVA)1 Gold catalogue ([Jarvis et al. 2016a](#)). The SVA1 Gold catalogue has 25 227 559 sources with photometric redshifts estimated using the Bayesian Photometric Redshifts (BPz; [Benítez 2000](#)). Spectroscopic redshifts are not available for our galaxy sample.

Optical Source Catalogue

The Science Verification Archive (SVA1; [Jarvis et al. 2016a](#)) Gold catalogue data products cover a region $\sim 250 \text{ sq deg}$ with non-uniform depth and data quality with a median 10σ limiting magnitude for galaxies approximately: $g = 24.0$, $r = 23.8$,

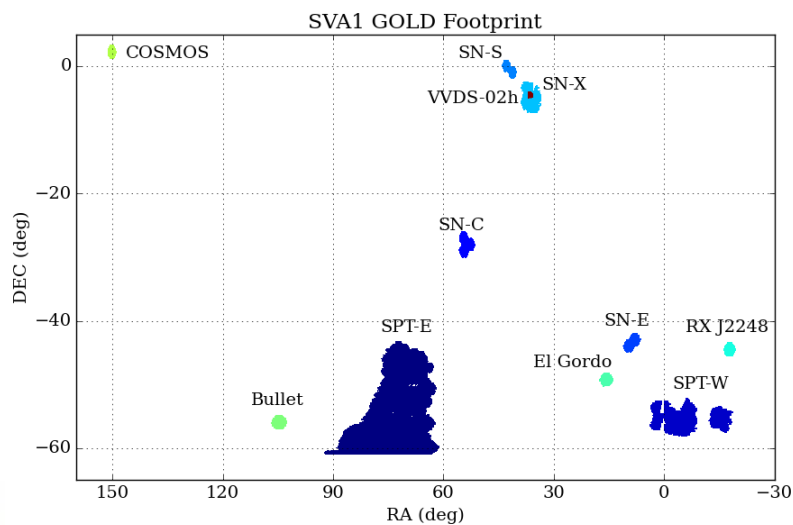


Figure 2.3: The DES SVA1 Gold catalogue footprint in equatorial coordinates using a cartesian projection. From [Dark Energy Survey Collaboration et al. \(2016\)](#).

$i = 23.0$, and $z = 22.3$. The SVA1 Gold catalogue data is broken into several fields:

1. SPT-E, which covers an area of ~ 160 sq deg. This overlaps with the Eastern part of the SPT footprint,
2. SPT-W, which covers an area of ~ 35 sq deg. This region overlaps with the western part of the SPT footprint,
3. DES SN, the region covers an area $\sim 5 - 15$ sq deg and it coincides with the DES supernova field SN-C, SN-E, SN-S, and SN-X,
4. cluster Field, the region covers an area ~ 3.5 sq deg. This area surrounds each of the rich galaxy clusters RXC J2248, Bullet Cluster, and El Gordo,
5. COSMOS, this region covers an area ~ 3.5 sq deg of imaging in the COSMOS field reaching 1 magnitude fainter than the nominal DES depth,
6. VVDS-02 h, covers an area of ~ 1 sq deg of the SN-X fields overlap the VVDS-02 h region.

The SVA1 Gold catalogue consists of astrometry, photometry, and object classification for 25 227 559 objects. Figure 2.3 shows the distribution of the different regions surveyed. DES catalogue was compiled from the SVA1 data processed using an early version of the DES Data Management system that included image detrending, astrometric registration, global calibration and image coaddition. The relative

astrometric accuracy of the SVA1 Gold catalogue is ~ 100 mas per coordinate from multiple DES observations of the same source and an absolute astrometric precision of ~ 200 mas per coordinate (Zacharias et al. 2013). Photometry for each object in the SVA1 Gold catalogue is available in the DES g, r, i and z bands. The uncertainty calibration of the catalogue was estimated to be around $< 2\%$.

Optical Source Sample Selection

The optical data were accessed from DES online*. DES overlaps with the VHS survey, and in the region of overlap we found 9325566 sources. The DES also provides photometric redshifts for all of the sources with significant detections. We removed galaxies that were affected by bad pixels by rejecting objects with one of the following flags (Jarvis et al. 2016a):

`Modest_class \neq 1, flags_G > 0, flags_R > 0, flags_I > 0, flags_Z > 0, Badflags_G > 0.`

In this work we take the photometric redshift measurements from the largest portion of the SV survey. The SV region is approximately 148sqdeg contained within the Eastern part of the region observed by the SPT-E. The DES optical imaging coverage is shown in Figure 2.4 and has a seeing-limited resolution of ~ 1 arcsec.

Common Region for Three Surveys

In this study, we wish to cross-match radio data from SUMSS, NIR data from VHS, and optical data from the DES. We chose a region of the sky between $60^\circ < \alpha' < 90^\circ$ and $-60^\circ < \delta < -45^\circ$ as it covers an area containing all three surveys, see Figure 2.4.

2.4 Conclusions

In this Chapter, we described three surveys: SUMSS, VHS, and DES. We chose a region bound by $-60^\circ < \delta < -45^\circ$ and $60^\circ < \alpha' < 90^\circ$. This covers an area of 148sqdeg. We used the sky coverage of the combined Dark Energy Survey and VISTA Hemisphere Survey DR3 and overlaid with the final cross-matched sample of 249 radio sources from SUMSS. We include galaxies whether they have full wavelength coverage or not. The SUMSS (radio sources) and VHS (NIR sources) samples were accessed online using SQL. DES (optical sources) photometric redshifts were found from the SVA1 Gold catalogue. Chapter 3 gives the properties of this sample that form the catalogue that we have found.

*opensource.ncsa.illinois.edu

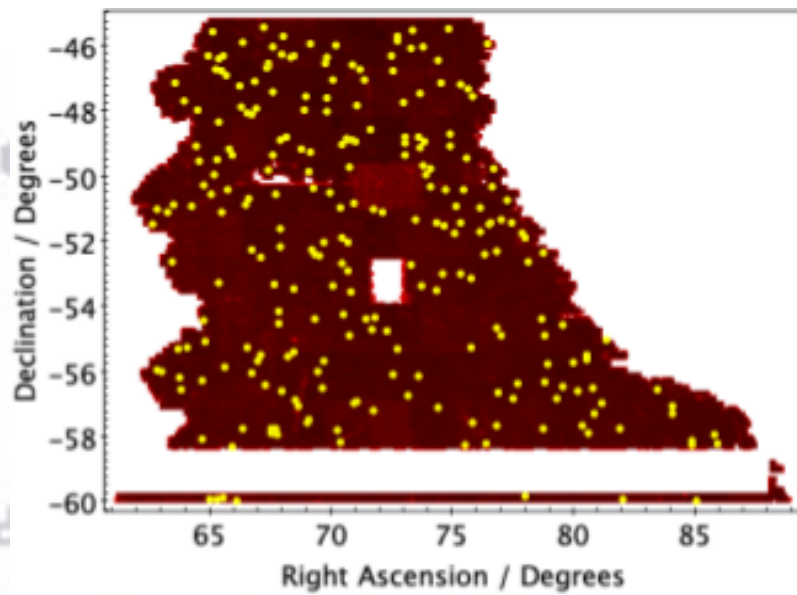


Figure 2.4: Sky coverage of the combined Dark Energy Survey and VISTA Hemisphere Survey DR3 (red background), overlaid with the final cross-matched sample of 249 radio sources (filled yellow circles). The white strip at a declination $\sim -59^\circ$ and the white rectangle in the middle of the field denote areas that have no NIR data from the VHS in DR3.

Chapter 3

A New Sample of Southern Radio Galaxies

3.1 Introduction

Powerful radio galaxies and radio-loud quasars ($L_{1.4\text{GHz}} \gtrsim 10^{25} \text{ W Hz}^{-1}$) form an important subset of the general AGN population. Their large-scale radio emission permits them to be selected at radio wavelengths where dust-obscuration is unimportant, thus plausibly allowing a census of a population to be made (e.g., [Willott et al. 2001](#), [McAlpine et al. 2013](#), [Smolčić et al. 2017](#)). Furthermore, over the past decade, radio galaxies have become a key component in simulations and models of the formation and evolution of massive galaxies. The radiative emission from the high-accretion rate sources can heat up the gas in and around the host galaxy, and the powerful radio jets that emanate from such galaxies, along with their lower-accretion rate counterparts can provide a form of feedback, due to the mechanical work that the jets can do against the ISM and IGM (e.g., [Rawlings & Jarvis 2004](#), [Croton et al. 2006](#), [Bower et al. 2006](#), [Schaye et al. 2015](#), [Sijacki et al. 2015](#), [Beckmann et al. 2017](#)).

For many decades, the best studied sample of radio galaxies was derived from the Third Cambridge (3C) survey, and the revised version (3CRR; [Laing et al. 1983](#)). A large observational campaign to obtain spectroscopic redshifts for these sources provided the benchmark for detailed studies of powerful radio galaxies across all wavelengths (e.g., [Lilly & Longair 1984](#), [Best et al. 1998b](#), [Willott et al. 2003](#)). However, although the basis for a huge amount of studies, 3CRR is a single flux-density limited sample and as such is subject to Malmquist bias. For this reason, observational campaigns towards the end of the 20th Century concentrated on obtaining complete redshift information for progressively fainter radio surveys (e.g., [Rawlings](#)

et al. 2001, Willott et al. 2001, Jarvis et al. 2001a).

These surveys were the bedrock for gaining an understanding the physics of powerful radio-loud AGN (e.g., Kaiser & Alexander 1997, Hardcastle et al. 1998, Blundell et al. 1999), their space density evolution (e.g., Willott et al. 2001, Jarvis & Rawlings 2000, Jarvis et al. 2001c, Cruz et al. 2007) and their host galaxies across cosmic time. Firstly using the observed relationship between the NIR K band magnitude and redshift (the radio galaxy $K - z$ relation, e.g., Lilly & Longair 1984, Eales et al. 1997, Jarvis et al. 2001b, Willott et al. 2003), and subsequently through deep *Spitzer* observations (e.g., Seymour et al. 2007) and multi-band photometry (e.g., Fernandes et al. 2015). In recent years, there has been a shift in focus towards the less luminous population of radio sources, for which the evolution is less well understood (e.g., Clewley & Jarvis 2004, Sadler et al. 2007, McAlpine et al. 2013, Rigby et al. 2015, Smolčić et al. 2017). Such studies require deeper radio data, whilst retaining the ability to measure redshifts for the radio sources. This has led these studies to rely predominantly on photometric redshifts, but see Prescott et al. (2016) and Pracy et al. (2016) who make use of spectroscopy.

Creating new samples of powerful radio sources, with redshift information is still important. This is because they are intrinsically rare and even the spectroscopically complete 3CRR, 6C and 7CRS samples only contain a few hundred objects. Our ability to create new samples of powerful AGN with redshift information has traditionally been hampered by the need to image the region around the radio source, preferably at NIR wavelengths, and then target the most probable host galaxies with time-intensive spectroscopic observations. Such observational campaigns, which took many years to complete, are now becoming less critical due to the plethora of large and deep imaging surveys covering optical and NIR wavebands (e.g., Abazajian et al. 2009, Wright et al. 2010, De Jong et al. 2015, Banerji et al. 2015).

Moreover, previous radio surveys (e.g., NVSS) were predominantly conducted in the Northern Hemisphere, as such the wealth of Southern Hemisphere facilities, such as the Atacama Large Millimetre Array (ALMA), cannot easily be used to obtain more detailed information the physics at play.

Given the importance of understanding the fuelling of and feedback from powerful radio galaxies, one of the key observations that can be made is that of the neutral and molecular gas in and around the AGN host galaxy. There are several ways of probing this gas, but the most powerful facilities are based in the Southern Hemisphere. Namely the ALMA operating in the millimetre waveband, thus enabling the detection and study of carbon monoxide, see Section 1.9, and by inference the molecular hydrogen, and starting in 2018 the MeerKaroo Array Telescope

(MeerKAT; Jonas 2009, Camilo et al. 2018) and the Australian Square Kilometre Array Pathfinder (ASKAP; Johnston et al. 2008, Norris et al. 2011) operating at or below 1.4 GHz, allowing the observation of HI in both absorption (e.g., Allison et al. 2016, Gupta et al. 2016, Jarvis et al. 2016b) and emission (e.g., Duffy et al. 2012, Holwerda et al. 2012, Jarvis et al. 2016b).

Since most of the new all-sky radio continuum surveys are being conducted in the Southern Hemisphere, e.g., ASKAP and eventually SKA, these surveys will need a catalogue of HzRGS. The main aim of this study is to cross-match radio sources from SUMSS and NIR from VISTA Hemisphere Survey sources and then use the DES optical data to obtain photometric redshifts to produce a catalogue of powerful radio source for absorption line studies with MeerKAT and other radio facilities, to understand the population of bright AGN at high redshift, and to understand the NIR properties of radio sources. The technique used for identifying high redshift radio galaxies from SUMSS and VHS will also be crucial for MeerKAT/SKA. This Chapter is organised as follows: In Section 3.2, we discuss how we use the Likelihood Ratio (LR) technique to define a sample of radio galaxies. In Section 3.3, we describe the photometric redshifts. In Section 3.4, we discuss our results on $K - z$ relation, results of our stellar masses are discussed in Section 3.5, in Section 3.6, we discuss the results of our SFRs and we give conclusion of our sample in Section 3.7. Throughout this Chapter, we have assumed *Planck* cosmology with $H_0 = 67.6 \text{ km s}^{-1} \text{ Mpc}^{-1}$, $\Omega_M = 0.31$ and $\Omega_\Lambda = 0.69$. We use AB magnitudes unless stated otherwise.

3.2 The Likelihood Ratio

Given the large discrepancy between the resolution of SUMSS and the optical and NIR data, we employ the LR technique to associate the radio sources, which are predominantly unresolved at the resolution of SUMSS, with the NIR catalogue. The LR is the ratio of the probability that two sources are associated, to the probability that the two sources are unrelated (e.g., Sutherland & Saunders 1992, Smith et al. 2011, Fleuren et al. 2012, McAlpine et al. 2012), and can be expressed as

$$\text{LR} = \frac{q(m)f(r)}{n(m)}, \quad (3.1)$$

where $q(m)$ is the true distribution of NIR counterparts (from VHS in this case) as a function of magnitude, $f(r)$ is the radial probability distribution function of the offset between the SUMSS position and the position of a galaxy in the VHS catalogue, and $n(m)$ in the LR formalism represents the number of unrelated galaxies in the

background catalogue. We use the K_s band as the band to perform the LR analysis with SUMSS due to the fact that we expect the host galaxies to be massive and NIR bright for the more powerful radio sources (Jarvis et al. 2001b, Willott et al. 2003, Seymour et al. 2007).

The radial probability distribution for NIR counterparts to the SUMSS radio sources is then given by:

$$f(r) = \frac{1}{2\pi\sigma_{\text{pos}}^2} \exp\left(-\frac{r^2}{2\sigma_{\text{pos}}^2}\right), \quad (3.2)$$

where r is the positional offset between the radio and K_s band sources and σ_{pos} is the combined positional error of the radio and NIR positions. In this study, σ_{pos} is dominated by the positional error of the SUMSS radio sources, and we therefore neglect the contribution to this term from the NIR sources. Following, Smith et al. (2011), we assume that the positional error for the radio sources can be described by

$$\sigma_{\text{pos}} = 0.655 \frac{\theta_{\text{FWHM}}}{\text{SNR}}, \quad (3.3)$$

where θ_{FWHM} is the full-width at half maximum of the synthesised beam, and the Signal-to-Noise Ratio (SNR) is simply the SNR for the detected source. We note that the resolution of SUMSS is declination dependent, but our data only span ~ 15 deg in declination, we therefore take the median resolution of our sample to fix θ_{FWHM} .

The source density term $n(m)$, is estimated from the source counts of the input VHS catalogue. We can estimate $q(m)$ following Ciliegi et al. (2003) and Fleuren et al. (2012). First we calculate the magnitude distribution, $total(m)$ for all NIR objects within a fixed search radius, r_{max} of the centroid of the radio source. The real distribution of counterparts, $real(m)$ can then be determined by subtracting the background number density $n(m)$ normalised to the area defined by r_{max} ,

$$real(m) = total(m) - [n(m) N_{\text{radio}} \pi r_{\text{max}}^2], \quad (3.4)$$

where N_{radio} is the total number of radio sources in the input catalogue, see Figure 3.1. The magnitude distribution of all the possible counterparts within r_{max} of the radio positions is then given by,

$$q(m) = \frac{real(m)}{\sum_m real(m)} Q_0, \quad (3.5)$$

where Q_0 is an estimate of the fraction of SUMSS radio sources with NIR counterparts above the magnitude limit of VHS.

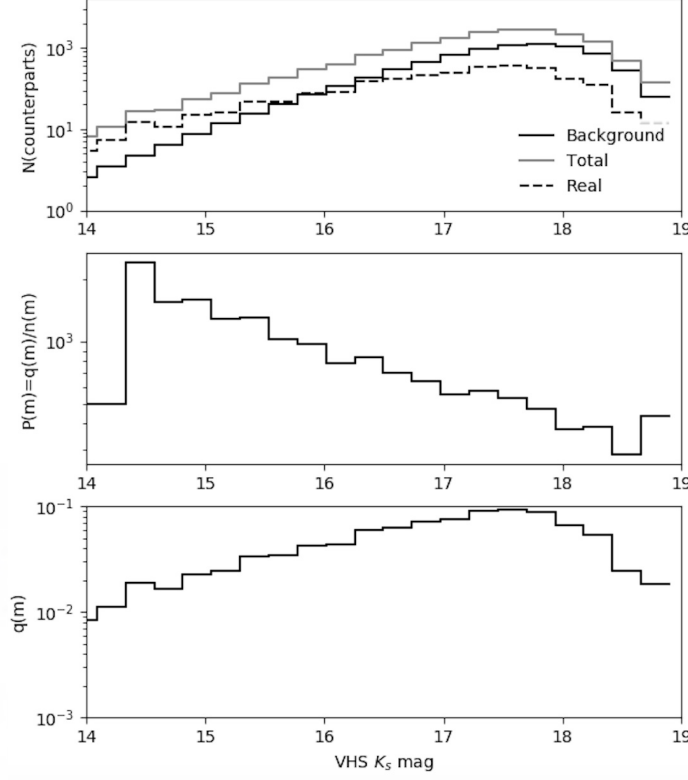


Figure 3.1: (*top*): The magnitude distribution of the background galaxy number density, $n(m)$ derived directly from the VHS catalogue, the $total(m)$ denoting all possible matched within radius r_{\max} , as defined in the text, and the $real(m)$ distribution of actual counterparts. (*middle*): Shows the magnitude dependent $q(m)/n(m)$ distribution calculated from the data as described. (*bottom*): The true distribution, $q(m)$ of the NIR counterparts.

The fraction of true counterpart of the sources which are above the NIR/optical limit is given by,

$$Q_0 = \frac{N_{\text{matches}} - \sum_m n(m) \pi r_{\max}^2 N_{\text{radio}}}{N_{\text{radio}}}, \quad (3.6)$$

where N_{matches} is the number of counterparts within r_{\max} of the radio positions.

To determine Q_0 we need to determine the number of sources in the radio catalogue with no NIR counterparts within a search radius r_{\max} . We again adopt the method of (Fleuren et al. 2012). The number of sources in the radio catalogue without a NIR match $U_{\text{obs}}(r)$, and the number without a NIR identification for a random position within the survey area $U_{\text{random}}(r)$, can be related to Q_0 via

$$\frac{U_{\text{obs}}(r)}{U_{\text{random}}(r)} = 1 - Q_0 F(r), \quad (3.7)$$

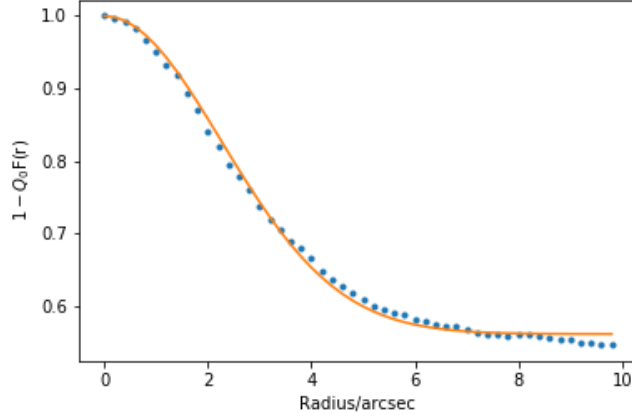


Figure 3.2: Method to estimate $1 - Q_0$. The solid yellow line is the best fit to the model $1 - Q_0 F(r)$, with $Q_0 = 0.395$. The points represent the data obtained by dividing the number of sources in the SUMSS catalogue without an NIR match by the number of random positions that did not have a NIR counterpart within radius r , i.e., $U_{\text{obs}}(r)/U_{\text{random}}(r)$.

where

$$F(r) = 1 - \exp\left(-\frac{r^2}{2\sigma_{\text{pos}}^2}\right). \quad (3.8)$$

We determine Q_0 via a fit to the observed ratio of $U_{\text{obs}}(r)$ to $U_{\text{random}}(r)$, we obtained $Q_0 = 0.395$ as our best-fitting value for radio galaxies. Figure 3.2 shows the best-fitting model denoted by the yellow line and our data is denoted by the blue points.

The reliability of the counterparts can then be calculated using,

$$\text{Rel}_i = \frac{\text{LR}_i}{\sum_j \text{LR}_j + (1 - Q_0)}, \quad (3.9)$$

where i is the index for the radio sources and j is the index of all the possible NIR counterparts. The reliability as a function of the K_s band magnitude is shown in Figure 3.3. Similarly, the number of sources with a false identification N_{cont} can be expressed as

$$N_{\text{cont}} = \sum_{\text{Rel} > 0.8} (1 - \text{Rel}). \quad (3.10)$$

The LR technique was used in our study to identify the NIR VHS counterparts to all the SUMSS radio sources in the overlap area. We ensured that our search radius includes all possible real counterparts to the radio sources by setting r_{max} to 5 times the largest expected positional error, $\sigma_{\text{pos}} = 30$ arcsec. Of the 5380 radio sources

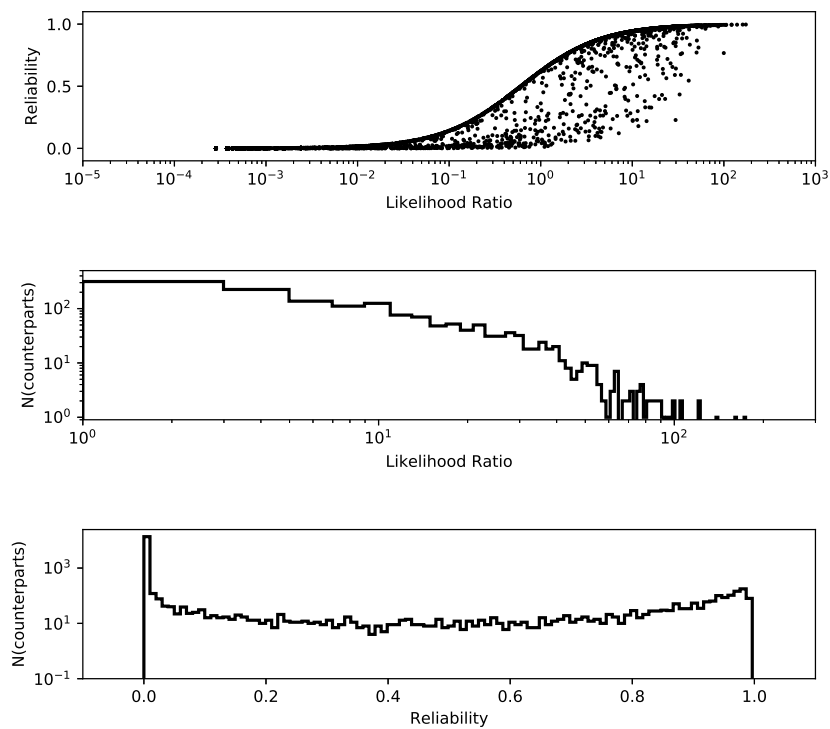


Figure 3.3: (*top*): The variation of the reliability as a function of the LR. (*middle*): Histogram of the LR values for SUMSS radio catalogue with 5380 sources with NIR counterparts to the 2287733 VHS catalogue. (*bottom*): Reliabilities for each counterpart. There are a total of 1195 sources which have a reliability $Rel > 0.8$.

above 10σ in our radio sample, we find that 1 195 have a near-infrared counterpart with a reliability of $\text{Rel} > 0.8$, following the threshold used in previous studies using this technique (e.g., [Smith et al. 2011](#), [Fleuren et al. 2012](#)). Thus, the majority of radio sources do not have a NIR counterpart at the depth of the VHS data. This is in line with expectations given the low-resolution radio data and the relatively shallow depth of the NIR data (see e.g., Table 2 in [McAlpine et al. 2012](#)). Furthermore, we expect 81 sources from our sample to have a false identification, corresponding to a contamination of 6.8%.

It is also worth noting that the resolution of SUMSS means that we cannot disentangle what could be multiple sources within the restoring beam. This is likely to increase the number of radio sources without NIR counterparts using the LR technique, as the centroid of the radio source may not represent the position of the core associated with the host galaxy. Instead the peak of the emission will have a flux-weighted position that is dependent on the source structure, the relative brightness of any lobe emission, and whether there is indeed a strong core at all. Thus, we emphasise that our final sample is not complete but should be representative of the powerful radio galaxy population out to $z \sim 1$, beyond which our optical and NIR data are too shallow to consistently detect counterparts to the radio sources.

3.3 Photometric redshifts

Photometric redshifts are an estimate of the redshift of an astronomical object using multi-band photometry instead of spectroscopy. This technique relies on identifying the passage of continuum features within the SED across a series of photometric passbands. Photometric redshifts are essential in the $1 < z < 2$ range where it is difficult to measure redshifts from optical spectroscopy due to the absence of strong, accessible emission or absorption features. Photometric redshifts are also crucial for detecting galaxies that are fainter than the spectroscopic limits, and useful for obtaining the redshifts for large numbers of galaxies.

In order to obtain the redshifts for our sample, we cross-matched the radio sources with identifications in VHS to the DES catalogue with a search radius of 1 arcsec. Since the VHS and DES surveys have high positional accuracy, this 1 arcsec radius should be sufficient to locate the VHS counterpart in DES. We do not perform any quality cuts on the photometric redshifts.

Of the 1 195 DES+VHS sources cross-matched to the SUMSS data, we find that 249 have good photometric information that allow the determination of photometric redshifts, see [Appendix A](#) and these form the sample used in this Chapter. These

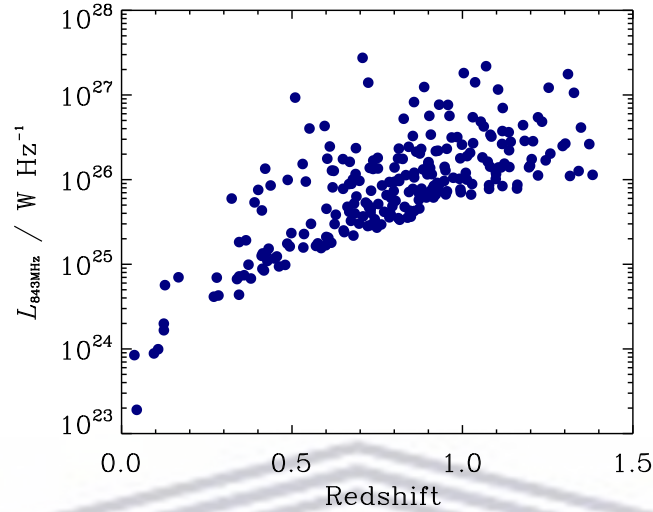


Figure 3.4: Rest-frame 843 MHz radio luminosity (calculated assuming a spectral index of $\alpha = 0.7$) versus redshift for radio galaxies samples from our SUMSS+DES+VHS sample.

are sources overlaid on the coverage map in Figure 2.4. We note that the sample is broadly restricted to $z \leq 1.4$, as the 4000 \AA break, which is a key spectral feature for fitting photometric redshifts, is redshifted into the NIR filters for $z > 1$. However, one still requires relatively deep data blue-ward of the 4000 \AA break for the photometric redshifts to be accurate. As the main science goal for this sample will be to conduct follow-up studies of the HI, this approximate redshift limit will not adversely effect this goal for current facilities. Thus, we restrict our sample to the DES only derived photometric redshifts, but use the NIR data when performing spectral energy distribution fitting. Figure 3.4 shows the photometric redshift versus radio luminosity for our final sample, where we assume a spectral index of $\alpha = 0.7$ to the rest-frame 843 MHz, where $S_\nu \propto \nu^{-\alpha}$.

3.4 The $K - z$ Relation

The study of high-redshift radio galaxies can give us a useful insight to the formation of massive galaxies. Many previous studies of the properties of radio galaxy hosts have utilised the so-called $K - z$ relation, which has traditionally been used to demonstrate that powerful radio galaxies tend to reside in the most massive galaxies at all epochs (e.g., Eales et al. 1997, Jarvis et al. 2001a, Willott et al. 2003, Rocca-Volmerange et al. 2004). In Figure 3.5, we show the $K - z$ relation for the radio

galaxies in our joint SUMSS+DES+VHS sample, using the photometric redshifts. It is clear that the radio galaxies in our sample broadly follow the $K - z$ relation based on a range of complete samples of radio sources from 3CRR, 6CE, 6C* and 7C, although we note that there is evidence that some of the lower-redshift radio sources in our sample tend to have fainter hosts. This could be due to a relation between radio luminosity and host galaxy mass (McLure et al. 2004a), given that our radio sources are derived from a deeper parent radio survey (10 mJy at 843 MHz compared to 50 mJy at 151 MHz in the case of 7CRS; Willott et al. 2003). However, at these low-redshifts and flux-density limit, we are close to the radio luminosity where star-forming galaxies may be being included ($L_{1.4\text{GHz}} > 10^{23} \text{ W Hz}^{-1}$; Mauch & Sadler 2007) in the sample selection, and we would expect such galaxies to show a marked difference in their host galaxy properties compared with the massive ellipticals that tend to host more powerful radio sources. Another possibility is that these are misidentifications in our LR analysis, as we expect 6.8% from our total NIR sample to be contaminants. After cross-matching with DES, we may expect this fraction to decrease as we are biased towards brighter objects that are detected at high signal-to-noise at the visible as well as NIR wavelengths. However, we would still expect some fraction of our sources to be false associations. We explore this further in Section 3.6.

3.5 Stellar Masses of Radio Galaxies

Unlike many past studies of radio host galaxies, given the multi-band photometry we are not limited to just using the K_s band magnitude in order to compare the radio galaxy hosts to the general galaxy population. We can use the optical photometry from the DES and NIR photometry from the VHS to fit stellar population synthesis (SPS) models in order to obtain estimates of the stellar mass and SFRs of the radio galaxy hosts. We therefore use the Fitting and Assessment of Synthetic Templates (FAST; Kriek et al. 2009) code to find the best-fit galaxy templates to the combination of the DES and VHS photometry, using the photometric redshifts described in Section 3.3. No uncertainty information on the photometric redshifts was included in the FAST fitting. The uncertainty on the measured photometry is based on the noise estimated from parts of the image that do not have any detected galaxies and we adopt a floor of 5% on the noise to account for any slight mismatch between templates and the photometry.

We ran the FAST code using two different SPS models from Bruzual & Charlot (2003) and Maraston (2005), with both fixed metallicity, Z_m and allowing the metal-

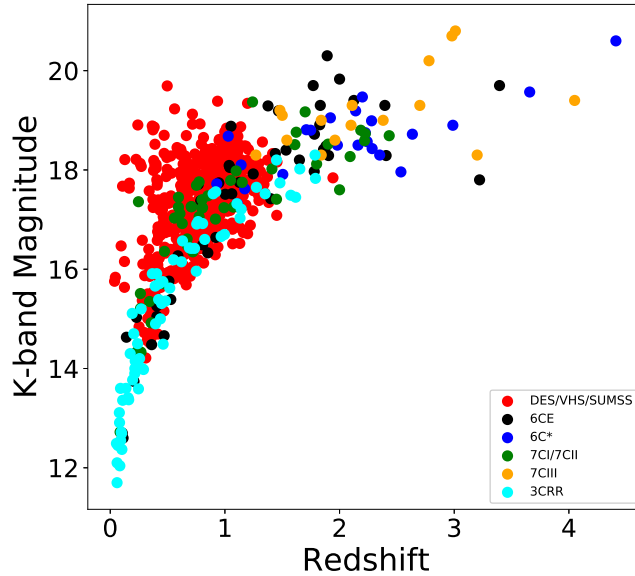


Figure 3.5: K band (in Vega magnitude) versus redshift for radio galaxies from our SUMSS+DES+VHS (using the K_s band) catalogue (red circles). We also show the points from 6CE, 6C*, 7C-I, II, III and 3CRR complete samples, with colours denoted in the legend.

licity to vary, see Figures 3.6 to 3.9. These models were fitted with a total dust extinction (A_V) in the range $0.0 < A_V < 0.3$. The relationship between two different stellar population synthesis models (Bruzual & Charlot 2003, Maraston 2005, hereafter BC03 and Ma05) was investigated, see Figure 3.6 to 3.9. The Ma05 stellar masses are displayed on the horizontal axis and BC03 stellar masses are displayed on the vertical axis. The masses range from $10^8 M_\odot$ to $10^{12} M_\odot$ for both BC03 and Ma05, and the results scatter about the 1:1 yellow line. We see that many of the stellar masses are concentrated between $10^{10} M_\odot$ and $10^{12} M_\odot$ with very few outside this range. In the bottom left panel of Figure 3.8, one can see that the scatter is reduced when comparing the BC03 and Ma05 models for the same metallicity of $Z_m = 0.02$. For this study we assumed an exponentially declining SFH in all different models with a Salpeter Initial Mass Function (IMF; Salpeter 1955). We also investigated how different choices for the SFH and IMF alter our results, and find that the choice of IMF and SFH does not affect our results. We note that adopting a Chabrier IMF does not make a difference to the general trends that we observe, however the absolute mass measurement may change by around 0.2 – 0.3 dex.

Figure 3.10 shows the redshift against stellar mass of the radio galaxy hosts after fitting Simple Stellar Population (SSP) to the broad-band photometry using FAST.

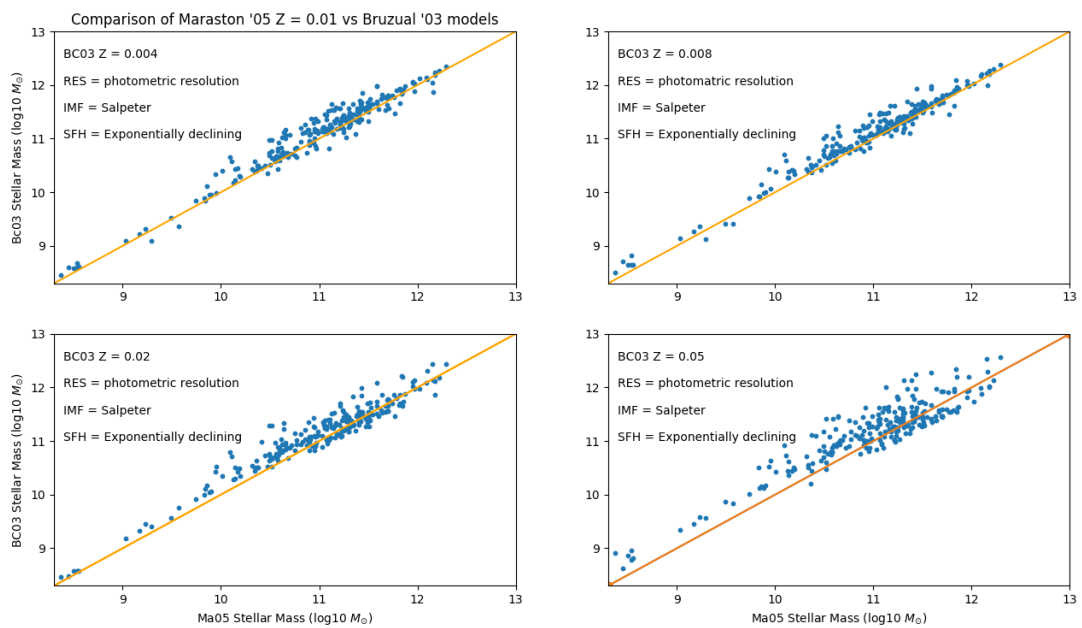


Figure 3.6: Comparison of mass of the two different stellar population synthesis (Bruzual & Charlot 2003, Maraston 2005) with $Z_m = 0.01$, and a total dust extinction in the range $0.0 < A_V < 0.3$.

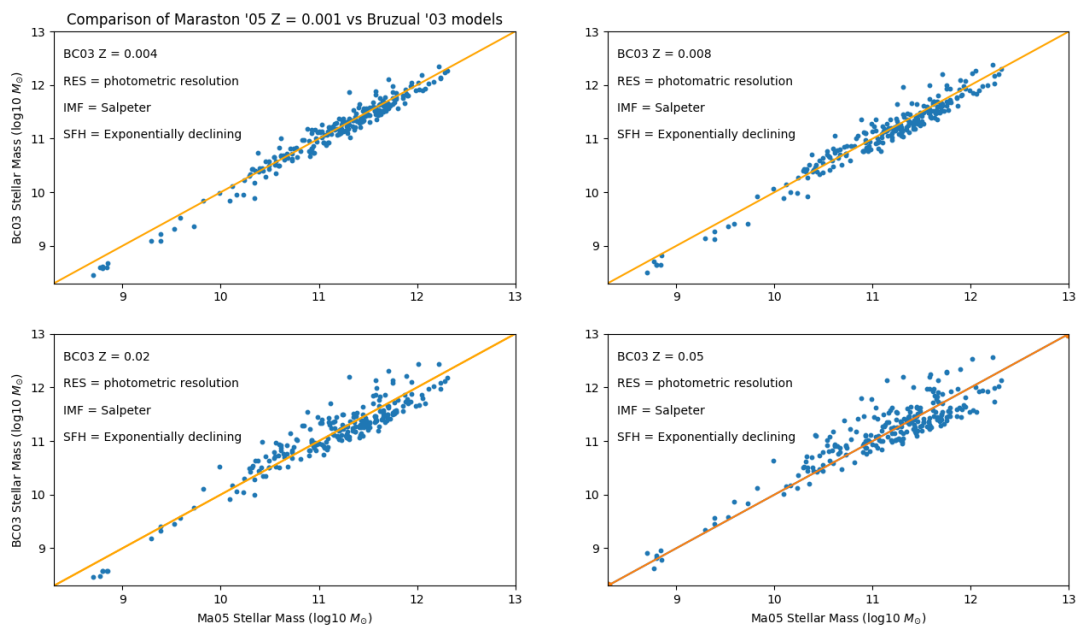


Figure 3.7: Comparison of mass of the two different stellar population synthesis (Bruzual & Charlot 2003, Maraston 2005) with $Z_m = 0.001$, and a total dust extinction in the range $0.0 < A_V < 0.3$.

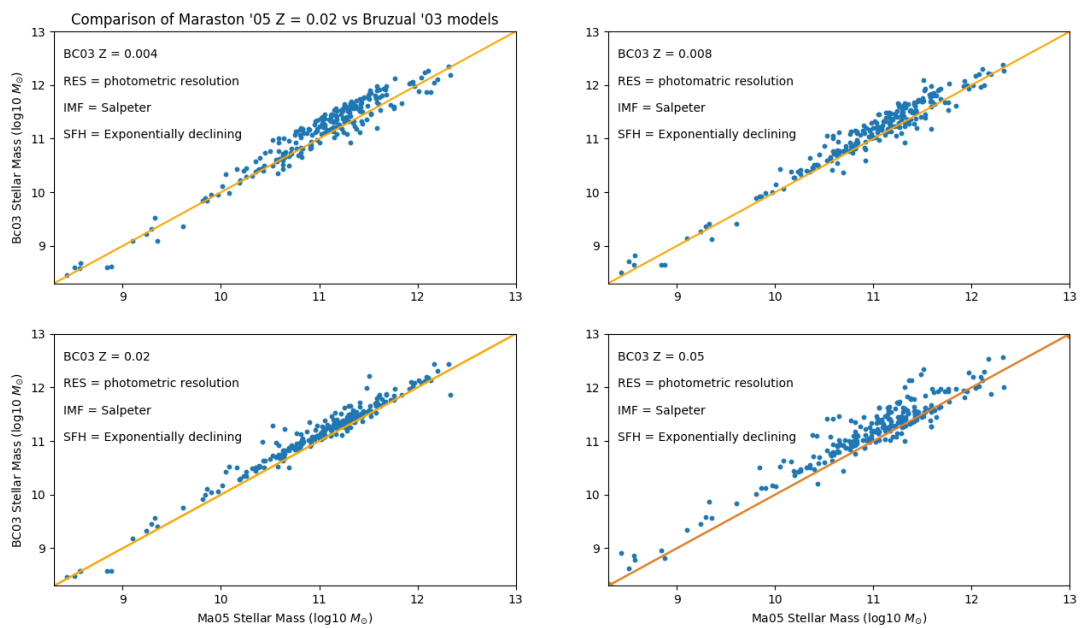


Figure 3.8: Comparison of mass of the two different stellar population synthesis (Bruzual & Charlot 2003, Maraston 2005) with $Z_m = 0.02$, and a total dust extinction in the range $0.0 < A_V < 0.3$.

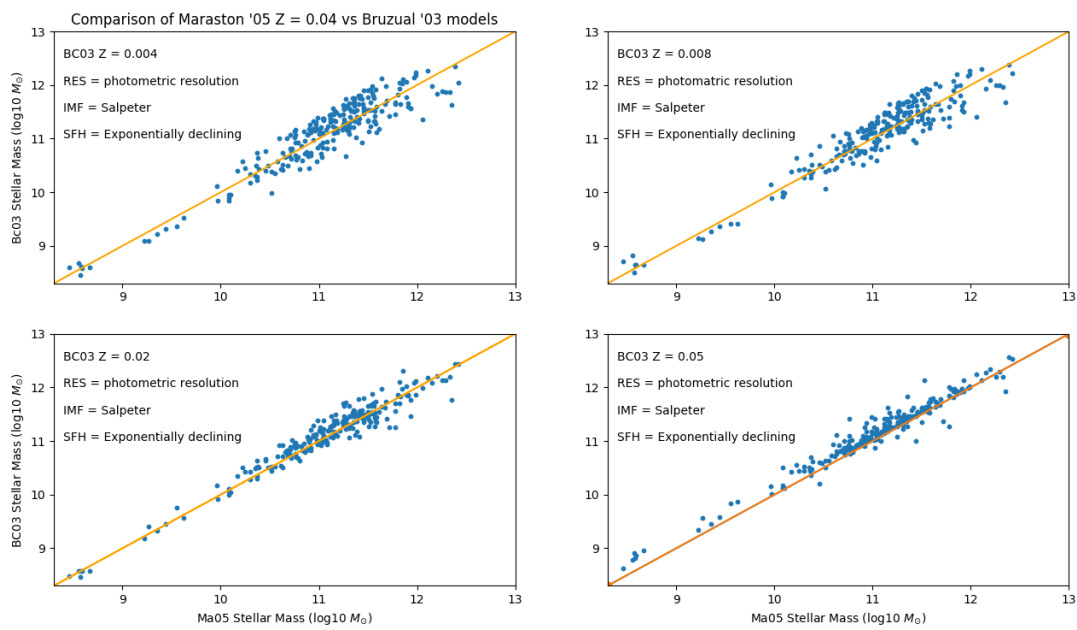


Figure 3.9: Comparison of mass of the two different stellar population synthesis (Bruzual & Charlot 2003, Maraston 2005) with $Z_m = 0.04$, and a total dust extinction in the range $0.0 < A_V < 0.3$.

We find a broad range in stellar masses, but with the bulk of the high-redshift radio source hosts lying between stellar masses of $10^{11} - 10^{12} M_{\odot}$. This is consistent with the range in stellar masses for the much more radio luminous radio sources that have been studied in detail from surveys such as 3CRR, 6C and 7CRS amongst others. For example, [Seymour et al. \(2007\)](#) undertook a study of the host galaxies of a large sample of powerful radio galaxies using *Spitzer* and found host galaxy masses of $10^{11} - 10^{11.5} M_{\odot}$. Comparing to the non-active galaxy population, this range corresponds to the most massive subset of galaxies in the Universe, at $1 - 10 M_{*}$ using the galaxy mass functions from [Wright et al. \(2017\)](#) and [Ilbert et al. \(2013\)](#). The $\chi^2 < 20$ is conservative and removes those data with particularly poor fits, see [Figure 3.11](#).

Although some studies have found a link between radio luminosity and host galaxy mass (e.g., [Jarvis et al. 2001b](#), [McLure et al. 2004a](#)), we find no evidence for this in our sample. However, the fact that we only have used a single flux-limited radio survey means that the range in radio luminosity for a given redshift range is limited. Combining the sample discussed here with both wider area brighter samples, and fainter samples over smaller areas would allow this question to be investigated in much more detail, as this would increase the range in radio luminosity that could be probed, across the full redshift range.

3.6 Star Forming Galaxies

There are clearly some radio sources in our sample where the host galaxy is significantly less massive than $\sim 10^{11} M_{\odot}$. These are predominantly at low-redshift, which is likely due to the depth of the optical and NIR data. These galaxies, although relatively bright radio sources, are also much less massive. The majority of these sources tend to be much bluer than the more massive galaxies, with $0 < (g - r) < 0.5$ for the galaxies with $M < 10^{10} M_{\odot}$, compared to $0.5 < (g - r) < 2.5$ for the higher-mass galaxies, see [Figure 3.12](#). This suggests that these lower-mass, lower-redshift sources are a distinct population from the higher redshift, more powerful sources.

Using the radio luminosity function determined by [Mauch & Sadler \(2007\)](#), the dominant population at $z < 0.3$, $L_{1.4\text{GHz}} < 10^{23} \text{ W Hz}^{-1}$ are star-forming galaxies, which corresponds to a radio luminosity of $L_{843\text{MHz}} = 1.4 \times 10^{23} \text{ W Hz}^{-1}$ at 843 MHz, assuming $\alpha = 0.7$. This is less luminous than the radio luminosity of the sources with low stellar mass and blue colours in our sample. However, using the radio luminosity function for star-forming galaxies from [Mauch & Sadler \(2007\)](#) we expect to find around 2 – 3 star-forming galaxies at $z < 0.2$ with $L_{843\text{MHz}} > 1.4 \times 10^{23} \text{ W Hz}^{-1}$

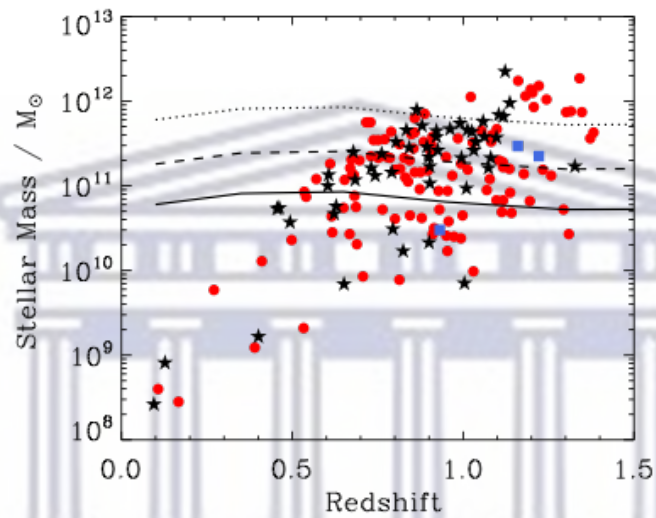


Figure 3.10: Redshift versus stellar mass for radio galaxies in our sample. The red circles denote those radio sources missing J and H bands data, the blue squares are those missing just J band data and the black stars denote those radio galaxies with a full complement of g, r, i, z, J, H, K_s data, demonstrating that the lack of information in some filters does not introduce any obvious systematics in our stellar mass estimates. We only show points with SED fits with $\chi^2 < 20$, thereby including the bulk of our fits, see Figure 3.11. The solid line represents M_\star from Wright et al. (2017) at $z < 0.1$ and Ilbert et al. (2013) at $z > 0.1$. The dashed line corresponds to $5 M_\star$ and the dotted line to $10 M_\star$. We did not consider uncertainties on the redshift or inferred stellar mass.

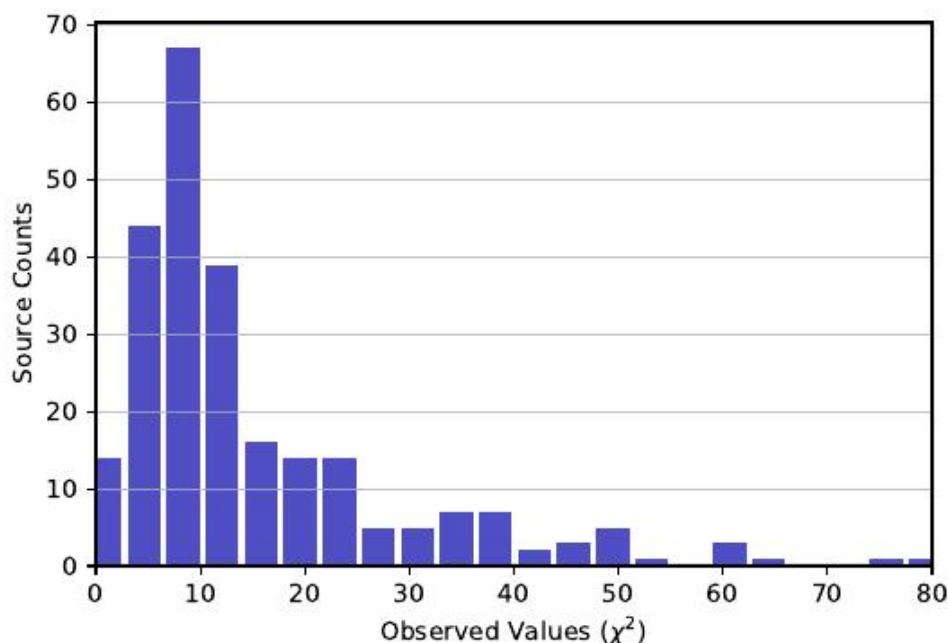


Figure 3.11: Source counts versus χ^2 -distribution for radio galaxies in our sample.

in our survey area, which is marginally consistent with the number of radio sources with blue colours at these luminosities within our sample. We obtained 15 radio sources associated with blue colours within our sample. Furthermore, to explain the higher redshift, higher radio luminosity blue galaxies only requires a moderate amount of evolution in the star-forming galaxy population, which is consistent with studies of the evolution in the radio luminosity function of star-forming galaxies (e.g., [McAlpine et al. 2013](#), [Novak et al. 2017](#)).

We can use the outputs of the FAST code in order to investigate whether the star-formation rate that we infer from the radio luminosity is consistent with that using the optical and NIR photometry. Figure 3.13 shows the star-formation rate derived from FAST and the 843 MHz radio luminosity, which clearly shows that the radio power of our low-redshift radio galaxies far exceed that expected from star-formation alone.

We therefore suggest that these sources are more likely to be the small number of low-redshift interlopers that we expect from the estimated false positives in our LR analysis. We checked the reliability from the LR of these low-mass, low-redshift galaxies and they are not near to the cut-off of 0.8. However, we show the radio contours overlaid on the VHS K_s band images of our sample in Appendix B. There is no obvious indication of these being misidentified but we cannot rule out fainter

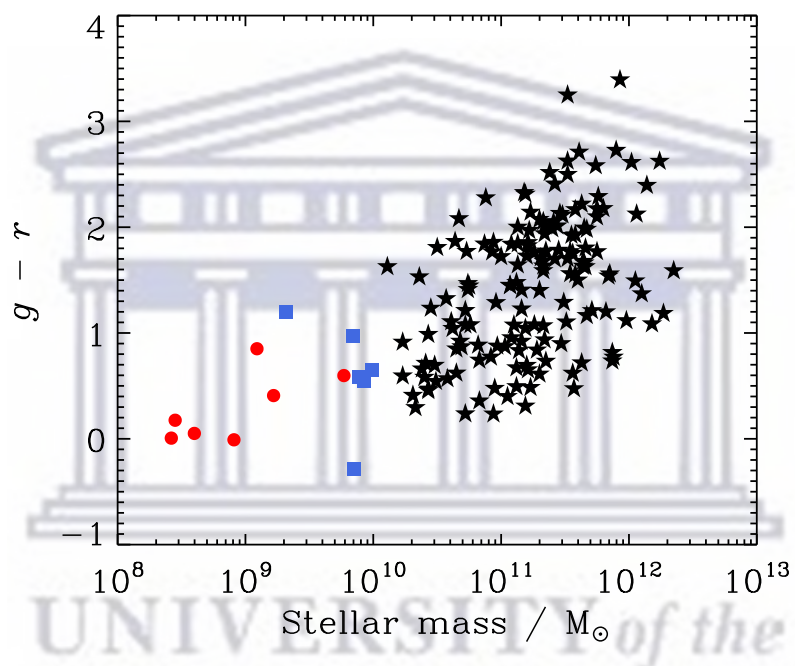


Figure 3.12: Stellar mass versus $g - r$ colour for the radio galaxies in our sample. The red circles denote galaxies at $z < 0.5$, whereas the blue squares represent those galaxies at $z > 0.5$ with stellar mass of $M_{\star} < 10^{10} M_{\odot}$. We only show points with SED fits with $\chi^2 < 20$.

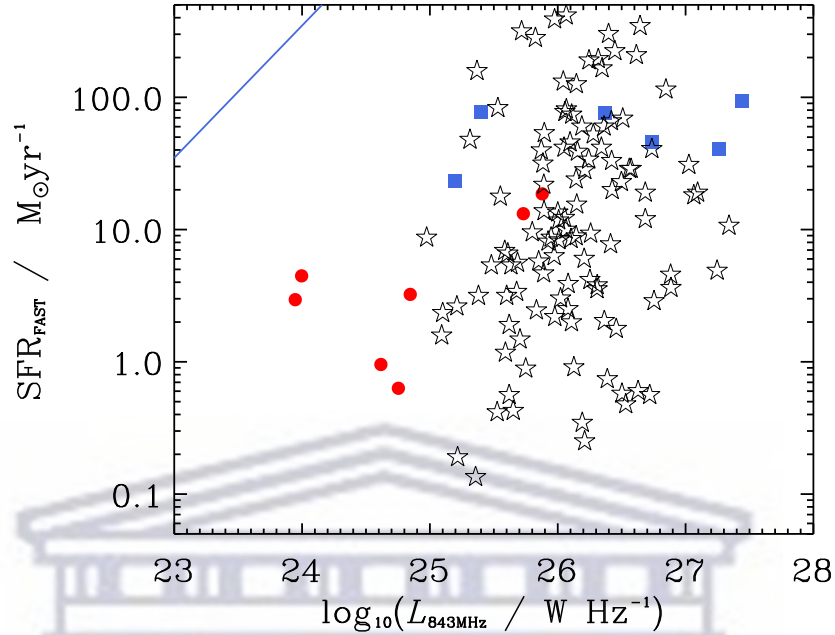


Figure 3.13: Radio luminosity against SFR derived using SED fitting in FAST for the host galaxies of the radio sources in our sample. The red circles denote galaxies at $z < 0.5$ with $M < 10^{10} M_{\odot}$, whereas the blue squares represent those galaxies at $z > 0.5$ with $M < 10^{10} M_{\odot}$. The open stars are the galaxies with $M > 10^{10} M_{\odot}$ from the SED fitting. We only show points with SED fits with $\chi^2 < 20$. The solid line represents the expected correlation using the relationship between SFR and radio luminosity used in [Delhaize et al. \(2017\)](#) and [Novak et al. \(2017\)](#).

high-redshift true counterparts. On the other hand they could be low-mass blue galaxies that host powerful radio sources or their photometric redshifts could be significantly wrong. Higher resolution radio data and/or deep optical/NIR data would be needed to confirm which of these scenarios is correct.

3.7 Conclusions

We have described the process of obtaining reliable optical and NIR counterparts to a relatively bright sample of radio sources in order to provide a catalogue for follow-up observations with the new generation of radio telescopes. We found 1 195 radio source counterparts with reliability above 0.8, with 81 of these sources expected to be falsely identified. After cross-matching these sources with the DES photometric redshift catalogue, we form a sample of 249 radio galaxies with redshift information.

Using this sample we investigate the host galaxy properties of these powerful

radio galaxies. We find that they follow the well-known radio galaxy $K - z$ relation when compared to previous complete samples selected at higher radio flux-density limits.

We then performed SED fitting to the optical and NIR photometry to investigate the host galaxy properties. We found that the radio galaxies fall into two broad populations, low-mass blue galaxies and high-mass red galaxies. The red galaxies, which are dominated by the radio-AGN, typically have host galaxy stellar masses in the range $10^{11} - 10^{12} M_{\odot}$, which corresponds to $1 - 10 M_{\star}$ from the galaxy mass function, suggesting that in order to produce powerful radio emission, the galaxy needs to be sufficiently massive to host SMBH of $> 10^8 M_{\odot}$, if the $M_{\text{bulge}} - M_{\text{BH}}$ relation holds to high redshift. This would be in line with studies of radio-loud quasars, where the BH mass is measured via the virial method (e.g., [McLure et al. 2004b](#)). The lower-mass $M < 10^{10} M_{\odot}$ galaxies in our sample of radio sources are consistent with being blue star-forming galaxies. We compare the star-formation rates derived from SED fitting to those based on the radio luminosity and find that the radio luminosity is significantly higher than one would expect. We therefore suggest that these sources are likely to be made up of the small fraction of high-reliability identifications that are actually false positives. On the other hand they could be lower-mass blue galaxies hosting bright radio sources, or for these small number of cases the photometric redshift could be wrong, as we would expect a small number of catastrophic outliers. This could only be addressed by obtaining better photometry or more data using other filters, or via spectroscopy. Follow-up, higher-resolution radio imaging would help alleviate mis-identifications, as the limiting factor in our cross-identifications is the low resolution of the SUMSS radio imaging. Spectroscopy to confirm their redshifts would also be useful to determine their nature.

We find a broad range in stellar masses, but with the bulk of the high-redshift radio source hosts lying between stellar masses of $10^{11} - 10^{12} M_{\odot}$. Comparing to the non-active galaxy population, this range corresponds to the most massive subset of galaxies in the Universe, at $1 - 10 M_{\star}$ using the galaxy mass functions from [Wright et al. \(2017\)](#) and [Ilbert et al. \(2013\)](#). The $\chi^2 < 20$ is conservative and removes those data with particularly poor fits, see [Figure 3.11](#).

This sample of Southern bright radio sources will be used as a basis for studying the fuelling and feedback from powerful radio galaxies using the new generation of radio telescopes. In particular, we plan to undertake a comprehensive study of HI absorption against these powerful sources with the MeerKAT radio telescope.



UNIVERSITY *of the*
WESTERN CAPE

Chapter 4

MeerKAT HI Study of High-powered AGNs

In this Chapter we use shared-risk early science data from MeerKAT to observe the cold ($T < 10\,000\text{ K}$) HI gas in a sample of powerful AGN. The project is called the MeerKAT HI Study of High-powered AGN: a PILOT SURVEY (MHISHAPS). This work has been done with the collaboration of James Allison. Allison's contributions to this Chapter are described in Section 4.1, Section 4.4, and Section 4.3. My contribution in particular was Section 4.2, Section 4.5, and Section 4.6.

4.1 Introduction

AGNs are thought to have a substantial impact on their host galaxy, shaping their evolution over cosmic time. In the nearby Universe, this AGN feedback is categorised into quasar (radiative) and radio (kinetic) modes. The former is associated with the central AGN of SFGs of the radiatively efficient AGN population (i.e., Seyferts, High Excitation Radio Galaxy (HERGs), and quasars). It is possible that the quasar mode may have a significant effect on impeding further star-formation by removing the gas from the ISM. In contrast, radio mode feedback typically occurs in higher mass passive galaxies that have a radiatively inefficient AGN dominated by synchrotron radio emission (i.e., Low Excitation Radio Galaxy (LERGs); e.g., [Best & Heckman 2012](#)). Regular mechanical feedback from the radio jets regulates cooling of circumgalactic gas onto these massive galaxies, thereby preventing further stellar mass growth ([Nulsen & Fabian 2000](#), [Croton et al. 2006](#)).

Establishing the physical mechanisms by which cool gas reaches the nucleus is key to understanding these AGN populations and their role in galaxy evolution through-

out the history of the Universe. Radiatively-efficient AGN seem to be triggered by accreting from an existing cold gas reservoir, which loses angular momentum through either an interaction or secular event (e.g., [Hopkins & Hernquist 2006](#), [Hopkins et al. 2008](#)). In the case of radiatively-inefficient AGN the picture is likely far more complex than simple Bondi accretion ([Allen et al. 2006](#), [Hardcastle et al. 2007](#), [Russell et al. 2013](#)). Current models suggest that gas clouds condense from the hot halo and lose their net angular momentum through chaotic collisions within a few Bondi radii of the BH (e.g., [Li & Bryan 2014](#)). Examples of filamentary gas structures in nearby cool-core clusters (e.g., [Salomé et al. 2006](#), [Lim et al. 2008](#), [McNamara et al. 2014](#), [Russell et al. 2016](#)) and inward radial motion of individual atomic and molecular gas clouds seen in absorption towards radio AGN (e.g., [David et al. 2014](#), [Maccagni et al. 2014](#), [Tremblay et al. 2016](#), [Maccagni et al. 2018](#)) support this chaotic cold accretion model.

HI 21 cm absorption is a powerful probe of cold gas kinematics in radio-loud AGN. Detection is independent of luminosity distance thus allowing spectroscopic surveys to be carried at cosmological distances (e.g., [Kanekar & Briggs 2004](#), [Morganti et al. 2015](#)). The pathfinder telescopes to the planned Square Kilometre Array have sufficient bandwidth and survey speeds to carry out 21 cm line surveys for intervening and intrinsic absorption towards thousands of radio sources ([Morganti & Oosterloo 2018](#)). The MeerKAT radio telescope in South Africa will carry out surveys for HI absorption between $z = 0$ and $z \sim 1.4$. The MeerKAT Absorption Line Survey (MALS; [Gupta et al. 2016](#)) will target fields containing several hundred radio-loud quasars, while the MeerKAT International GHz Tiered Extragalactic Exploration Survey (MIGHTEE; [Jarvis et al. 2016b](#)) will carry out deep observations of four fields covering roughly 20 sq deg.

At low frequencies, instruments, for example, the Low-Frequency Array (LOFAR; [van Haarlem et al. 2013](#)) in Europe, and the Murchison Wide field Array (MWA; [Tingay et al. 2013](#)) in Australia utilise a large number of modest dipole antennas organised inside stations without moving parts; the signals from these stations are digitised, transported to a focal processor and combined to imitate conventional dish antennas. These telescopes process the signal on adequately short time scales to address the ionospheric changes, seriously influencing radio observations below two or three hundred MHz. At higher frequencies (from several hundred MHz to a couple of GHz), two main examples are being built, Australian Square Kilometre Array Pathfinder (ASKAP; [Johnston et al. 2008](#), [Norris et al. 2011](#)) in Australia and Meer Karoo Array Telescope (MeerKAT; [Jonas & MeerKAT Team 2016](#), [Camilo et al. 2018](#)) in South Africa respectively. Moreover, a few significant radio facilities

have been upgraded to improve their performance. Such facilities includes the Jansky Very Large Array (JVLA; [Perley et al. 2011](#)) in New Mexico, the Giant Meterwave Radio Telescope (GMRT; [Gupta et al. 2017](#)) in India and the Westerbork Synthesis Radio Telescope (WSRT; [Oosterloo et al. 2009](#)) in the Netherlands. These telescopes will perform multi-tiered HI surveys, which will increase HI sample size by several orders of magnitude.

In this Chapter we present the first observations with MeerKAT for HI absorption towards a sample of radio luminous ($L_{1.4\text{GHz}} > 10^{26} \text{ W Hz}^{-1}$) AGN covering both low and high excitation radio galaxies at cosmological redshifts. The aim of this study is to establish the feasibility of carrying out such a survey with MeerKAT and to study a representative sample of radio AGN beyond the nearby Universe. The structure of this Chapter is as follows, Section 4.2 discusses about the MeerKAT radio telescope, sampling of data is given in Section 4.3, data analysis is given in Section 4.4, results are presented in Section 4.5. Finally, conclusion is given in Section 4.6

4.2 MeerKAT Radio Telescope

The MeerKAT radio telescope is a precursor for the Square Kilometre Array (SKA) mid-frequency telescope. The term MeerKAT simply stands for more of Karoo Array Telescope (but is also a word play on the name of an indigenous animal). It is located in the Karoo region of the Northern Cape Province in South Africa, at approximate coordinates $21^{\circ}26'$ East, $30^{\circ}42'$ South. MeerKAT is and will remain the largest and most sensitive radio telescope in the Southern Hemisphere until it will be surpassed by the SKA. Its antennas, receiver and digitiser will form part of SKA1-MID at the end of the construction phase of the larger array. This implies that the SKA1-mid array core will be centred on the MeerKAT array core, and the MeerKAT antennas will contribute a significant fraction of the SKA1-mid aperture within the core ([Booth et al. 2009](#)). The MeerKAT telescope consists of 64 antennas of interlinked receptors, with the main reflector made up of 13.5 m effective in diameter equipped with cryogenic cooler receivers and a 3.8 m diameter sub-reflector, each with an offset-Gregorian lay out. This design allows for excellent optical efficiency, sensitivity, image quality and removal of any undesired Radio Frequency Interference (RFI) from radio signal transmissions and orbiting satellites. Furthermore, in the primary and secondary focal points, the design also makes it possible to mount several receiver systems offering a range of additional operational benefits. The total surface precision of the two reflectors is exceptionally high with a deviation from the most ideal shape not exceeding 0.6 mm RMS. Each of the 16 antennas has four

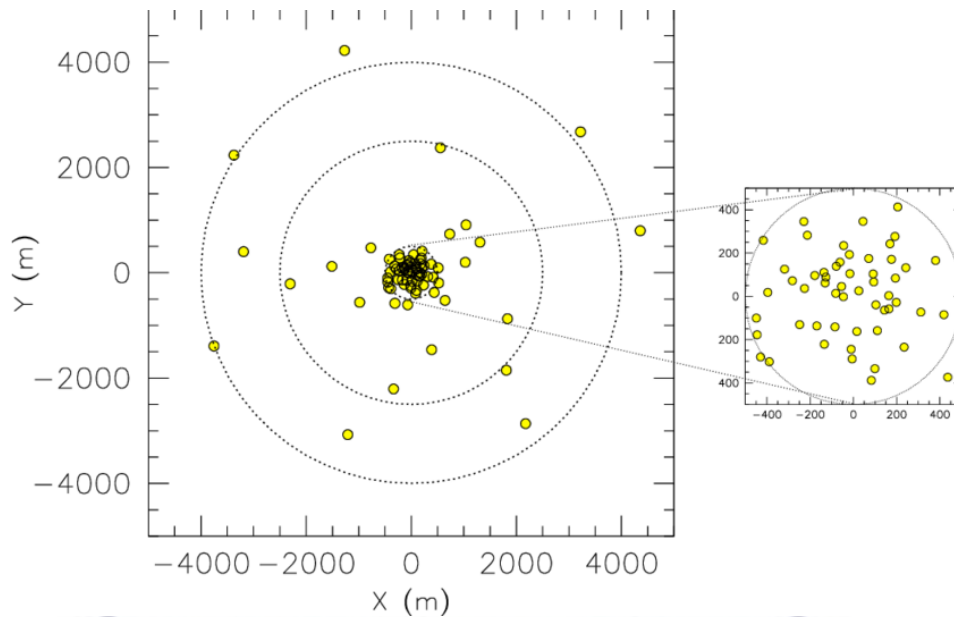


Figure 4.1: Overview of the 64 MeerKAT dishes distributed in two components. The inner component consists of 48 antennas, using a two-dimensional Gaussian uv -distribution with a dispersion of 300 m and a maximum baseline of 1 km. There are 16 antennas in the outer component, which is also distributed as a two-dimensional fashion with Gaussian uv -distribution with a dispersion of 2.5 km and a maximum baseline of 8 km. The minimum baseline is 20 m. The two circles have a diameter of 1.5 and 8 km. A more detailed view of the inner component is shown in the inset on the right (Booth et al. 2009)

receiver positions, and the S-band receiver given by the Max Planck Institute for Radio Astronomy (MPIfRA) will occupy one of three empty slots. The design of the array has 75% of the antennas positioned within a diameter of 1 km, and the remainder are spread over a radius of 4 km, see Figure 4.1. The MeerKAT receptors are determined by the scientific goals of the telescope. The MeerKAT telescope was inaugurated on 13 July 2018.

Observation modes that are currently supported by MeerKAT are deep continuum, polarisation and spectral line imaging, pulsar timing and transient searches. A variety of standard data products are offered, such as an imaging pipeline, and numerous 'data spigots' are also available for instrumentation support (Booth et al. 2009, Jonas & MeerKAT Team 2016).

The primary purpose of the Correlator/Beam-former (CBF) is to process the antenna signals, see Section 4.2. The signal passes to the science processor computer cluster and disc storage modules. Inside a shielding chamber commonly called the Faraday cage, the vast computing and digital signal storage facility housed at the

Karoo Array Processor Building (KAPB) is held to protect sensitive radio signals from devices interacting with the sensitive radio receiver. A Faraday cage or Faraday shield is an enclosure used to block electromagnetic fields. The receiver outputs are immediately digitised on the antenna and the digital data streams are transmitted through optical fibres to the KAPB. The KAPB is partially buried below ground level to provide additional Electromagnetic Interference (EMI) protection against RFI emission, and to provide temperature stability. The KAPB also has a power conditioning plant for the entire site (Jonas & MeerKAT Team 2016).

The three major MeerKAT receptor components are:

1. the positioner of the antenna, which is a steerable dish on a pedestal,
2. a selection of radio receivers, and
3. associated digitisers.

MeerKAT *L* Band Receptors

The primary goal of the receiver is to capture electromagnetic radiation and convert it to a voltage signal that is then amplified by a cryogenic receiver with some addition of a little noise to the signal. The first two receivers are the *L* band (900 – 1 670 MHz), with a sensitivity of approximately 220 m²/K required (> 300 m²/K achievable). The MeerKAT *L* band receiver consists of the complete antenna structure, with the primary reflector, sub-reflector, the feed horns, cryogenically cooled receiver, digitisers mounted on the feed indexer, and drive system, all mounted on a pedestal (Jonas & MeerKAT Team 2016). MeerKAT has a pointing accuracy of 5'' (optimal condition, 20 min); 25'' (normal condition, 24 hours). The physical temperature of the crossed-dipole Ortho-mode Transducer (OMT) is ~ 90 K for the *L* band receivers. For this Chapter we present a sample of nine radio sources observed utilising *L* band frequency.

Four digitisers are installed on the receiver indexer, next to each of the corresponding receivers. The four digitisers are designed to convert the radio frequency (RF) voltage signal from the receiver to electronic circuits. For example, the RF signal from the *L* band receiver is transferred through coaxial cables to the shielded digitiser package which is ~ 1 m away. The digitiser samples the signal directly in the Nyquist zone without converting it to a heterodyne receiver. This sampling is done by using an electronic component known as Analog to Digital Converter (ADC). After RF conditioning and conversion by ADC, a 10-bit voltage is generated by a single horizontal and vertical polarisation encapsulated in 4 × 10 Gbps transmission channels

through the use of underground optical fibres cables to the correlator situated inside the KAPB at the Losberg site.

How MeerKAT Operates

The receptors are connected by underground fibre cables for a distance of 170 km to the KAPB, with a maximum length of 12 km between the KAPB and a single antenna. For thermal stability, the fibre cables travel within conduits hidden 1 m underneath the ground. The signals perform different phases of digital processing at the KAPB, such as correlation, and incorporates all the signals from all the receptors to make an image of the region of the sky at which the antennas point, and beam-forming, continuously adding the signals from all the receptors to form a number of narrow, high-sensitivity beams used for pulsar research, see Section 4.2. Science data products are therefore archived at the KAPB with a part of the science archive data transferred through a fibre connection and stored in Cape Town.

The Time and Frequency Reference (TFR) subsystem provides a reference clock and one pulse per second at the array processor and is situated in the KAPB. TFR signals are distributed through buried optical fibres to every receptor and are synchronised to the same clock (Jonas & MeerKAT Team 2016). The primary goal of synchronising is to properly align the signals from all receptors. The two hydrogen maser clocks and the time transfer GPS receivers make it possible to track time stamping within 5 ns of the UTC. The interim TFR system offers precise time stamps within 1μ of the UTC with GPS-disciplined rubidium clocks.

Correlator/Beam-former

The MeerKAT CBF is implemented as an FX/B-style in the central real-time signal processor of the KAPB. In order to correct for geometric and instrumental delays, the antenna voltage streams are coarsely aligned, separated into frequency channels, and then phase-aligned by frequency channels before beam-forming (B) and/or cross-correlation (X). This is achieved in the processing nodes of the 'F-engine', where a Polyphase Filter-bank (PFB) is used to maximise the correct channelisation with sufficient channel-to-channel separation (Jonas & MeerKAT Team 2016).

The CBF subsystem is focused on the principle of CASPER, which uses digital data transfer and re-ordering between processing nodes utilising commodity network devices (for MeerKAT array, 40 Gbps Mellanox SX1710 36-port Ethernet switches arranged in a two-layer CLOS network generating 384 ports). The processing nodes is a combination of the CPUs and GPUs. The switch allows multicast data with non-blocking capabilities to make parallel processing possible. The full MeerKAT array

processing nodes compose of the so-called SKARAB boards equipped with Virtex 7 VX690T field-programmable Gate Arrays (FPGAs). A ROACH2 board equipped with Virtex 6 SX475T FPGAs is used by the interim CBF and can accommodate a total of 32 inputs with two polarisations in each 16-antenna (Jonas & MeerKAT Team 2016).

Science with MeerKAT

MeerKAT has a variety of scientific projects with diverse capabilities. Its key and the preliminary science case in the low frequency bands (580 MHz - 2.5 GHz) includes (Booth et al. 2009):

1. extremely sensitive study of HI emission,
2. study of extragalactic HI science and the Universe's evolution,
3. deep HI surveys at high-redshift out to $z \sim 1.4$,
4. studies of low column density in the nearby Universe,
5. a sub-kpc observations of the HI distribution in 1 000 nearby galaxies,
6. analysis of HI absorption line measurements,
7. the amplification of HI by stacking and gravitational lensing to $z = 1.4$, and
8. highly sensitive continuum surveys at μJy levels.

4.3 Sample Selection

We selected our sample of radio AGN from the Large Area Radio Galaxy Evolution Spectroscopic Survey (LARGESS; Ching et al. 2017). This catalogue provides optical identifications for 19 179 radio sources from the Faint Images of Radio Source Twenty-cm (FIRST; Becker et al. 1995) survey that are brighter than an extinction-corrected I band magnitude of 20.5 in the SDSS. Of these optical identifications, 10 856 have reliable spectroscopic redshifts of which 85% are classified as radio AGN. The redshift range spanned by the radio AGN sample ($z \gtrsim 0.8$; $\langle z \rangle = 0.44$) is well matched to the 21 cm line redshifts available to the MeerKAT L band receiver ($z_{\text{HI}} = 0 - 0.58$).

To achieve our aim of detecting HI 21 cm absorption with MeerKAT, we selected 15 radio AGN from the LARGESS catalogue with the following properties:

1. a total flux density in FIRST greater than 500 mJy,

2. a reliable spectroscopic redshift between $z = 0.1$ and 0.58 ,
3. a redshift that avoided the known RFI-afflicted regions of the MeerKAT L band ($900 - 915$, $925 - 960$, $1217 - 1237$, $1242 - 1249$, $1191 - 1217$, and $1260 - 1300$ MHz).

We then selected 11 sources that have an unresolved FIRST flux density greater than 100 mJy at the position of the host galaxy. At the median redshift $\langle z \rangle = 0.38$ of our sample, the FIRST resolution of 5 arcsec corresponds to a physical scale of 26 kpc, which is well matched to the typical scale of HI discs in galaxies. Assuming that all of the peak FIRST flux density is subtended by foreground HI, we aimed to achieve an rms sensitivity per 26 kHz channel of better than 2% continuum absorption within 2 hrs of observing time. Finally, we selected 9 targets that were visible at night with MeerKAT during 2018 March and April. This is the sample we used for testing MeerKAT as a HI absorption detection machine. We summarise the key properties of these radio galaxies in Table 4.1. We note that our sample is split roughly equally between sources that have been spectroscopically identified as either HERG or LERG, and all have radio luminosities greater than $L_{1.4\text{GHz}} = 10^{26} \text{ W Hz}^{-1}$.

4.4 Observations and Data

Observations of our sample were undertaken in two sessions on 2018 April 24/25 and 30, using 16-antenna sub-arrays of MeerKAT during the shared-risk early science programme. The integration times for each source ranged between 1 and 5.6 hrs, depending on visibility. A standard radio source, (3C 286 $S_{1.4\text{GHz}} = 14.9 \text{ Jy}$; Perley & Butler 2013), was observed in 5 min scans every 1 hr for reference calibration. We used the L band receiver, covering frequencies in the range 900 to 1670 MHz. The ROACH2 correlator was used in wideband-fine mode to generate 32 768 channels at 26 kHz resolution (equivalent to a rest-frame velocity resolution of $\Delta\nu_{\text{chan}} \sim 8 \text{ km s}^{-1}$ at $z_{\text{HI}} \sim 0.4$). Due to observing constraints, two different 16-antenna sub-arrays were used for each session. On 2018 April 24/25 the majority (14 out of 16) of the antennas were in a compact configuration (baselines less than 1 km), resulting in an effective resolution of only 1 arcmin, while the more extended configuration available on April 30 provided a spatial resolution of approximately 10 arcsec.

Initial flagging and reference calibration of the bandpass, antenna gains and flux density scale using 3C 286 was carried out using standard tasks from the Common Astronomy Software Application (CASA; McMullin et al. 2007). To reduce the data further we extracted the flagged and calibrated visibilities for each source at the expected position of the redshifted 21 cm line, retaining 5 MHz bandwidth either side.

In the AGN rest frame this retained band-width corresponds to shifted H I velocities of $\Delta\nu = \pm 1480 \text{ km s}^{-1}$, which is sufficient to identify absorption associated with the ISM of the host galaxy.

We imaged the reduced visibility data for each source using the MIRIAD package (Sault et al. 1995). Using the CLEAN* deconvolution algorithm we constructed an initial model of the continuum flux density in the field, which we then used for phase-only self calibration of the antenna gains at 5 min temporal resolution. The self-calibrated visibilities were then re-imaged and CLEAN was again used to construct a continuum model. After a second iteration of phase-only self-calibration, we subtracted the final continuum model from the visibilities using the UVMODEL† task. Further subtraction of any residual un-modelled continuum flux density was carried out using UVLIN‡. The final calibrated and continuum-subtracted visibilities were then imaged at full spectral resolution to produce data cubes ready for spectroscopic analysis.

The images and MeerKAT 21 cm absorption spectra for each source are shown in Figures 4.2 and 4.3. We constructed these spectra by taking the following weighted average over the source:

$$\left\langle \frac{\Delta S_\nu}{S_c} \right\rangle = \left(\sum_i \sum_j \frac{\Delta S_{i,j}}{S_c(i,j)} \right) / \left(\sum_i \sum_j w_{i,j} \right) \quad (4.1)$$

where $\Delta S_{i,j}$ is the continuum-subtracted flux density at pixel i, j , and $S_c(i, j)$ is the corresponding flux density measured from the continuum image. We set the weights ($w_{i,j}$) as a positive power of the continuum flux density, thereby optimizing the expected SNR for continuum absorption. In the limit that this power becomes large, the weighted spectrum tends to that seen against the peak flux density in the continuum image.

4.5 Results and Discussion

Our results are summarised in Tables 4.1 and 4.2. Two spectral features are detected towards J145859.35+041613.8, however they arise from known radio frequency interference (1024 MHz; positive) and a correlator-related artefact (1018.5 MHz; negative). An absorption feature is detected towards J114108.31+011418.1 and the absence of a similar feature in the spectrum of J144839.94+001816.7 at the same

*<http://casa.nrao.edu>

†<http://www.atnf.csiro.au/computing/software/miriad>

‡<http://www.atnf.csiro.au/computing/software/miriad/doc/uvlin>

Table 4.1: Summary of our target sample.

SDSS Name	z_{HI}	$\log_{10} L_{1.4}$ [$W H z^{-1}$]	S_{int} [mJy]	S_{peak} [mJy]	ν_{HI} [MHz]	Class
J094319.23-000424.8	0.4642	26.08	1150	830	970	HERG
J105425.96+031445.9	0.3812	26.55	613	105	1028	LERG
J112437.40+045618.9	0.2828	26.44	918	101	1107	HERG
J113729.58+011613.9	0.4300	26.97	1074	435	993	HERG
J114108.31+011418.1	0.4422	27.42	2847	1239	985	LERG
J115025.25+011601.6	0.54067	26.92	509	301	922	HERG
J121031.30-013649.1	0.28901	26.31	650	111	1102	LERG
J144839.94+001816.7	0.43783	27.19	1722	449	988	LERG
J145859.35+041613.8	0.3915	26.80	938	151	1021	-

Table 4.2: Summary of our target sample (continued).

SDSS Name	t_{obs} [h:mm]	σ_{chan} [τ]	$\Delta\nu_{chan}$ [$km s^{-1}$]	τ_{peak}	$\Delta\nu_{line}$ [$km s^{-1}$]
J094319.23-000424.8	2:00	0.0021	8.1	-	-
J105425.96+031445.9	0:59	0.0053	7.6	-	-
J112437.40+045618.9	1:18	0.0032	7.1	-	-
J113729.58+011613.9	2:39	0.0019	7.9	-	-
J114108.31+011418.1	2:41	0.0009	7.9	0.0060(5)	68(6)
J115025.25+011601.6	1:59	0.0048	8.5	-	-
J121031.30-013649.1	2:01	0.0041	7.1	-	-
J144839.94+001816.7	3:58	0.0018	7.9	-	-
J145859.35+041613.8	5:39	0.0017	7.7	-	-

frequency and depth suggests that this is likely to be HI absorption.

Our observations have a 5σ column density sensitivity in the range $1.6 - 9.6 \times 10^{19} \text{ cm}^{-2}$, assuming a spin temperature of 100 K and an effective line width of 50 km s^{-1} . This is sufficient to detect the HI column densities typically found by absorption in radio galaxies and comparable to previous surveys. We obtain a detection rate of 11% (1/9 detections), which is statistically consistent with that expected from previous surveys of radio galaxies (see e.g., [Morganti & Oosterloo 2018](#), and references therein). In the most statistically significant survey of 248 nearby radio galaxies ($0.02 < z < 0.25$), [Maccagni et al. \(2017\)](#) found that the rate of HI absorption is three times higher in host galaxies that are rich in dust. Our sample has a distribution of observer-frame Wide-Field Infrared Survey Explorer (WISE; [Wright et al. 2010](#)) colours ($[3.4 - 4.6 \mu\text{m}]$ mean = 0.47, standard deviation = 0.35, $[4.6 - 12 \mu\text{m}]$ mean = 2.52, standard deviation = 0.61) that is consistent with dust-

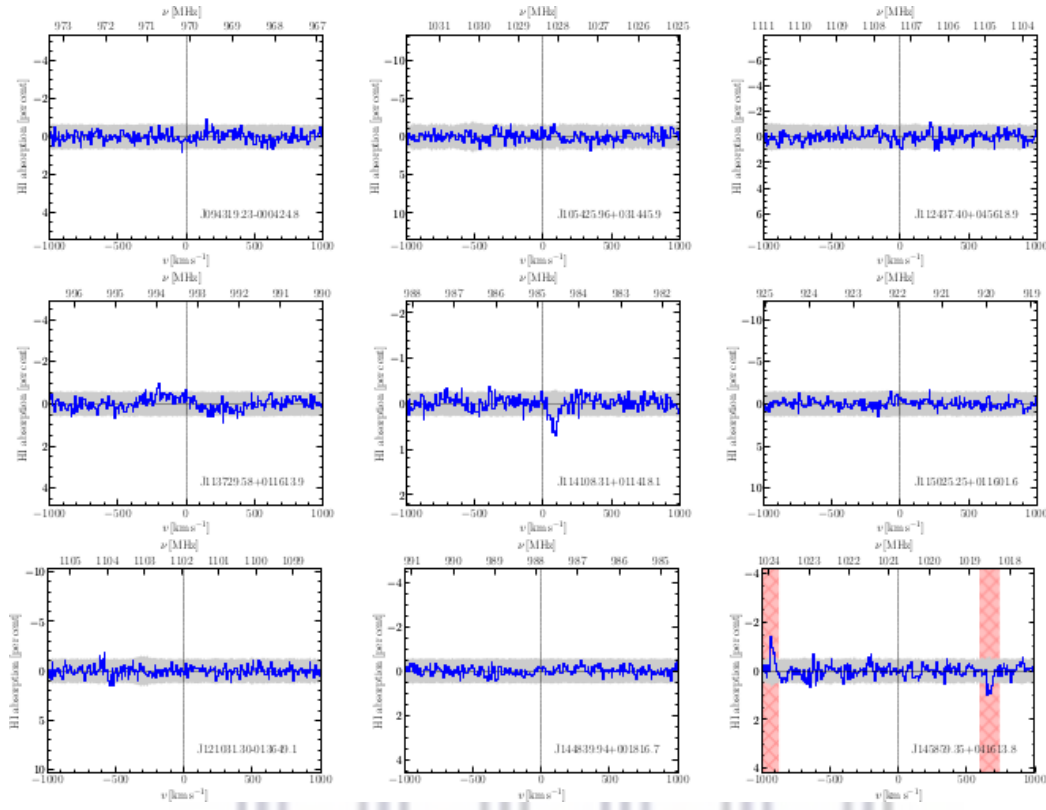


Figure 4.2: HI absorption spectra from MeerKAT observations of our sample. The velocity axis is given in the rest frame defined by the AGN redshift. The grey shaded region denotes three times the rms noise. The red shaded regions indicated the positions of known spectral artefacts due to RFI and correlator issues.

rich hosts, but in many cases the dust is not AGN-heated. We obtained a relatively low detection rate compared with Maccagni et al. (2017) probably due to statistical fluctuation. We also note that our sources are not dominated by compact radio emission close to an obscured AGN that would ensure a higher detection rate.

HI Absorption in 3C 262

We use the spectral line detection and parametrisation method discussed by Allison et al. (2014) to model the absorption towards J114108.31+011418.1 (also known as 3C 262). We find that a single Gaussian component best fits the data, with peak optical depth $\tau_{\text{peak}} = 0.0060(5)$, effective line width* $\Delta\nu_{\text{line}} = 68(6) \text{ km s}^{-1}$, and radial motion $79(21) \text{ km s}^{-1}$ towards the radio source. Note that this is the average HI 21 cm optical depth across the source. Assuming an HI spin temperature in the

*We define the effective width as the integrated line area divided by its peak (Dickey 1982, Allison et al. 2013)

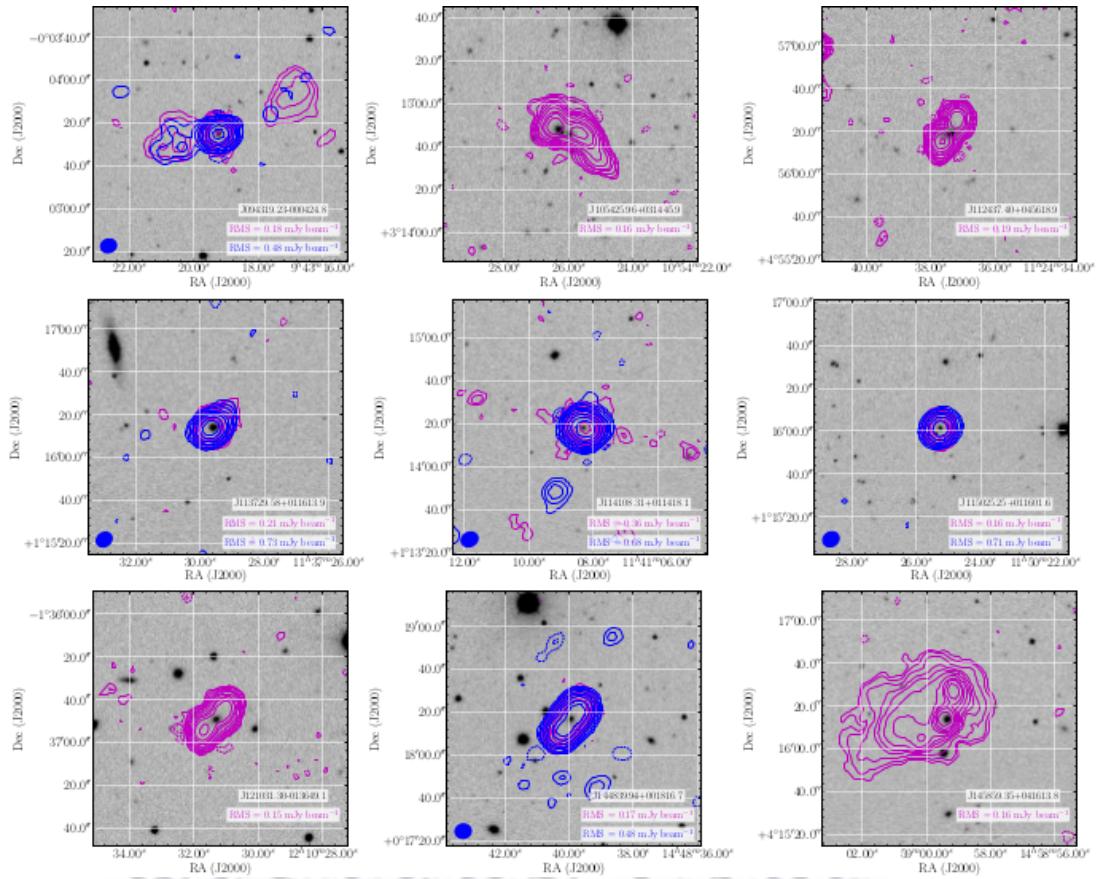


Figure 4.3: Images of our radio AGN sample: SDSS *I* band (greyscale), FIRST radio (magenta contours), and MeerKAT radio (blue contours). Contours are given in units of -5, 5, 10, 20, 50, 100, 200, 500, 1000, 2000, 5000, and 10000 times the image rms noise. Note that MeerKAT contours are not shown for observations where the resolution was less than 1 arcmin.

range between 100 and 1000 K we estimate an average HI column density across the source of $N_{\text{HI}} = 7.4(6) \times 10^{19-20} \text{ cm}^{-2}$. This is lower by a factor of ~ 10 than typically found in HI absorption surveys of radio galaxies (see the review by [Morganti & Oosterloo 2018](#)). Either a smaller fraction of the source is subtended (i.e., $\sim 10\%$) or a smaller column density of foreground gas is detected than is typical in radio galaxies).

The radio source is unresolved in FIRST, but higher-resolution imaging by [Best et al. \(1999\)](#) using archival VLA data shows two radio lobes separated by 5 arcsec ($\sim 28.5 \text{ kpc}$ at $z = 0.44224$), with no evidence of compact core emission (see also [Preston et al. 1983](#)). The absorbing gas is therefore located at large galactocentric radius ($\gtrsim 28 \text{ kpc}$), possibly in an extended disc of HI. The line width and velocity offset are consistent with an inclined disc of neutral gas obscuring one lobe of the radio source. Although 3C 262 is formally classified by [Ching et al. \(2017\)](#) as a LERG, [OIII] $\lambda 5007$ emission is prominent in the optical spectrum at the level of $\text{EW [OIII]} \sim 4.02 \text{ \AA}$. Despite the lack of efficient accretion in these low luminosity active galaxies, they can still contain significant amounts of cold neutral gas (e.g., [Ruffa et al. 2019](#)).

Evidence of star forming cold gas in the ISM is seen in the Mid-Infrared (MIR) colour $[4.6 - 12 \mu\text{m}] = 2.5$ ([Wright et al. 2010](#)) and strong [OII] $\lambda 3727$ emission ($\text{EW [OII]} = 207 \pm 55 \text{ \AA}$; [Best et al. 1999](#)). From the [OII] luminosity ($L [\text{OII}] = 1.60 \pm 0.18 \times 10^{42} \text{ erg s}^{-1}$) we estimate a SFR of $\sim 10.5 M_{\odot} \text{ yr}^{-1}$ ([Kewley et al. 2004](#)), which over the extent of the putative HI disc gives an average surface density of $\sum_{\text{SFR}} \sim 4.1 \times 10^{-3} M_{\odot} \text{ yr}^{-1} \text{ kpc}^{-2}$. From the Kennicutt-Schmidt law ([Kennicutt 1998](#)) this equates to an average gas surface density of $\sum_{\text{gas}} \sim 7.4 M_{\odot} \text{ pc}^{-2}$. Assuming approximate parity of mass in atomic and molecular gas, and a 37% correction for helium and metals, we estimate a hydrogen column density of $N_{\text{HI}} \sim 3.4 \times 10^{20} \text{ cm}^{-2}$. The level of star-formation evident in the host galaxy is therefore consistent with the absorption line detected in the MeerKAT spectrum.

The ‘Detection’ is an Artefact

Unfortunately, further tests reveal that the apparent detection arises from an artefact in the ROACH2 correlator. The reason this has been verified is because 3C 262 is the brightest source of our sample with sufficient SNR to reveal the artefact at the level of 5%. An earlier test using the next brightest source had not revealed anything. This latest test was to look at the spectra of the calibrator sources with similar SNR, and look at the same place in the spectrum. Unfortunately (as can be seen in the uncalibrated spectra of a bright phase calibrator) we can see a feature at 984.5 MHz,

the same as the reported “detection” in 3C 262. The other “absorption like” features seen in this spectrum highlight the problems with the ROACH2 correlator similar to the early commissioning science work with MeerKAT 16*. We concluded that we will have to wait until the new correlator has 32k channel resolution before we can start looking for associated absorption in MIGHTEE data.

4.6 Conclusions

We have carried out the first dedicated search for associated HI 21 cm absorption using a 16-antenna sub-array of the new MeerKAT radio telescope in South Africa, in a sample of nine powerful radio galaxies of $L_{1.4\text{GHz}} > 10^{26} \text{ W Hz}^{-1}$ at cosmological distances. We checked whether our radio galaxies sample falls in the region affected by the RFI or not. For all this nine sources we found that they do not fall in the region affected by RFI. We again fit the one-dimensional spectrum. We only detected a tentative HI absorption toward 3C 262. However, the detection rate is statistically consistent with previous surveys of radio galaxies in the nearby Universe.

The radio source has two lobes separated by approximately 28.5 kpc, with no evidence of any emission from a compact core, implying that the absorption is arising in an extended gaseous structure such as a disc. The line is redshifted with respect to the AGN, suggesting that the disc is inclined and obscuring only one of the lobes. There appears to be significant ongoing star-formation at the level $\sim 10.5 M_{\odot} \text{ yr}^{-1}$, which using the Kennicutt-Schmidt law is consistent with the detected absorption line. We note that successful detection of associated HI absorption against an extended radio source is promising for studying the cold gas in radio galaxies at cosmological distances using the MeerKAT telescope.

*Allison 2019, private communication

Chapter 5

Conclusions and Future Work

This thesis was focused on the following: First, the construction of a catalogue of powerful radio sources for follow-up with the next generation of telescopes such as MeerKAT. Second, attempting to detect neutral Hydrogen in a sample of nine radio AGN using 16 antennas of the MeerKAT array.

In Chapter 1, I gave an overview of HzRGs including their history of the field, their nature, their properties of HzRGs, how to search for them, their relativistic plasma found in these galaxies, ionised gas, neutral gas, the star-formation rate, the molecular torus, dust and massive stellar hosts and a discussion on the AGN. This Chapter therefore provides the necessary context and background for the rest of the thesis.

In Chapter 2, I gave an overview of the three surveys we used to construct our sample of Southern radio galaxies. We found that the largest overlapping region of the sky among the three surveys we used was defined by $60^\circ < \alpha' < 90^\circ$ and $-60^\circ < \delta < -45^\circ$. The field overlapping for the three telescopes was 148 sq deg. We also gave details of how we have sampled our data.

In Chapter 3, we constructed a catalogue for the Southern Hemisphere. We have described the process of obtaining reliable radio sources from SUMSS and NIR counterparts from VHS using the LR technique. We searched for counterparts within r_{\max} of the radio position with flux limit down to the 10σ level, which corresponds to a flux density below 12 mJy. By setting the reliability above 0.8, we obtained 1 195 radio sources with NIR counterparts, with 81 of these sources being falsely identified. We then cross-matched 1 195 radio sources with the DES catalogue to obtain the photometric redshifts and form a sample of 249 radio galaxies over a region of 148 sq deg.

We used this sample to investigate host galaxy properties. We found that our sample broadly follows the galaxy $K-z$ relation based on a range of complete samples

of radio sources from 3CRR, 6CE, 6C* and 7C. We then used the FAST code using two different stellar population syntheses, with both fixed metallicity and allowing the metallicity to vary, and with a total dust extinction in the range $0.0 < A_V < 0.3$. We investigated the effect of different choices for SFH and IMF from our sample, and find that the choice of IMF and SFH does not affect our results. We also do not find any link between radio luminosity and host galaxy mass. We used SED fitting to the optical and NIR photometry. We found that our sample broadly falls into two populations, low-mass blue and high-mass red galaxies. We also found a broad range of stellar masses of $10^{11} - 10^{12} M_{\odot}$. We found that the radio power of our sample of low-redshift radio galaxies far exceeded that expected from the star formation alone. We interpret this to mean that these sources are more likely to be small number of low-redshift interlopers that we expect from the estimated false positives in our LR analysis.

In Chapter 4, we reported the first search for associated HI 21 cm line absorption with the new MeerKAT radio telescope. We used the 16 antenna sub-array of MeerKAT during the shared-risk early science programme. It is worth mentioning that the sample used for this work is not from the catalogue we constructed from Chapter 3. We found a tentative source detection rate of 11% (1/9 detections) which is statistically consistent with that expected from previous surveys of radio galaxies. We found a relatively low detection rate compared with [Maccagni et al. \(2017\)](#), probably due to statistical fluctuations and that our sources are not dominated by compact radio emission close to an obscured AGN that would ensure a higher detection rate. We also found that a single Gaussian component best fits our sample, with a peak optical depth $\tau_{\text{peak}} = 0.0060(5)$, effective line width $\Delta\nu_{\text{line}} = 68(6) \text{ km s}^{-1}$, and radial motion $79(21) \text{ km s}^{-1}$ towards the tentative radio source. We also found significant ongoing SF at the level $\sim 10.5 M_{\odot} \text{ yr}^{-1}$, which using the KS law is consistent with the detected absorption lines. However, the additional source test conducted by the old ROACH2 correlator eliminates the presence of absorption originally detected in the MeerKAT spectrum. This has forced the project to wait until the new correlator has 32k channel resolution before we can start looking for the associated absorption in MIGHTEE data.

5.1 Future Work

Several of the latest radio telescopes and equipment that are now being constructed will provide new insights into the existence of powerful radio galaxies and their environments. A combination of wider fields of view and improved simultaneous band-

width will be offered by interferometers such as the JVLA, ASKAP, MeerKAT and the Aperture Tile In Focus (APERTIF) on Westerbork, while retaining good collection area and angular resolution. In the Southern Hemisphere, it is also anticipated that the SKA will uncover larger powerful radio galaxy populations, revolutionising our knowledge of the evolution of galaxies. We thus recommend continued observations by future telescopes to uncover more galaxies and probe remaining mysteries pertaining to these sources.

The catalogue presented in Chapter 3 will be used as a basis for studying the fuelling of and feedback in powerful radio galaxies using the new generation of radio telescopes. In particular, we plan to undertake a comprehensive study of HI absorption against these powerful sources with the MeerKAT radio telescope.

The central role of HI mass in galaxy formation is that it is the source of material from which stars and galaxies are generated, but most of what we know about the HI content of galaxies comes from the nearby Universe. The MeerKAT receiver also has an Ultra High Frequency (UHF) band receiver that covers the frequency range of 580–1015 MHz. The sensitivity of this frequency band is $\sim 220 \text{ m}^2/\text{K}$ and is expected to reach better than the L band receiver. However, the full SKA will revolutionise our understanding of the evolution of galaxies and dynamics across the redshift range (thus moving beyond the near Universe) even beyond what currently accessible to the largest optical telescopes. In the meantime, the use of the 64 telescopes of the full MeerKAT array will afford more sensitivity.



UNIVERSITY *of the*
WESTERN CAPE



UNIVERSITY *of the*
WESTERN CAPE

Appendix A

Tables of Radio Galaxy Properties

Table A.1: The new sample of 249 radio galaxies overlapping SUMSS+VHS+DES. The photometric redshifts given are from the DES SVA Gold data release. Looking at [Sánchez et al. \(2014\)](#) the typical 1σ photo-z accuracy of BPz is ~ 0.1

(ID)	RA	Dec	g	r	i	z
1	04:50:00.67	-46:18:12.9	24.190±0.159	22.426±0.040	21.307±0.026	20.242±0.017
2	05:10:03.35	-56:51:59.8	21.006±0.008	20.769±0.009	20.426±0.012	20.014±0.015
3	05:03:02.42	-55:17:54.9	25.479±0.488	22.897±0.063	21.752±0.041	20.810±0.035
4	04:21:14.97	-59:55:37.6	22.399±0.028	21.922±0.039	21.364±0.025	20.786±0.030
5	04:30:31.14	-46:02:48.6	21.900±0.025	20.118±0.006	19.430±0.006	19.065±0.008
6	04:39:53.16	-50:31:04.4	25.398±0.487	23.897±0.178	23.007±0.135	21.880±0.072
7	05:06:05.83	-51:28:35.2	24.312±0.262	22.320±0.048	21.192±0.039	20.342±0.029
8	05:02:02.65	-58:17:14.8	23.722±0.103	22.162±0.033	20.934±0.022	20.174±0.018
9	04:33:00.00	-55:33:39.5	23.583±0.107	21.975±0.030	20.967±0.042	20.123±0.024
10	04:31:08.78	-57:58:21.9	23.292±0.104	22.982±0.097	22.308±0.081	21.490±0.071
11	05:07:14.53	-57:40:15.7	23.246±0.069	22.032±0.029	21.386±0.035	20.657±0.030
12	04:47:14.55	-54:22:54.1	24.600±0.209	23.555±0.082	22.337±0.096	21.606±0.076
13	04:38:48.72	-52:03:53.8	23.454±0.089	21.810±0.027	20.960±0.032	20.433±0.031
14	05:22:14.89	-55:40:15.2	24.427±0.341	22.426±0.078	21.357±0.037	20.937±0.044
15	05:33:59.02	-56:33:45.0	24.286±0.422	22.238±0.084	21.247±0.043	20.479±0.063
16	04:23:17.83	-49:10:38.7	22.445±0.079	20.684±0.021	19.545±0.011	19.067±0.013
17	04:21:07.26	-46:43:59.7	23.587±0.134	21.910±0.040	20.717±0.018	20.128±0.020
18	04:31:39.18	-51:39:15.2	23.795±0.074	22.821±0.040	22.393±0.078	21.787±0.059
19	04:54:42.47	-49:07:21.8	20.926±0.012	19.507±0.004	19.002±0.004	18.692±0.007
20	04:19:43.21	-46:19:14.3	27.491±1.000	24.673±0.396	23.150±0.138	22.550±0.144
21	05:14:55.14	-52:23:33.3	18.677±0.008	18.285±0.006	18.000±0.009	17.849±0.012
22	04:20:39.09	-45:33:35.6	21.659±0.024	20.612±0.016	19.822±0.013	19.434±0.021
23	05:02:18.39	-49:28:39.1	23.610±0.237	22.504±0.109	21.573±0.053	20.772±0.051
24	05:43:19.85	-57:57:56.1	24.208±0.223	23.368±0.135	22.603±0.145	21.656±0.116

Continued on next page

Table A.1 – *continued from previous page*

(ID)	RA	Dec	g	r	i	z
25	04:43:11.81	-49:45:23.1	25.168±0.439	23.577±0.140	22.496±0.063	21.647±0.077
26	05:36:25.22	-57:04:12.6	22.634±0.044	21.711±0.024	20.796±0.018	20.296±0.022
27	05:15:07.46	-57:47:43.0	23.287±0.062	22.515±0.039	21.841±0.047	21.001±0.038
28	04:54:42.12	-47:27:29.4	23.195±0.065	21.425±0.016	20.248±0.008	19.753±0.010
29	04:29:42.16	-46:33:35.9	23.989±0.155	22.003±0.034	20.992±0.027	20.458±0.025
30	04:39:20.94	-46:20:57.5	23.441±0.088	22.034±0.034	21.041±0.025	20.458±0.027
31	04:44:05.69	-48:56:26.6	23.901±0.133	21.977±0.028	20.696±0.014	20.168±0.019
32	04:43:40.03	-46:34:31.3	23.179±0.067	21.854±0.028	21.260±0.027	20.942±0.037
33	04:25:33.27	-45:53:24.8	24.442±0.209	22.810±0.069	21.745±0.051	20.796±0.038
34	04:45:50.18	-54:23:32.1	23.215±0.084	21.305±0.015	20.146±0.018	19.660±0.017
35	05:36:14.85	-57:19:29.6	25.023±0.664	22.399±0.076	21.042±0.032	20.157±0.032
36	04:21:26.04	-46:24:16.2	23.572±0.100	22.695±0.075	22.053±0.066	21.332±0.060
37	04:32:10.93	-45:42:53.8	23.867±0.146	22.422±0.052	21.561±0.048	20.987±0.049
38	04:57:29.91	-53:31:50.4	24.908±0.392	22.690±0.053	21.606±0.055	20.745±0.044
39	04:57:48.21	-57:08:57.3	25.884±0.869	23.272±0.087	21.878±0.051	21.020±0.040
40	04:34:02.58	-55:24:58.7	22.918±0.075	21.128±0.017	20.203±0.018	19.820±0.019
41	04:15:54.28	-47:41:38.7	24.190±0.148	23.543±0.133	23.153±0.126	22.435±0.123
42	04:10:36.83	-51:28:32.6	22.223±0.099	20.443±0.018	19.370±0.012	18.916±0.016
43	05:02:01.93	-50:25:26.5	25.581±0.482	23.456±0.084	22.119±0.064	21.007±0.039
44	04:32:36.27	-48:48:18.5	24.096±0.259	21.625±0.033	20.365±0.018	19.664±0.017
45	04:24:31.06	-59:58:40.9	24.613±0.165	22.600±0.050	21.467±0.022	20.770±0.023
46	04:41:56.25	-49:01:25.8	24.789±0.264	23.126±0.079	22.152±0.056	21.157±0.040
47	05:17:18.82	-56:50:44.2	23.068±0.064	21.992±0.032	21.070±0.027	20.570±0.029
48	04:15:23.15	-56:33:17.3		23.865±0.252	22.661±0.136	21.750±0.107
49	05:20:49.81	-56:37:24.1	20.975±0.012	19.784±0.005	19.384±0.005	18.993±0.007
50	04:21:16.89	-49:31:03.0	24.794±0.379	22.575±0.050	21.375±0.030	20.652±0.034
51	04:31:51.19	-46:15:51.0	24.364±0.205	22.384±0.045	21.290±0.033	20.369±0.024
52	04:18:15.77	-49:33:01.8	21.297±0.021	19.750±0.008	19.134±0.006	18.787±0.012
53	04:16:58.69	-50:55:24.7	23.864±0.131	22.386±0.045	21.236±0.020	20.760±0.026
54	04:44:13.18	-56:55:38.5	23.361±0.078	22.643±0.047	22.024±0.045	21.107±0.038
55	04:58:19.96	-53:02:08.3	24.250±0.261	22.711±0.059	21.835±0.051	20.754±0.040
56	04:52:41.05	-56:44:40.8	22.932±0.038	22.218±0.022	21.667±0.025	21.060±0.025
57	04:25:17.24	-47:54:13.5	22.806±0.043	21.403±0.015	20.452±0.013	20.041±0.013
58	04:29:32.04	-46:40:11.1	23.743±0.070	22.829±0.046	22.140±0.044	21.587±0.045
59	04:46:40.89	-54:43:10.8		24.420±0.193	23.054±0.209	21.862±0.085
60	05:22:25.63	-57:53:44.3	23.696±0.077	22.846±0.046	21.88±0.040	21.497±0.051
61	04:39:25.50	-47:37:56.8	25.060±0.287	22.349±0.032	21.269±0.024	20.625±0.020
62	04:33:57.08	-53:28:04.5	27.333±1.000	23.409±0.100	22.099±0.081	21.488±0.080
63	05:05:32.97	-58:14:53.1	23.607±0.084	21.726±0.02	20.462±0.013	19.795±0.012

Continued on next page

Table A.1 – *continued from previous page*

(ID)	RA	Dec	g	r	i	z
64	04:55:16.27	-46:03:54.7	22.834±0.038	21.366±0.012	20.803±0.018	20.441±0.024
65	04:28:34.66	-52:30:23.2	23.689±0.115	21.592±0.023	20.352±0.016	19.750±0.016
66	04:44:42.42	-46:44:06.5	23.324±0.064	21.563±0.017	20.503±0.011	20.249±0.017
67	05:21:25.13	-57:40:00.3	23.220±0.043	22.217±0.023	21.530±0.023	20.833±0.022
68	04:43:41.05	-48:54:58.0	21.557±0.017	21.157±0.014	20.445±0.013	20.218±0.019
69	05:06:57.49	-49:47:31.9	23.635±0.127	22.648±0.066	21.985±0.075	21.649±0.086
70	04:53:18.26	-46:05:09.3	20.929±0.011	19.568±0.004	19.146±0.005	18.794±0.008
71	04:28:34.13	-55:29:28.6	20.658±0.014	19.111±0.005	18.643±0.007	18.320±0.007
72	04:42:54.78	-52:56:34.3	23.752±0.072	23.169±0.056	22.512±0.057	21.951±0.076
73	04:40:15.13	-47:04:31.4	25.452±0.397	25.094±0.374	23.824±0.202	22.851±0.143
74	05:04:42.82	-51:43:55.4	24.948±0.182	24.077±0.109	23.094±0.086	22.274±0.078
75	04:18:51.86	-58:05:24.2	24.805±0.391	23.311±0.330	21.945±0.093	21.009±0.056
76	04:37:08.54	-50:23:37.0	22.914±0.034	22.619±0.035	21.989±0.042	21.671±0.052
77	05:06:30.40	-50:20:49.6	23.530±0.184	21.851±0.043	20.708±0.064	20.105±0.060
78	04:19:14.40	-55:06:00.7	24.327±0.321	23.784±0.227	22.253±0.105	22.019±0.131
79	04:37:17.36	-52:23:58.5	28.532±1.000	24.025±0.175	22.752±0.127	21.822±0.079
80	05:08:10.31	-54:55:47.4	22.856±0.090	21.186±0.025	20.004±0.011	19.456±0.012
81	05:27:41.84	-57:47:10.4	24.234±0.142	22.946±0.053	22.015±0.039	21.364±0.047
82	04:31:43.56	-48:53:07.6		23.268±0.108	22.103±0.071	21.348±0.058
83	04:42:41.00	-48:54:37.4	24.029±0.114	22.349±0.029	21.061±0.019	20.507±0.018
84	04:59:20.96	-45:28:45.0	24.000±0.133	23.304±0.087	22.612±0.102	21.984±0.119
85	04:18:48.14	-56:18:36.1	24.506±0.279	22.640±0.062	21.724±0.040	21.402±0.052
86	04:43:00.45	-54:53:33.5	22.333±0.035	21.255±0.012	20.604±0.024	20.330±0.027
87	04:30:39.80	-53:19:42.2	20.833±0.012	19.487±0.004	19.001±0.007	18.694±0.008
88	04:43:46.59	-50:51:01.1	26.385±0.735	24.415±0.159	24.506±0.420	22.627±0.107
89	04:23:53.34	-49:21:46.3	24.621±0.218	24.026±0.151	23.171±0.152	22.609±0.133
90	05:40:21.90	-59:58:51.5	24.094±0.201	22.233±0.035	21.020±0.026	20.242±0.026
91	05:07:16.58	-52:19:57.6	25.032±0.362	24.076±0.187	22.835±0.099	21.948±0.087
92	05:43:41.20	-58:13:16.4	24.053±0.191	22.497±0.057	21.379±0.043	20.616±0.035
93	04:51:01.65	-45:41:58.7	25.167±0.344	24.266±0.179	22.881±0.089	21.840±0.069
94	04:55:48.18	-49:59:23.1	24.311±0.382	22.485±0.059	21.420±0.028	20.902±0.036
95	05:07:15.52	-54:40:36.3	25.063±0.542	23.336±0.162	22.071±0.053	21.473±0.058
96	04:57:37.66	-46:28:19.5	23.683±0.082	22.866±0.051	22.180±0.044	21.299±0.042
97	05:18:13.81	-54:35:28.8		24.493±0.967	23.439±0.177	22.730±0.153
98	04:28:52.91	-45:27:52.7	25.610±0.724	23.093±0.104	21.693±0.054	21.243±0.065
99	04:56:26.68	-49:47:45.6	18.943±0.003	18.759±0.002	18.562±0.003	18.179±0.005
100	05:01:25.04	-47:11:49.6	21.267±0.008	21.092±0.009	20.827±0.011	20.747±0.021
101	04:25:36.32	-57:45:18.6	27.139±1.000	23.746±0.149	22.238±0.055	21.447±0.043
102	04:31:43.24	-52:11:19.0	22.632±0.043	21.146±0.015	20.074±0.014	19.675±0.016

Continued on next page

Table A.1 – *continued from previous page*

(ID)	RA	Dec	g	r	i	z
103	04:30:31.20	-47:26:15.5	21.631±0.019	20.583±0.010	19.787±0.007	19.434±0.009
104	05:01:29.02	-51:26:45.1	23.807±0.091	22.084±0.023	21.090±0.024	20.789±0.029
105	04:50:09.12	-46:46:12.9	24.615±0.151	23.728±0.096	22.997±0.088	22.168±0.067
106	04:40:51.51	-46:01:01.5	23.056±0.053	22.184±0.034	21.451±0.033	20.811±0.034
107	04:23:51.08	-58:19:30.1	23.364±0.078	22.245±0.043	21.173±0.025	20.533±0.025
108	04:22:17.28	-46:19:54.3	25.840±0.545	24.031±0.180	23.311±0.127	22.515±0.109
109	04:51:00.28	-55:21:04.7	22.741±0.048	21.024±0.012	20.145±0.027	19.711±0.016
110	04:48:30.50	-51:08:09.9	24.182±0.094	23.259±0.054	22.669±0.072	21.872±0.056
111	04:26:19.31	-55:16:26.8	25.111±0.386	22.820±0.057	21.789±0.078	20.701±0.034
112	05:07:43.01	-56:41:07.9	23.230±0.069	21.778±0.023	20.874±0.019	20.495±0.022
113	04:41:50.41	-52:42:01.3	25.027±0.300	24.366±0.213	23.747±0.239	22.787±0.204
114	04:38:55.68	-55:40:45.2	21.248±0.011	20.651±0.008	20.422±0.017	20.261±0.021
115	04:50:54.97	-45:52:12.5	21.351±0.014	19.638±0.004	19.062±0.004	18.713±0.006
116	04:40:28.26	-53:24:22.5	24.382±0.219	23.265±0.098	22.372±0.101	21.104±0.049
117	05:39:28.98	-58:10:05.7	26.094±0.793	24.908±0.352	23.004±0.113	21.924±0.079
118	05:12:03.22	-51:54:29.7	24.636±0.819	22.832±0.145	21.481±0.073	20.619±0.055
119	04:12:06.23	-56:01:01.9	23.103±0.111	21.336±0.047	20.541±0.027	20.192±0.030
120	04:31:23.74	-54:32:02.0		23.732±0.168	22.147±0.137	21.159±0.078
121	04:53:08.23	-52:44:22.7	21.804±0.015	21.396±0.012	21.218±0.029	20.905±0.036
122	04:58:37.16	-51:32:29.2	23.969±0.099	22.342±0.028	21.118±0.023	20.454±0.022
123	04:37:52.91	-56:00:14.2	23.218±0.076	21.377±0.018	20.527±0.019	20.087±0.022
124	04:46:37.74	-48:34:33.5	25.381±0.414	23.068±0.062	21.932±0.037	21.319±0.049
125	04:11:16.56	-51:00:47.1	25.700±1.000	23.291±0.135	22.280±0.084	21.313±0.067
126	04:52:21.94	-49:23:30.2	22.016±0.028	20.535±0.010	19.972±0.007	19.728±0.013
127	04:13:04.11	-51:07:37.6	24.974±0.472	23.808±0.171	22.826±0.116	21.713±0.080
128	04:53:29.57	-45:33:16.7	22.733±0.037	20.961±0.009	20.295±0.011	19.976±0.018
129	05:25:29.41	-55:04:17.3		22.321±0.488	21.271±0.057	20.761±0.061
130	05:03:29.60	-57:35:40.3	20.310±0.004	19.775±0.004	19.682±0.006	19.157±0.007
131	04:55:32.80	-48:56:53.1	24.343±0.225	22.589±0.056	21.492±0.031	20.577±0.028
132	04:37:29.38	-54:25:19.2	20.181±0.008	18.750±0.003	18.289±0.007	17.959±0.007
133	04:58:09.61	-47:09:43.5	23.540±0.062	23.070±0.052	22.308±0.040	21.932±0.059
134	04:49:16.75	-54:45:21.1	23.585±0.102	22.137±0.029	21.120±0.051	20.734±0.035
135	05:15:14.89	-54:55:15.9	23.854±0.212	22.777±0.137	22.627±0.088	21.793±0.070
136	05:24:40.12	-56:58:50.6	22.128±0.017	21.581±0.014	21.208±0.018	20.882±0.025
137	04:22:38.31	-55:53:10.6	25.166±0.427	23.308±0.110	22.439±0.073	21.622±0.067
138	05:12:10.87	-59:51:10.5	24.644±0.256	23.566±0.108	22.490±0.075	21.742±0.061
139	04:29:37.20	-46:38:17.1	24.606±0.224	22.823±0.058	21.621±0.043	20.942±0.037
140	04:45:38.05	-47:04:19.4	27.041±1.000	25.670±0.542	24.080±0.208	22.689±0.103
141	05:03:28.30	-47:34:16.6	25.436±0.609	24.824±0.403	23.568±0.227	22.466±0.139

Continued on next page

Table A.1 – *continued from previous page*

(ID)	RA	Dec	g	r	i	z
142	04:39:24.66	-48:00:50.2	23.849±0.063	23.355±0.050	22.649±0.071	21.839±0.043
143	04:27:25.18	-47:04:59.7	24.128±0.128	22.494±0.036	21.402±0.027	20.761±0.022
144	04:27:37.44	-47:54:59.4	23.486±0.083	21.581±0.018	20.407±0.012	19.850±0.012
145	04:56:28.63	-50:20:36.6	24.968±0.340	22.802±0.057	21.621±0.038	20.768±0.031
146	05:39:30.30	-58:16:56.0	26.740±1.000	23.489±0.100	22.707±0.101	21.475±0.058
147	04:54:04.00	-51:22:26.9	25.143±0.281	23.000±0.058	21.966±0.044	21.179±0.034
148	05:05:56.38	-45:56:39.8	23.338±0.252	21.710±0.071	21.328±0.058	20.943±0.077
149	04:59:38.06	-49:05:06.0	23.013±0.128	20.843±0.022	19.709±0.010	19.282±0.015
150	04:39:02.07	-46:33:05.6	25.821±0.451	25.048±0.305	23.880±0.181	22.753±0.117
151	04:50:15.52	-56:05:50.4	20.002±0.011	18.553±0.003	18.035±0.005	17.743±0.006
152	04:21:31.12	-53:17:25.7	22.776±0.052	21.564±0.020	20.455±0.024	19.846±0.025
153	04:42:57.40	-52:01:50.1	22.814±0.048	20.945±0.012	19.945±0.010	19.502±0.013
154	04:32:03.14	-56:36:47.9	25.302±0.322	24.557±0.215	23.735±0.214	22.735±0.159
155	04:33:32.25	-46:23:19.5	24.094±0.113	23.608±0.108	23.018±0.113	21.799±0.063
156	04:17:50.86	-49:06:32.9	24.460±0.443	22.182±0.094	21.724±0.087	20.754±0.093
157	05:09:06.27	-50:46:26.8	24.329±0.413	22.152±0.067	20.947±0.051	20.220±0.041
158	05:14:52.11	-54:24:42.6	20.914±0.024	19.665±0.012	19.155±0.006	18.854±0.007
159	04:36:36.68	-49:17:32.2	23.288±0.057	22.702±0.042	22.086±0.044	21.737±0.056
160	04:34:02.56	-46:19:03.9	25.556±0.423	24.355±0.190	23.240±0.145	21.961±0.078
161	04:36:30.74	-49:51:40.1	28.830±1.000	24.691±0.296	24.199±0.278	22.809±0.151
162	04:38:12.57	-52:27:05.2	24.904±0.228	23.861±0.119	22.659±0.113	22.124±0.112
163	05:19:56.30	-55:46:02.8		24.535±0.697	22.831±0.145	21.614±0.082
164	04:20:51.55	-49:59:10.7	22.193±0.061	20.926±0.019	20.080±0.015	19.679±0.031
165	04:41:34.93	-51:00:11.0	24.655±0.219	22.374±0.034	21.192±0.027	20.298±0.018
166	04:23:03.86	-50:24:54.0	20.446±0.006	19.468±0.004	19.206±0.004	18.637±0.004
167	04:26:59.71	-48:06:30.7	23.062±0.046	22.326±0.028	21.601±0.032	20.718±0.022
168	04:22:02.10	-46:46:18.8	22.935±0.047	22.314±0.034	21.727±0.032	20.723±0.023
169	05:00:35.22	-50:56:04.1	25.091±0.322	23.152±0.071	21.881±0.052	21.088±0.041
170	04:28:03.30	-55:41:57.0	24.331±0.165	23.709±0.106	22.931±0.152	22.280±0.124
171	05:02:38.04	-47:19:28.2	23.428±0.107	21.866±0.034	20.713±0.018	20.186±0.024
172	04:36:34.18	-45:56:03.9	23.624±0.082	21.605±0.018	20.458±0.013	20.004±0.017
173	05:28:05.07	-59:56:38.8	23.607±0.151	21.508±0.027	20.307±0.019	19.868±0.031
174	04:29:43.10	-49:48:52.6	22.040±0.068	20.530±0.012	19.703±0.008	19.289±0.011
175	04:31:22.63	-54:09:35.3	24.649±0.389	22.575±0.073	21.651±0.104	20.874±0.083
176	04:20:20.53	-50:34:26.8	23.104±0.060	22.451±0.049	21.768±0.035	21.053±0.034
177	05:11:28.75	-51:47:12.2	23.178±0.206	21.469±0.041	20.531±0.030	20.127±0.034
178	04:44:18.83	-47:51:31.6	20.732±0.008	20.339±0.007	20.169±0.010	19.671±0.011
179	04:52:09.95	-49:00:19.4	24.759±0.307	22.742±0.051	21.521±0.025	20.961±0.027
180	04:16:27.47	-55:17:04.2	24.259±0.488	23.785±0.255	22.524±0.112	21.542±0.090

Continued on next page

Table A.1 – *continued from previous page*

(ID)	RA	Dec	g	r	i	z
181	04:35:47.64	-47:33:16.4	22.330±0.034	20.793±0.011	19.894±0.011	19.468±0.011
182	05:03:16.10	-53:08:12.6	24.642±0.350	23.573±0.115	22.381±0.078	21.458±0.073
183	04:30:33.81	-49:21:17.8	24.947±0.306	23.750±0.112	23.306±0.121	22.840±0.147
184	04:21:56.28	-51:07:34.6	23.526±0.106	22.792±0.068	22.009±0.075	20.912±0.048
185	04:26:06.18	-50:54:08.0	25.846±0.635	23.347±0.079	22.319±0.059	21.302±0.042
186	04:30:06.10	-57:54:00.5	23.683±0.120	21.828±0.030	20.801±0.024	20.303±0.023
187	04:22:09.80	-59:54:06.1	23.490±0.082	22.655±0.073	21.922±0.044	21.138±0.045
188	04:41:36.17	-58:10:13.9	25.799±0.544	23.471±0.081	22.332±0.051	21.552±0.047
189	05:04:37.69	-50:58:58.4	25.104±0.544	22.708±0.074	21.359±0.049	20.467±0.037
190	05:01:21.08	-52:59:59.1	22.821±0.068	21.159±0.014	20.227±0.012	19.817±0.018
191	05:15:50.51	-55:46:32.5	22.629±0.055	21.173±0.022	20.079±0.009	19.626±0.010
192	04:42:30.96	-48:50:51.6	23.501±0.068	22.932±0.048	22.173±0.051	21.657±0.052
193	04:15:00.51	-56:13:08.3	20.932±0.010	20.696±0.011	20.253±0.012	19.882±0.016
194	04:42:05.32	-54:14:54.6	20.605±0.005	20.615±0.006	20.272±0.014	20.265±0.021
195	05:10:50.32	-56:23:18.5	23.669±0.131	21.957±0.038	20.847±0.020	20.453±0.023
196	05:23:06.46	-56:32:23.6	23.976±0.135	22.748±0.061	21.716±0.041	21.105±0.043
197	04:38:31.34	-56:31:15.9	23.712±0.112	21.937±0.027	20.700±0.016	20.241±0.020
198	04:52:05.61	-47:45:40.9	23.348±0.060	21.506±0.013	20.695±0.011	20.320±0.015
199	04:55:05.47	-53:23:47.6	20.753±0.015	18.887±0.003	18.297±0.006	17.957±0.007
200	05:00:31.55	-51:46:50.1	24.763±0.331	22.036±0.033	20.822±0.023	20.123±0.023
201	04:20:00.93	-59:56:13.6	21.793±0.016	21.382±0.021	20.745±0.015	20.733±0.025
202	04:34:41.13	-57:04:11.6	25.082±0.197	24.625±0.179	24.363±0.278	22.946±0.137
203	04:11:25.01	-55:58:45.8	23.032±0.065	22.181±0.053	22.256±0.078	21.529±0.068
204	05:23:22.61	-57:18:48.6	23.289±0.081	21.758±0.026	21.207±0.025	20.653±0.029
205	05:12:40.85	-52:37:42.0	22.472±0.099	20.853±0.028	19.950±0.023	19.553±0.026
206	04:14:50.68	-55:21:06.4	23.818±0.232	22.118±0.069	21.203±0.042	20.413±0.039
207	04:52:15.55	-48:49:30.0	23.252±0.072	21.840±0.025	21.087±0.021	20.507±0.026
208	05:06:29.11	-51:26:34.6	24.941±0.344	22.810±0.056	21.654±0.056	20.864±0.047
209	04:54:21.77	-56:11:00.4	23.943±0.135	22.707±0.052	22.012±0.063	21.666±0.063
210	04:54:30.89	-48:48:11.4	24.752±0.258	22.698±0.048	21.540±0.026	20.991±0.034
211	04:36:09.64	-57:36:19.8	20.978±0.009	20.593±0.008	20.037±0.008	19.742±0.011
212	05:15:14.44	-56:19:41.9	25.258±0.441	23.141±0.092	21.759±0.037	21.013±0.033
213	04:30:17.10	-57:46:49.6	23.536±0.068	22.429±0.037	21.586±0.033	21.077±0.034
214	04:29:16.92	-56:25:51.6	24.238±0.257	22.394±0.051	21.344±0.041	20.907±0.047
215	05:05:17.81	-52:26:27.1	24.834±0.366	22.752±0.066	21.927±0.045	21.373±0.058
216	05:18:09.22	-56:29:34.0	20.163±0.004	20.112±0.006	19.615±0.005	19.551±0.009
217	04:19:02.65	-54:27:39.0	25.605±1.000	24.015±0.280	23.034±0.312	21.388±0.099
218	04:36:52.01	-52:16:38.8	19.557±0.003	19.550±0.003	19.335±0.007	19.275±0.010
219	04:59:37.55	-48:42:52.8	23.732±0.190	21.962±0.044	20.824±0.027	20.290±0.033

Continued on next page

Table A.1 – *continued from previous page*

(ID)	RA	Dec	g	r	i	z
220	04:13:48.74	-52:39:04.9	21.129±0.012	21.415±0.022	21.114±0.029	20.917±0.044
221	04:14:11.70	-50:54:33.3			25.362±1.000	21.933±0.090
222	04:26:37.21	-50:43:36.3	23.562±0.102	21.858±0.026	20.816±0.022	20.164±0.024
223	05:08:11.85	-51:20:52.7	22.284±0.058	20.532±0.012	19.842±0.013	19.456±0.015
224	04:35:04.43	-49:10:55.9	22.866±0.057	21.576±0.019	20.493±0.013	19.988±0.015
225	04:18:04.68	-47:58:20.7	24.702±0.287	24.007±0.174	22.821±0.116	21.825±0.088
226	05:09:54.23	-51:27:33.3	22.095±0.037	20.676±0.012	20.113±0.019	19.766±0.022
227	04:57:23.33	-51:28:01.7	25.027±0.327	23.099±0.077	22.009±0.058	20.962±0.036
228	04:35:44.20	-47:59:31.2	21.574±0.015	19.980±0.004	19.396±0.007	19.069±0.006
229	05:22:06.41	-55:30:50.8	22.414±0.071	20.920±0.029	20.086±0.014	19.735±0.017
230	04:21:26.81	-48:21:08.7	22.036±0.042	20.299±0.011	19.725±0.014	19.405±0.012
231	04:24:55.33	-47:14:27.4	23.214±0.072	22.278±0.037	21.155±0.028	20.554±0.026
232	04:43:54.03	-56:59:58.9	25.781±0.780	23.155±0.081	21.838±0.044	21.079±0.043
233	04:47:09.05	-57:13:51.3	23.429±0.124	21.254±0.018	20.177±0.011	19.724±0.013
234	04:41:58.31	-51:54:53.3	22.642±0.053	21.447±0.025	20.431±0.018	19.849±0.025
235	04:47:03.35	-51:02:48.3	22.624±0.027	21.952±0.019	21.294±0.025	20.677±0.021
236	04:58:52.04	-50:25:55.6	20.930±0.008	20.123±0.005	19.589±0.006	19.407±0.009
237	04:34:06.44	-56:53:12.0	21.697±0.024	20.202±0.008	19.365±0.007	18.954±0.009
238	04:22:48.16	-46:55:02.8	21.489±0.023	19.779±0.006	19.189±0.005	18.837±0.007
239	04:26:53.21	-52:15:29.8	22.185±0.040	20.526±0.011	19.839±0.014	19.361±0.013
240	04:14:28.10	-47:10:03.6	21.754±0.067	20.110±0.017	19.280±0.009	18.867±0.012
241	04:31:02.11	-57:46:03.8	24.330±0.161	23.242±0.086	21.936±0.049	20.915±0.036
242	04:36:21.44	-57:30:52.8	21.966±0.027	20.551±0.009	19.690±0.008	19.284±0.010
243	04:41:00.55	-57:50:18.5	19.373±0.002	19.012±0.002	18.673±0.003	18.554±0.004
244	04:55:20.58	-49:41:05.8	19.036±0.005	18.112±0.002	17.720±0.002	17.514±0.004
245	04:43:13.32	-53:34:59.4	21.683±0.026	19.881±0.006	19.188±0.009	18.814±0.011
246	04:31:00.81	-50:34:32.5	18.843±0.002	18.490±0.001	18.472±0.003	17.988±0.003
247	04:27:02.60	-56:03:15.2	21.589±0.019	19.936±0.006	19.110±0.005	18.782±0.007
248	04:18:59.42	-50:18:34.2	21.841±0.037	20.095±0.007	19.228±0.006	18.854±0.010
249	04:26:11.31	-48:03:56.4	19.182±0.004	17.993±0.002	17.515±0.002	17.180±0.003

Table A.2: Table A.1 extended with further properties.

(ID)	J	H	K_s	$S_{843}/$ mJy	z_{phot}	$\log_{10}(M_{\star}/$ $M_{\odot})$	$\log_{10}(\text{SFR}/$ $M_{\odot}\text{yr}^{-1})$
1	19.281±0.159	19.096±0.183	18.711±0.182	17.0±1.0	1.08	12.04	3.24
2	19.870±0.129		19.328±0.255	20.7±1.5	0.93	10.72	1.60
3	20.110±0.199	19.603±0.209	19.071±0.231	24.6±1.0	0.99	11.74	-2.06
4	20.008±0.168		19.428±0.189	441±13	1.07	10.95	1.03
5	18.628±0.091	18.093±0.099	18.150±0.120	12.7±1.0	0.48	11.17	0.64
6			20.461±0.328	62.9±2.1	1.08	11.60	1.84
7	19.828±0.225	19.402±0.248	18.984±0.247	19.0±0.9	0.92	11.65	-2.15
8	19.442±0.135		18.843±0.202	386±12	0.89	11.85	1.28
9	19.315±0.097		18.552±0.128	25.8±1.1	0.95	11.46	-0.35
10	20.344±0.185		19.916±0.256	70.1±2.3	1.23	11.19	1.28
11	19.988±0.177		19.640±0.319	37.6±1.8	0.76	10.72	2.77
12			20.667±0.505	43.3±1.7	1.01	11.19	1.72
13	20.286±0.320	19.618±0.251	19.200±0.254	15.5±0.9	0.61	11.06	1.94
14	19.792±0.156		19.849±0.272	12.6±0.8	0.68	11.13	-5.85
15	20.104±0.183		19.180±0.227	40.8±1.8	0.91	11.41	-2.39
16	18.299±0.048		17.686±0.079	52.7±1.8	0.70	11.98	0.40
17	19.028±0.106		18.546±0.170	15.9±1.3	0.79	11.64	0.07
18	21.640±0.731	20.590±0.368	19.881±0.280	16.0±1.2	0.65	9.84	1.89
19	18.240±0.046		17.771±0.096	46.3±1.7	0.36	11.07	0.50
20		20.507±0.417	19.782±0.291	16.7±0.9	0.91	-1.00	-1.00
21	17.760±0.072	17.578±0.094	17.462±0.092	51.2±1.8	0.12	10.06	-0.02
22	18.905±0.155	18.510±0.149	18.370±0.142	80.1±2.6	0.74	11.37	0.80
23	20.253±0.208		19.498±0.228	19.6±1.1	1.03	11.51	0.94
24	20.438±0.186		19.807±0.304	48.2±1.7	1.12	11.28	1.52
25	21.426±0.543	20.584±0.395	20.344±0.441	16.9±0.9	1.00	11.33	0.76
26	19.773±0.154		19.532±0.344	40.5±1.6	0.86	11.16	0.59
27	19.804±0.162		19.420±0.249	13.8±1.0	1.32	11.88	2.12
28	19.120±0.131		18.565±0.183	25.4±1.6	0.72	11.75	0.17
29	20.181±0.280	19.746±0.276	19.522±0.276	58.4±2.0	0.68	11.40	-5.59
30	19.904±0.205	19.505±0.213	19.249±0.241	24.6±1.2	0.79	11.16	3.02
31	19.782±0.100		18.888±0.164	18.0±1.0	0.77	11.55	-0.25
32	20.221±0.260	20.441±0.366	20.077±0.342	19.7±1.1	0.49	10.57	0.42
33	20.171±0.253	19.569±0.226	19.247±0.234	14.8±0.9	1.03	11.64	3.12
34	19.025±0.122	18.560±0.155	18.200±0.129	23.2±1.2	0.73	11.77	-5.21
35	19.525±0.154		18.566±0.169	14.5±1.2	1.16	12.24	-1.57
36	20.885±0.499	19.976±0.331	19.813±0.324	27.7±1.2	1.01	10.97	0.40
37	21.163±0.351		19.948±0.341	65.8±2.2	0.69	10.75	2.62
38	19.942±0.224	17.696±0.076	19.277±0.249	24.4±1.0	0.93	11.53	-2.27

Continued on next page

Table A.2 : Table A.1 extended with further properties.

(ID)	J	H	K_s	$S_{843}/$ mJy	z_{phot}	$\log_{10}(M_{\star}/$ $M_{\odot})$	$\log_{10}(\text{SFR}/$ $M_{\odot}\text{yr}^{-1})$
39	19.750±0.144		19.002±0.205	24.0±1.1	1.24	12.02	-1.78
40	19.373±0.178	18.722±0.178	18.878±0.190	12.7±1.1	0.59	11.23	-0.58
41	21.205±0.319		20.051±0.373	120±3.7	1.03	9.99	1.66
42	18.468±0.12	17.909±0.082	17.512±0.089	29.3±1.2	0.66	11.92	-5.07
43	19.979±0.203		19.121±0.223	45.8±1.6	1.18	12.06	0.25
44	18.970±0.097		18.332±0.136	26.4±1.4	0.85	12.13	-4.86
45	20.004±0.231		19.146±0.206	111±3.5	0.85	11.44	-5.55
46	20.397±0.176		20.012±0.382	101±3.2	1.05	11.65	1.08
47	19.973±0.177		19.168±0.236	17.3±1.1	0.83	11.10	0.53
48	20.856±0.258		19.497±0.185	20.7±1.8	1.06	-1.00	-1.00
49	18.627±0.050		18.043±0.074	19.1±1.0	0.34	10.91	1.11
50	19.994±0.168		18.931±0.174	14.3±1.0	0.86	11.63	-5.35
51	20.285±0.276	19.847±0.243	19.461±0.352	146±4.5	0.96	11.67	-2.13
52	18.205±0.059		17.726±0.103	17.7±1.0	0.45	11.30	0.73
53	20.161±0.311	19.837±0.292	19.617±0.318	16.0±0.9	0.74	11.12	1.92
54	20.617±0.295		19.172±0.210	12.7±0.9	1.38	11.63	1.89
55	19.941±0.243	19.944±0.295	19.245±0.282	217.0±6.6	1.10	11.84	1.26
56	19.877±0.175		19.591±0.270	17.7±0.9	0.95	10.41	2.45
57	19.385±0.087		18.735±0.150	16.5±1.0	0.70	11.30	0.73
58	20.301±0.239	19.988±0.277	20.174±0.443	64.8±2.1	0.82	10.23	2.28
59			20.239±0.373	21.6±1.0	1.21	-1.00	-1.00
60	20.292±0.193		19.834±0.283	15.0±1.2	0.84	10.65	0.73
61	20.238±0.189		19.131±0.236	12.6±1.2	0.85	11.61	-5.37
62			19.601±0.278	20.1±1.1	0.88	-1.00	-1.00
63	18.822±0.087		17.951±0.127	36.6±1.4	0.81	11.90	0.32
64	20.313±0.343	19.784±0.346	18.884±0.198	13.3±1.8	0.46	10.74	0.94
65	19.124±0.134	18.762±0.143	18.459±0.118	13.4±1.2	0.81	11.91	-5.07
66	19.621±0.132		19.064±0.224	182±5.5	0.61	11.26	-5.72
67	19.790±0.196		18.928±0.139	18.7±1.3	0.87	10.92	0.35
68	19.418±0.100		19.495±0.258	12.6±0.9	0.84	11.05	1.25
69	20.340±0.206		19.508±0.256	25.1±1.5	0.67	10.43	0.28
70	18.556±0.072	18.141±0.080	17.821±0.075	19.7±1.6	0.34	10.82	1.08
71	17.788±0.053		17.380±0.089	15.0±0.9	0.38	11.11	0.58
72			20.213±0.400	26.4±1.3	0.97	10.40	0.48
73	21.272±0.422		20.351±0.364	15.3±1.3	1.12	10.83	0.91
74	20.978±0.303		20.504±0.449	25.6±1.1	1.11	10.69	0.95
75	20.221±0.188		19.594±0.300	46.4±1.9	1.02	12.05	2.29

Continued on next page

Table A.2 : Table A.1 extended with further properties.

(ID)	J	H	K_s	$S_{843}/$ mJy	z_{phot}	$\log_{10}(M_{\star}/$ $M_{\odot})$	$\log_{10}(\text{SFR}/$ $M_{\odot}\text{yr}^{-1})$
76	21.208±0.372	20.545±0.354	19.967±0.337	48.4±1.8	0.90	10.33	0.78
77	17.432±0.045		18.244±0.122	14.8±1.3	0.79	11.60	0.02
78	21.586±0.503	20.668±0.449	20.348±0.373	19.5±1.3	0.79	10.49	0.75
79			19.441±0.220	17.3±1.1	1.07	-1.00	-1.00
80	18.954±0.136	18.340±0.120	18.263±0.149	12.5±0.8	0.75	11.77	2.57
81	20.849±0.255		20.198±0.319	22.0±1.1	0.87	10.96	0.39
82	20.360±0.164		20.046±0.323	694±20	0.97	-1.00	-1.00
83	19.757±0.117		19.303±0.206	38.7±1.5	0.79	11.33	0.80
84		20.587±0.495	19.478±0.279	213±6.5	0.93	10.48	0.56
85	20.562±0.233		20.242±0.351	13.1±1.2	0.62	10.64	-3.17
86	20.200±0.305	19.289±0.261	19.217±0.197	26.7±1.3	0.63	10.76	0.84
87	18.233±0.082	17.974±0.076	17.683±0.090	12.0±1.1	0.34	11.03	0.46
88			19.706±0.231	68.3±2.2	1.12	11.22	1.46
89	20.882±0.229		19.904±0.232	60.8±2.0	0.95	10.23	0.31
90	19.174±0.107		18.482±0.141	14.7±1.0	0.87	11.81	0.23
91	20.637±0.262		20.056±0.297	15.4±1.0	1.08	11.08	1.34
92	19.604±0.119		18.917±0.201	34.0±1.4	0.91	11.58	1.00
93		20.265±0.282	19.313±0.221	13.1±1.1	1.16	11.47	1.73
94	20.013±0.196	20.040±0.291	19.544±0.257	21.9±1.1	0.73	11.10	-2.70
95			19.583±0.214	12.7±1.0	0.82	11.20	-0.38
96			19.364±0.212	48.7±2.0	1.35	11.87	2.32
97			20.220±0.350	14.1±1.0	0.96	-1.00	-1.00
98	21.063±0.320	20.602±0.282	20.016±0.297	13.1±1.1	0.76	11.38	-5.61
99	18.311±0.054	18.004±0.067	17.665±0.064	41.6±1.5	0.04	8.52	0.39
100			19.561±0.252	95.4±3.0	0.17	8.45	0.51
101	20.542±0.233		19.629±0.306	43.3±1.7	1.21	11.93	-1.87
102	19.251±0.143	18.495±0.128	18.216±0.096	132±4.1	0.69	11.58	1.01
103	18.973±0.099		18.083±0.092	67.8±2.2	0.73	11.38	0.81
104	20.348±0.250	20.061±0.296	19.776±0.331	13.5±1.1	0.60	11.00	-5.98
105	21.260±0.187		20.021±0.221	21.8±1.2	1.20	10.82	2.10
106	20.195±0.226	19.538±0.199	19.762±0.281	169±5.2	0.90	11.03	0.46
107	19.622±0.106		18.118±0.080	24.4±1.4	0.92	11.38	0.80
108			20.117±0.362	17.8±1.0	0.92	10.50	-3.30
109	19.331±0.145	18.990±0.17	18.444±0.140	15.0±0.8	0.58	11.38	-5.60
110			19.711±0.262	48.5±1.8	1.14	10.68	2.35
111	20.261±0.201	19.671±0.202	19.888±0.502	37.8±1.6	1.06	11.76	-2.05
112	19.585±0.147		19.226±0.266	15.2±0.9	0.65	11.07	0.50

Continued on next page

Table A.2 : Table A.1 extended with further properties.

(ID)	J	H	K_s	$S_{843}/$ mJy	z_{phot}	$\log_{10}(M_{\star}/$ $M_{\odot})$	$\log_{10}(\text{SFR}/$ $M_{\odot}\text{yr}^{-1})$
113			19.732±0.291	42.7±1.6	0.99	10.38	0.62
114	19.776±0.188		19.897±0.346	19.5±1.1	0.27	9.77	-0.02
115	18.208±0.067	17.848±0.087	17.685±0.073	15.0±1.0	0.42	11.09	0.56
116	20.223±0.241	19.672±0.269	19.572±0.278	38.9±1.5	1.14	11.98	2.22
117	21.096±0.418		19.539±0.303	15.1±1.2	1.34	12.27	-1.53
118	20.320±0.217	19.653±0.234	19.037±0.223	22.9±1.2	1.01	11.66	1.13
119	19.475±0.136		19.182±0.213	22.9±1.9	0.54	10.93	-0.87
120		20.233±0.271	19.494±0.257	170±5.2	1.25	-1.00	-1.00
121	20.724±0.415	20.378±0.401	19.868±0.317	147±4.5	0.40	9.22	1.27
122	20.276±0.291	19.598±0.280	19.158±0.248	40.6±1.6	0.83	11.66	1.09
123	19.484±0.119		18.837±0.162	14.3±1.0	0.57	11.08	-0.72
124	20.324±0.216		19.732±0.278	55.0±1.9	0.80	11.19	-5.80
125	20.952±0.396	20.076±0.347	19.748±0.363	59.1±2.0	1.03	11.42	-2.39
126	19.200±0.082		18.584±0.114	16.1±1.1	0.41	10.86	-0.72
127			20.073±0.268	22.1±1.3	1.10	11.67	1.91
128	19.699±0.228	19.041±0.205	19.100±0.273	18.0±1.2	0.46	10.73	0.20
129	19.913±0.174	19.810±0.267	19.579±0.306	14.0±0.9	0.76	-1.00	-1.00
130	19.180±0.074		18.505±0.131	234±7.1	0.42	9.95	2.00
131	19.973±0.178		19.037±0.230	77.6±2.5	0.98	11.56	-0.24
132	17.505±0.062	17.302±0.080	17.041±0.057	18.5±1.3	0.36	11.36	0.79
133			19.272±0.259	22.7±1.5	0.91	10.43	0.67
134	19.915±0.223	20.065±0.406	19.553±0.314	22.7±1.2	0.68	11.07	0.50
135	20.841±0.316		19.311±0.245	32.4±1.3	1.29	10.72	2.48
136	19.766±0.191		18.944±0.165	1449±43	0.71	9.93	1.97
137	20.328±0.211		19.773±0.298	19.1±1.0	0.95	10.94	-2.87
138	20.724±0.228		19.938±0.336	18.3±1.0	0.99	11.26	1.50
139	20.480±0.312	19.870±0.231	19.240±0.222	85.7±2.7	0.84	11.45	-0.13
140	21.395±0.279		19.875±0.236	26.8±1.1	1.20	12.10	1.53
141	21.664±0.578		20.274±0.416	26.0±1.1	1.11	11.30	1.38
142	20.427±0.216		19.657±0.303	28.1±1.2	1.26	11.12	0.55
143	19.982±0.210		19.154±0.196	191±5.8	0.83	11.33	-0.25
144	18.965±0.068		18.331±0.133	23.5±1.2	0.75	11.65	-2.15
145	20.078±0.217	19.877±0.271	19.466±0.276	61.8±2.1	0.92	11.58	-2.22
146	20.245±0.214		19.514±0.285	66.5±2.2	1.08	11.52	-2.28
147	20.278±0.191	20.601±0.343	19.716±0.276	21.3±1.4	0.90	11.23	-2.57
148	20.612±0.293		19.585±0.347	23.2±1.3	0.41	10.11	0.37
149	18.683±0.064		17.886±0.094	14.2±1.1	0.72	11.98	-5.01

Continued on next page

Table A.2 : Table A.1 extended with further properties.

(ID)	J	H	K_s	$S_{843}/$ mJy	z_{phot}	$\log_{10}(M_{\star}/$ $M_{\odot})$	$\log_{10}(\text{SFR}/$ $M_{\odot}\text{yr}^{-1})$
150			20.696±0.511	24.6±1.2	1.14	10.92	1.19
151	17.241±0.028		16.802±0.049	22.8±1.0	0.37	11.49	0.92
152	19.309±0.196	19.527±0.308	18.552±0.197	24.8±1.3	0.88	11.71	1.14
153	19.011±0.127	18.621±0.155	18.497±0.135	53.5±2.0	0.67	11.50	-0.31
154	23.047±1.959		20.326±0.348	19.3±1.0	1.10	10.83	1.07
155	21.019±0.294	20.550±0.354	20.390±0.381	130±4.0	1.33	11.23	1.49
156	19.971±0.169		19.117±0.211	29.9±1.1	0.68	10.88	2.50
157	18.879±0.071		18.636±0.151	35.7±1.4	0.86	11.80	-5.18
158	18.316±0.067	18.142±0.081	18.034±0.092	50.1±1.7	0.34	11.04	0.89
159	21.162±0.289		20.481±0.401	88.5±2.8	0.81	9.89	1.88
160	21.060±0.283	19.937±0.223	19.872±0.259	128±4.0	1.12	11.82	2.06
161			20.068±0.229	24.3±1.3	1.08	-1.00	-1.00
162			20.133±0.349	73.3±2.4	0.88	10.62	1.78
163	20.492±0.252		19.978±0.331	28.1±1.2	1.11	-1.00	-1.00
164	19.451±0.182	18.807±0.154	18.732±0.165	19.3±1.2	0.71	11.31	0.74
165	19.368±0.144	18.891±0.169	18.728±0.179	37.8±1.4	0.95	11.81	-2.00
166	18.433±0.053	18.343±0.067	17.931±0.064	18.1±1.0	0.28	10.27	2.26
167	19.968±0.125		19.577±0.243	34.1±1.4	1.30	11.87	1.30
168	20.094±0.126		20.024±0.354	29.8±1.4	1.37	11.56	1.82
169	19.867±0.191	20.173±0.225	19.710±0.316	46.8±1.7	0.90	11.34	-0.46
170	20.616±0.272		19.716±0.350	61.2±2.0	1.00	10.65	0.89
171	19.537±0.163		18.628±0.220	82.8±2.6	0.75	11.54	0.97
172	19.442±0.142	18.985±0.144	18.588±0.163	36.0±1.6	0.73	11.70	-5.29
173	19.109±0.115		18.903±0.247	14.2±1.0	0.73	11.75	-5.24
174	18.795±0.125	18.586±0.106	17.930±0.105	338±10	0.60	11.44	0.87
175			19.527±0.196	25.0±1.2	0.84	11.30	-5.69
176	20.439±0.261	20.491±0.407	19.508±0.232	32.5±1.2	1.07	11.21	1.45
177	19.327±0.161	18.814±0.145	18.825±0.189	21.0±1.2	0.62	11.19	-2.61
178	19.174±0.068		19.138±0.223	29.2±1.3	0.80	10.32	2.37
179	20.095±0.188		19.156±0.199	27.8±1.3	0.78	11.34	-5.65
180	20.109±0.233	20.434±0.49	19.456±0.284	23.7±1.2	1.10	11.57	1.66
181	18.973±0.081		18.415±0.116	58.2±2.0	0.62	11.45	0.88
182	20.601±0.283	20.529±0.376	19.707±0.311	28.0±1.2	1.08	11.33	1.59
183	20.650±0.246		19.761±0.287	16.0±0.9	0.53	9.32	1.37
184		19.868±0.201	19.501±0.254	16.6±0.9	1.22	11.35	1.62
185	20.487±0.255	19.658±0.209	19.569±0.276	306±9.2	1.04	11.52	-2.28
186	19.701±0.147		18.953±0.207	97.2±3.1	0.67	11.21	-0.60

Continued on next page

Table A.2 : Table A.1 extended with further properties.

(ID)	J	H	K_s	$S_{843}/$ mJy	z_{phot}	$\log_{10}(M_{\star}/$ $M_{\odot})$	$\log_{10}(\text{SFR}/$ $M_{\odot}\text{yr}^{-1})$
187	20.173±0.195		19.848±0.329	71.0±2.4	1.18	11.14	2.54
188	21.080±0.342		20.215±0.374	35.0±1.4	0.90	11.18	-2.62
189	18.999±0.114		18.542±0.160	22.6±1.1	1.20	12.14	-1.66
190	18.925±0.153	18.916±0.190	18.680±0.158	34.8±1.3	0.60	11.37	-5.61
191	18.995±0.087		18.338±0.109	699±21	0.72	11.85	1.70
192	20.989±0.253		19.899±0.339	199±6.1	0.96	10.58	0.66
193	19.463±0.119		18.724±0.174	61.5±2.3	0.93	10.94	1.62
194	20.472±0.261	20.621±0.488	20.036±0.357	138±4.3	0.13	8.57	0.56
195	19.629±0.164		19.249±0.239	19.3±1.1	0.67	11.31	-5.67
196	20.269±0.216		19.134±0.207	65.4±2.1	0.88	11.16	0.58
197	19.455±0.140		18.970±0.176	19.9±1.0	0.73	11.35	0.82
198	19.964±0.251		18.590±0.202	93.2±2.9	0.54	10.87	0.34
199	17.535±0.047	17.352±0.070	17.062±0.063	25.2±1.1	0.43	11.59	1.85
200	19.908±0.219	19.253±0.178	18.939±0.203	70.7±2.3	0.86	11.90	-5.09
201	20.679±0.343		19.828±0.296	35.4±1.5	0.69	10.31	0.98
202			19.798±0.288	223±6.7	1.31	10.43	0.69
203	20.409±0.230		20.344±0.350	112±3.7	0.39	9.09	1.12
204	19.918±0.212		18.697±0.196	27.7±1.5	0.50	10.36	2.20
205	19.035±0.151	18.640±0.175	18.256±0.164	13.0±0.8	0.60	11.46	-0.12
206	19.707±0.204	19.339±0.247	18.691±0.175	25.8±1.3	0.93	11.42	-2.38
207	19.949±0.170		19.391±0.217	50.0±1.7	0.65	10.74	2.79
208	20.077±0.243	20.190±0.378	19.367±0.282	18.8±1.0	0.89	11.46	-2.35
209	21.504±0.399		20.205±0.257	92.6±2.9	0.62	10.45	0.30
210	19.991±0.167		19.760±0.206	61.9±2.1	0.75	11.33	-5.66
211	19.313±0.104		18.541±0.112	68.2±2.3	0.81	10.97	1.42
212	20.325±0.227		19.219±0.230	101±3.2	0.91	11.48	-0.32
213	20.588±0.221		19.467±0.221	37.3±1.4	0.80	10.61	2.59
214			19.362±0.234	52.6±1.7	0.67	11.13	-5.86
215	21.392±0.396	20.494±0.354	19.685±0.250	90.0±2.9	0.62	10.67	0.93
216	18.738±0.054		19.499±0.236	34.7±1.4	0.11	8.60	0.65
217	20.230±0.250	20.591±0.342	19.468±0.261	27.8±1.2	1.12	12.35	1.78
218	19.080±0.143	19.089±0.228	18.296±0.117	40.0±1.5	0.09	8.53	0.58
219	19.520±0.139		19.081±0.231	63.9±2.2	0.74	11.54	-0.04
220	20.616±0.333	20.298±0.320	19.427±0.237	424±13	1.00	9.85	1.61
221	20.614±0.293	19.763±0.290	19.668±0.325	57.6±2.0	1.94	-1.00	-1.00
222	19.346±0.154	19.484±0.240	18.808±0.205	22.0±1.0	0.80	11.52	-0.05
223	19.492±0.176	18.558±0.137	18.611±0.189	22.0±1.1	0.49	11.15	-0.65

Continued on next page

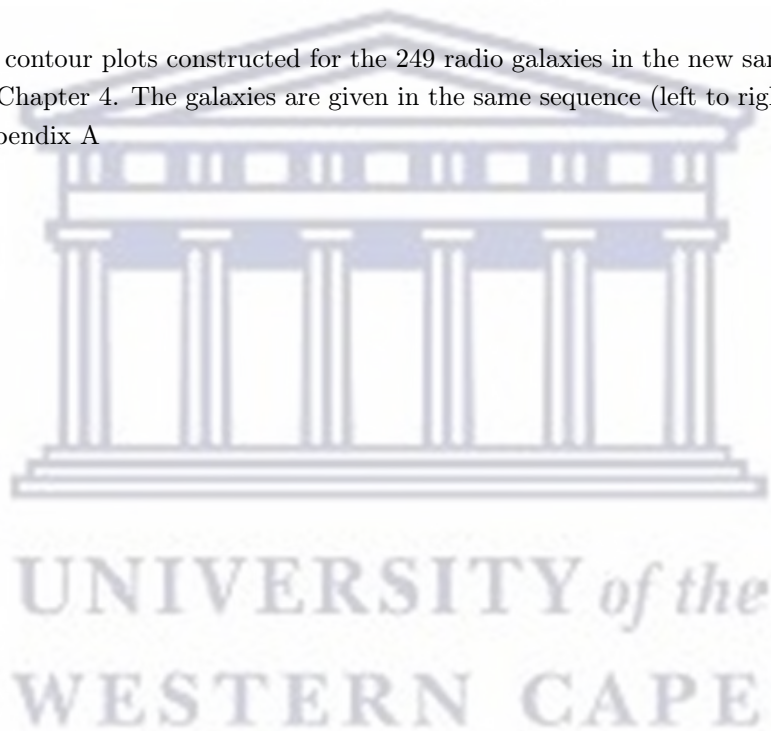
Table A.2 : Table A.1 extended with further properties.

(ID)	J	H	K_s	$S_{843}/$ mJy	z_{phot}	$\log_{10}(M_{\star}/$ $M_{\odot})$	$\log_{10}(\text{SFR}/$ $M_{\odot}\text{yr}^{-1})$
224	19.630±0.131		18.828±0.215	38.8±1.4	0.81	11.49	0.92
225	20.650±0.288		19.712±0.277	63.7±2.1	1.14	11.20	1.46
226	19.407±0.169	18.922±0.141	18.509±0.162	136±4.2	0.44	11.00	0.85
227	20.504±0.302	19.465±0.216	19.331±0.237	87.0±2.8	1.06	11.58	-0.22
228	18.537±0.048		18.052±0.077	18.4±0.9	0.43	11.20	0.63
229	19.251±0.082		18.361±0.130	16.2±0.9	0.60	11.27	-0.31
230	18.741±0.053		18.036±0.108	24.3±1.1	0.41	10.82	0.29
231	19.598±0.146		18.913±0.145	34.1±1.3	0.95	11.34	1.87
232	20.291±0.190		19.588±0.296	41.3±1.5	0.88	11.52	-2.28
233	19.271±0.141		18.346±0.173	27.4±1.2	0.72	11.75	-5.23
234	19.201±0.191	19.212±0.240	18.498±0.141	277±8.4	0.86	11.52	0.95
235			19.185±0.289	79.9±2.5	0.97	11.12	1.36
236	19.079±0.099	18.487±0.101	18.076±0.079	79.4±2.5	0.41	10.17	2.22
237	18.315±0.057		17.761±0.079	135±4.1	0.60	11.57	1.00
238	18.286±0.040		17.661±0.069	23.4±1.2	0.42	11.04	0.50
239	19.034±0.127	18.615±0.127	18.589±0.135	1050±31	0.51	11.35	1.59
240	18.382±0.075		17.637±0.093	27.7±1.2	0.56	11.66	0.08
241	19.382±0.108		18.714±0.163	80.7±2.5	1.22	12.18	1.61
242	18.728±0.081		18.125±0.125	112±3.5	0.65	11.51	0.94
243	18.328±0.038		17.983±0.105	42.7±1.5	0.12	9.77	-0.31
244	17.174±0.051	16.450±0.032	17.198±0.114	30.6±1.4	0.28	11.34	1.26
245	18.118±0.082	17.635±0.090	17.741±0.077	124±3.8	0.49	11.31	0.78
246	18.053±0.030	17.919±0.044	17.584±0.049	260±7.8	0.04	9.02	-0.53
247	18.372±0.073		17.795±0.095	157±4.7	0.53	11.57	-2.23
248	18.328±0.054	17.943±0.062	17.671±0.066	377±11	0.55	11.62	-2.19
249	16.713±0.014		16.493±0.026	190±5.8	0.32	11.64	1.56

Appendix B

Radio Galaxy Contour Plots

We present the contour plots constructed for the 249 radio galaxies in the new sample that is described in Chapter 4. The galaxies are given in the same sequence (left to right, top to bottom) as Appendix A



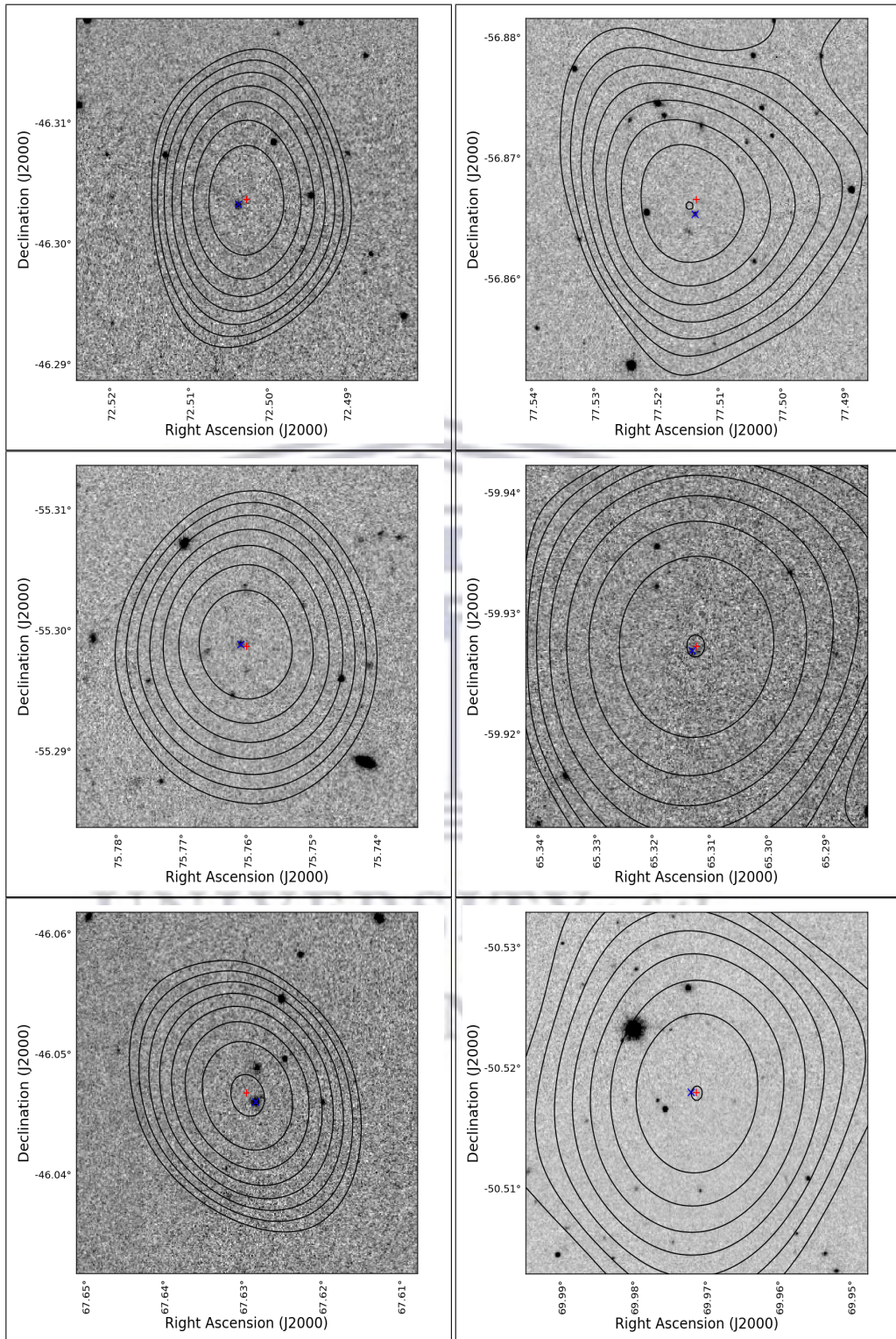


Figure B.1

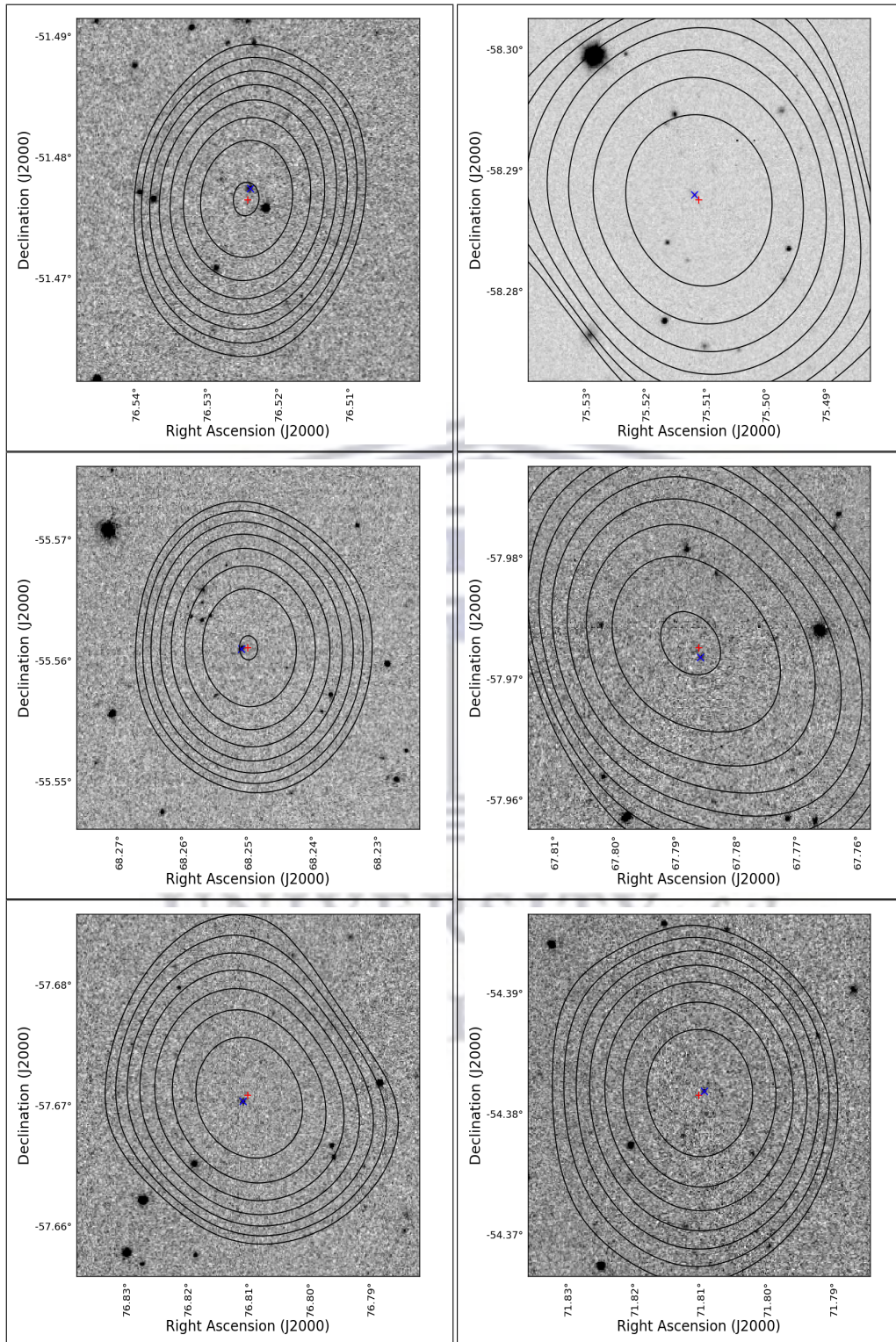


Figure B.2

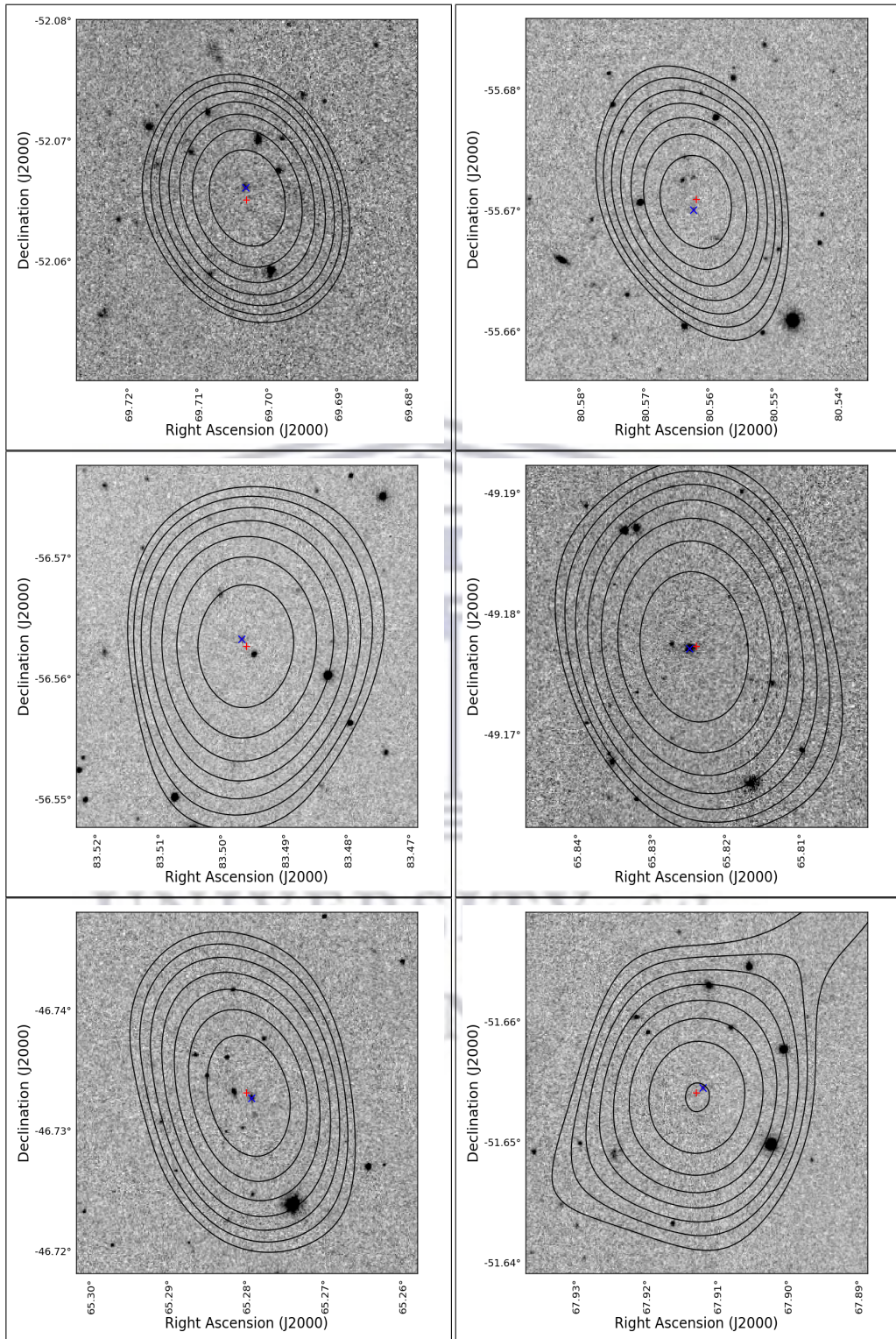


Figure B.3

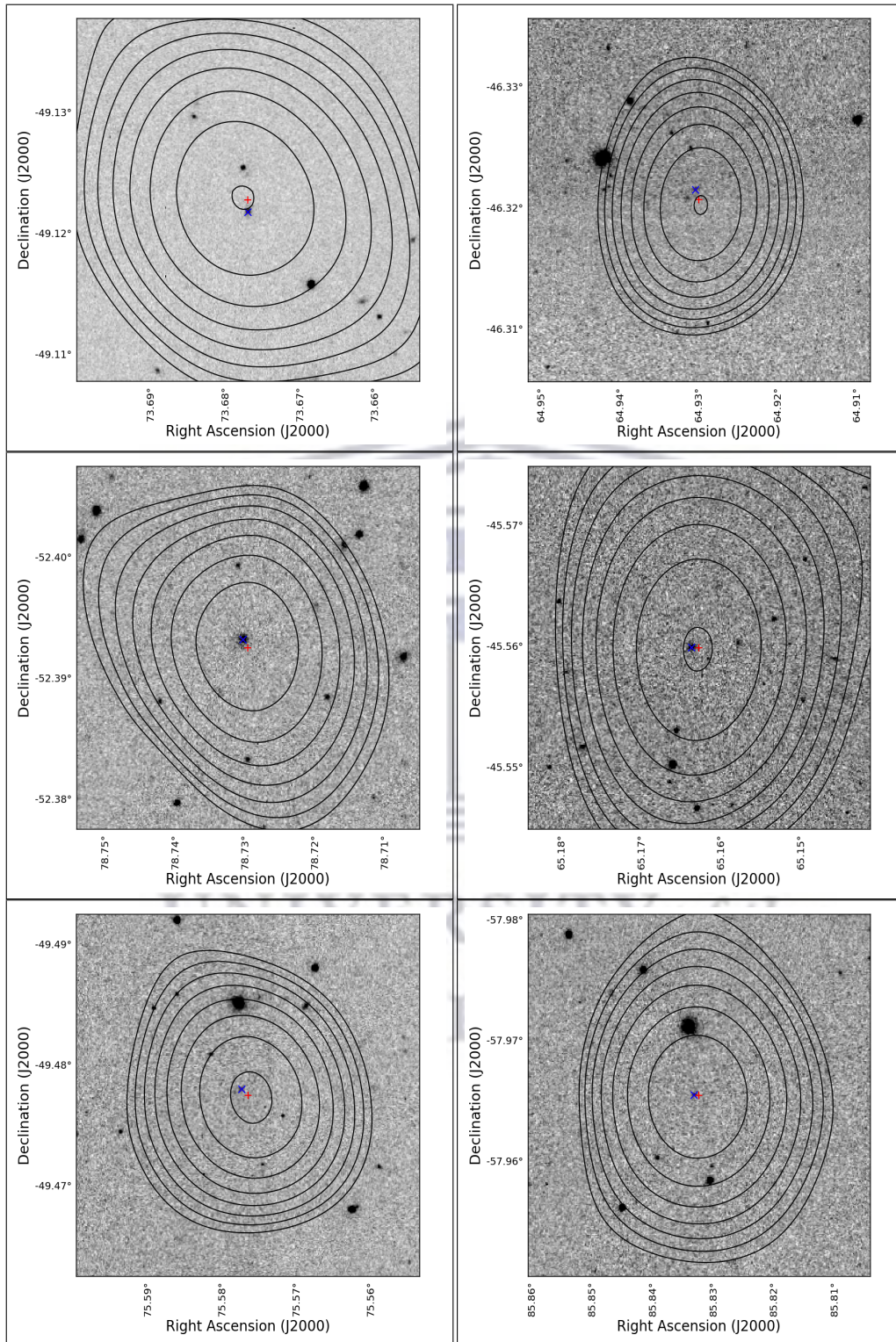


Figure B.4

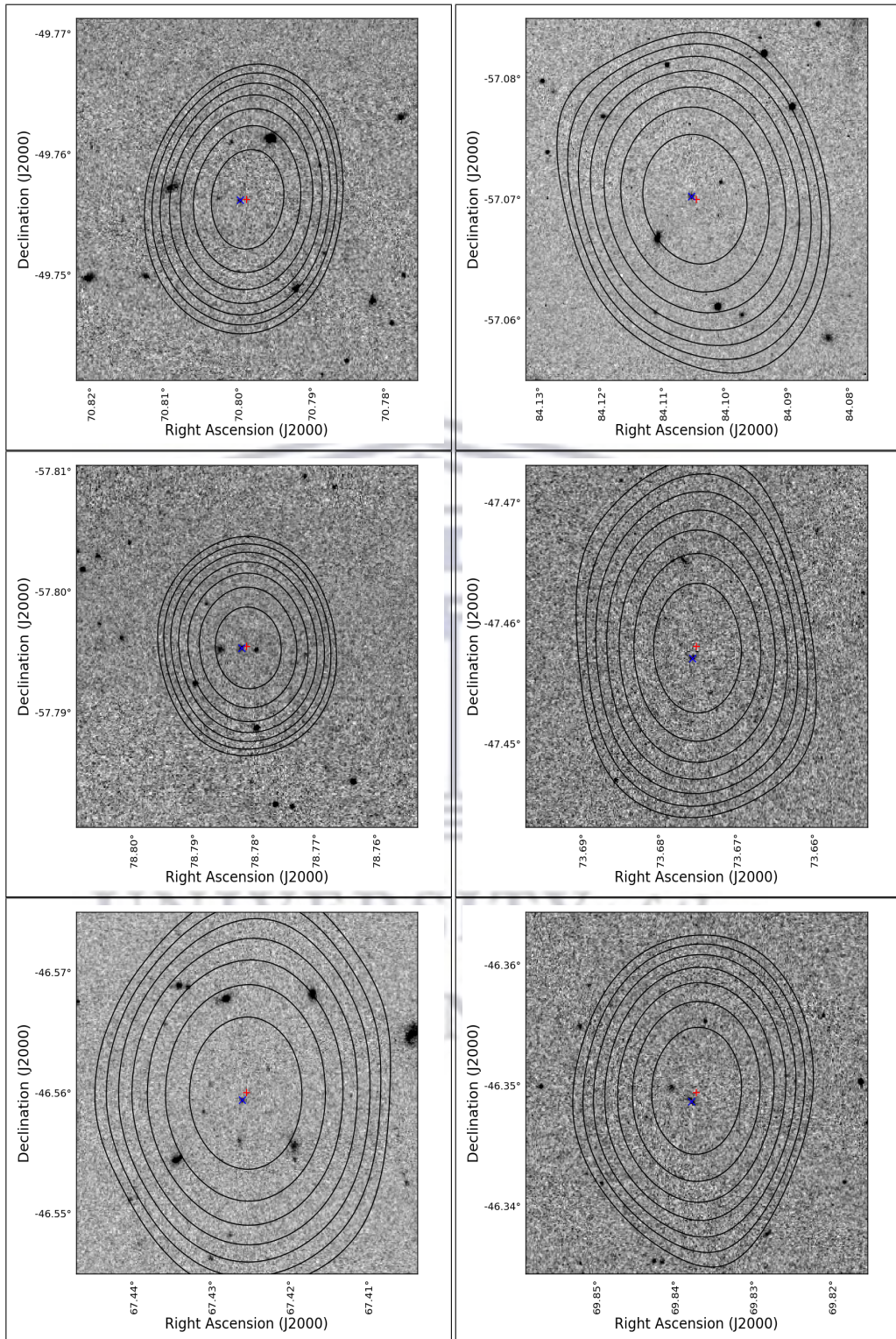


Figure B.5

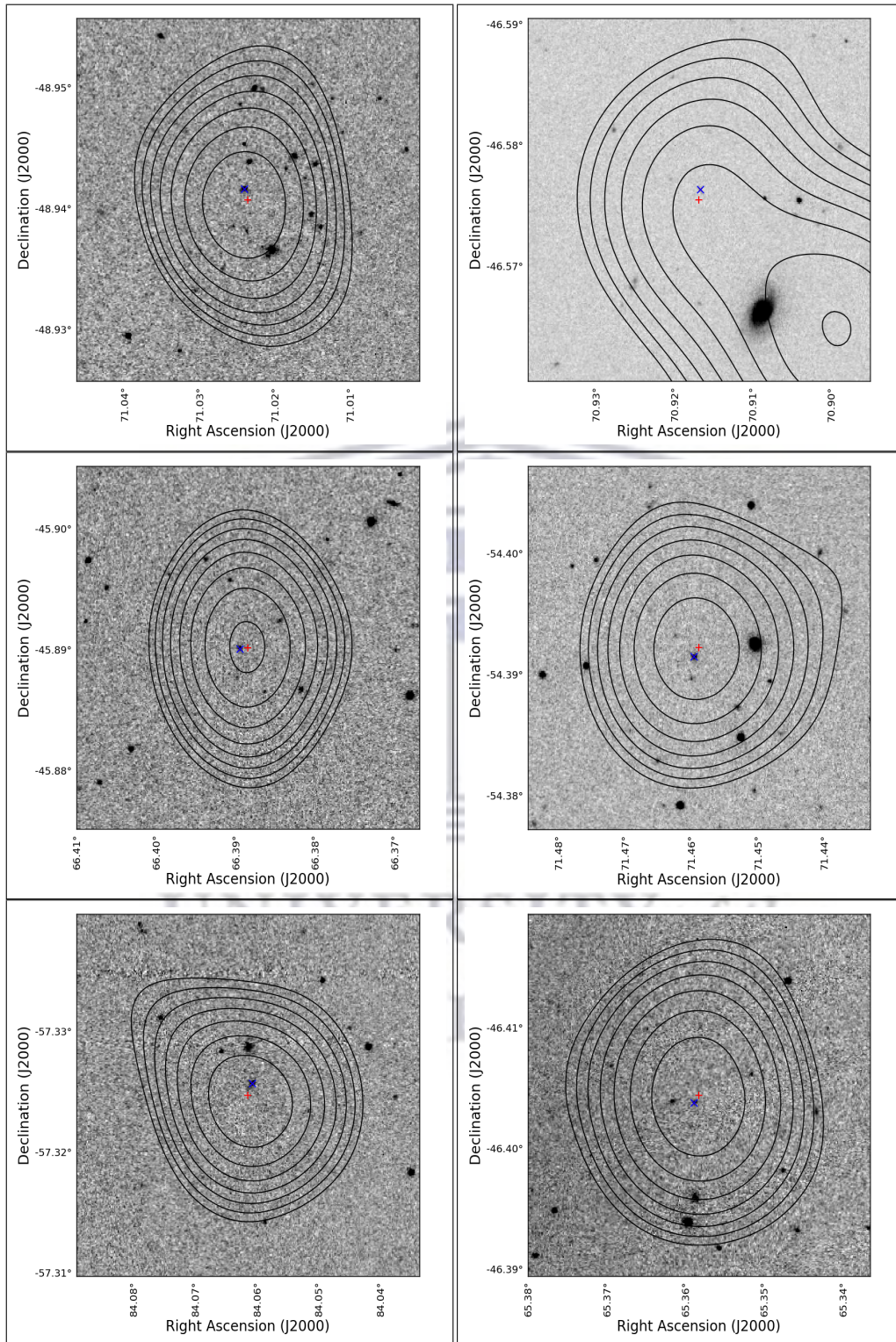


Figure B.6

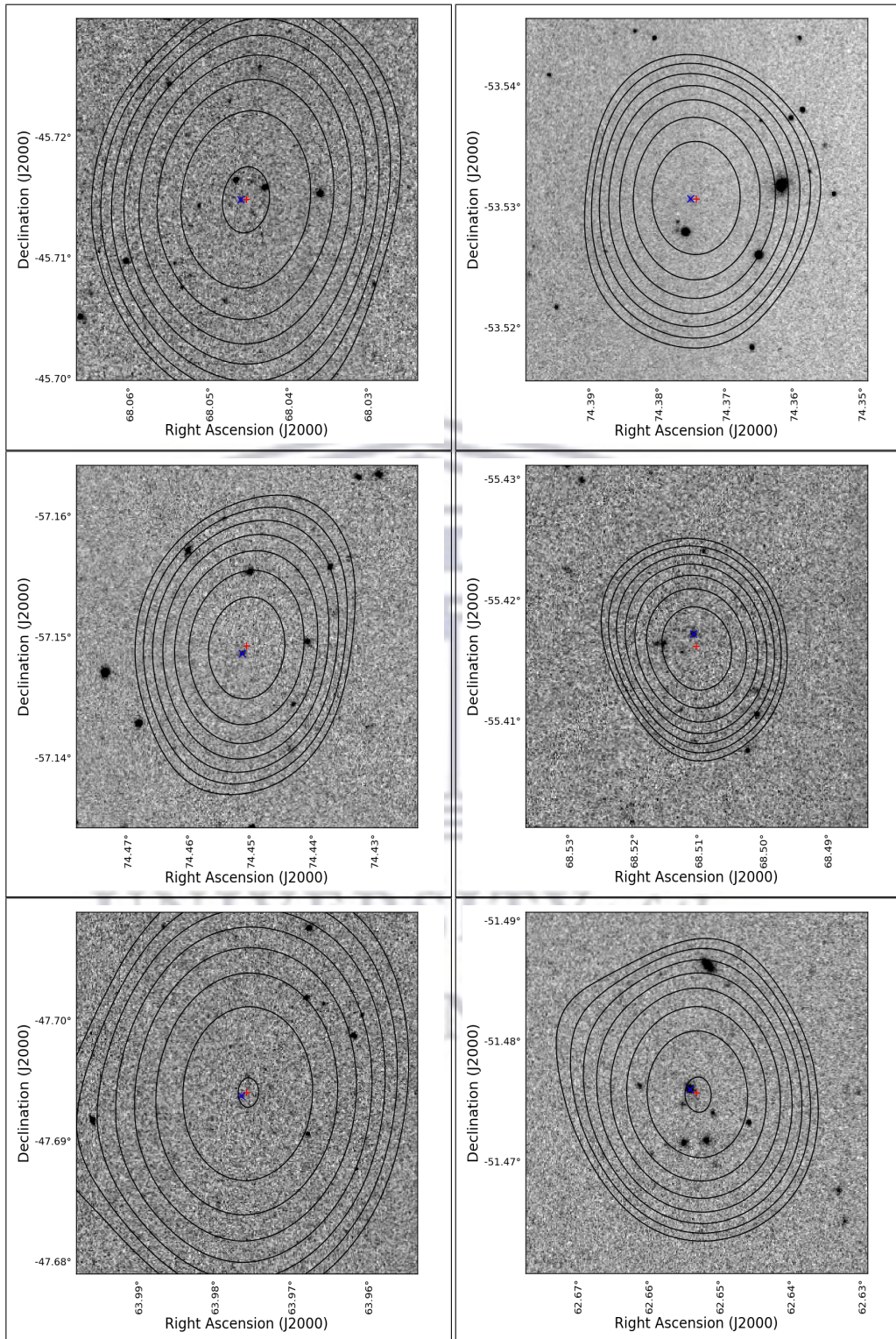


Figure B.7

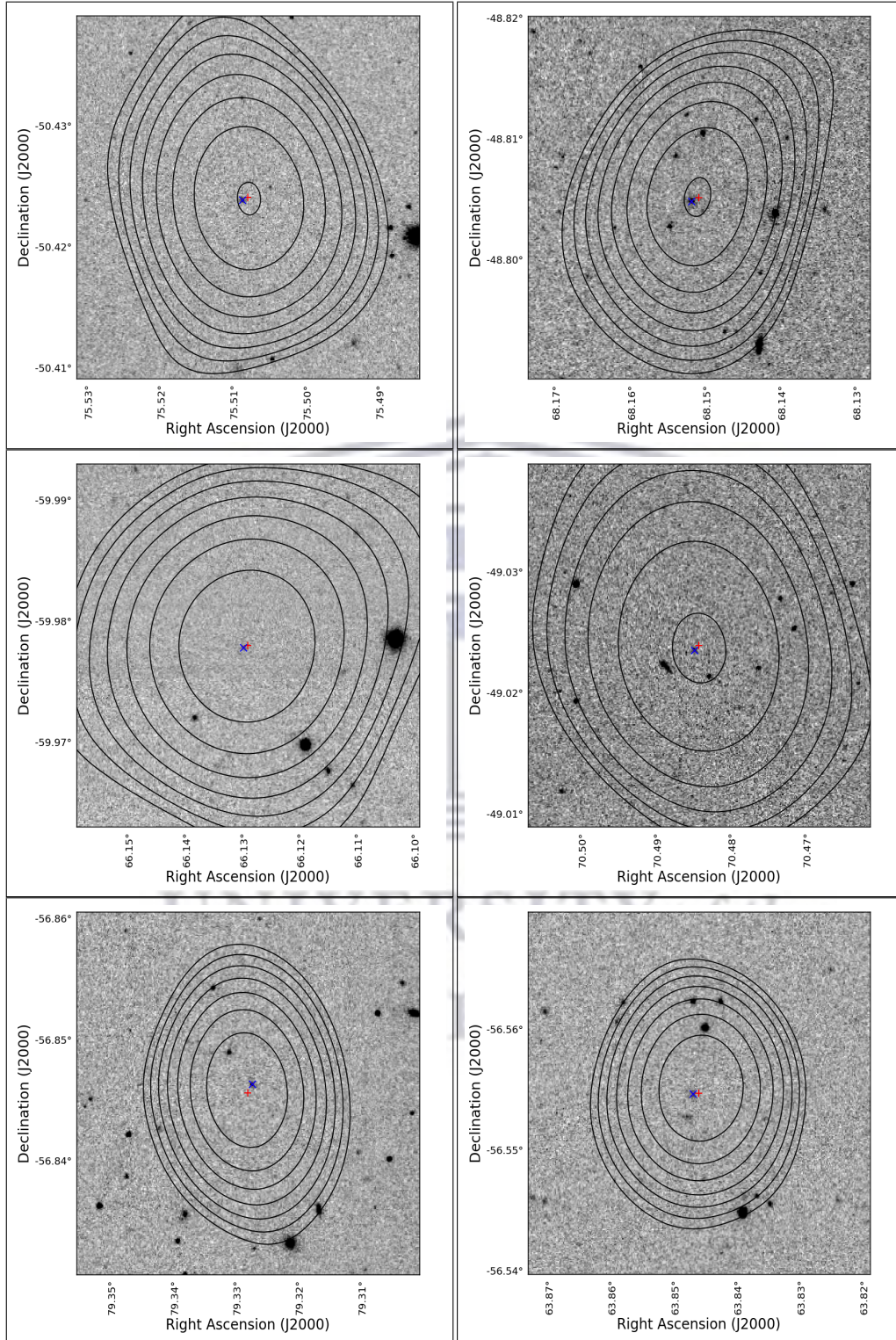


Figure B.8

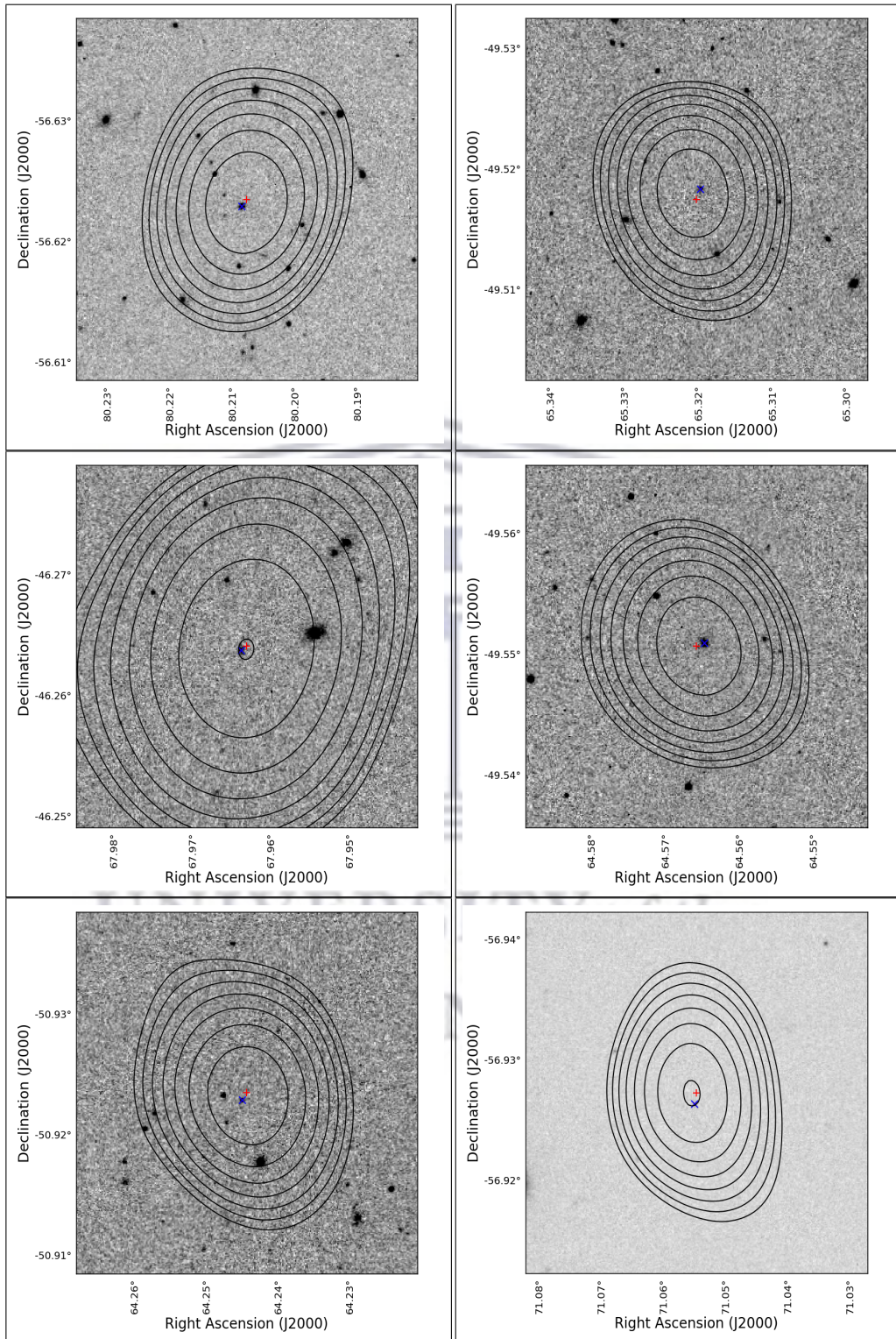


Figure B.9

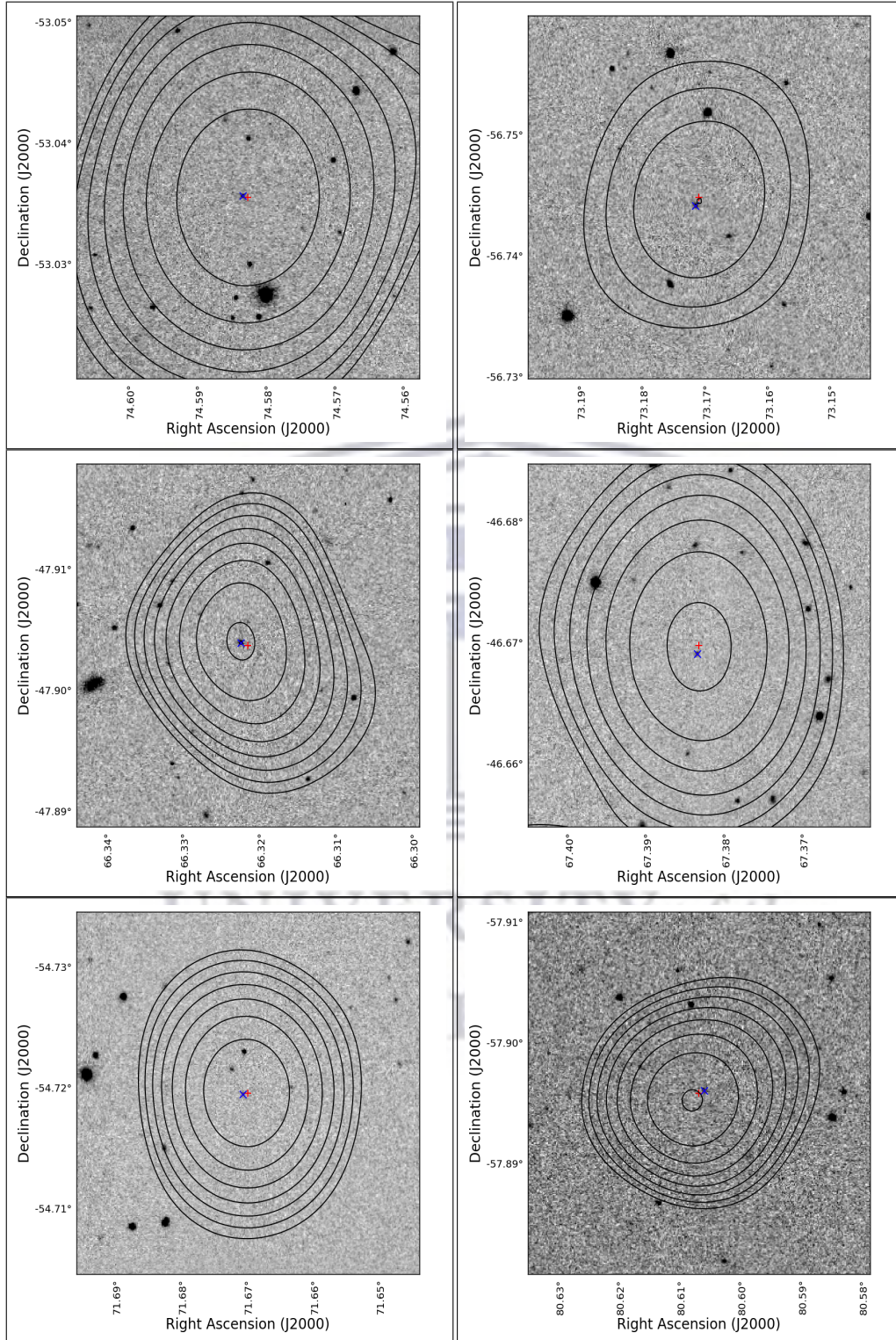


Figure B.10

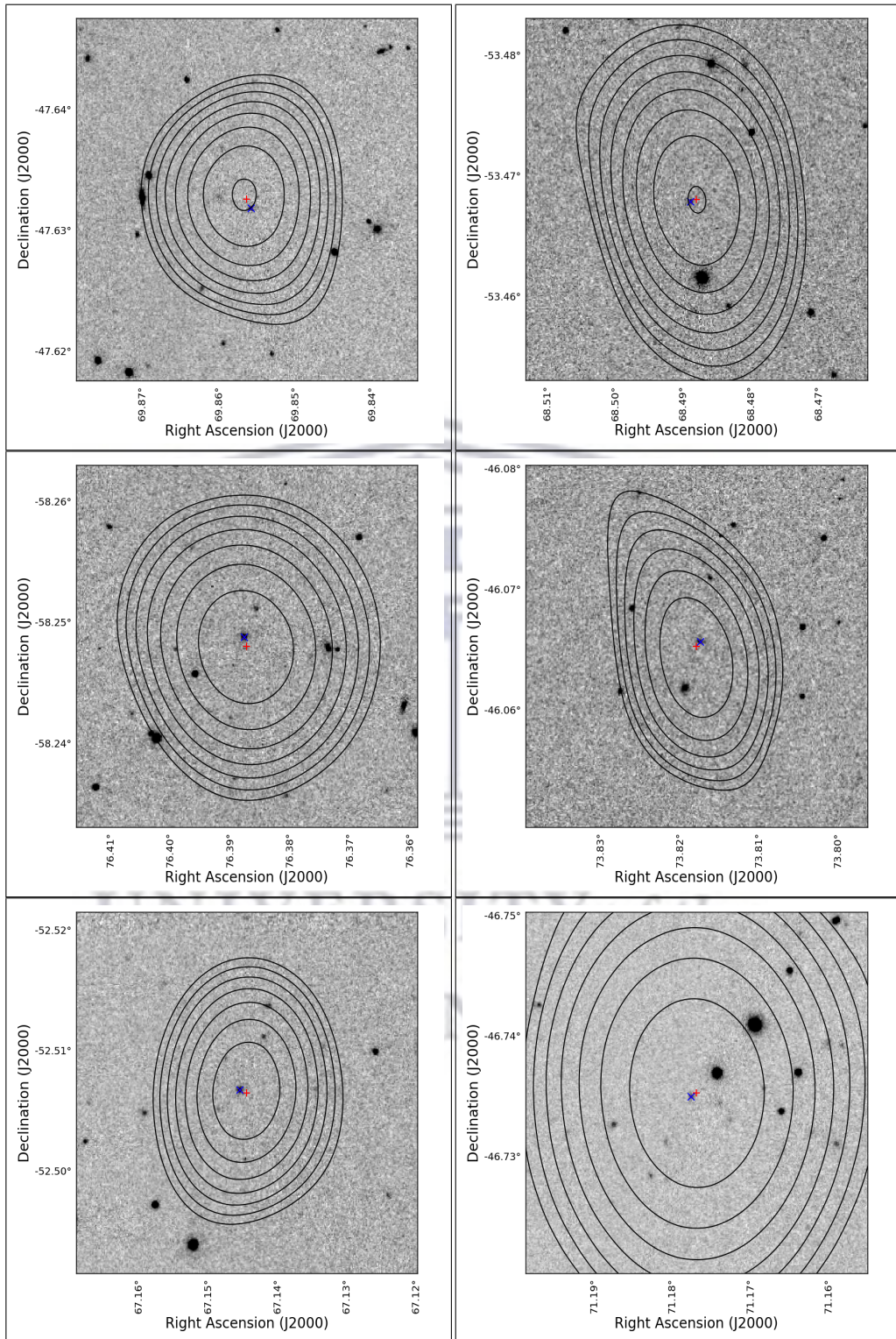


Figure B.11

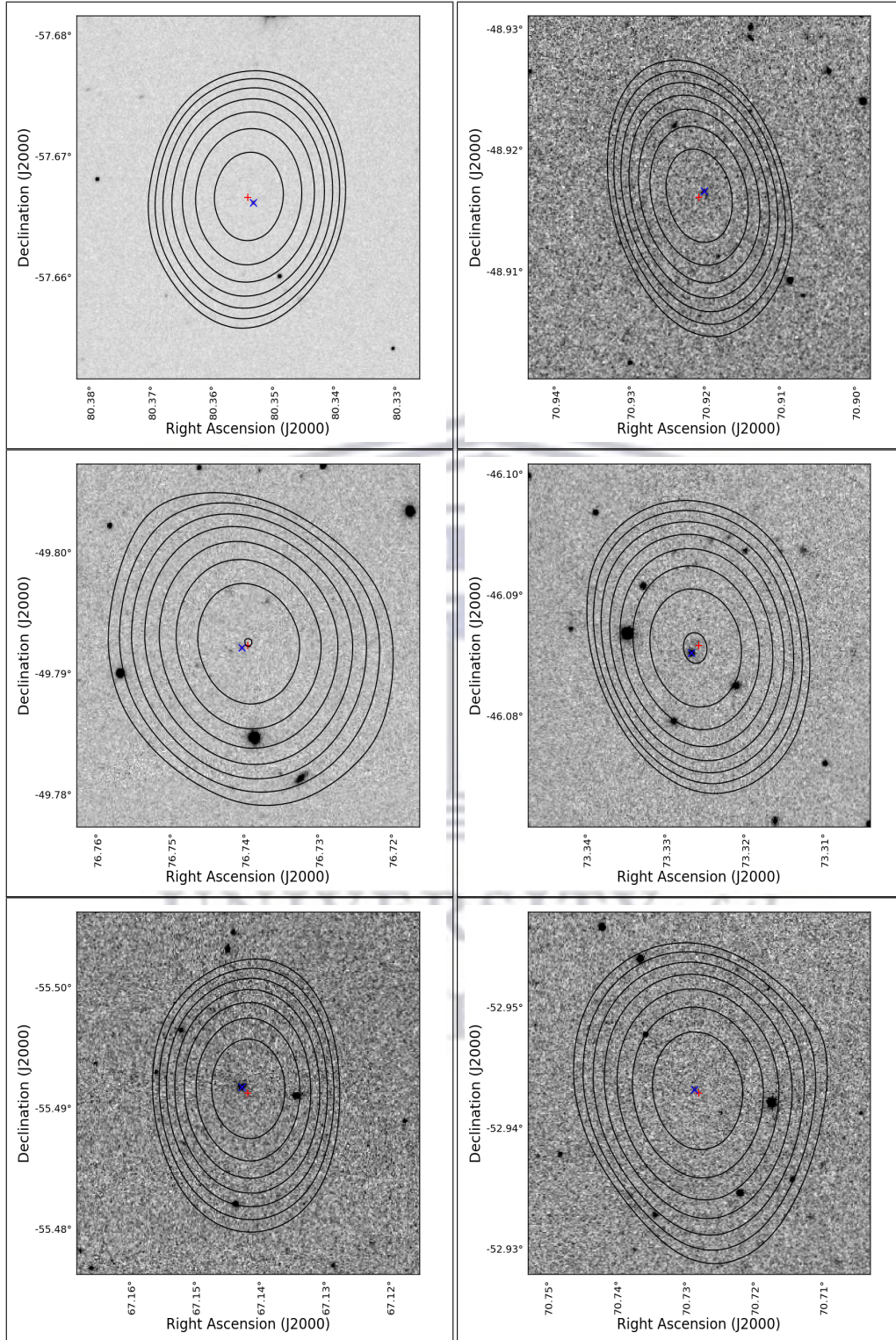


Figure B.12

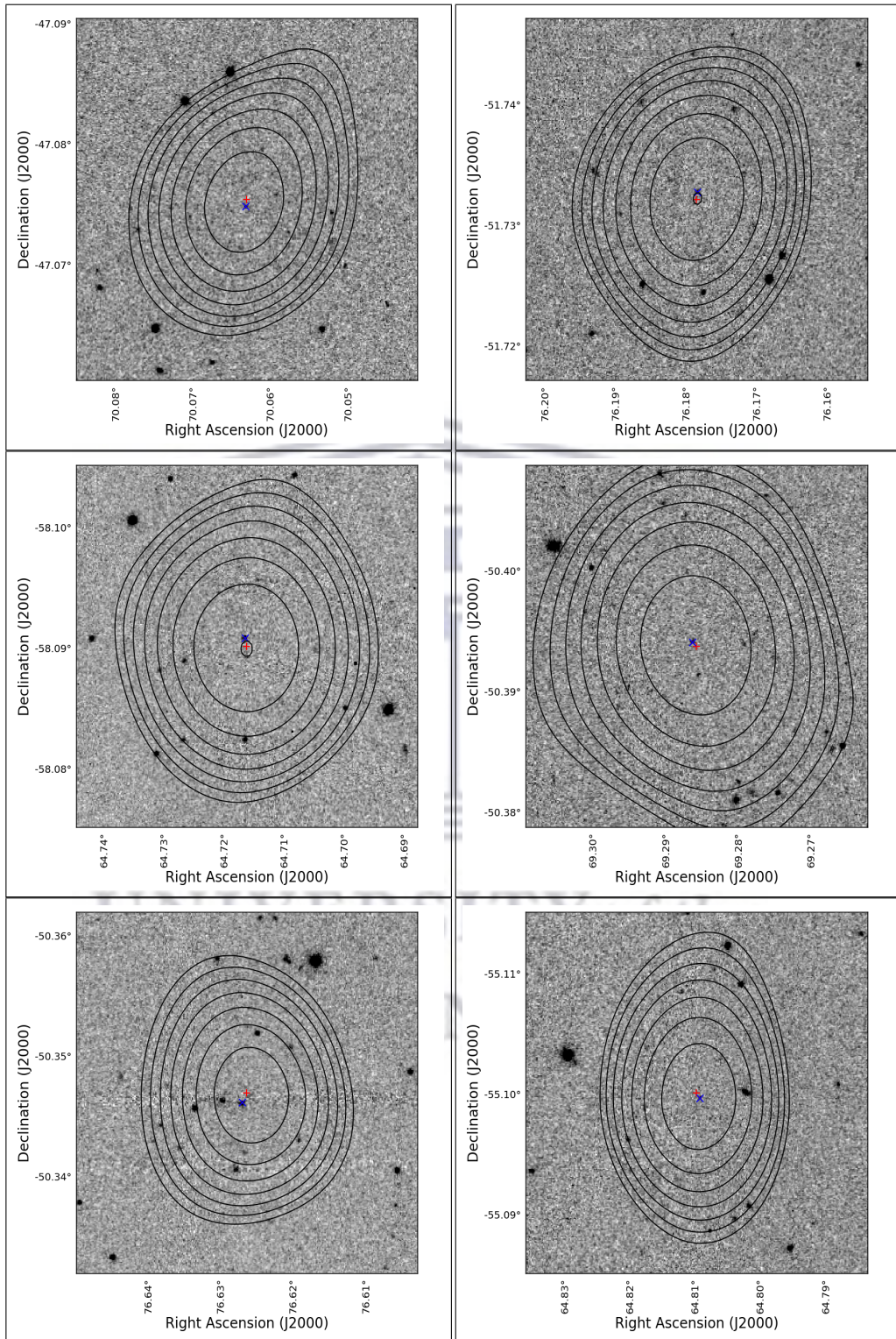


Figure B.13

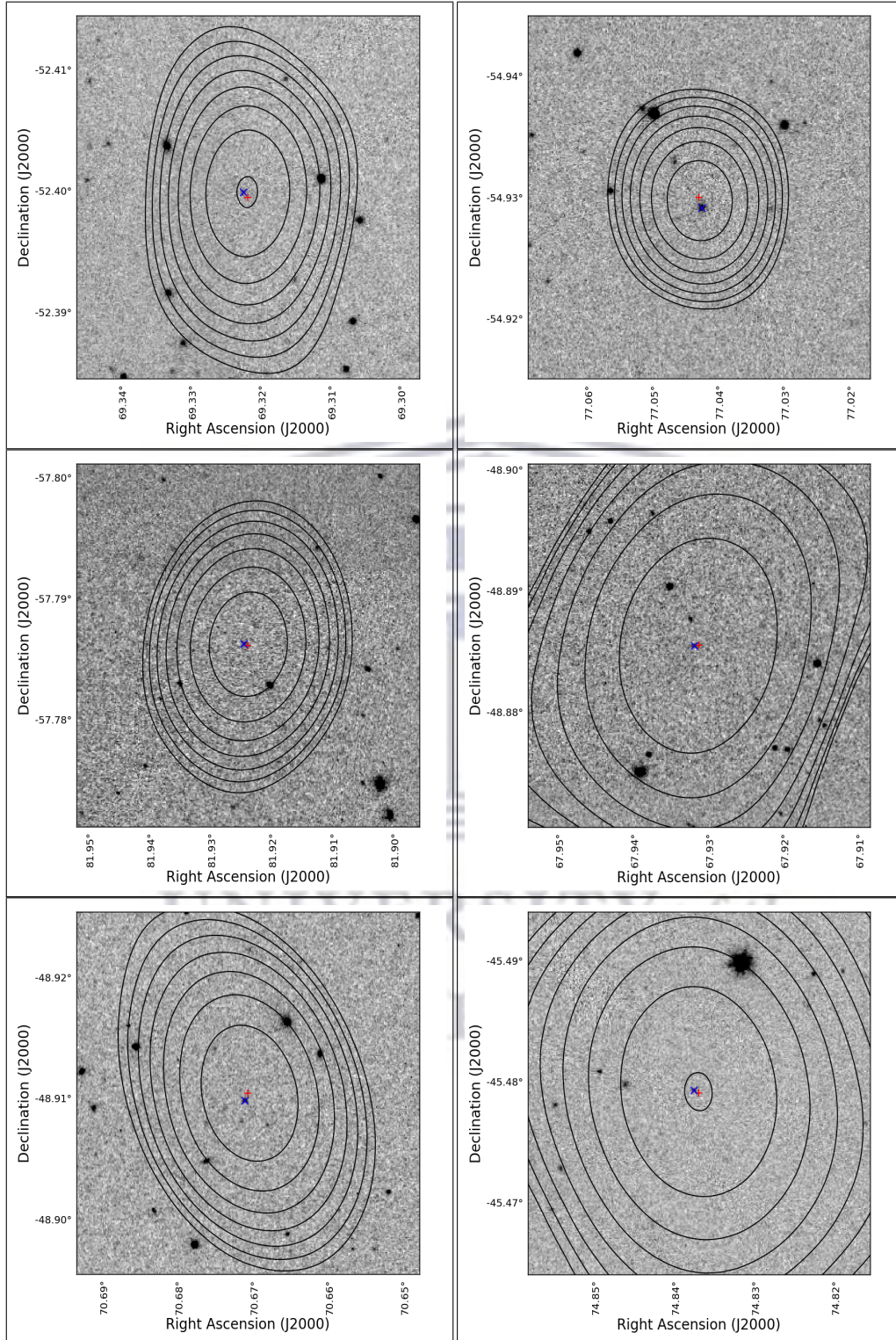


Figure B.14

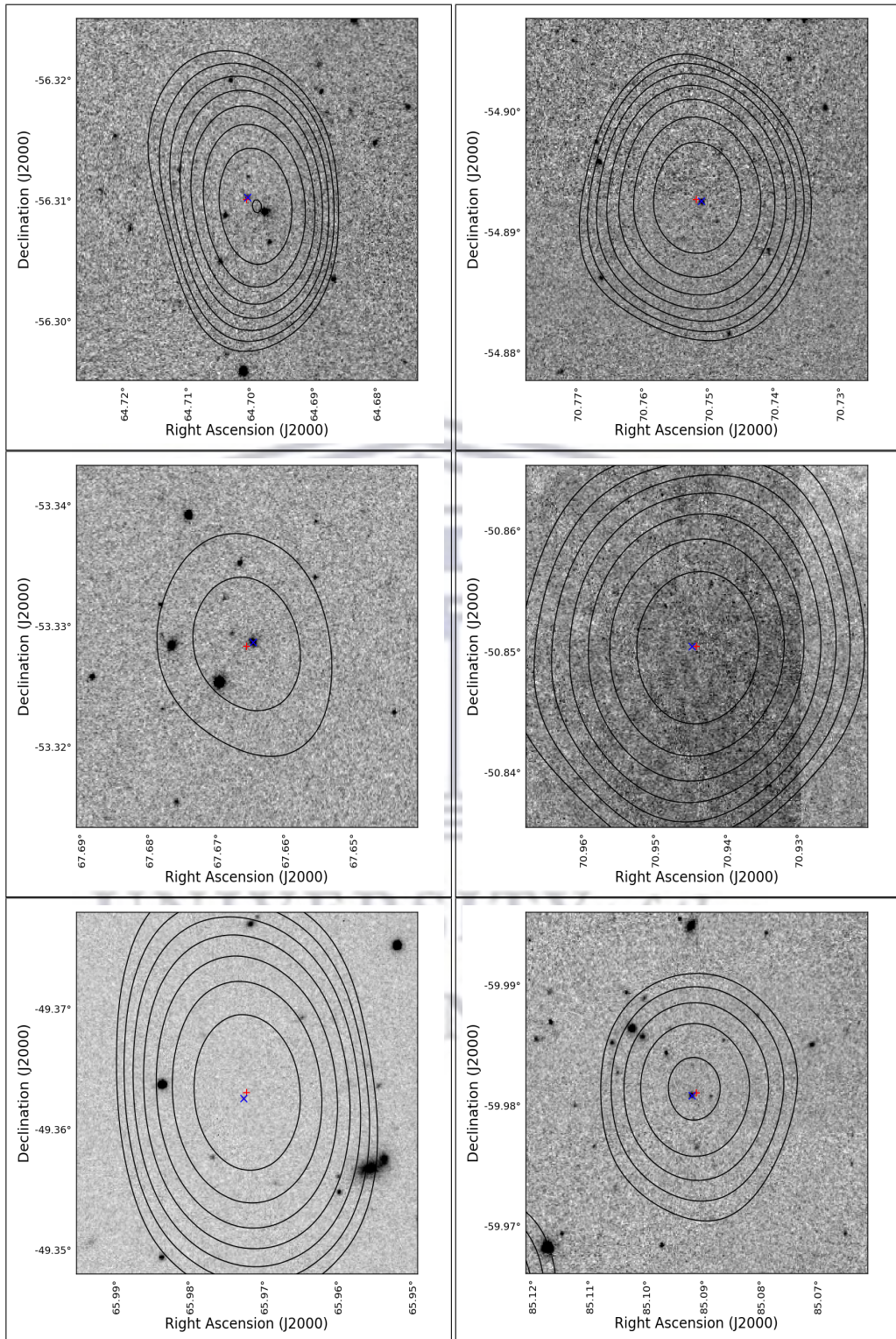


Figure B.15

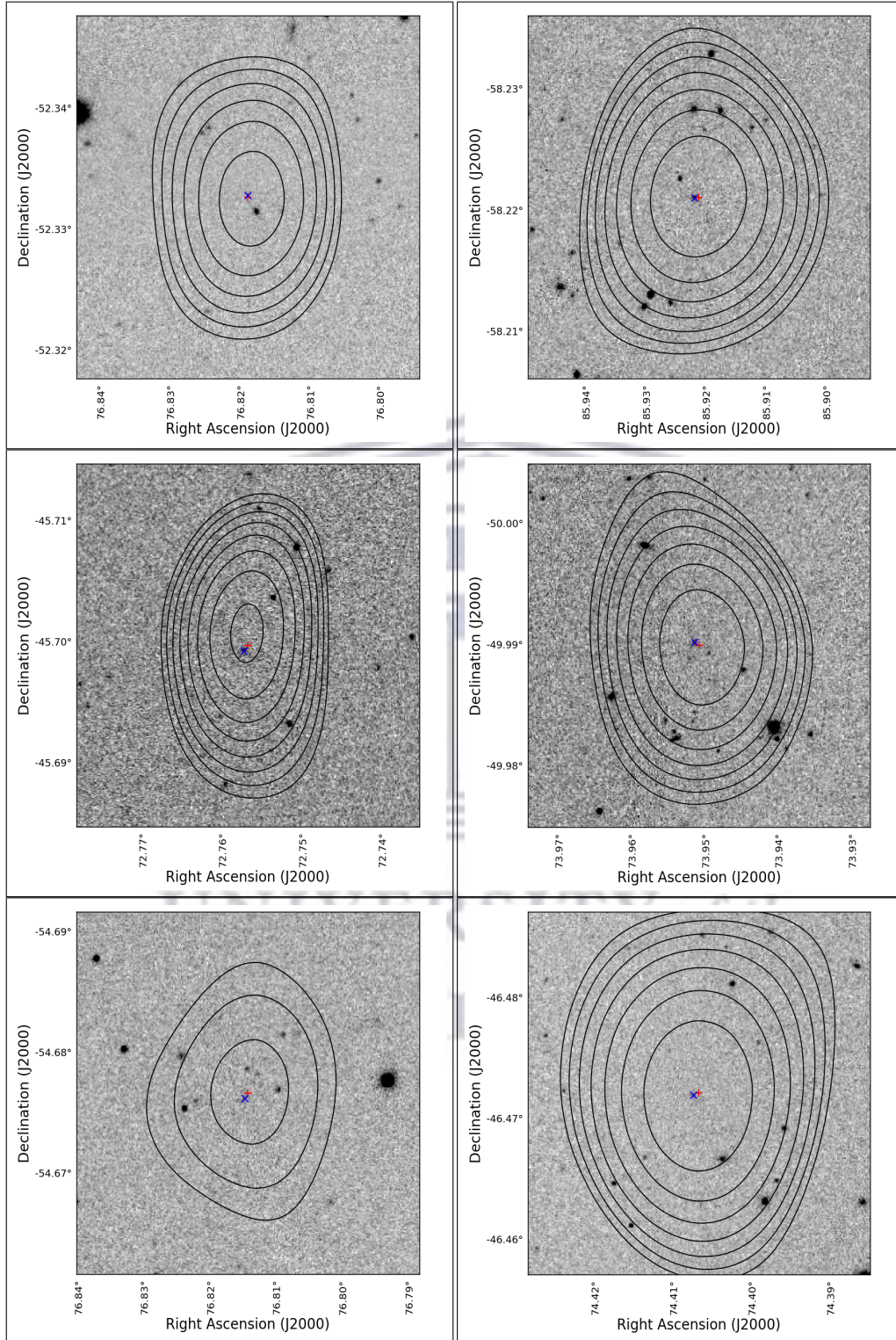


Figure B.16

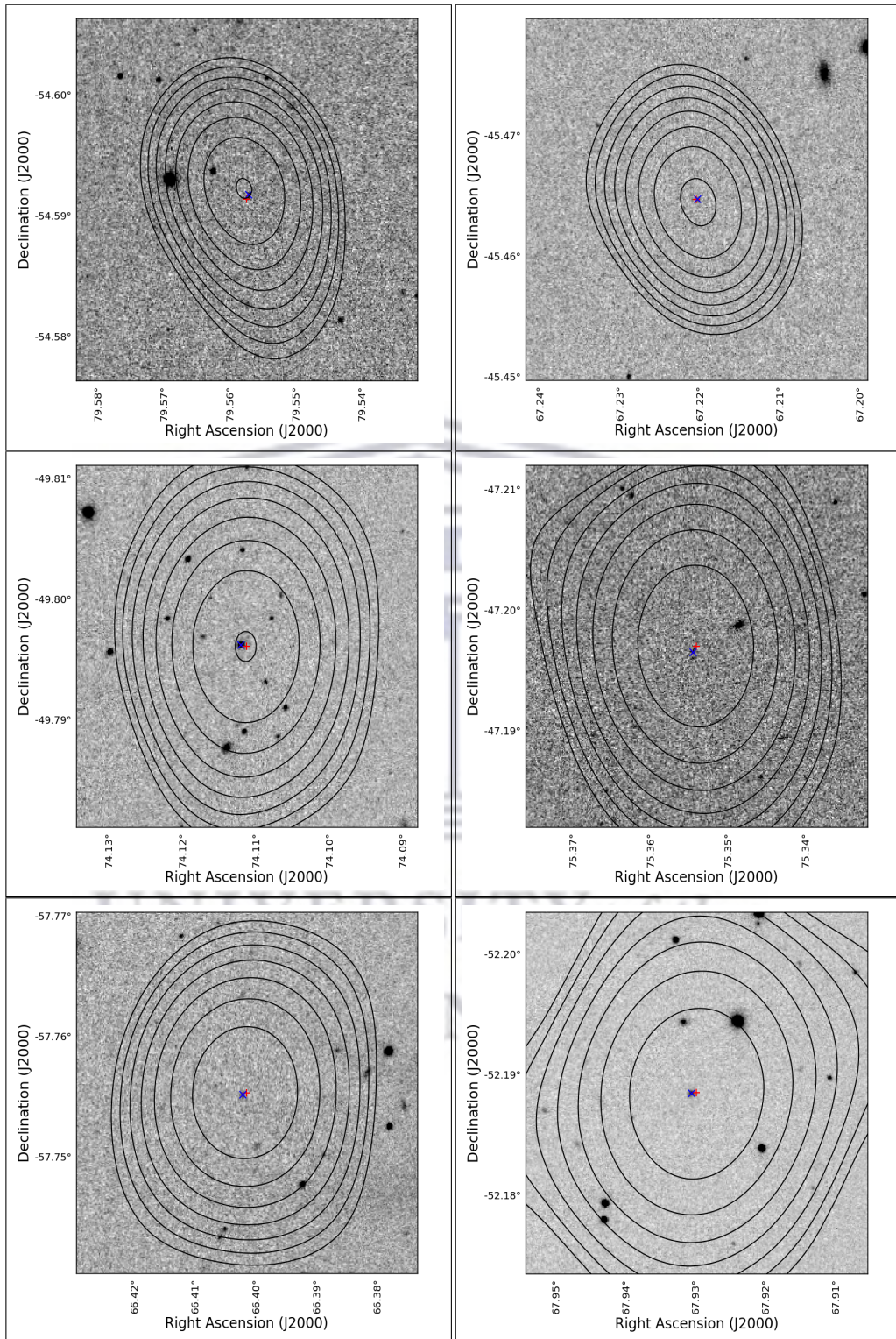


Figure B.17

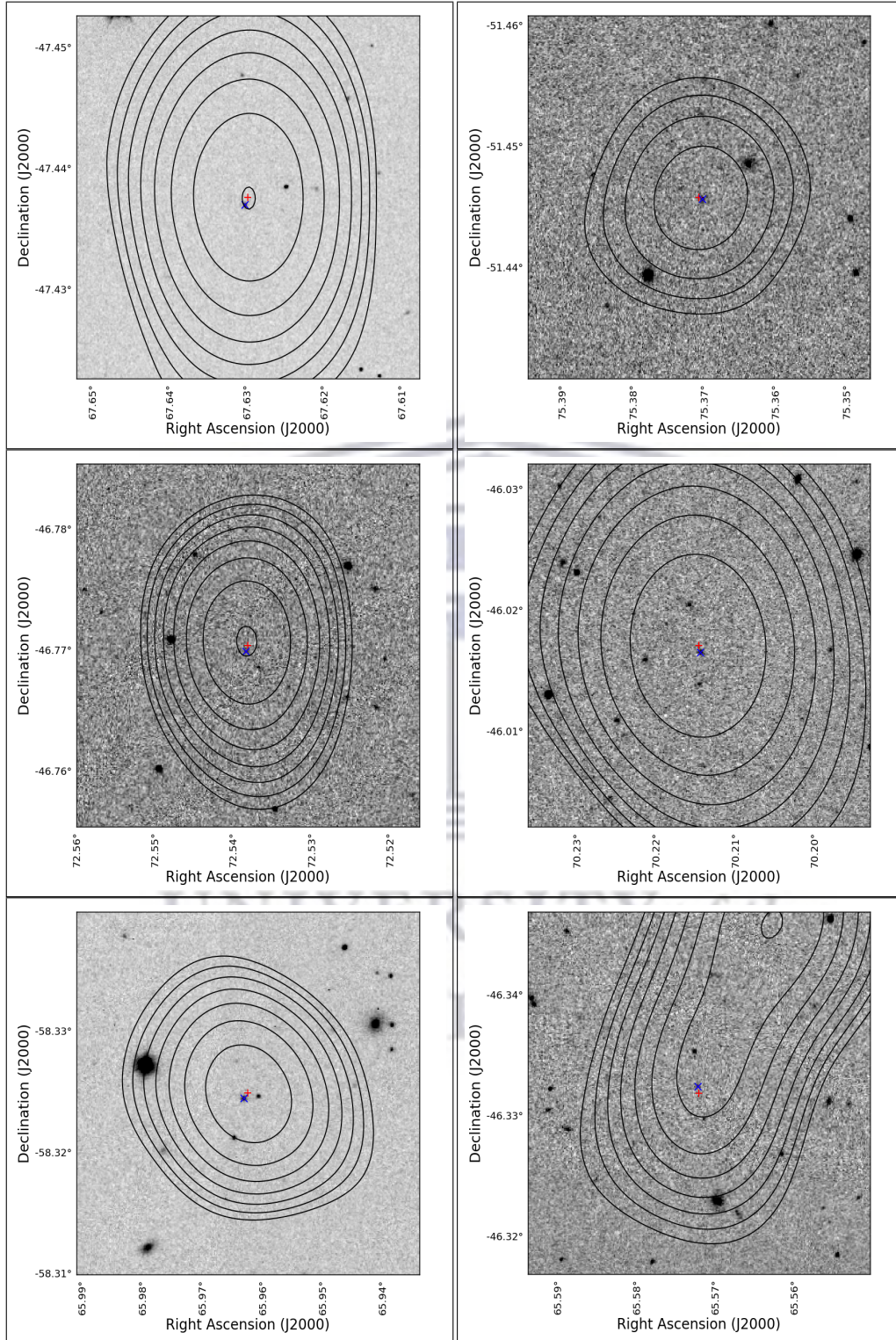


Figure B.18

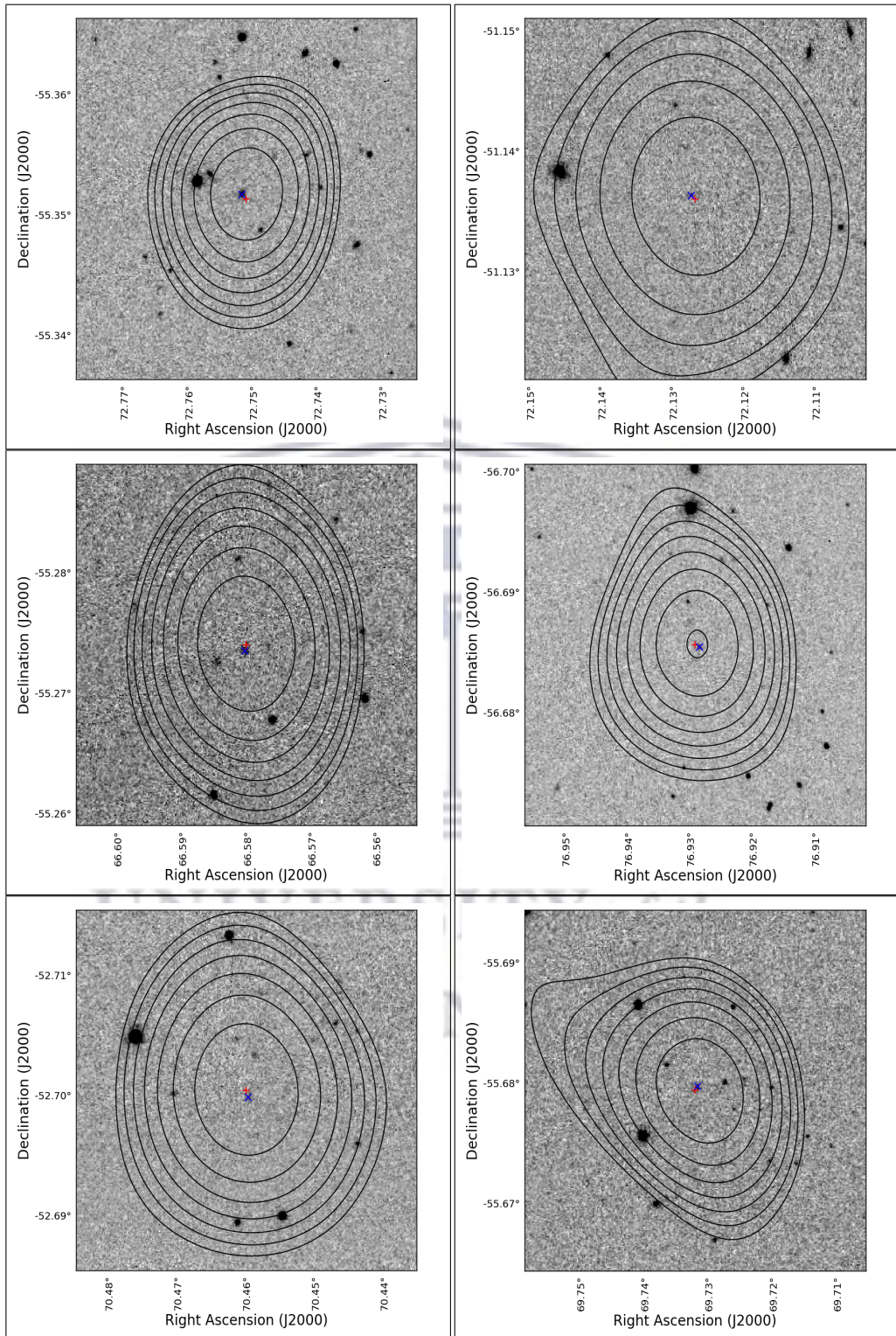


Figure B.19

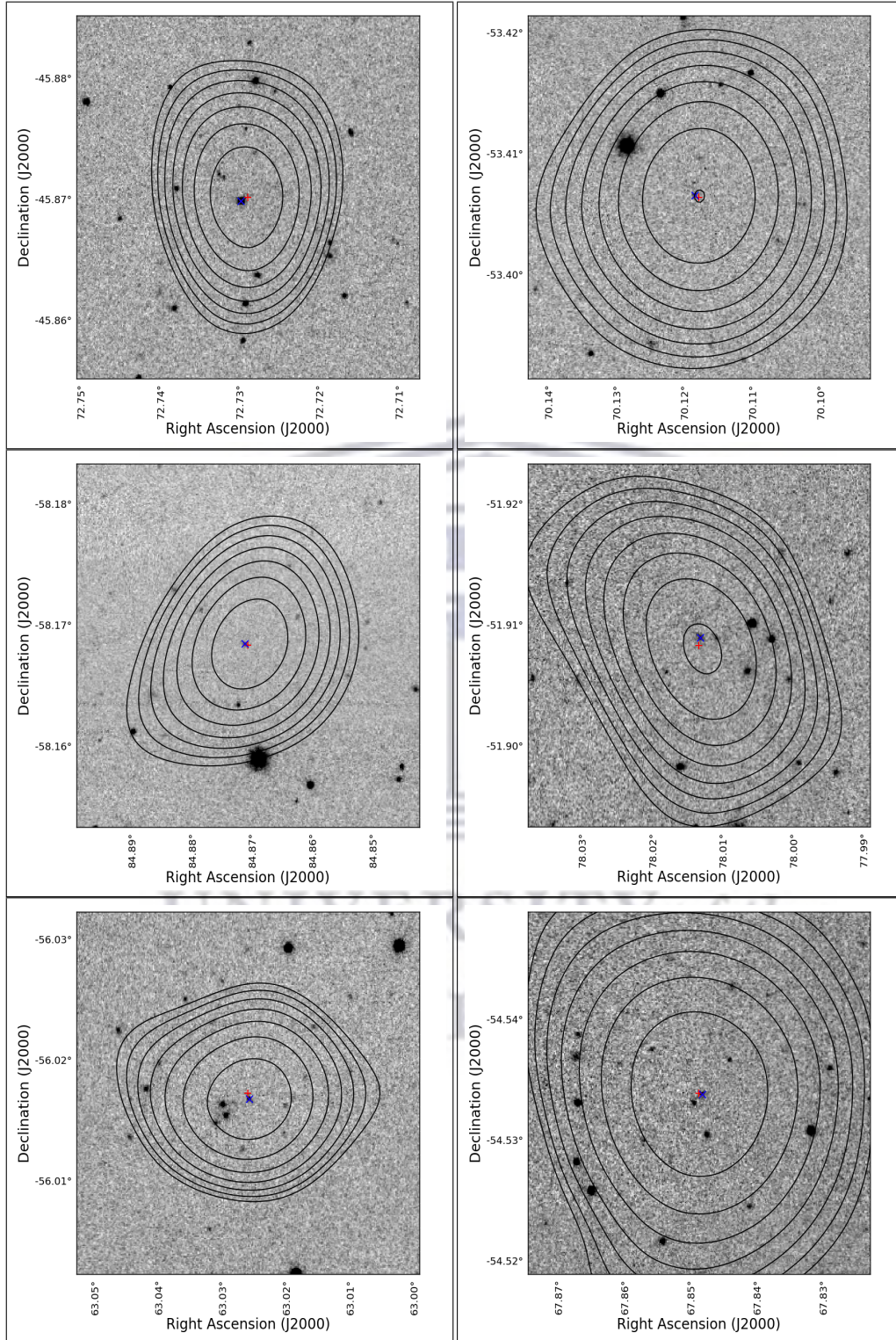


Figure B.20

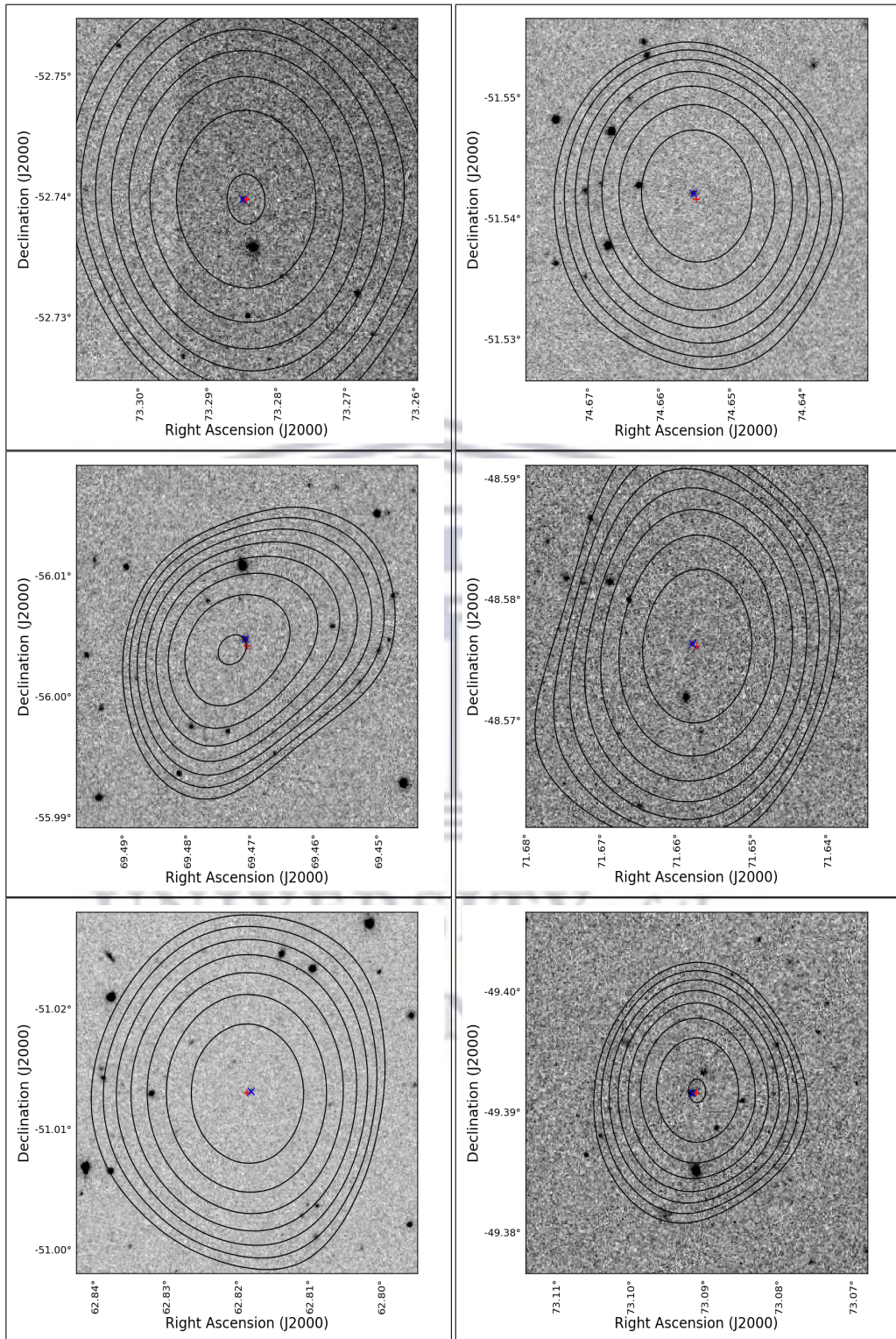


Figure B.21

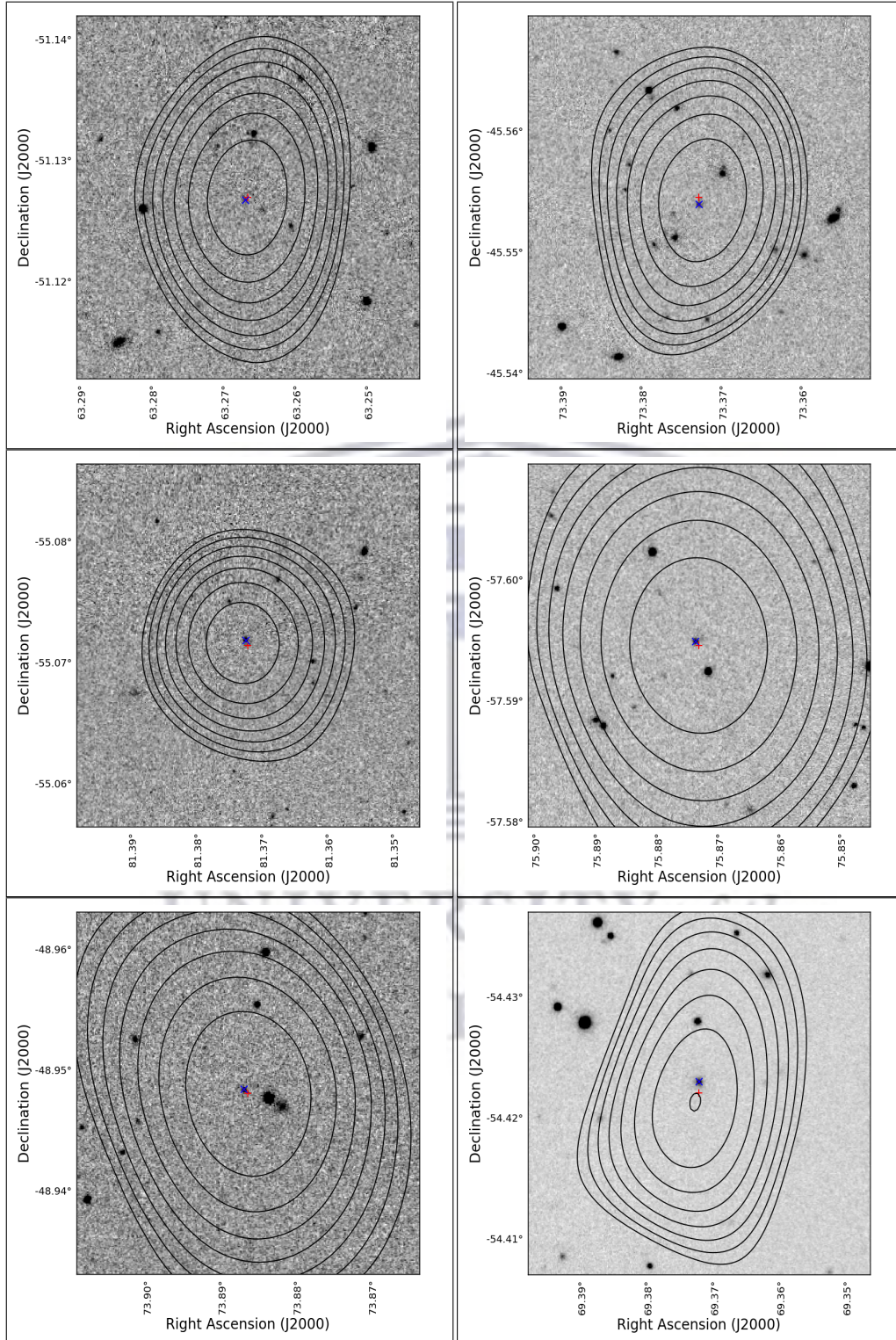


Figure B.22

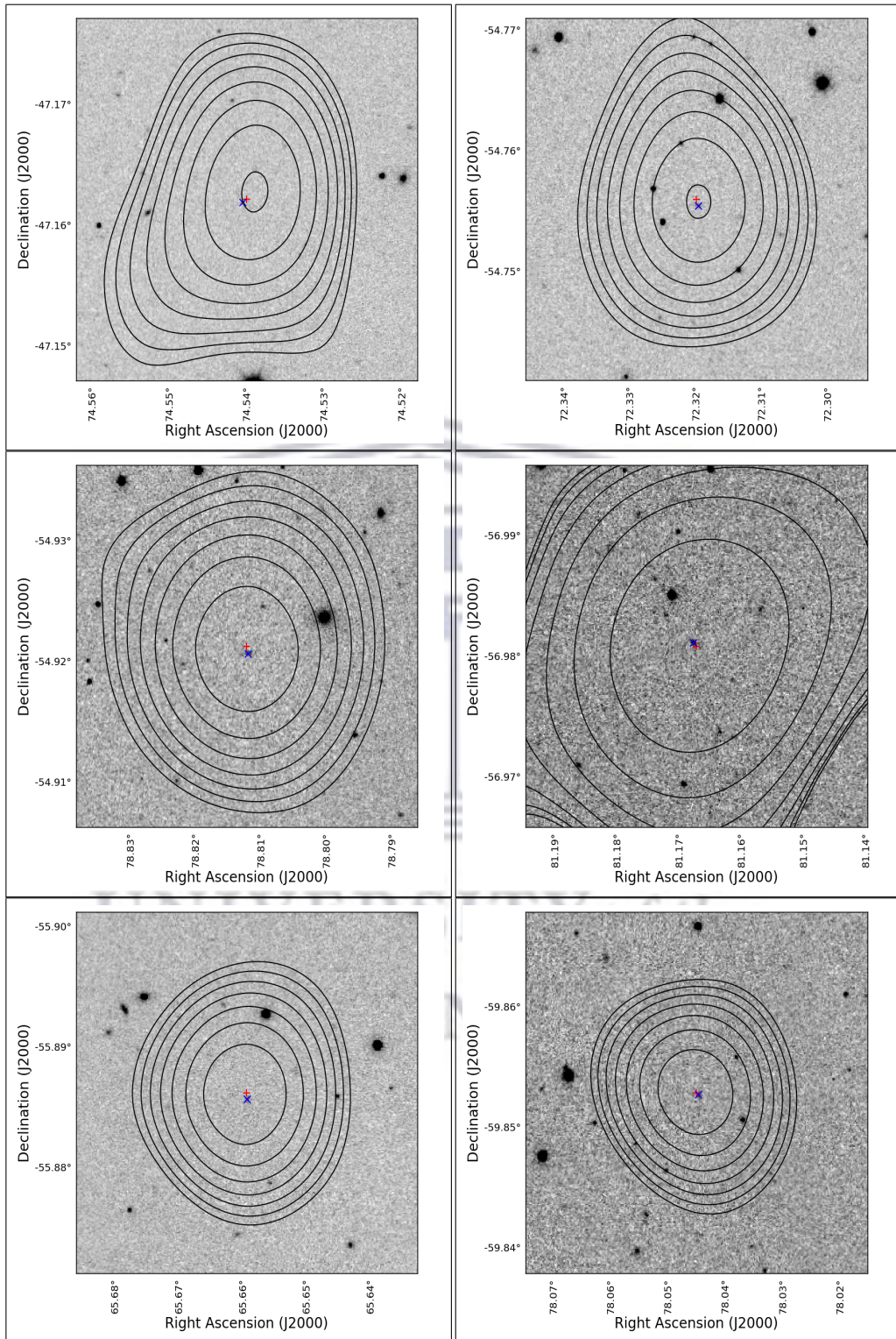


Figure B.23

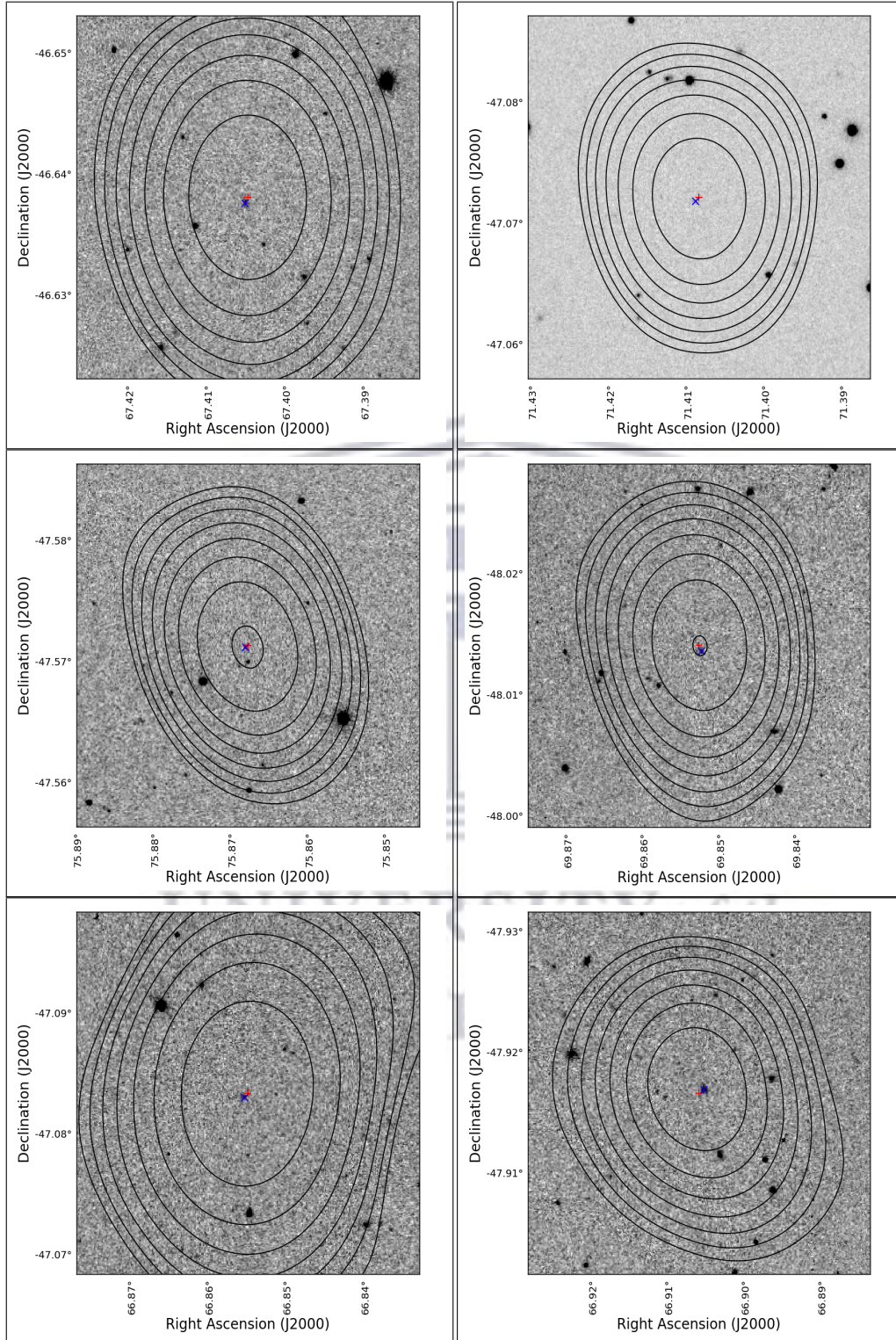


Figure B.24

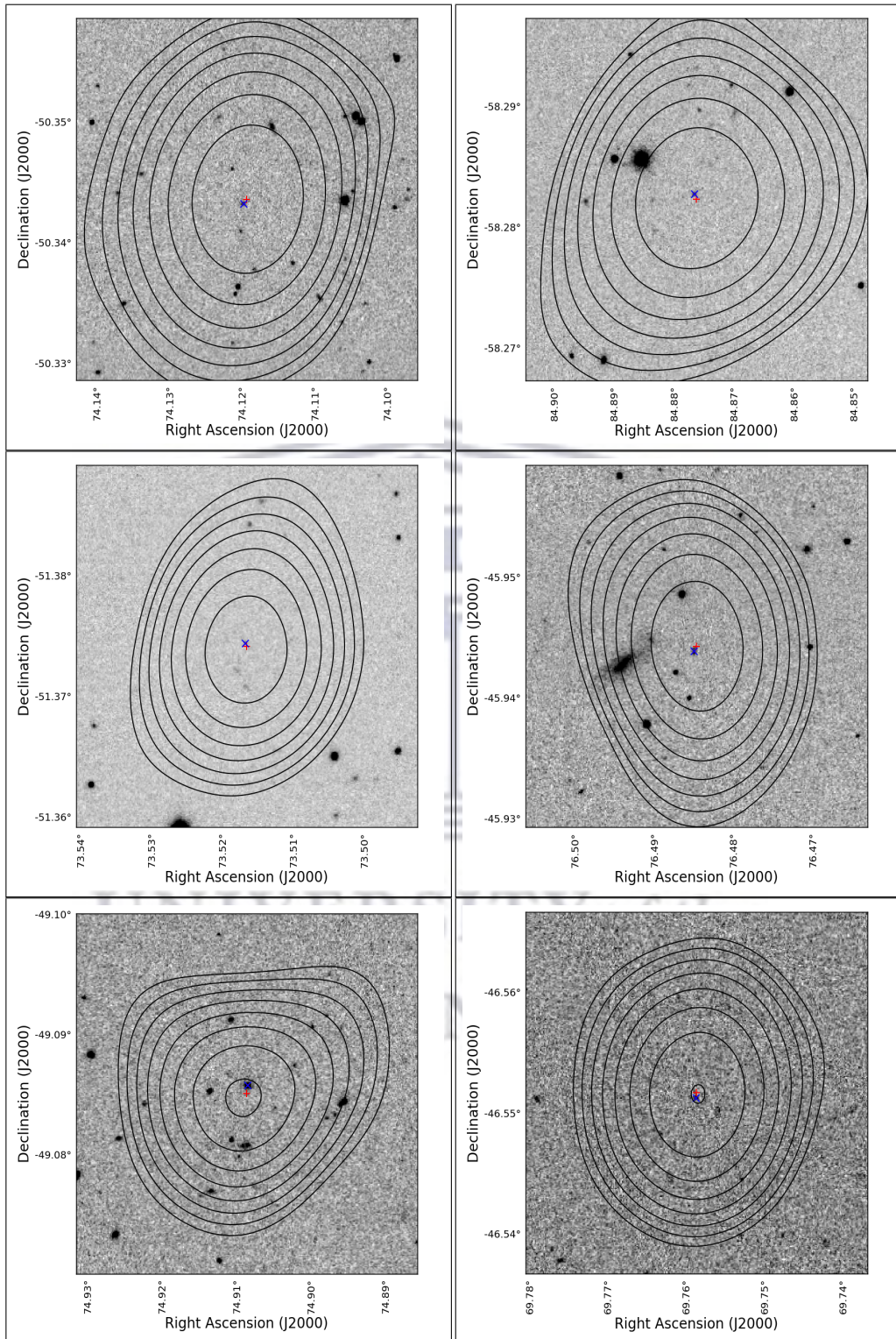


Figure B.25

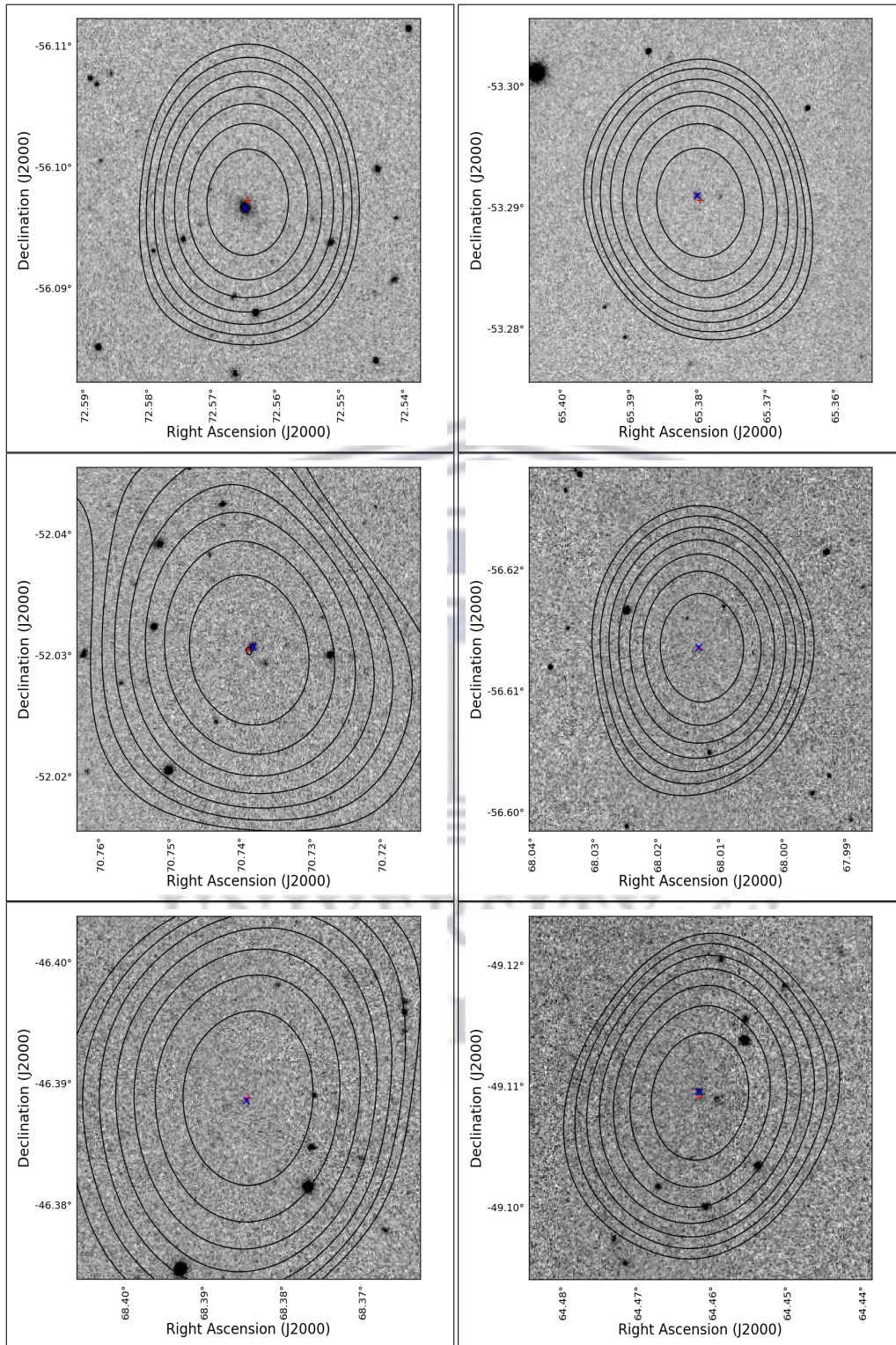


Figure B.26

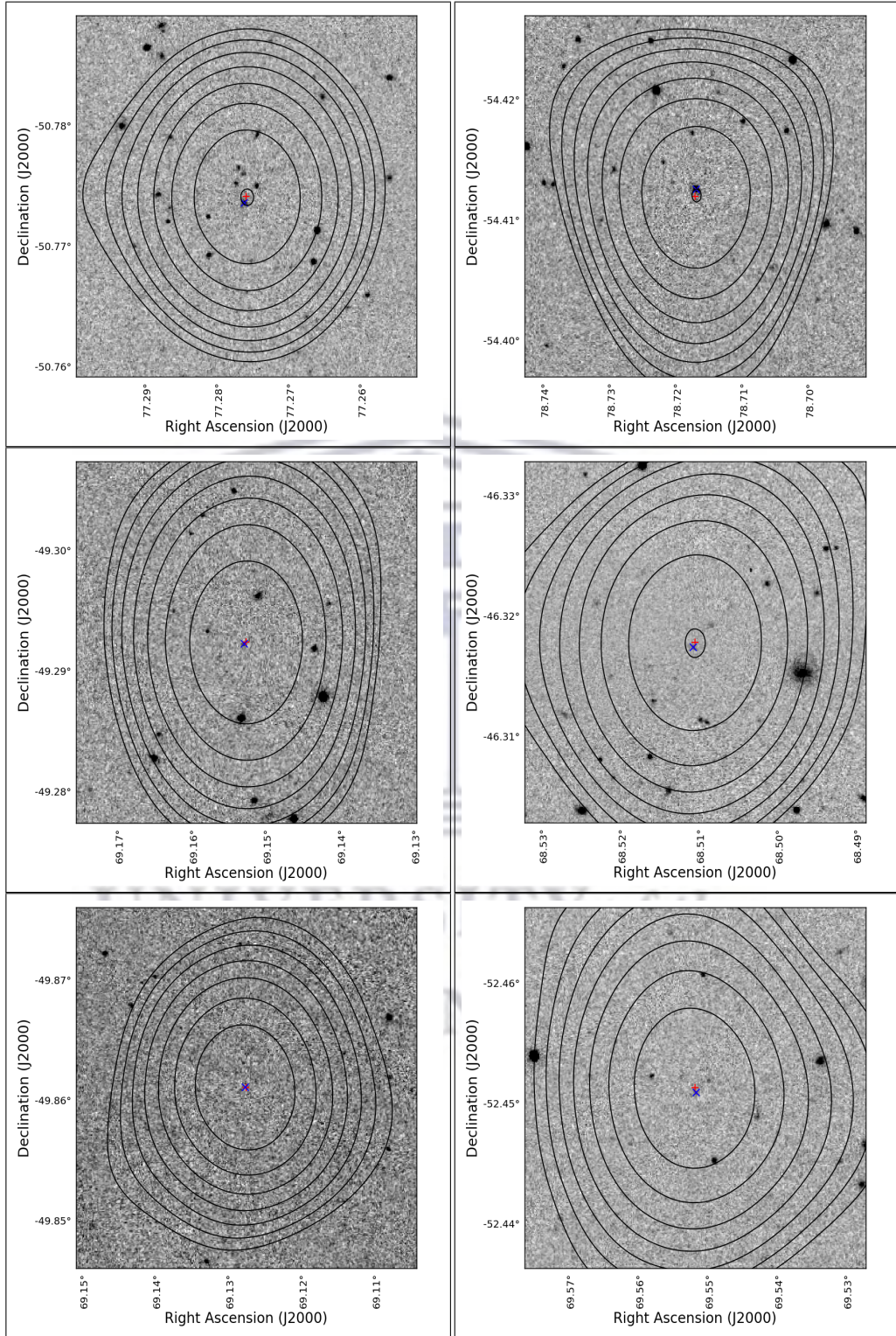


Figure B.27

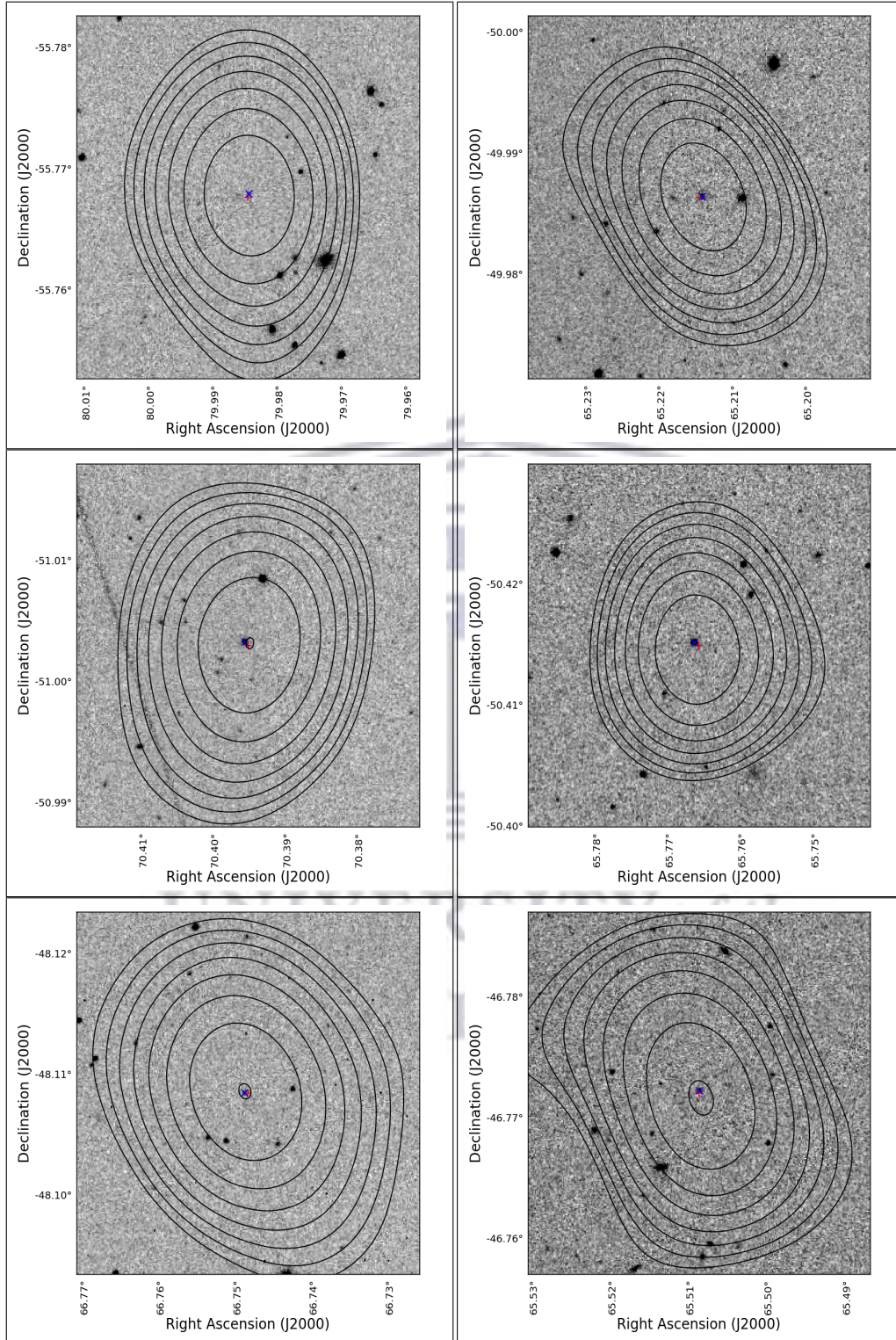


Figure B.28

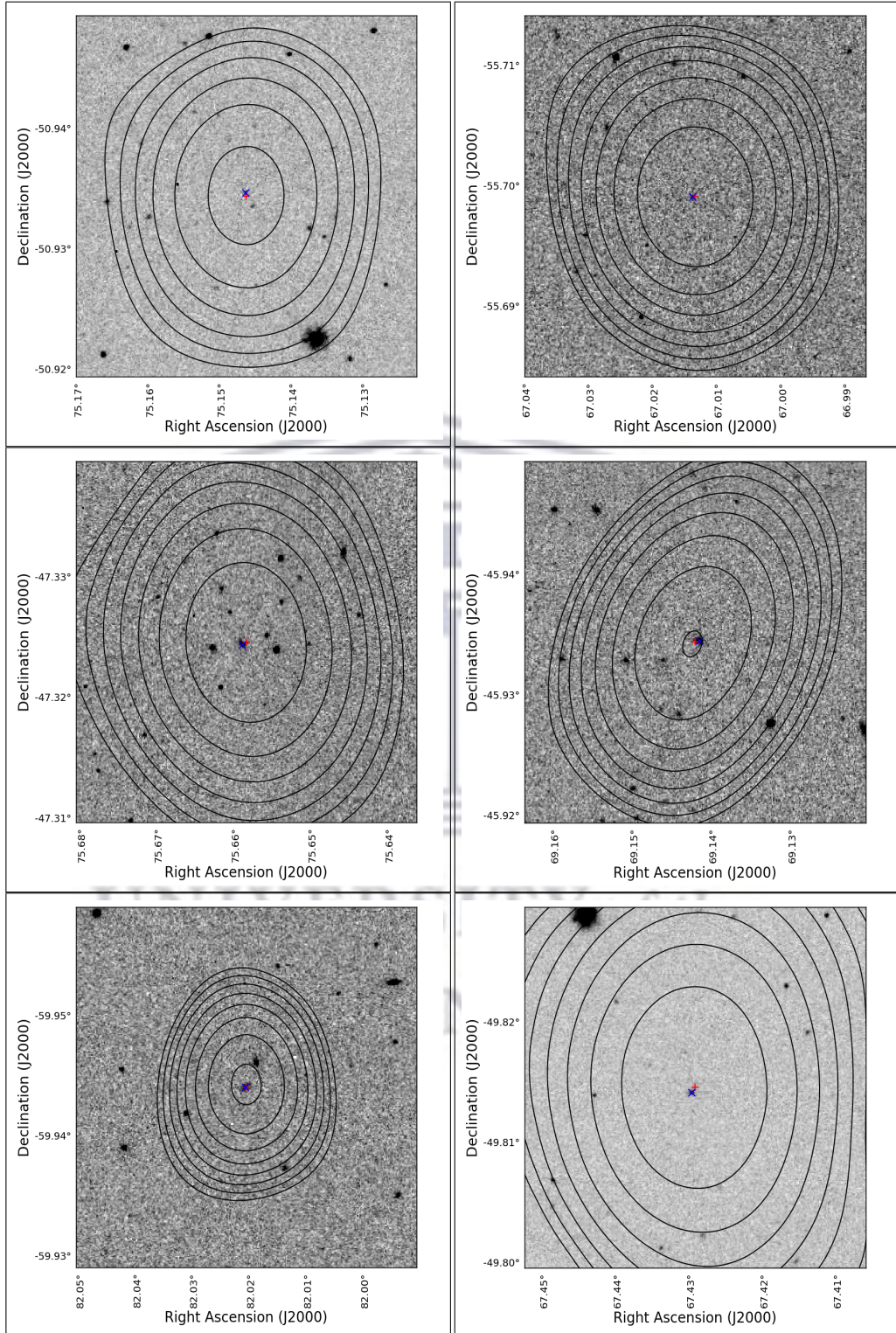


Figure B.29

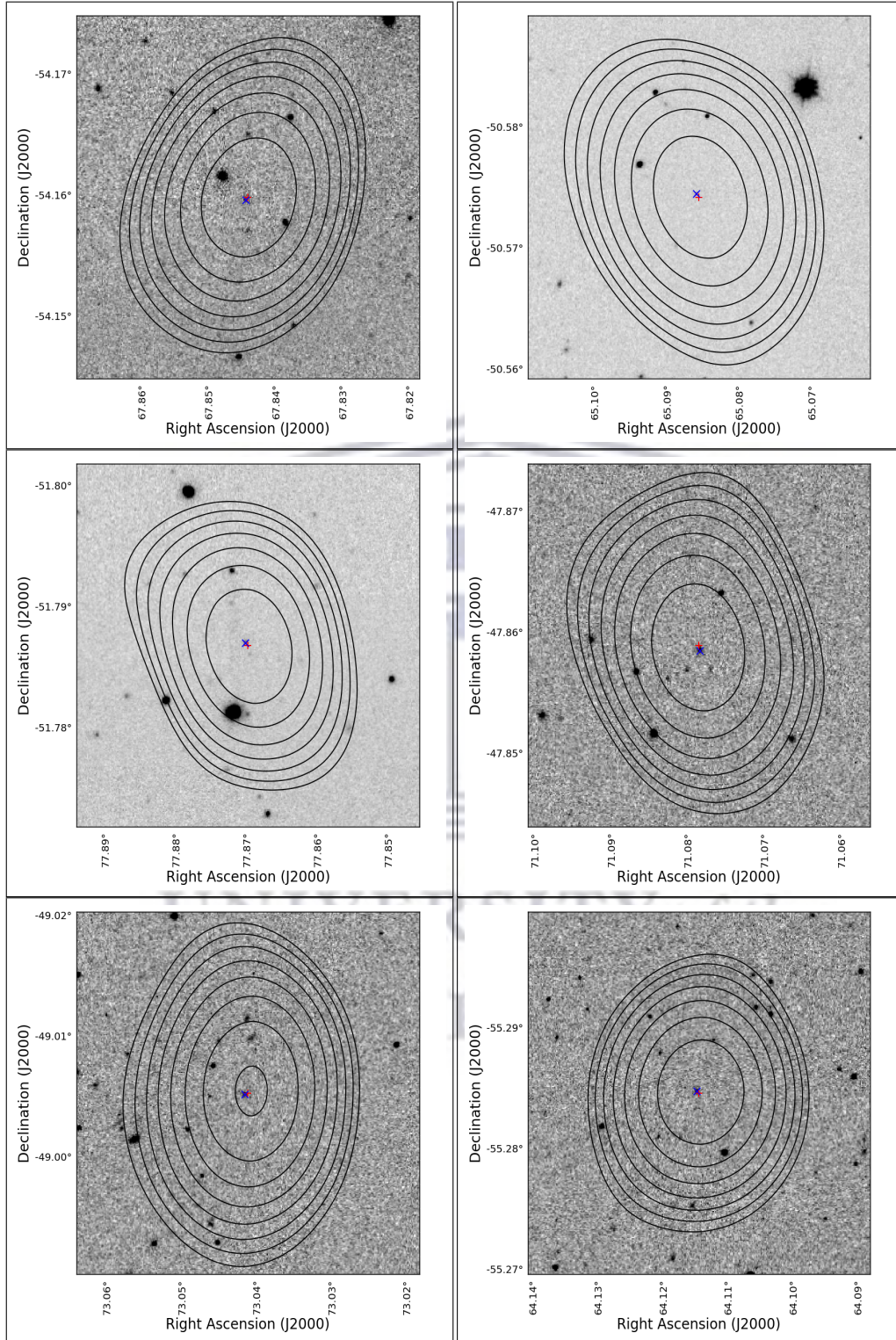


Figure B.30

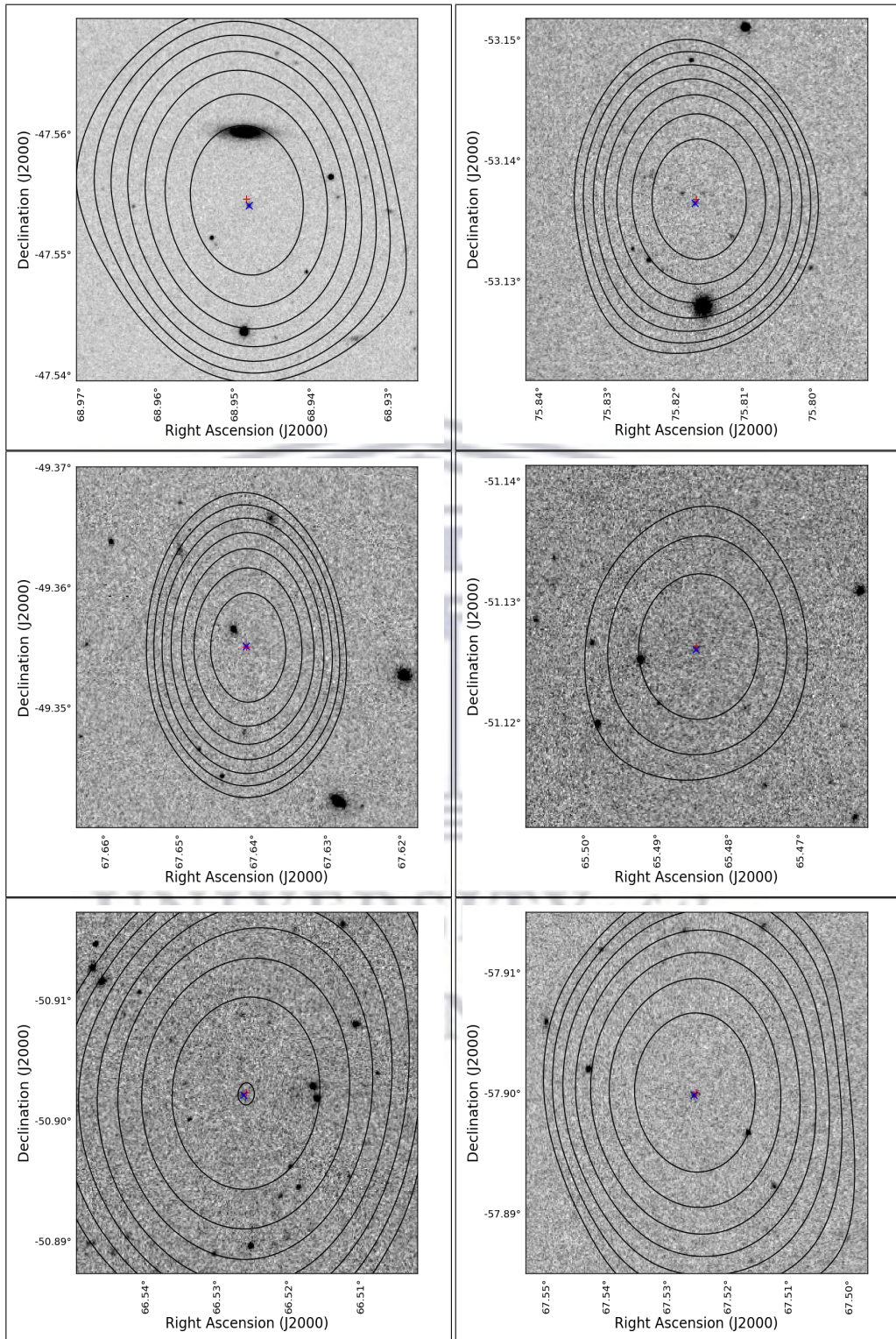


Figure B.31

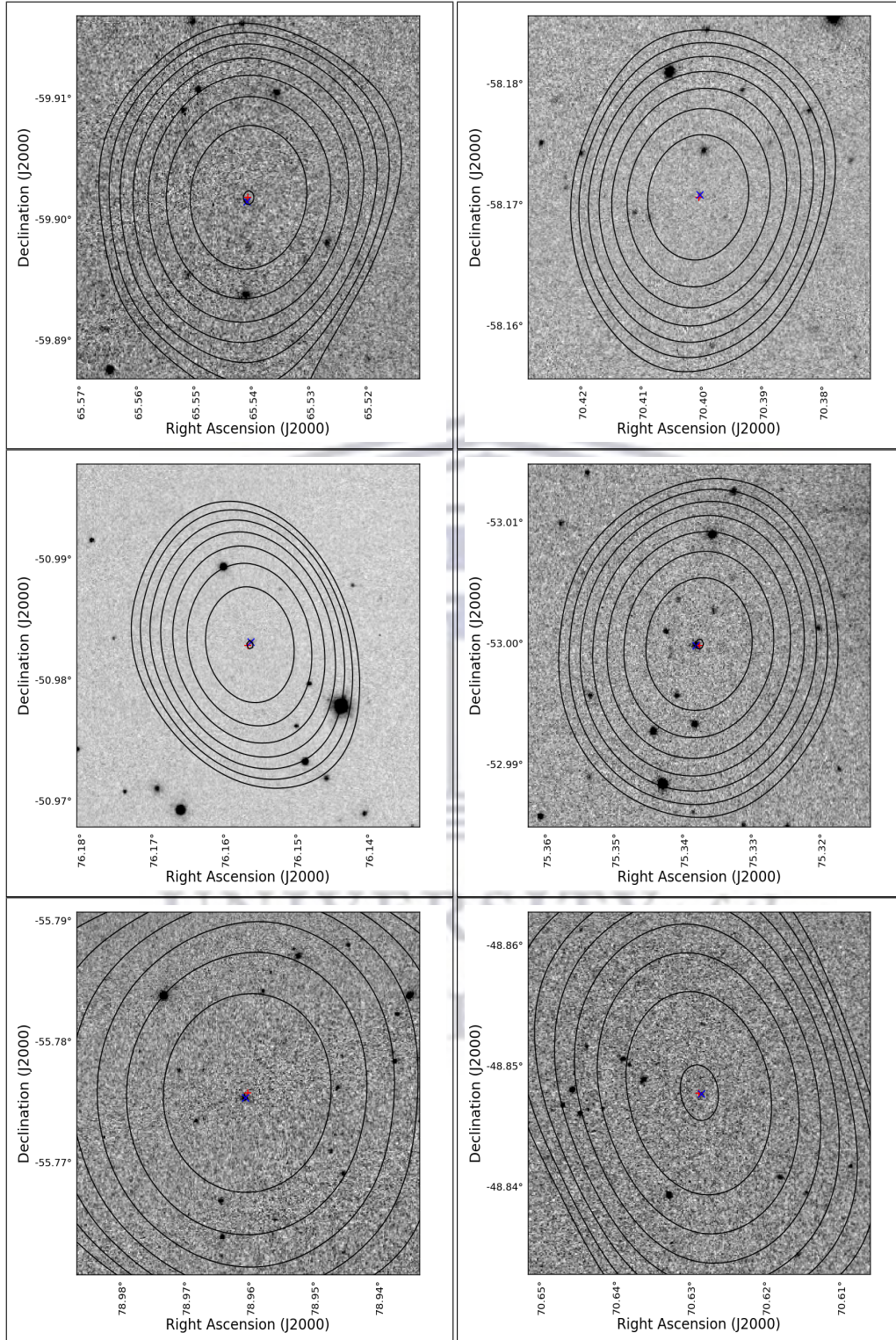


Figure B.32

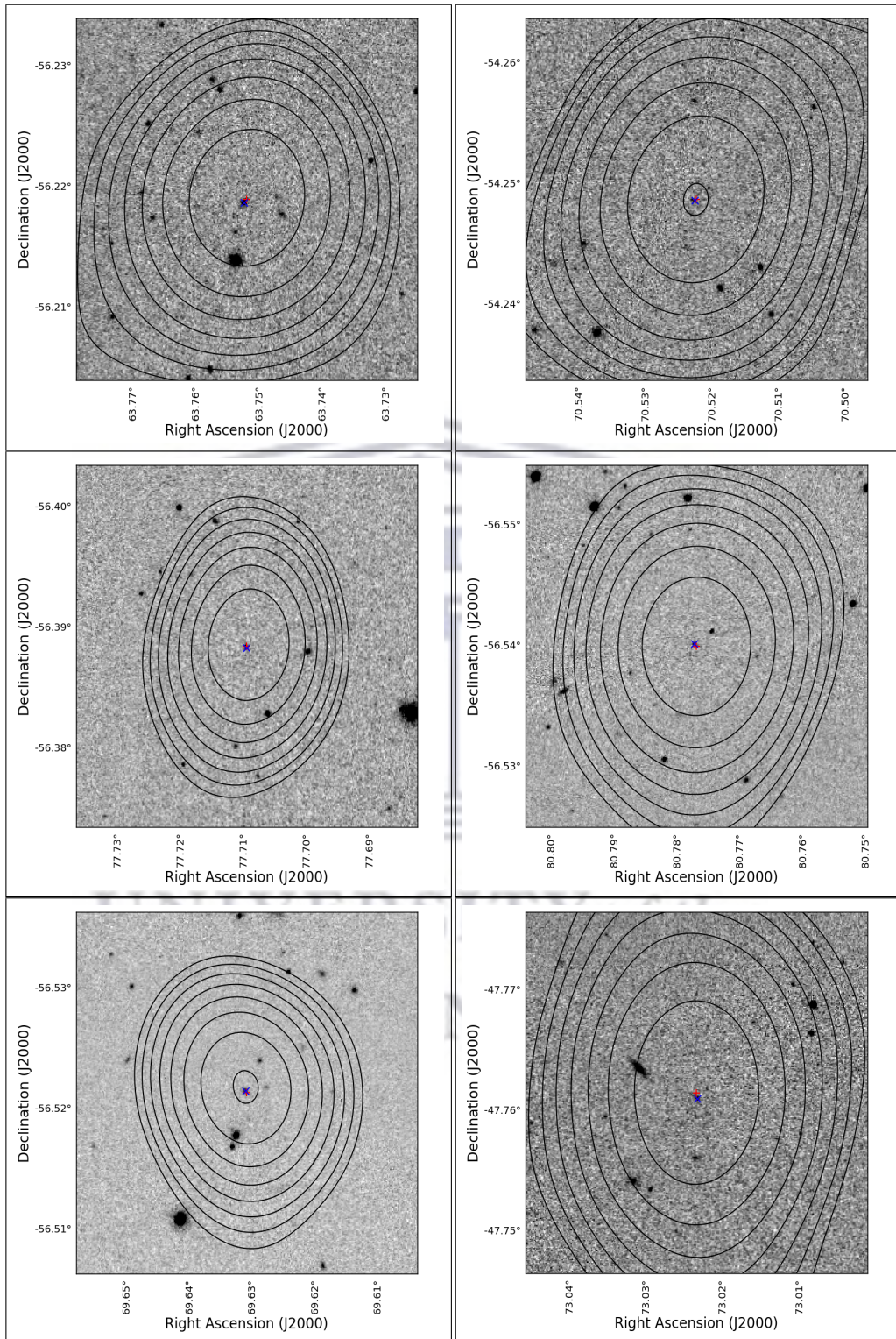


Figure B.33

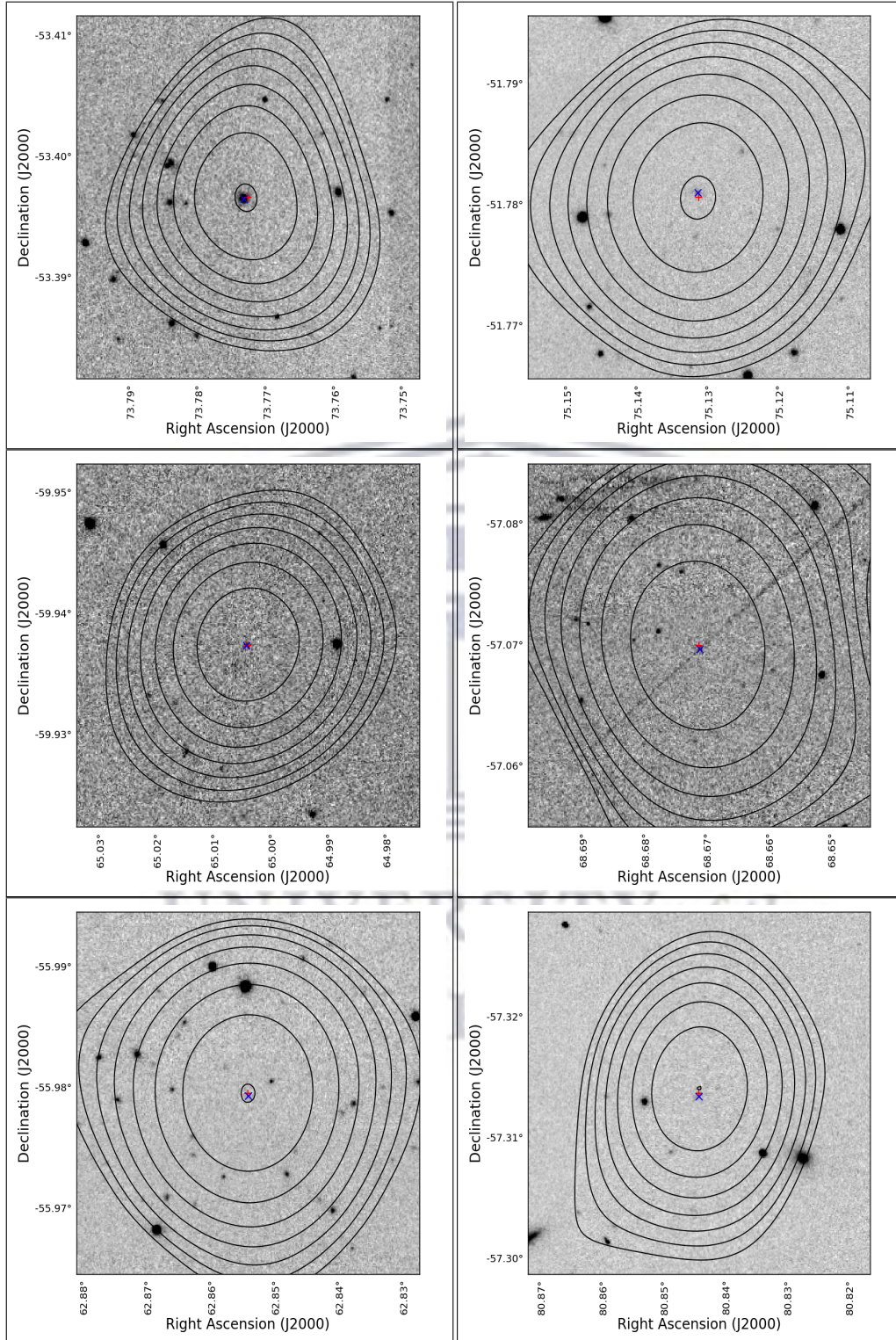


Figure B.34

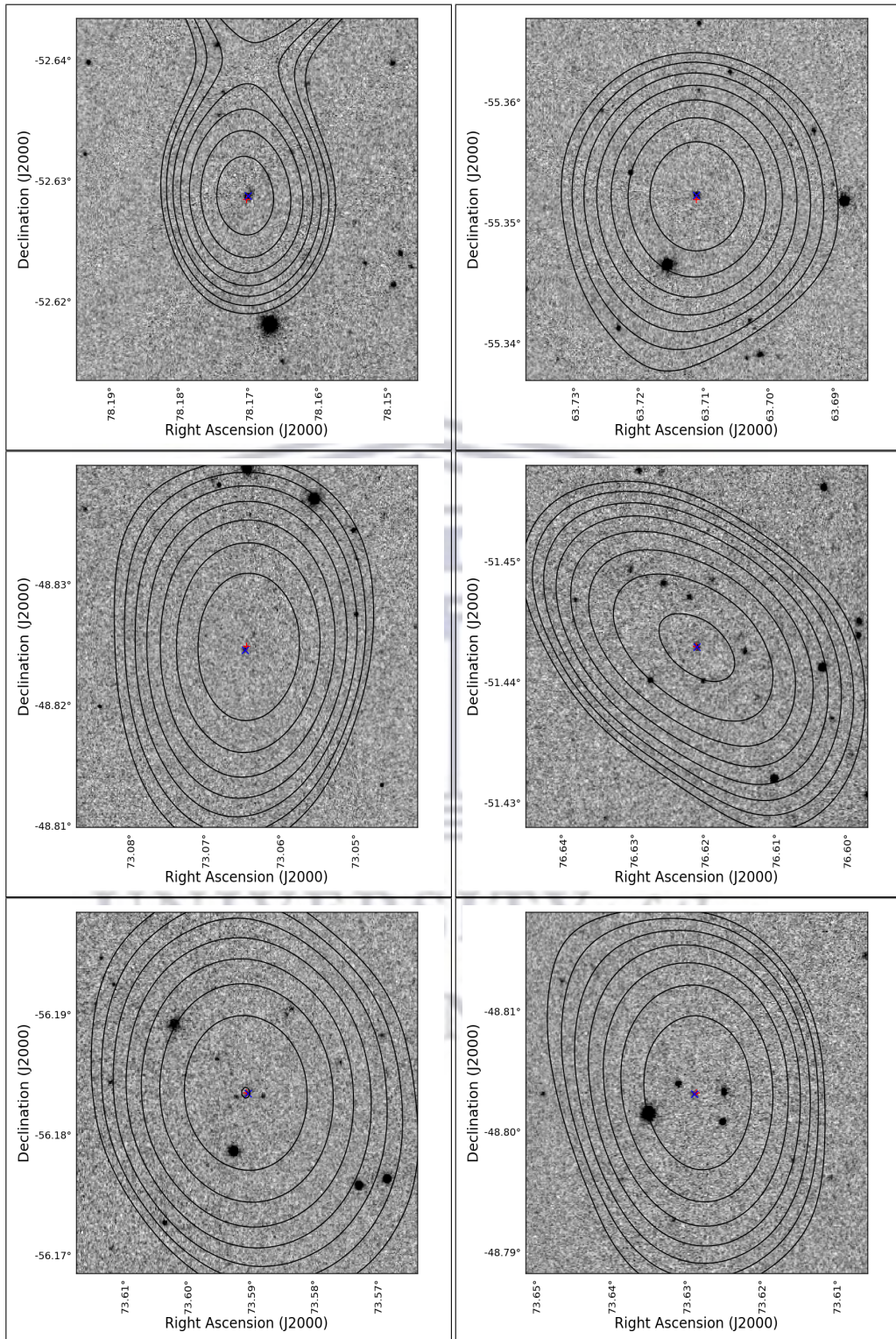


Figure B.35

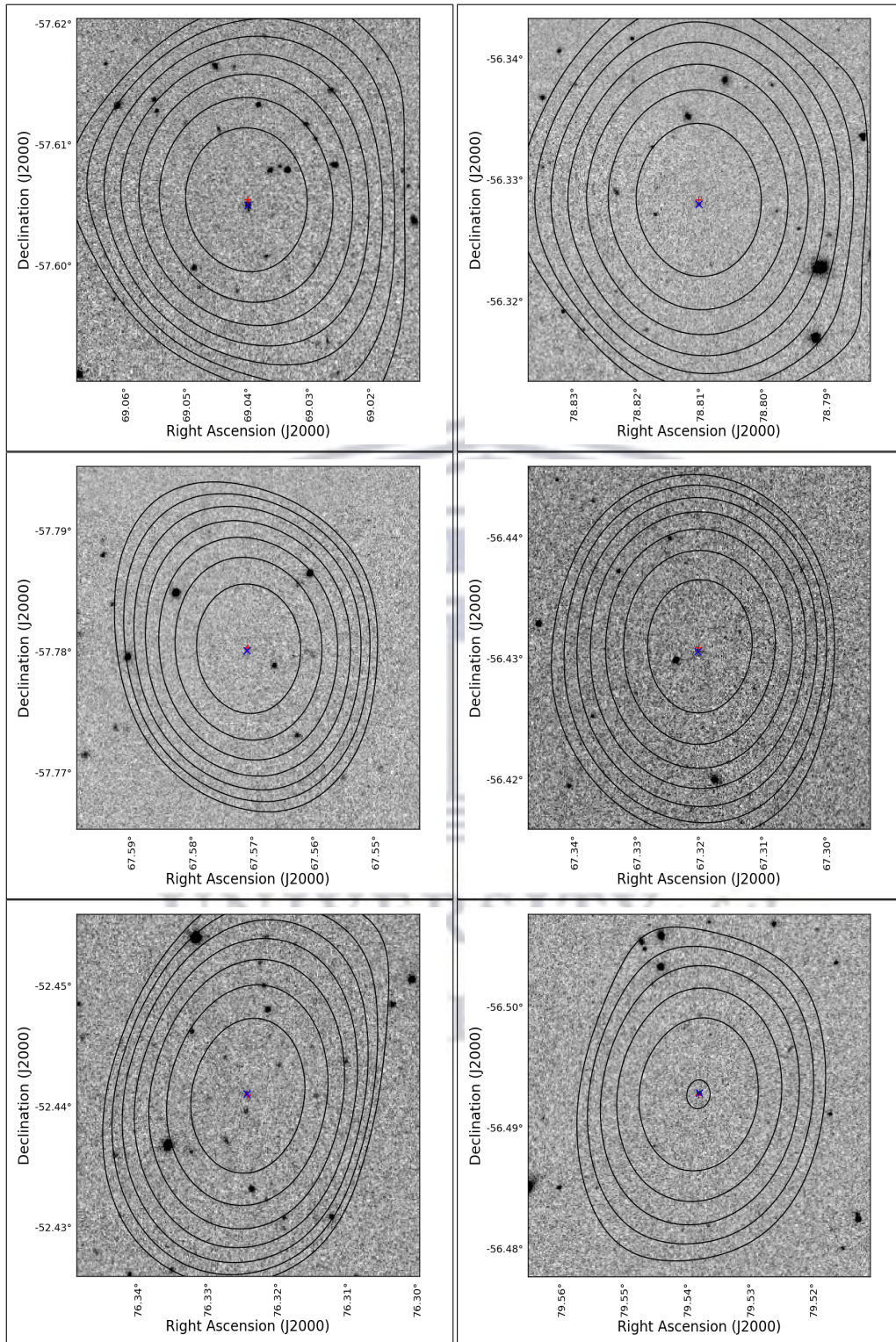


Figure B.36

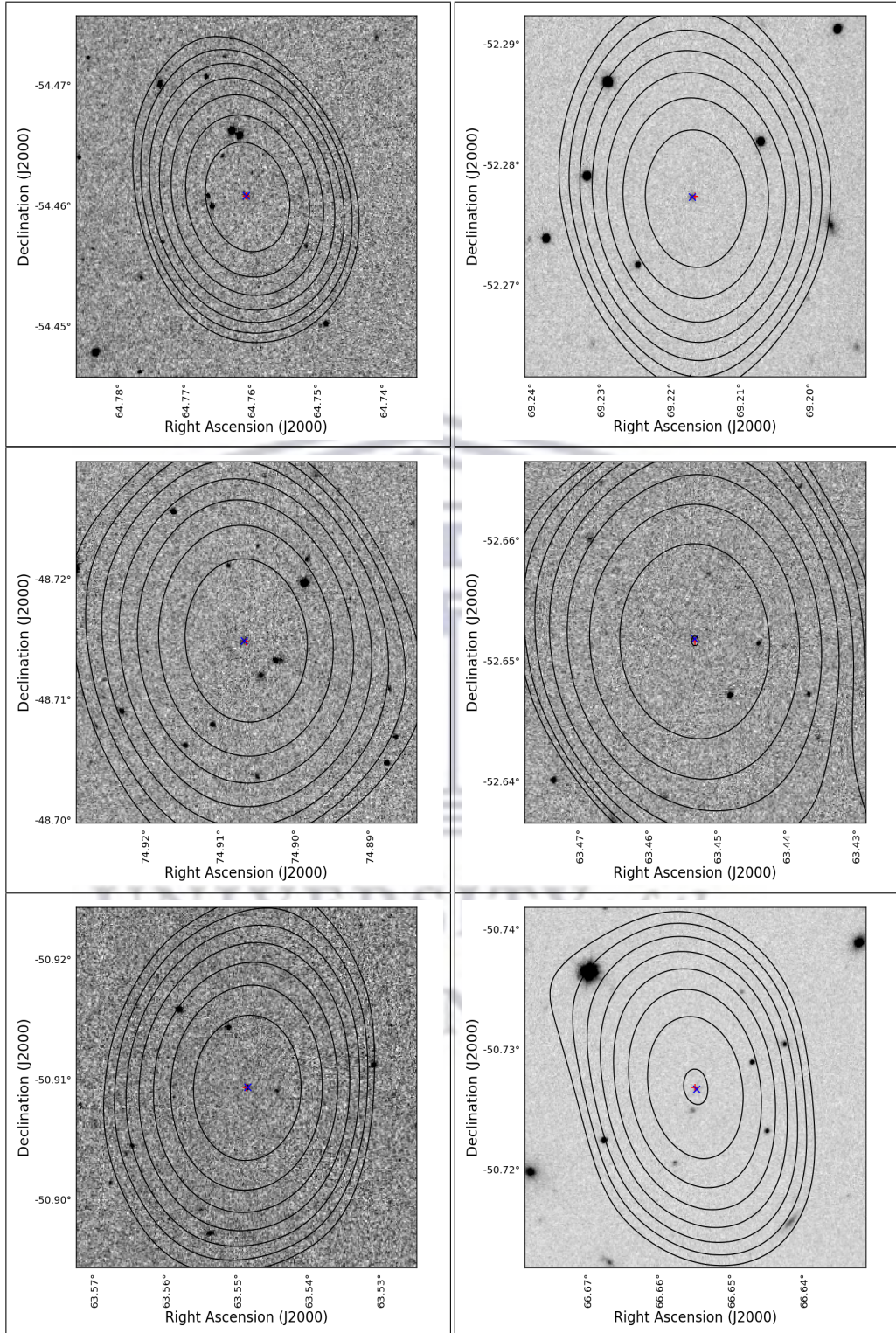


Figure B.37

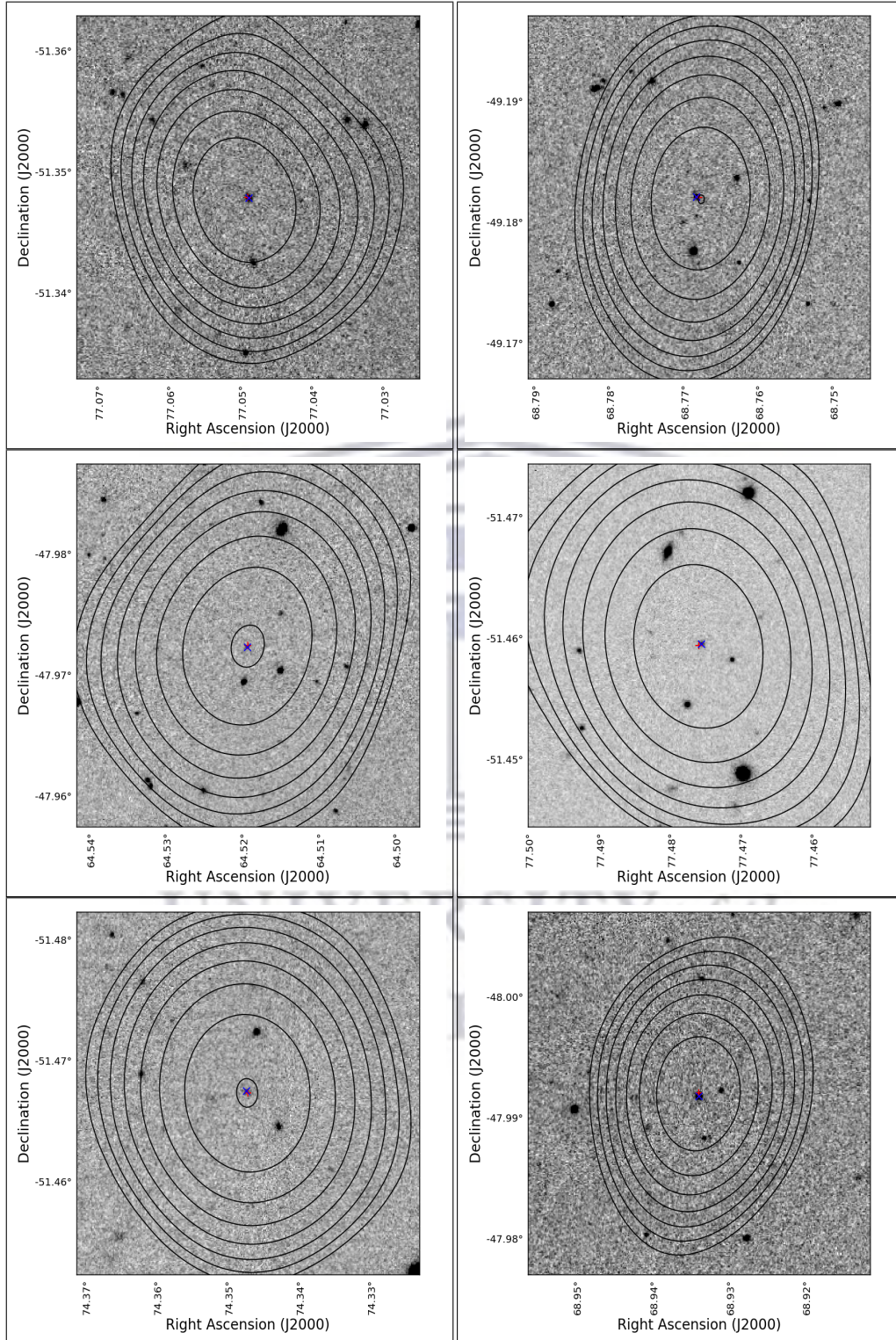


Figure B.38

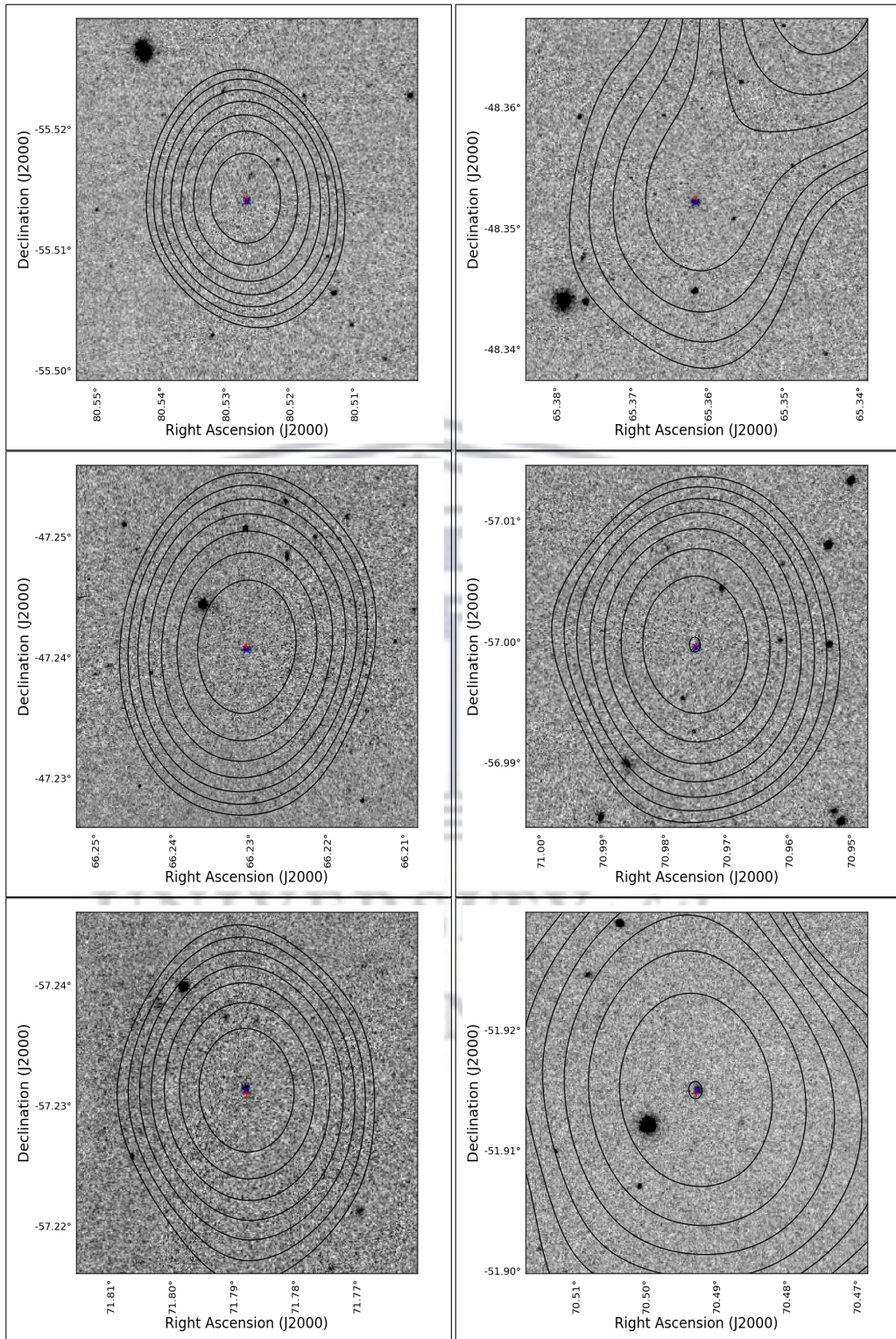


Figure B.39

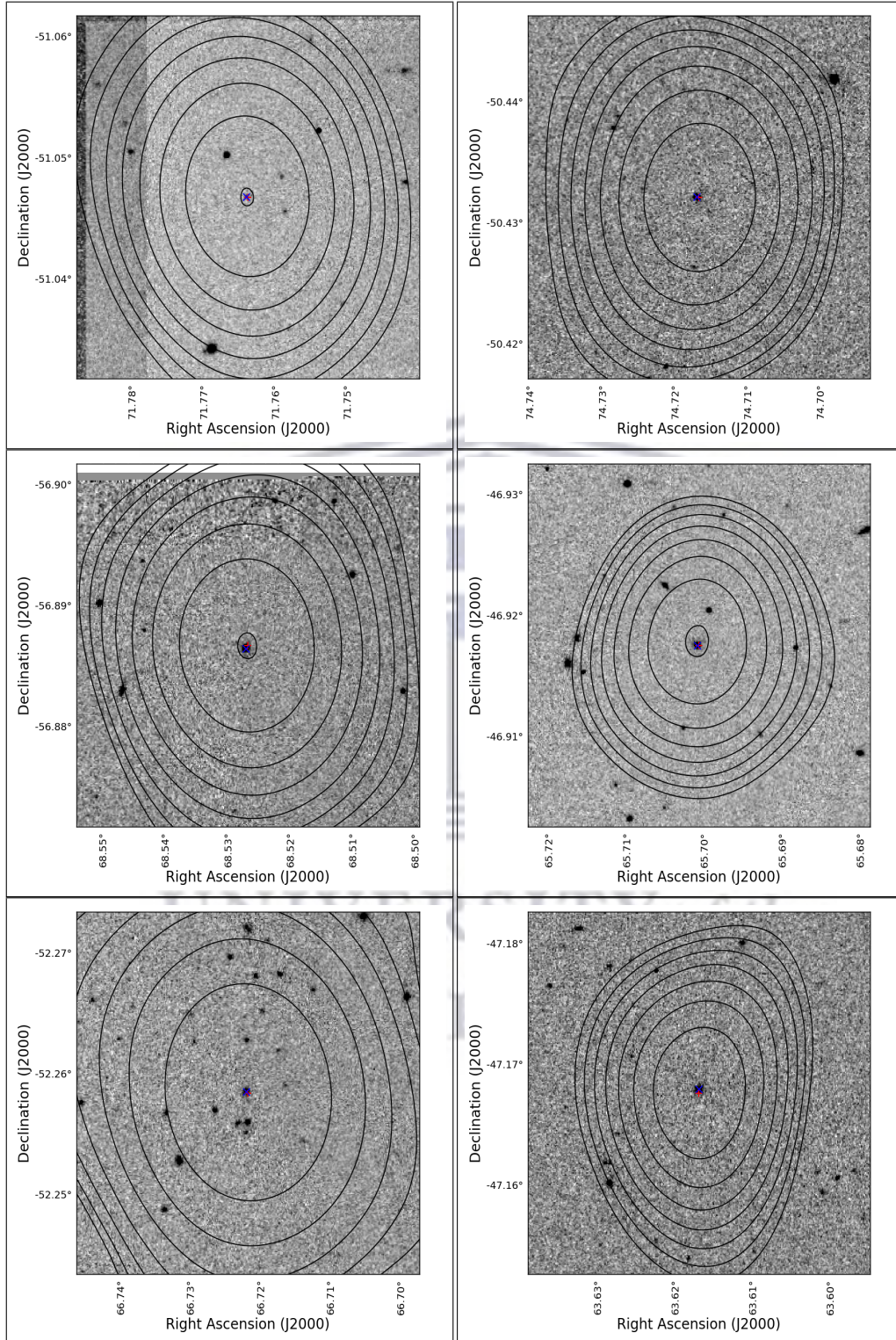


Figure B.40

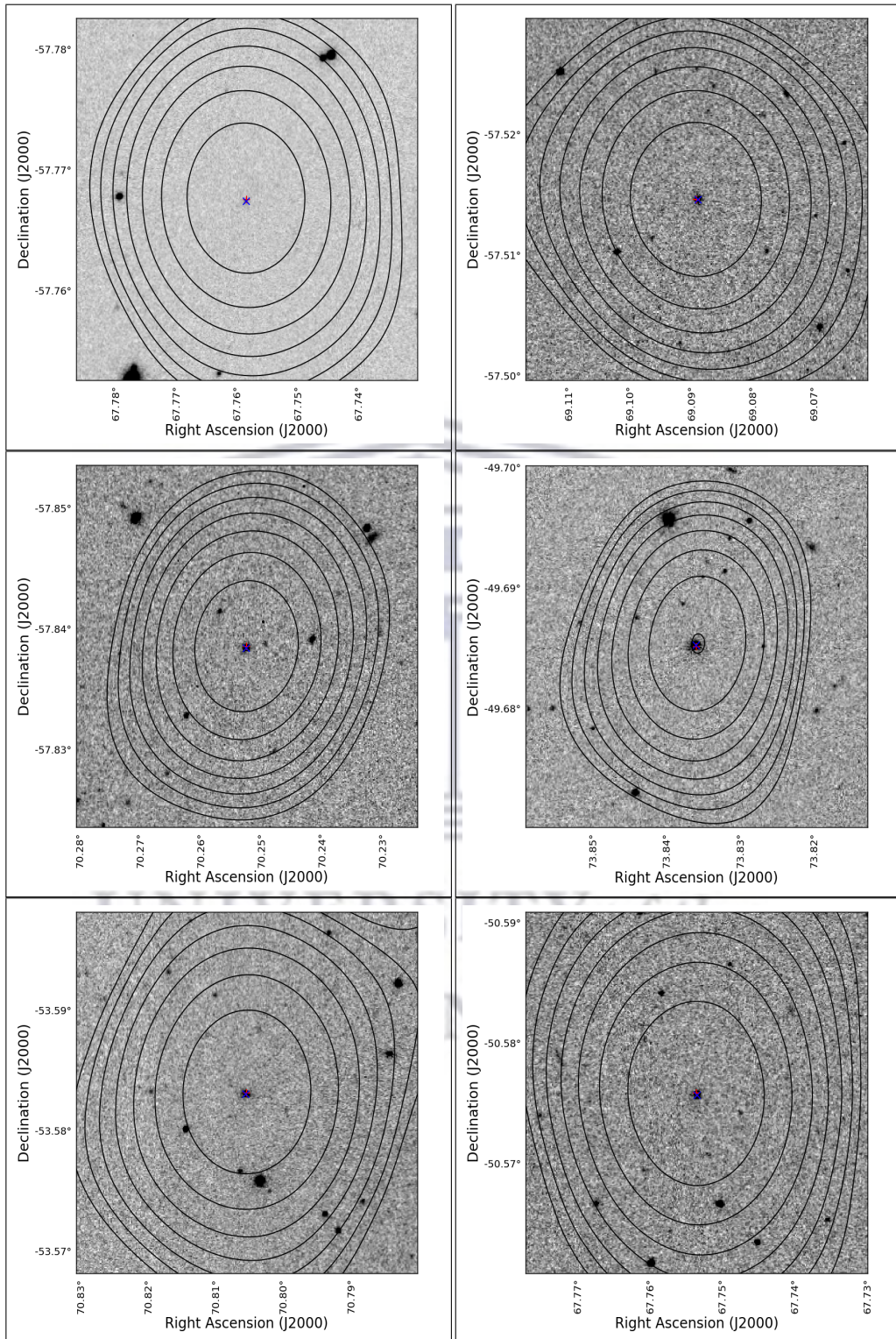


Figure B.41

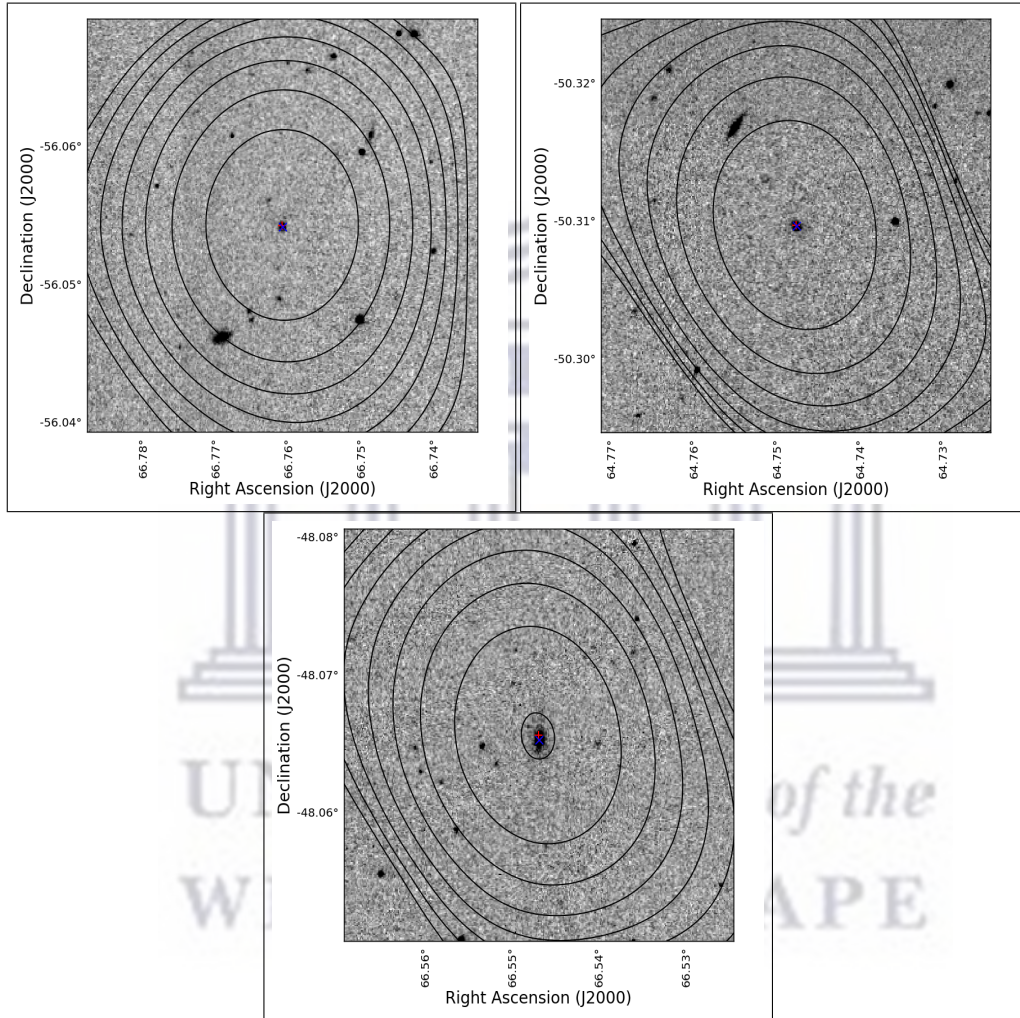


Figure B.42



UNIVERSITY *of the*
WESTERN CAPE

Bibliography

- Abazajian, K. N. et al. 2009, *ApJS*, 182, 543
- Adelman-McCarthy, J. K. et al. 2008, *ApJS*, 175, 297
- Allen, M. G., Dopita, M. A., & Tsvetanov, Z. I. 1998, *ApJ*, 493, 571
- Allen, S. W., Dunn, R. J. H., Fabian, A. C., Taylor, G. B., & Reynolds, C. S. 2006, *MNRAS*, 372, 21
- Allison, J. R., Curran, S. J., Sadler, E. M., & Reeves, S. N. 2013, *MNRAS*, 430, 157
- Allison, J. R., Sadler, E. M., & Meekin, A. M. 2014, *MNRAS*, 440, 696
- Allison, J. R. et al. 2016, *MNRAS*, 456, 3030
- Alloin, D., Barvainis, R., & Guilloteau, S. 2000, *ApJ*, 528, L81
- Andrews, B. H. & Thompson, T. A. 2011, *ApJ*, 727, 97
- Antonucci, R. R. J. & Miller, J. S. 1985, *ApJ*, 297, 621
- Archibald, E. N., Dunlop, J. S., Hughes, D. H., Rawlings, S., Eales, S. A., & Ivison, R. J. 2001, *MNRAS*, 323, 417
- Armus, L., Heckman, T. M., & Miley, G. K. 1990, *ApJ*, 364, 471
- Athreya, R. M. & Kapahi, V. K. 1998, *Journal of Astrophysics and Astronomy*, 19, 63
- Baade, W. & Minkowski, R. 1954, *ApJ*, 119, 206
- Baldi, R. D., Capetti, A., & Giovannini, G. 2015, *A&A*, 576, A38
- Banerji, M. et al. 2015, *MNRAS*, 446, 2523
- Becker, R. H., White, R. L., & Helfand, D. J. 1995, *ApJ*, 450, 559
- Beckmann, R. S., Devriendt, J., Slyz, A., Peirani, S., Richardson, M. L. A., Dubois, Y., Pichon, C., Chisari, N. E., Kaviraj, S., Laigle, C., & Volonteri, M. 2017, *MNRAS*, 472, 949

- Belsole, E., Worrall, D. M., Hardcastle, M. J., Birkinshaw, M., & Lawrence, C. R. 2004, MNRAS, 352, 924
- Benítez, N. 2000, ApJ, 536, 571
- Best, P. N. 2007, NAR, 51, 168
- Best, P. N. & Heckman, T. M. 2012, MNRAS, 421, 1569
- Best, P. N., Kauffmann, G., Heckman, T. M., Brinchmann, J., Charlot, S., Ivezić, Ž., & White, S. D. M. 2005, MNRAS, 362, 25
- Best, P. N., Longair, M. S., & Roettgering, H. J. A. 1998a, MNRAS, 295, 549
- Best, P. N., Röttgering, H. J. A., & Lehnert, M. D. 1999, MNRAS, 310, 223
- Best, P. N., Röttgering, H. J. A., & Longair, M. S. 2000, MNRAS, 311, 23
- Best, P. N. et al. 1998b, MNRAS, 295, 549
- Bicknell, G. V., Sutherland, R. S., van Breugel, W. J. M., Dopita, M. A., Dey, A., & Miley, G. K. 2000, ApJ, 540, 678
- Bigiel, F., Leroy, A., Walter, F., Brinks, E., de Blok, W. J. G., Madore, B., & Thornley, M. D. 2008, AJ, 136, 2846
- Binette, L., Kurk, J. D., Villar-Martín, M., & Röttgering, H. J. A. 2000, A&A, 356, 23
- Binette, L., Wilman, R. J., Villar-Martín, M., Fosbury, R. A. E., Jarvis, M. J., & Röttgering, H. J. A. 2006, A&A, 459, 31
- Blandford, R. D. 2001, Progress of Theoretical Physics Supplement, 143, 182
- Blumenthal, G. & Miley, G. 1979, A&A, 80, 13
- Blundell, K. M., Fabian, A. C., Crawford, C. S., Erlund, M. C., & Celotti, A. 2006, ApJ, 644, L13
- Blundell, K. M. & Rawlings, S. 1999, Nature, 399, 330
- Blundell, K. M., Rawlings, S., Eales, S. A., Taylor, G. B., & Bradley, A. D. 1998, MNRAS, 295, 265
- Blundell, K. M., Rawlings, S., & Willott, C. J. 1999, AJ, 117, 677
- Bock, D. C.-J., Large, M. I., & Sadler, E. M. 1999, AJ, 117, 1578
- Bock, H. & Wagner, S. J. 1994, in Astronomische Gesellschaft Abstract Series, Vol. 10, Astronomische Gesellschaft Abstract Series, ed. G. Klare, 225
- Boissier, S. et al. 2007, ApJS, 173, 524

- Bolatto, A. D., Wolfire, M., & Leroy, A. K. 2013, *ARA&A*, 51, 207
- Booth, R. S., de Blok, W. J. G., Jonas, J. L., & Fanaroff, B. 2009, arXiv e-prints, arXiv:0910.2935
- Bornancini, C. G., De Breuck, C., de Vries, W., Croft, S., van Breugel, W., Röttgering, H., & Minniti, D. 2007, *MNRAS*, 378, 551
- Bornancini, C. G., O'Mill, A. L., Gurovich, S., & Lambas, D. G. 2010, *MNRAS*, 406, 197
- Bower, R. G., Benson, A. J., Malbon, R., Helly, J. C., Frenk, C. S., Baugh, C. M., Cole, S., & Lacey, C. G. 2006, *MNRAS*, 370, 645
- Briggs, F. H., Sorar, E., & Taramopoulos, A. 1993, *ApJ*, 415, L99
- Bruzual, G. & Charlot, S. 2003, *MNRAS*, 344, 1000
- Buchalter, A., Helfand, D. J., Becker, R. H., & White, R. L. 1998, *ApJ*, 494, 503
- Burke, D. L. et al. 2018, *AJ*, 155, 41
- Cai, Z. et al. 2002, *A&A*, 381, 401
- Camilo, F., Scholz, P., Serylak, M., Buchner, S., Merryfield, M., Kaspi, V. M., Archibald, R. F., Bailes, M., Jameson, A., van Straten, W., & et al. 2018, *ApJ*, 856, 180
- Carilli, C. L., Harris, D. E., Pentericci, L., Röttgering, H. J. A., Miley, G. K., Kurk, J. D., & van Breugel, W. 2002, *ApJ*, 567, 781
- Carilli, C. L., Owen, F. N., & Harris, D. E. 1994, *AJ*, 107, 480
- Carilli, C. L., Röttgering, H. J. A., van Ojik, R., Miley, G. K., & van Breugel, W. J. M. 1997, *ApJS*, 109, 1
- Casey, C. M., Narayanan, D., & Cooray, A. 2014, *Phys. Rep.*, 541, 45
- Chambers, K. C., Miley, G. K., & van Breugel, W. 1987, *Nature*, 329, 604
- Chambers, K. C., Miley, G. K., & van Breugel, W. J. M. 1990, *ApJ*, 363, 21
- Chambers, K. C., Miley, G. K., van Breugel, W. J. M., & Huang, J. S. 1996, *ApJS*, 106, 215
- Chandra, P., Swarup, G., Kulkarni, V. K., & Kantharia, N. G. 2004, *Journal of Astrophysics and Astronomy*, 25, 57
- Ching, J. H. Y., Sadler, E. M., Croom, S. M., Johnston, H. M., Pracy, M. B., Couch, W. J., Hopkins, A. M., Jurek, R. J., & Pimblett, K. A. 2017, *MNRAS*, 464, 1306
- Chini, R. & Kruegel, E. 1994, *A&A*, 288, L33

- Cileigi, P., Zamorani, G., Hasinger, G., Lehmann, I., Szokoly, G., & Wilson, G. 2003, *A&A*, 398, 901
- Cimatti, A., di Serego Alighieri, S., Fosbury, R. A. E., Salvati, M., & Taylor, D. 1993, *MNRAS*, 264, 421
- Cimatti, A., di Serego Alighieri, S., Vernet, J., Cohen, M. H., & Fosbury, R. A. E. 1998, *ApJ*, 499, L21
- Clewley, L. & Jarvis, M. J. 2004, *MNRAS*, 352, 909
- Cody, A. M. & Braun, R. 2003, *A&A*, 400, 871
- Condon, J. J., Cotton, W. D., Greisen, E. W., Yin, Q. F., Perley, R. A., Taylor, G. B., & Broderick, J. J. 1998a, *AJ*, 115, 1693
- . 1998b, *AJ*, 115, 1693
- Cooper, M. C. et al. 2012, *MNRAS*, 425, 2116
- Cowie, L. L., Songaila, A., Hu, E. M., & Cohen, J. G. 1996, *AJ*, 112, 839
- Croton, D. J. et al. 2006, *MNRAS*, 367, 864
- Cruz, M. J., Jarvis, M. J., Blundell, K. M., Rawlings, S., Croft, S., Klöckner, H.-R., McLure, R. J., Simpson, C., Targett, T. A., & Willott, C. J. 2006, *MNRAS*, 373, 1531
- Cruz, M. J., Jarvis, M. J., Rawlings, S., & Blundell, K. M. 2007, *MNRAS*, 375, 1349
- Dallacasa, D., Fanti, C., & Fanti, R. 1993, *Compact Steep-Spectrum Radio Sources: A Progress Report*, ed. H.-J. Röser & K. Meisenheimer, Vol. 421, 27
- Daly, R. A. & Guerra, E. J. 2002, *AJ*, 124, 1831
- Dark Energy Survey Collaboration et al. 2016, *MNRAS*, 460, 1270
- David, L. P. et al. 2014, *ApJ*, 792, 94
- De Breuck, C., Downes, D., Neri, R., van Breugel, W., Reuland, M., Omont, A., & Ivison, R. 2005, *A&A*, 430, L1
- De Breuck, C., Hunstead, R. W., Sadler, E. M., Rocca-Volmerange, B., & Klamer, I. 2004, *MNRAS*, 347, 837
- De Breuck, C., Klamer, I., Johnston, H., Hunstead, R. W., Bryant, J., Rocca-Volmerange, B., & Sadler, E. M. 2006, *MNRAS*, 366, 58
- De Breuck, C., Neri, R., & Omont, A. 2003a, *NAR*, 47, 285
- De Breuck, C. & Reuland, M. 2005, in *Multiwavelength Mapping of Galaxy Formation and Evolution*, ed. A. Renzini & R. Bender, 374

- De Breuck, C., van Breugel, W., Röttgering, H., Stern, D., Miley, G., de Vries, W., Stanford, S. A., Kurk, J., & Overzier, R. 2001, *AJ*, 121, 1241
- De Breuck, C., van Breugel, W., Röttgering, H. J. A., & Miley, G. 2000, *A&AS*, 143, 303
- De Breuck, C., van Breugel, W., Stanford, S. A., Röttgering, H., Miley, G., & Stern, D. 2002, *AJ*, 123, 637
- De Breuck, C. et al. 2003b, *A&A*, 401, 911
- De Bruyn, A. G. 1996, *Astrophysics and Space Science Library*, Vol. 206, *H I at High Redshift*, ed. M. N. Bremer & N. Malcolm, 171
- De Jong, J. T. et al. 2015, *A&A*, 582, A62
- Delhaize, J. et al. 2017, *A&A*, 602, A4
- Dey, A., van Breugel, W., Vacca, W. D., & Antonucci, R. 1997, *ApJ*, 490, 698
- Di Matteo, T., Springel, V., & Hernquist, L. 2005, *Nature*, 433, 604
- Di Serego Alighieri, S. 1997, *Polarimetry with large telescopes.*, ed. J. M. Rodríguez Espinosa, A. Herrero, & F. Sánchez, 287–329
- Di Serego Alighieri, S., Fosbury, R. A. E., Quinn, P. J., & Tadhunter, C. N. 1989, *Nature*, 341, 307
- Dickey, J. M. 1982, *ApJ*, 263, 87
- Dickey, J. M. & Lockman, F. J. 1990, *ARA&A*, 28, 215
- Dickinson, M. 1998, in *The Hubble Deep Field*, ed. M. Livio, S. M. Fall, & P. Madau, 219
- Downes, D., Solomon, P. M., & Radford, S. J. E. 1993, *ApJ*, 414, L13
- Drouart, G., De Breuck, C., Vernet, J., Laing, R. A., Seymour, N., Stern, D., Haas, M., Pier, E. A., & Rocca-Volmerange, B. 2012, *A&A*, 548, A45
- Drouart, G. et al. 2014, *A&A*, 566, A53
- Dubinski, J. 1998, *ApJ*, 502, 141
- Duffy et al. 2012, *MNRAS*, 426, 3385
- Dunlop, J. S., Hughes, D. H., Rawlings, S., Eales, S. A., & Ward, M. J. 1994, *Nature*, 370, 347
- Eales, S., Rawlings, S., Law-Green, D., Cotter, G., & Lacy, M. 1997, *MNRAS*, 291, 593
- Emerson, J. P., McPherson, A., & Sutherland, W. 2006, *The Messenger*, 126, 41

- Emerson, J. P. et al. 2004, in Proc. SPIE, Vol. 5493, Optimizing Scientific Return for Astronomy through Information Technologies, ed. P. J. Quinn & A. Bridger, 401–410
- Emonts, B. H. C., Mao, M. Y., Stroe, A., Pentericci, L., Villar-Martín, M., et al. 2015, MNRAS, 451, 1025
- Emonts, B. H. C. et al. 2014, MNRAS, 438, 2898
- Erlund, M. C., Fabian, A. C., Blundell, K. M., Celotti, A., & Crawford, C. S. 2006, MNRAS, 371, 29
- Fabian, A. C., Sanders, J. S., Crawford, C. S., & Etori, S. 2003, MNRAS, 341, 729
- Fall, S. M. & Rees, M. J. 1977, MNRAS, 181, 37P
- Fan, X. et al. 2001, AJ, 122, 2833
- Fanaroff, B. L. & Riley, J. M. 1974, MNRAS, 167, 31P
- Fanti, C. & Fanti, R. 1994, in Astronomical Society of the Pacific Conference Series, Vol. 54, The Physics of Active Galaxies, ed. G. V. Bicknell, M. A. Dopita, & P. J. Quinn, 341
- Felten, J. E. & Rees, M. J. 1969, Nature, 221, 924
- Feltre, A., Charlot, S., & Gutkin, J. 2016, MNRAS, 456, 3354
- Fernandes, C. A. C. et al. 2015, MNRAS, 447, 1184
- Flaugher, B. et al. 2015, AJ, 150, 150
- Fleuren, S. et al. 2012, MNRAS, 423, 2407
- Fosbury, R. A. E., De Breuck, C., Mainieri, V., Robertson, G., & Vernet, J. 2007, The Messenger, 129, 64
- Gao, L., Loeb, A., Peebles, P. J. E., White, S. D. M., & Jenkins, A. 2004a, ApJ, 614, 17
- Gao, Y., Carilli, C. L., Solomon, P. M., & Vand en Bout, P. A. 2007, ApJ, 660, L93
- Gao, Y. & Solomon, P. M. 2004, ApJS, 152, 63
- Gao, Y. et al. 2004b, ApJ, 606, 271
- Ge, J. & Owen, F. N. 1994, AJ, 108, 1523
- Glover, S. C. O. & Clark, P. C. 2012, MNRAS, 426, 377
- Greve, T. R., Ivison, R. J., & Papadopoulos, P. P. 2004, A&A, 419, 99
- Greve, T. R., Ivison, R. J., & Stevens, J. A. 2006, Astronomische Nachrichten, 327, 208
- Groves, B. A., Cecil, G., Ferruit, P., & Dopita, M. A. 2004, ApJ, 611, 786

- Gullberg, B. et al. 2015, MNRAS, 449, 2883
- Gupta, N. et al. 2016, in Proceedings of MeerKAT Science: On the Pathway to the SKA. 25-27 May, 2016 Stellenbosch, South Africa (MeerKAT2016), 14
- Gupta, Y., Ajithkumar, B., Kale, H. S., Nayak, S., Sabhapathy, S., Sureshkumar, S., Swami, R. V., Chengalur, J. N., Ghosh, S. K., Ishwara-Chandra, C. H., Joshi, B. C., Kanekar, N., Lal, D. V., & Roy, S. 2017, Current Science, 113, 707
- Gurvits, L. I., Kellermann, K. I., & Frey, S. 1999, A&A, 342, 378
- Gurvits, L. I., Schilizzi, R. T., Miley, G. K., Peck, A., Bremer, M. N., Roettgering, H., & van Breugel, W. 1997, A&A, 318, 11
- Hardcastle, M. J., Alexander, P., Pooley, G. G., & Riley, J. M. 1998, MNRAS, 296, 445
- Hardcastle, M. J., Evans, D. A., & Croston, J. H. 2007, MNRAS, 376, 1849
- Häring, N. & Rix, H.-W. 2004, ApJ, 604, L89
- Harris, D. E. & Krawczynski, H. 2002, ApJ, 565, 244
- Hatch, N. A., Overzier, R. A., Röttgering, H. J. A., Kurk, J. D., & Miley, G. K. 2008, MNRAS, 383, 931
- Heavens, A., Panter, B., Jimenez, R., & Dunlop, J. 2004, Nature, 428, 625
- Heckman, T. M. & Best, P. N. 2014, ARA&A, 52, 589
- Heckman, T. M., Miley, G. K., Balick, B., van Breugel, W. J. M., & Butcher, H. R. 1982, ApJ, 262, 529
- Heckman, T. M., van Breugel, W. J. M., & Miley, G. K. 1984, ApJ, 286, 509
- Heckman, T. M. et al. 1986, ApJ, 311, 526
- Helfer, T. T., Thornley, M. D., Regan, M. W., Wong, T., Sheth, K., Vogel, S. N., Blitz, L., & Bock, D. C. J. 2003, ApJS, 145, 259
- Heyer, M. H., Corbelli, E., Schneider, S. E., & Young, J. S. 2004, ApJ, 602, 723
- Hirschmann, M., Charlot, S., Feltre, A., Naab, T., Somerville, R. S., & Choi, E. 2019, MNRAS, 487, 333
- Ho, L. & Kormendy, J. 2000, Supermassive Black Holes in Active Galactic Nuclei, ed. P. Murdin, 2365
- Holwerda, B. W., Blyth, S.-L., & Baker, A. J. 2012, in IAU Symposium, Vol. 284, The Spectral Energy Distribution of Galaxies - SED 2011, ed. R. J. Tuffs & C. C. Popescu, 496–499

- Hopkins, P. F. & Hernquist, L. 2006, *ApJS*, 166, 1
- Hopkins, P. F., Hernquist, L., Cox, T. J., & Kereš, D. 2008, *ApJS*, 175, 356
- Hopkins, P. F., Narayanan, D., Murray, N., & Quataert, E. 2013, *MNRAS*, 433, 69
- Humphrey, A., Villar-Martín, M., Fosbury, R., Binette, L., Vernet, J., De Breuck, C., & di Serego Alighieri, S. 2007, *MNRAS*, 375, 705
- Humphrey, A., Villar-Martín, M., Fosbury, R., Vernet, J., & di Serego Alighieri, S. 2006, *MNRAS*, 369, 1103
- Ilbert, O. et al. 2013, *A&A*, 556, A55
- Iverson, R. J. 1995, *MNRAS*, 275, L33
- Iverson, R. J., Papadopoulos, P., Seaquist, E. R., & Eales, S. A. 1996, *MNRAS*, 278, 669
- Jaffe, W. & Bremer, M. N. 1997, *MNRAS*, 284, L1
- Jaffe, W., Bremer, M. N., & Baker, K. 2005, *MNRAS*, 360, 748
- Jarvis, M., Sheldon, E., Zuntz, J., Kacprzak, T., Bridle, et al. 2016a, *MNRAS*, 460, 2245
- Jarvis, M. J., Cruz, M. J., Cohen, A. S., Röttgering, H. J. A., & Kassim, N. E. 2004, *MNRAS*, 355, 20
- Jarvis, M. J. & Rawlings, S. 2000, *MNRAS*, 319, 121
- Jarvis, M. J., Rawlings, S., Eales, S., Blundell, K. M., Bunker, A. J., Croft, S., McLure, R. J., & Willott, C. J. 2001a, *MNRAS*, 326, 1585
- Jarvis, M. J., Rawlings, S., Lacy, M., Blundell, K. M., Bunker, A. J., Eales, S., Saunders, R., Spinrad, H., Stern, D., & Willott, C. J. 2001b, *MNRAS*, 326, 1563
- Jarvis, M. J., Teimourian, H., Simpson, C., Smith, D. J. B., Rawlings, S., & Bonfield, D. 2009, *MNRAS*, 398, L83
- Jarvis, M. J., Wilman, R. J., Röttgering, H. J. A., & Binette, L. 2003, *MNRAS*, 338, 263
- Jarvis, M. J. et al. 2001c, *MNRAS*, 327, 907
- Jarvis, M. J. et al. 2016b, in *Proceedings of MeerKAT Science: On the Pathway to the SKA*. 25-27 May, 2016 Stellenbosch, South Africa (MeerKAT2016), 6
- Johnson, O., Almaini, O., Best, P. N., & Dunlop, J. 2007, *MNRAS*, 376, 151
- Johnston, S. et al. 2008, *Experimental Astronomy*, 22, 151
- Jonas, J. & MeerKAT Team. 2016, in *MeerKAT Science: On the Pathway to the SKA*, 1

- Jonas, J. L. 2009, *IEEE Proceedings*, 97, 1522
- Junor, W., Biretta, J. A., & Livio, M. 1999, *Nature*, 401, 891
- Kaiser, C. R. & Alexander, P. 1997, *MNRAS*, 286, 215
- Kanekar, N. & Briggs, F. H. 2004, *NAR*, 48, 1259
- Kellermann, K. I. 2003, in *Astronomical Society of the Pacific Conference Series*, Vol. 300, *Radio Astronomy at the Fringe*, ed. J. A. Zensus, M. H. Cohen, & E. Ros, 185
- Kennicutt, C. J. 1998, *ApJ*, 498, 541
- Kewley, L. J., Geller, M. J., & Jansen, R. A. 2004, *AJ*, 127, 2002
- Klamer, I. J., Ekers, R. D., Sadler, E. M., & Hunstead, R. W. 2004, *ApJ*, 612, L97
- Klamer, I. J. et al. 2006, *MNRAS*, 371, 852
- Kormendy, J. & Gebhardt, K. 2001, in *American Institute of Physics Conference Series*, Vol. 586, *20th Texas Symposium on relativistic astrophysics*, ed. J. C. Wheeler & H. Martel, 363–381
- Kriek, M., van Dokkum, P. G., Labbé, I., Franx, M., Illingworth, G. D., Marchesini, D., & Quadri, R. F. 2009, *ApJ*, 700, 221
- Krishna, G., Wiita, P. J., & Barai, P. 2004, *Journal of Korean Astronomical Society*, 37, 517
- Krolik, J. H. & Chen, W. 1991, *AJ*, 102, 1659
- Krumholz, M. R., Leroy, A. K., & McKee, C. F. 2011, *ApJ*, 731, 25
- Krumholz, M. R. & McKee, C. F. 2005, *ApJ*, 630, 250
- Krumholz, M. R. & Thompson, T. A. 2007, *ApJ*, 669, 289
- Kulkarni, S. R. & Heiles, C. 1987, *The Atomic Component*, ed. D. J. Hollenbach & J. Thronson, Harley A., Vol. 134, 87
- Laing, R. A., Riley, J. M., & Longair, M. S. 1983, *MNRAS*, 204, 151
- Larson, R. 1992, in *Star Formation in Stellar Systems*, ed. G. Tenorio-Tagle, M. Prieto, & F. Sanchez, 125
- Leroy, A. K. et al. 2009, *AJ*, 137, 4670
- Lewis, J. R. et al. 2006, in *Astronomical Society of the Pacific Conference Series*, Vol. 351, *Astronomical Data Analysis Software and Systems XV*, ed. C. Gabriel, C. Arviset, D. Ponz, & S. Enrique, 255
- Li, Y. & Bryan, G. L. 2014, *ApJ*, 789, 153

- Lilly, S. J. & Longair, M. S. 1984, MNRAS, 211, 833
- Lim, J., Ao, Y., & Dinh-V-Trung. 2008, ApJ, 672, 252
- Lynden-Bell, D. 1969, Nature, 223, 690
- Maccagni, F. M., Morganti, R., Oosterloo, T. A., Geréb, K., & Maddox, N. 2017, A&A, 604, A43
- Maccagni, F. M., Morganti, R., Oosterloo, T. A., & Mahony, E. K. 2014, A&A, 571, A67
- Maccagni, F. M., Morganti, R., Oosterloo, T. A., Oonk, J. B. R., & Emonts, B. H. C. 2018, A&A, 614, A42
- Madau, P., Pozzetti, L., & Dickinson, M. 1998, ApJ, 498, 106
- Magorrian, J., Tremaine, S., Richstone, D., Bender, R., Bower, G., Dressler, A., Faber, S. M., Gebhardt, K., Green, R., Grillmair, C., Kormendy, J., & Lauer, T. 1998, AJ, 115, 2285
- Malmquist, K. G. 1924, Meddelanden fran Lunds Astronomiska Observatorium Serie II, 32, 3
- Maraston, C. 2005, MNRAS, 362, 799
- Mauch et al. 2003, MNRAS, 342, 1117
- Mauch, T. & Sadler, E. M. 2007, MNRAS, 375, 931
- McAlpine, K., Jarvis, M. J., & Bonfield, D. G. 2013, MNRAS, 436, 1084
- McAlpine, K., Smith, D. J. B., Jarvis, M. J., Bonfield, D. G., & Fleuren, S. 2012, MNRAS, 423, 132
- McCarthy, P. J. 1993, ARA&A, 31, 639
- McCarthy, P. J., Kapahi, V. K., van Breugel, W., Persson, S. E., Athreya, R., & Subrahmanya, C. R. 1996, ApJS, 107, 19
- McCarthy, P. J., van Breugel, W., Spinrad, H., & Djorgovski, S. 1987, ApJ, 321, L29
- McKee, C. F. & Ostriker, J. P. 1977, ApJ, 218, 148
- McLure, R. J. & Jarvis, M. J. 2002, MNRAS, 337, 109
- McLure, R. J., Willott, C. J., Jarvis, M. J., Rawlings, S., Hill, G. J., Mitchell, E., Dunlop, J. S., & Wold, M. 2004a, MNRAS, 351, 347
- McLure, R. J. et al. 2004b, MNRAS, 353, L45
- McMahon, R. et al. 2013, The Messenger, 154, 35

- McMullin, J. P., Waters, B., Schiebel, D., Young, W., & Golap, K. 2007, in *Astronomical Society of the Pacific Conference Series*, Vol. 376, *Astronomical Data Analysis Software and Systems XVI*, ed. R. A. Shaw, F. Hill, & D. J. Bell, 127
- McNamara, B. R., Wise, M., Nulsen, P. E. J., David, L. P., Sarazin, C. L., Bautz, M., Markevitch, M., Vikhlinin, A., Forman, W. R., Jones, C., & Harris, D. E. 2000, *ApJ*, 534, L135
- McNamara, B. R. et al. 2014, *ApJ*, 785, 44
- Mie, G. 1908, *Annalen der Physik*, 330, 377
- Miley, G. 1980, *ARA&A*, 18, 165
- Miley, G. & De Breuck, C. 2008, *A&A Rev.*, 15, 67
- Miley, G. K. 1968, *Nature*, 218, 933
- Miley, G. K., Overzier, R. A., Zirm, A. W., Ford, H. C., Kurk, J., Pentericci, L., Blakeslee, J. P., Franx, M., Illingworth, G. D., Postman, M., Rosati, P., Röttgering, H. J. A., Venemans, B. P., & Helder, E. 2006, *ApJ*, 650, L29
- Mills, B. Y. 1981, *Proceedings of the Astronomical Society of Australia*, 4, 156
- Minkowski, R. 1960, *ApJ*, 132, 908
- Miyoshi, M., Moran, J., Herrnstein, J., Greenhill, L., Nakai, N., Diamond, P., & Inoue, M. 1995, *Nature*, 373, 127
- Morganti, R. & Oosterloo, T. 2018, arXiv e-prints
- Morganti, R., Sadler, E. M., & Curran, S. 2015, *Advancing Astrophysics with the Square Kilometre Array (AASKA14)*, 134
- Narayanan, D., Cox, T. J., Shirley, Y., Davé, R., Hernquist, L., & Walker, C. K. 2008, *ApJ*, 684, 996
- Neeser, M. J., Eales, S. A., Law-Green, J. D., Leahy, J. P., & Rawlings, S. 1995, *ApJ*, 451, 76
- Nesvadba, N. P. H., Lehnert, M. D., Eisenhauer, F., Gilbert, A., Tecza, M., & Abuter, R. 2006, *ApJ*, 650, 693
- Neugebauer, G. et al. 1984, *ApJ*, 278, L1
- Nilsson, K., Valtonen, M. J., Kotilainen, J., & Jaakkola, T. 1993, *ApJ*, 413, 453
- Norris, R. P. et al. 2011, *PASA*, 28, 215
- Novak, G. S., Faber, S. M., & Dekel, A. 2006, *ApJ*, 637, 96

- Novak, M. et al. 2017, *A&A*, 602, A5
- Nulsen, P. E. J. & Fabian, A. C. 2000, *MNRAS*, 311, 346
- O'Dea, C. P., Baum, S. A., & Stanghellini, C. 1991, *ApJ*, 380, 66
- Omont, A. et al. 2013, *A&A*, 551, A115
- Oosterloo, T., Verheijen, M. A. W., van Cappellen, W., Bakker, L., Heald, G., & Ivashina, M. 2009, in *Wide Field Astronomy & Technology for the Square Kilometre Array*, 70
- Osterbrock, D. E. 1978, *Proceedings of the National Academy of Science*, 75, 540
- Osterbrock, D. E. & Ferland, G. J. 2006, *Astrophysics of gaseous nebulae and active galactic nuclei* (University science books)
- Overzier, R. A., Harris, D. E., Carilli, C. L., Pentericci, L., Röttgering, H. J. A., & Miley, G. K. 2005, *A&A*, 433, 87
- Panter, B., Jimenez, R., Heavens, A. F., & Charlot, S. 2007, *MNRAS*, 378, 1550
- Papadopoulos, P. P., Greve, T. R., Ivison, R. J., & De Breuck, C. 2005, *A&A*, 444, 813
- Papadopoulos, P. P., Röttgering, H. J. A., van der Werf, P. P., Guilloteau, S., Omont, A., van Breugel, W. J. M., & Tilanus, R. P. J. 2000, *ApJ*, 528, 626
- Papovich, C. 2008, *ApJ*, 676, 206
- Pei, Y. C. 1995, *ApJ*, 438, 623
- Pentericci, L., McCarthy, P. J., Röttgering, H. J. A., Miley, G. K., van Breugel, W. J. M., & Fosbury, R. 2001, *ApJS*, 135, 63
- Pentericci, L., Röttgering, H. J. A., Miley, G. K., McCarthy, P., Spinrad, H., van Breugel, W. J. M., & Macchetto, F. 1999, *A&A*, 341, 329
- Pentericci, L., Van Reeve, W., Carilli, C. L., Röttgering, H. J. A., & Miley, G. K. 2000, *A&AS*, 145, 121
- Pérez-Torres, M. A. & De Breuck, C. 2005, *MNRAS*, 363, L41
- Pérez-Torres, M. A., De Breuck, C., van Breugel, W., & Miley, G. 2006, *Astronomische Nachrichten*, 327, 245
- Perley, R. A. & Butler, B. J. 2013, *ApJS*, 204, 19
- Perley, R. A., Chandler, C. J., Butler, B. J., & Wrobel, J. M. 2011, *ApJ*, 739, L1
- Peterson, B. 1997, *An introduction to active galactic nuclei* (Cambridge university press)
- Podariu, S., Daly, R. A., Mory, M. P., & Ratra, B. 2003, *ApJ*, 584, 577

- Pracy, M. B. et al. 2016, MNRAS, 460, 2
- Prescott, M. et al. 2016, MNRAS, 457, 730
- Preston, R. A., Morabito, D. D., & Jauncey, D. L. 1983, ApJ, 269, 387
- Privon, G. C., Herrero-Illana, R., Evans, A. S., Iwasawa, K., Perez-Torres, M. A., Armus, L., Díaz-Santos, T., Murphy, E. J., Stierwalt, S., Aalto, S., Mazzarella, J. M., Barcos-Muñoz, L., Borish, H. J., Inami, H., Kim, D. C., Treister, E., Surace, J. A., Lord, S., Conway, J., Frayer, D. T., & Alberdi, A. 2015, ApJ, 814, 39
- Rawlings, S., Eales, S., & Lacy, M. 2001, MNRAS, 322, 523
- Rawlings, S. & Jarvis, M. J. 2004, MNRAS, 355, L9
- Rawlings, S. & Saunders, R. 1991, Nature, 349, 138
- Reuland et al. 2007, AJ, 133, 2607
- Reuland, M., Röttgering, H., van Breugel, W., & De Breuck, C. 2004, MNRAS, 353, 377
- Reuland, M., van Breugel, W., Röttgering, H., de Vries, W., De Breuck, C., & Stern, D. 2003, ApJ, 582, L71
- Riechers, D. A., Walter, F., Carilli, C. L., & Bertoldi, F. 2007, ApJ, 671, L13
- Riechers, D. A. et al. 2013, Nature, 496, 329
- Rigby, E. E., Argyle, J., Best, P. N., Rosario, D., & Röttgering, H. J. A. 2015, A&A, 581, A96
- Rocca-Volmerange, B., Le Borgne, D., De Breuck, C., Fioc, M., & Moy, E. 2004, A&A, 415, 931
- Rocca-Volmerange, B. & Remazeilles, M. 2005, A&A, 433, 73
- Röttgering, H., de Bruyn, G., & Pentericci, L. 1999, in *The Most Distant Radio Galaxies*, ed. H. J. A. Röttgering, P. N. Best, & M. D. Lehnert, 113
- Röttgering, H. J. A., Best, P. N., De Breuck, C., Kurk, J., Pentericci, L., & van Breugel, W. 2000, in *Perspectives on Radio Astronomy: Science with Large Antenna Arrays*, ed. M. P. van Haarlem, 65
- Röttgering, H. J. A., Lacy, M., Miley, G. K., Chambers, K. C., & Saunders, R. 1994, A&AS, 108, 79
- Röttgering, H. J. A., Miley, G. K., Chambers, K. C., & Macchetto, F. 1995, A&AS, 114, 51
- Röttgering, H. J. A., van Ojik, R., Miley, G. K., Chambers, K. C., van Breugel, W. J. M., & de Koff, S. 1997, A&A, 326, 505

- Roychowdhury, S., Chengalur, J. N., Begum, A., & Karachentsev, I. D. 2009, *MNRAS*, 397, 1435
- Ruffa, I. et al. 2019, *MNRAS*, 484, 4239
- Russell, H. R., McNamara, B. R., Edge, A. C., Hogan, M. T., Main, R. A., & Vantyghem, A. N. 2013, *MNRAS*, 432, 530
- Russell, H. R. et al. 2016, *MNRAS*, 458, 3134
- Sadler, E. M., Ekers, R. D., Mahony, E. K., Mauch, T., & Murphy, T. 2014, *MNRAS*, 438, 796
- Sadler, E. M. & Hunstead, R. W. 2002, in *IAU Symposium*, Vol. 199, *The Universe at Low Radio Frequencies*, ed. A. Pramesh Rao, G. Swarup, & Gopal-Krishna, 11
- Sadler, E. M. et al. 2007, *MNRAS*, 381, 211
- Salomé, P. et al. 2006, *A&A*, 454, 437
- Salpeter, E. E. 1955, *ApJ*, 121, 161
- Sánchez, C. et al. 2014, *MNRAS*, 445, 1482
- Sanders, D. B. & Mirabel, I. F. 1996, *ARA&A*, 34, 749
- Sanders, D. B., Scoville, N. Z., & Soifer, B. T. 1991, *ApJ*, 370, 158
- Sault, R. J., Teuben, P. J., & Wright, M. C. H. 1995, in *Astronomical Society of the Pacific Conference Series*, Vol. 77, *Astronomical Data Analysis Software and Systems IV*, ed. R. A. Shaw, H. E. Payne, & J. J. E. Hayes, 433
- Scharf, C., Smail, I., Ivison, R., Bower, R., van Breugel, W., & Reuland, M. 2003, *ApJ*, 596, 105
- Schaye, J. et al. 2015, *MNRAS*, 446, 521
- Schilizzi, R. T., Miley, G. K., van Ardenne, A., Baud, B., Bååth, L., Rönnäng, B. O., & Pauliny-Toth, I. I. K. 1979, *A&A*, 77, 1
- Schmidt, M. 1959, *ApJ*, 129, 243
- . 1963, *Nature*, 197, 1040
- Schmidt, S., Connolly, A., & Hopkins, A. 2006, in *American Astronomical Society Meeting Abstracts*, Vol. 209, 52.06
- Scoville, N. Z. & Solomon, P. M. 1975, *ApJ*, 199, L105
- Scoville, N. Z., Yun, M. S., Windhorst, R. A., Keel, W. C., & Armus, L. 1997, *ApJ*, 485, L21

- Seymour, N. et al. 2007, ApJS, 171, 353
- Sijacki, D. et al. 2015, MNRAS, 452, 575
- Silk, J. & Rees, M. J. 1998, A&A, 331, L1
- Simpson, C. & Eisenhardt, P. 1999, PASP, 111, 691
- Skrutskie, M. F. et al. 2006, AJ, 131, 1163
- Smith, D. J. B. et al. 2011, MNRAS, 416, 857
- Smith, H. E. & Spinrad, H. 1980, PASP, 92, 553
- Smolčić, V. et al. 2017, A&A, 602, A6
- Solomon, P. M., Downes, D., & Radford, S. J. E. 1992, ApJ, 387, L55
- Spinrad, H. 1976, PASP, 88, 565
- Spinrad, H., Westphal, J., Kristian, J., & Sandage, A. 1977, ApJ, 216, L87
- Springel, V. et al. 2005, Nature, 435, 629
- Stahler, S. W. & Palla, F. 2004, The Formation of Stars (Wiley-VCH Verlag GmbH & co.KGAA)
- Stevens, J. A. et al. 2003, Nature, 425, 264
- Sutherland, W. & Saunders, W. 1992, MNRAS, 259, 413
- Sutherland, W. et al. 2015, A&A, 575, A25
- Tadhunter, C. N., Morganti, R., Robinson, A., Dickson, R., Villar-Martin, M., & Fosbury, R. A. E. 1998, MNRAS, 298, 1035
- Tavecchio, F., Maraschi, L., Sambruna, R. M., & Urry, C. M. 2000, ApJ, 544, L23
- Taylor, M. B. 2005, in Astronomical Society of the Pacific Conference Series, Vol. 347, Astronomical Data Analysis Software and Systems XIV, ed. P. Shopbell, M. Britton, & R. Ebert, 29
- Thomas, D., Maraston, C., Bender, R., & Mendes de Oliveira, C. 2005, ApJ, 621, 673
- Tielens, A. G. G. M., Miley, G. K., & Willis, A. G. 1979, A&AS, 35, 153
- Tingay, S. J. et al. 2013, PASA, 30, e007
- Torres, D. F. 2003, arXiv Astrophysics e-prints
- Tremblay, G. R. et al. 2016, Nature, 534, 218

- Uson, J. M., Bagri, D. S., & Cornwell, T. J. 1991, *Phys. Rev. Lett.*, 67, 3328
- van Breugel, W., Filippenko, A. V., Heckman, T., & Miley, G. 1985a, *ApJ*, 293, 83
- van Breugel, W., Heckman, T., Butcher, H., & Miley, G. 1984, *ApJ*, 277, 82
- van Breugel, W., Miley, G., Heckman, T., Butcher, H., & Bridle, A. 1985b, *ApJ*, 290, 496
- van Breugel, W. J. M., Stanford, S. A., Spinrad, H., Stern, D., & Graham, J. R. 1998, *ApJ*, 502, 614
- van Haarlem, M. P. et al. 2013, *A&A*, 556, A2
- van Ojik, R., Roettgering, H. J. A., Carilli, C. L., Miley, G. K., Bremer, M. N., & Macchetto, F. 1996, *A&A*, 313, 25
- van Ojik, R., Roettgering, H. J. A., Miley, G. K., & Hunstead, R. W. 1997, *A&A*, 317, 358
- Venemans, B. et al. 2007, *MNRAS*, 376, L76
- Vernet, J., Fosbury, R. A. E., Villar-Martín, M., Cohen, M. H., Cimatti, A., di Serego Alighieri, S., & Goodrich, R. W. 2001a, *A&A*, 370, 407
- Vernet, J., Fosbury, R. A. E., Villar-Martín, M., et al. 2001b, *A&A*, 366, 7
- Villar-Martin, M. & Binette, L. 1997, *A&A*, 317, 350
- Villar-Martín, M., Sánchez, S. F., De Breuck, C., Peletier, R., Vernet, J., Rettura, A., Seymour, N., Humphrey, A., Stern, D., di Serego Alighieri, S., & Fosbury, R. 2006, *MNRAS*, 366, L1
- Villar-Martín, M., Sánchez, S. F., Humphrey, A., Dijkstra, M., di Serego Alighieri, S., De Breuck, C., & González Delgado, R. 2007, *MNRAS*, 378, 416
- Villar-Martin, M., Tadhunter, C., & Clark, N. 1997, *A&A*, 323, 21
- Villar-Martín, M., Tadhunter, C., Morganti, R., Axon, D., & Koekemoer, A. 1999, *MNRAS*, 307, 24
- Villar-Martin, M., Tadhunter, C., Morganti, R., Clark, N., Killeen, N., & Axon, D. 1998, *A&A*, 332, 479
- Villar-Martín, M., Vernet, J., di Serego Alighieri, S., Fosbury, R., Humphrey, A., & Pentericci, L. 2003, *MNRAS*, 346, 273
- Voges, W. 1993, *Advances in Space Research*, 13
- Waddington, I., Windhorst, R. A., Cohen, S. H., Partridge, R. B., Spinrad, H., & Stern, D. 1999, *ApJ*, 526, L77

- Walter, F., Brinks, E., de Blok, W. J. G., Thornley, M. D., & Kennicutt, R. C. 2005, in *Astronomical Society of the Pacific Conference Series*, Vol. 331, *Extra-Planar Gas*, ed. R. Braun, 269
- Williams, R. E., Blacker, B., Dickinson, M., Dixon, W. V. D., Ferguson, H. C., Fruchter, A. S., Giavalisco, M., Gilliland, R. L., Heyer, I., Katsanis, R., Levay, Z., Lucas, R. A., McElroy, D. B., Petro, L., Postman, M., Adorf, H.-M., & Hook, R. 1996, *AJ*, 112, 1335
- Willott, C. J., Rawlings, S., Blundell, K. M., Lacy, M., & Eales, S. A. 2001, *MNRAS*, 322, 536
- Willott, C. J., Rawlings, S., Jarvis, M. J., & Blundell, K. M. 2003, *MNRAS*, 339, 173
- Wilman, R. J., Jarvis, M. J., Röttgering, H. J. A., & Binette, L. 2004, *MNRAS*, 351, 1109
- Wolfire, M. G., Hollenbach, D., & McKee, C. F. 2010, *ApJ*, 716, 1191
- Wolfire, M. G., McKee, C. F., Hollenbach, D., & Tielens, A. G. G. M. 2003, *ApJ*, 587, 278
- Wong, T. & Blitz, L. 2002, *ApJ*, 569, 157
- Wright, A. H. et al. 2017, *MNRAS*, 470, 283
- Wright, E. L., Eisenhardt, P. R. M., Mainzer, A. K., et al. 2010, *AJ*, 140, 1868
- York, D. G. et al. 2000, *AJ*, 120, 1579
- Zacharias, N. et al. 2013, *AJ*, 145, 44
- Zirbel, E. L. 1996, *ApJ*, 473, 713
- Zirm, A. W. et al. 2005, *ApJ*, 630, 68





UNIVERSITY *of the*
WESTERN CAPE